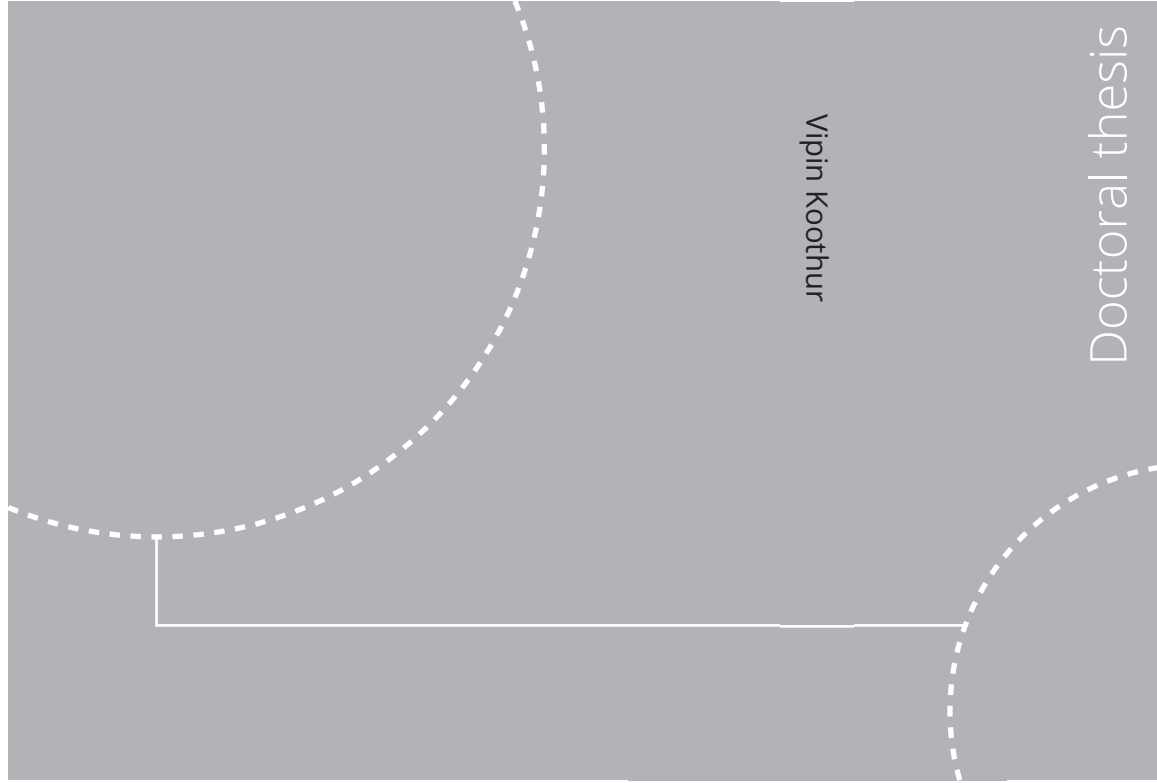


ISBN 978-82-326-6456-6 (printed ver.)
ISBN 978-82-326-6710-9 (electronic ver.)
ISSN 1503-8181 (printed ver.)
ISSN 2703-8084 (electronic ver.)



Doctoral theses at NTNU, 2020:219

Vipin Koothur

Tracking and sizing of particles
in the Mie scattering regime
using a laser scanning
technique

Doctoral theses at NTNU, 2020:219

NTNU
Norwegian University of
Science and Technology
Thesis for the degree of
Philosophiae Doctor
Faculty of Engineering
Department of Energy and Process Engineering

 **NTNU**
Norwegian University of
Science and Technology

 NTNU

 **NTNU**
Norwegian University of
Science and Technology

Vipin Koothur

Tracking and sizing of particles in the Mie scattering regime using a laser scanning technique

Thesis for the degree of Philosophiae Doctor

Trondheim, June 2021

Norwegian University of Science and Technology
Faculty of Engineering
Department of Energy and Process Engineering



Norwegian University of
Science and Technology

NTNU

Norwegian University of Science and Technology

Thesis for the degree of Philosophiae Doctor

Faculty of Engineering

Department of Energy and Process Engineering

© Vipin Koothur

ISBN 978-82-326-6456-6 (printed ver.)

ISBN 978-82-326-6710-9 (electronic ver.)

ISSN 1503-8181 (printed ver.)

ISSN 2703-8084 (electronic ver.)

Doctoral theses at NTNU, 2020:219



Printed by Skipnes Kommunikasjon AS

For the hard work and sacrifices of my family for my education

Declaration

I hereby declare that except where specific reference is made to the work of others, the contents of this dissertation are original and have not been submitted in whole or in part for consideration for any other degree or qualification in this, or any other university. This dissertation is my own work and contains nothing which is the outcome of work done in collaboration with others, except as specified in the text. This dissertation contains fewer than 45,000 words including appendices, bibliography, footnotes, tables and equations and has fewer than 200 figures.

Vipin Koothur

June 2021

Acknowledgements

First and foremost I extend my greatest gratitude for the love and support of my parents and my sister. Their love and patience from the other side of the world has been the main driving force behind the completion of this study. I am also thankful for the friendship and the support from Shareq, Niranjan, Athul, Renil, George, Akhil, Prajin, Anuvansh, Riju, Abilash and Vivek. The time spent with each of you have always made Trondheim a home away from home. I would also like to thank a few of my past and present colleagues Øyvind, Anna, Dhiren, Dirren, Yi Hao and Harish, for the good times we were able to spend in our office.

I would like to acknowledge the supervision I have received from my supervisor, James Dawson. Similarly, the discussions with Nicholas Worth and Melissa were very instructive and helpful. I am thankful for their valuable comments on my thesis.

Lastly Yamini, I thank you for your constant support. I consider myself very lucky to have you as my life partner. You soak up all my worries and keep me positive.

Table of contents

List of figures	11
List of tables	19
Nomenclature	21
Introduction	1
0.1 Background, motivation and objectives	1
0.2 Outline of the thesis	4
0.3 Papers included in the thesis	5
1 Literature review	7
1.1 Particle tracking	7
1.1.1 Comparison of the relevant particle tracking techniques	9
1.2 Scanning technique	14
1.3 Particles sizing in the Mie scattering regime	14
1.3.1 Description of particle diameter	17
1.3.2 Comparison of the relevant particle sizing techniques	19
1.3.3 Limitations of the existing particle sizing techniques	22
1.4 Summary	23
2 Methodology	25
2.1 Scanning system	25
2.2 Calibration	27
2.2.1 Camera model	28
2.2.2 Camera calibration	29
2.2.3 Laser sheet calibration	30
2.3 Data processing	30
2.3.1 Detection of particle image locations	32
2.3.2 Triangulation	32

Table of contents

2.3.3	Estimating the scattered intensity (I_s) of the particles	36
2.3.4	Building the trajectories	36
2.3.5	Particle trajectory processing	37
2.3.6	Estimating the scattering angle (θ_s) of the particles	40
2.3.7	Estimating particle sizes	41
2.4	Data verification	44
2.5	Summary	44
3	Numerical simulation	47
3.1	Introduction	47
3.2	Synthetic particle image generation for the scanning setup	49
3.3	Study of experimental parameters for particle tracking	49
3.3.1	Controllable experimental parameters	49
3.3.2	Uncontrollable experimental parameters	57
3.4	Verification of tracking via synthetic experiment	58
3.4.1	Lagrangian statistics	60
3.5	Experimental design for particle sizing	64
3.5.1	Measurement area and configuration	65
3.5.2	Camera angle	67
3.5.3	Measurable size range	67
3.5.4	Camera aperture	68
3.5.5	Number of Cameras	69
3.6	Synthetic experiments with known sizes	70
3.6.1	Effect of noise in scattered intensity	72
3.6.2	Effect of noise in scattering angle	75
3.7	Numerical experiment in a turbulent channel flow	79
3.7.1	Numerical experiment parameters	80
3.7.2	Results from particle tracking	83
3.7.3	Results from particle sizing	93
3.8	Summary	101
4	Experimental Results	103
4.1	Introduction	103
4.2	Experimental setup	103
4.2.1	Flow facility	105
4.2.2	Camera configuration	107
4.2.3	Scanning optics	107
4.2.4	Seeding and water temperature	108
4.2.5	Characteristic scales of the flow	108

4.3	Particle tracks	108
4.3.1	Algorithm parameters for tracking	108
4.3.2	Track length	109
4.4	Velocity fields and statistics	111
4.5	Velocity gradients	118
4.5.1	Quality of velocity gradients	120
4.5.2	Vorticity and strain	120
4.6	Acceleration measurements	123
4.6.1	Quality of the temporal derivatives	124
4.6.2	Acceleration alignment	124
4.6.3	Acceleration variance	124
4.6.4	Acceleration probability density functions	127
4.6.5	Acceleration intermittency	127
4.7	Particle size	129
4.7.1	Results from two camera combinations	132
4.7.2	Results from all three camera combination	138
4.7.3	Effect of track length on sizing	138
4.7.4	Sizing different sized particles simultaneously	141
4.8	Summary	144
5	Summary and conclusions	147
5.1	Scanning particle tracking	147
5.2	Scanning particle sizing	148
5.3	Future Work	149
5.4	Prospectives	150
	References	151
	Appendix A Generalized Mie theory for a spherical particle	157
	Appendix B Laser sheet calibration	159
	Appendix C Modified particle tracking heuristics	161

List of figures

1.1	The general setup of an epipolar geometry. The shaded gray region represents the epipolar plane and the red lines represents the epipolar lines. . .	9
1.2	Particle track obtained using 3D PTV. The spherical markers represents the particle position and the color code represents the magnitude of acceleration (Porta <i>et al.</i> (2001)).	10
1.3	Acceleration check to show a better assessment on the accuracy of the velocity derivatives. The x-axis represents the Lagrangian acceleration and the y-axis represents the sum of local and convective acceleration (Hoyer <i>et al.</i> (2005)).	11
1.4	(a) Particle linking procedure in TOMO-PTV, using the cross correlated velocity field as the predictor. (b) Polynomial fits of nth orders, to reduce the truncation error for complex trajectories (Novara & Scarano (2013)). .	12
1.5	A comparison isosurfaces of vortices obtained from (a) TOMO-PIV and (b) combination of STB and 'FlowFit' interpolation scheme. The colorcode represents streamwise velocity (Schanz <i>et al.</i> (2016)).	13
1.6	Relationship of the scattered intensity with respect to particle diameter, in the three scattering regimes. Adapted (Tropea (2011))	15
1.7	Scattered light by a $1\mu\text{m}$ (left) and a $10\mu\text{m}$ oil particle in air. Adapted (Raffel <i>et al.</i> , 2018)	16
1.8	Mie scattering geometry. Adpated LePera (2012)	17
1.9	Mie theory calculations of scattered intensity as a function of angle for water particles with refractive index n 1.33. The particle size parameters α are (a) 10, 50 and 100 (b) 59 and 60.	18
1.10	Optical schematic of a Phase Doppler Technique (Tropea <i>et al.</i> , 1996). . .	20
1.11	Generation of focused and defocused images from a spherical particle by using an optical imaging system (Damaschke <i>et al.</i> , 2005).	20
1.12	Optical Schematic of a Laser sheet droplet sizing.	21

2.1	a Schematic of a typical scanning setup. b Schematic of the optics used in a typical scanning experiment (Lawson (2015)).	26
2.2	Typical timing diagram of a scanning acquisition (Lawson, 2015).	27
2.3	Schematic of a pinhole camera model (Tsai (1987)).	28
2.4	Measured (o) and re-projected (x) measured marker positions for one position of the calibration plate, before (red) and after (blue) bundle calibration. The inset shows a zoomed in version of the marked region in either sub figure (Lawson, 2015).	30
2.5	Flow chart for scanning particle tracking and sizing.	31
2.6	Schematic comparison of particle matching in classical triangulation used by Maas <i>et al.</i> (1993), in scanning technique used by Hoyer <i>et al.</i> (2005) and in the present study	33
2.7	Variation in intensity of a particle as a function of nominal sheet number. A Gaussian fit gives the fractional sheet number and peak intensity at that fitted sheet number for the particle in the scan.	34
2.8	Schematic representation of three camera triangulation in the scanning technique. The epipolar lines of view a in view b is represented as e_{a-b}	35
2.9	Schematic representation of the particle tracking algorithm.	38
2.10	Schematic definition of (a) camera angle θ_0 and azimuthal angle ϕ_0 (b) scattering angle θ_s and the corresponding azimuthal angle ϕ_s of particle in the field of view.	40
2.11	(a) Number of peaks in the oscillation of scattering intensity per unit scattering angle, for increasing particle size (b) Relationship between the number of fringes to the fringe position in the Mie pattern for increasing particle size.	42
2.12	Scattering data for particles with (a) $50.4\mu\text{m}$ diameter ($\alpha = 59.5$) and (b) $56.2\mu\text{m}$ diameter ($\alpha = 66.4$); incident laser light ($\lambda = 532\text{nm}$). The best fit is to particles with $50.4\mu\text{m}$ and $56.6\mu\text{m}$	43
3.1	Fraction of successfully triangulated particles, given the known ‘ground truth’ locations: the nominal sheet number n_s as in Hoyer <i>et al.</i> (2005), and the fitted sheet number f_s	51
3.2	Positional error in ‘truly’ detected triangulated particle location for the current scanning PTV: \circ , mean error and ∇ , standard deviation in error	52
3.3	(a) Number of sheets N_s required as a function of sheet overlap $w/\Delta z$ for different sheet thicknesses L_z/w ; (b) fraction of particles successfully fitted	53
3.4	Fraction of overlapping particles for different sheet thicknesses L_z/w	55

3.5	Error in linearly-corrected triangulated particle locations for different sheet speeds u_s/u'_{rms} ; \circ , mean error and ∇ , standard deviation in error; curves in black, $N_V = 1.8 \times 10^{-4}$ ppv ($N_I \approx 0.05$ ppp); curves in blue, $N_V = 1.8 \times 10^{-5}$ ppv ($N_I \approx 0.005$ ppp)	56
3.6	(a) Mean error in 2D particle image detection as a function of particle density N_V for four different random noise levels {5%, 10%, 15%, 20%}, curves darkening with increasing noise level; (b) fraction of successfully triangulated particles, given the known ‘ground truth’ locations; curves and N_V range same as in (a)	57
3.7	(a) Intensity variation of a single particle over five sheets within a scan, for three different sheet shape factors s ; (b) error in triangulated particle location for the different shape factors for the medium-density case with $N_V = 1.8 \times 10^{-4}$ ppv ($N_I \approx 0.05$ ppp): \circ , mean positional error; ∇ , standard deviation of positional error	59
3.8	Particle tracks for two different samples, demonstrating variations in structures for the selected ‘slab’ of turbulence. Tracks are coloured by the magnitude of the velocity vector $\mathbf{u} = (u, v, w)$ along each track at each point in time. Subfigures a) and c) are the tracks obtained from measurement and subfigures b) and d) are their respective “true” tracks.	63
3.9	Probability density function (PDF) of the components of Lagrangian acceleration normalized by the standard deviation for each component: for the present LPT methodology: \bullet a_x , \bullet a_y , \bullet a_z ; from pseudo-tracking directly within the DNS fields: \blacktriangle a_x , \blacktriangle a_y , \blacktriangle a_z ; repeating the synthetic experiment with a lower equivalent particle image density $N_I \approx 0.005$ ppp: a_x , a_y , a_z . Accelerations are computed from tracks of length $\approx 0.75 \tau_\eta$ in time from which measurements are bootstrapped along the lengths to increase statistical convergence; 201, fit from Voth <i>et al.</i> (2002): $P(a) = C \exp(-a^2/((1 + a\beta/\sigma ^\gamma)\sigma^2))$, where $\beta = 0.539$, $\gamma = 1.588$, and $\sigma = 0.508$; , Gaussian distribution with the same standard deviation as $P(a_x)$	64
3.10	Acceleration check (joint PDF) relating Lagrangian, local and convective accelerations; in black, for the high density ($N_I \approx 0.05$ ppp) case; in blue, for the low density ($N_I \approx 0.005$ ppp) case. The high correlation coefficient (value of Q) between the two sides of (3.7) for the high density case demonstrates good spatial resolution	65
3.11	(a) The effect of increasing distance of imaging, on the minimum particle displacement required to cover two scattering peaks, for increasing water particle diameters (b) The minimum particle displacement required to cover two scattering peaks for three different angles with respect to the laser sheet.	66

3.12	The effect of increasing solid angle on the amplitude of the scattering intensity variation with scattering angles for a particle of size $50\mu m$	68
3.13	Comparison of the fraction of successfully triangulated particles using two camera, three and four camera views, at a seeding density of 0.05ppp. . .	70
3.14	Examples of particle images with added noise.	72
3.15	Number fraction of truly sized particles, for noise levels of 0, 2, 5 and 10 %. . .	73
3.16	Comparison of: (a) Lagrangian track of a particle for different noise cases; (b) scattering intensity distribution w.r.t scattering angle of the corresponding particle with the best Mie fit, for the different noise cases.	74
3.17	Percentage deviation in the measured scattered intensity from the actual scattered intensity for increasing noise.	75
3.18	(a) Comparison of fraction of successfully tracked and sized particles for increasing noise cases. Here I,G,P stands for ideal case, Gaussian noise and Poisson noise cases respectively. (b) Mean and rms error, normalized by η , for different levels of noise.	76
3.19	Comparison of: (a) Lagrangian track of a particle for different misalignment cases; (b) scattering intensity distribution w.r.t scattering angle of the corresponding particle with the best Mie fit, for the different camera misalignment cases.	77
3.20	a Comparison of fraction of successfully tracked and sized particles for increasing misalignment cases. Here M stands for misalignment. b Mean and rms error, normalized by η , for different levels of camera misalignment.	78
3.21	Rms error in the measured sizes for the varying size ranges, at different camera misalignment cases.	79
3.22	Measurement domain chosen for the numerical experiment for the turbulent channel flow with particle seeding density of 0.05 ppp (around 35000 particles).	81
3.23	Particle size distribution inserted in a sample of volume.	81
3.24	Comparison of the two schemes of linear approximation and central difference in estimating (a) velocity components (b) acceleration components for all points along a track and (c) acceleration components excluding the two end points of a track. The markers represent those calculated using linear approximation and solid lines represents values calculated using central difference scheme.	84
3.25	(a) Mean of the difference between measured and real DNS velocity; (b) rms of difference between measured and DNS velocity.	85
3.26	(a) Lagrangian tracks of the turbulent channel flow obtained from scanning particle tracking and (b) a snapshot of an instantaneous 3D velocity field obtained by interpolating the Lagrangian velocities to grid points.	87

3.27	(a) Measured particle tracks within the viscous sub-layer ($y^+ < 10^1$) and (b) buffer layer ($10^1 < y^+ < 10^2$).	88
3.28	Mean velocity profile from Lagrangian and interpolated Eulerian fields, plotted with the DNS of equal Reynolds number.	89
3.29	Comparison of probability density functions for the diagonal components of the velocity gradient tensor from the reference DNS to that calculated using 'n' nearest particles within a distance of (a) $3d_o$, (b) $4d_o$, (c) $5d_o$ and (d) $6d_o$, from the point of estimation for a seeding density of 0.025 ppp. . .	90
3.30	Comparison of probability density functions for the diagonal components of the velocity gradient tensor from the reference DNS to that calculated using 'n' nearest particles within a distance of (a) $3d_o$, (b) $4d_o$, (c) $5d_o$ and (d) $6d_o$, from the point of estimation for a seeding density of 0.05 ppp. . .	91
3.31	Comparison of probability density functions for the diagonal components of the velocity gradient tensor from the reference DNS to that calculated using 'n' nearest particles within a distance of (a) $3d_o$, (b) $4d_o$, (c) $5d_o$ and (d) $6d_o$, from the point of estimation for a seeding density of 0.1 ppp. . .	92
3.32	Average number of particles within the selected search radius for nearby particle for different seeding densities: \triangle $ppp = 0.025$, \square $ppp = 0.05$, \circ $ppp = 0.1$. . .	92
3.33	Mean acceleration profile obtained from the tracking measurement compared to the profile obtained from DNS at $Re_\tau = 1440$ by Nickolas <i>et al.</i> (2017). . .	94
3.34	(a) Example of scattering peaks within the measurement domain for particles of size $d_p = 20, 40$ & 80	95
3.35	(a) Minimum displacement required for each particle sizes to apply the mie fit, to retrieve their sizes. (b) Mean displacement estimated for each track length using the mean flow velocity $U_c = 1$	96
3.36	A comparison between the (a) expected size distribution from the measured tracks and (b) measured size distribution using the Mie fitting routine. . .	97
3.37	Number distribution of wrongly sized particles for the chosen track lengths. . .	98
3.38	A comparison between the (a) number distribution of the wrongly sized particle that did not fulfill the minimum displacement criteria for Mie fitting and (b) that in the case of the rightly sized particles.	99
3.39	A comparison between the (a) expected size distribution from the measured tracks and (b) measured size distribution using the Mie fitting routine on interpolated data.	100
4.1	Schematic of the experimental setup.	104
4.2	Flow structures seen when the impeller speed ratio is varied (Poncet <i>et al.</i> , 2008).	105
4.3	Schematic of large mixing tank facility.	106

4.4	Image of the impeller used to rotate the water in the mixing tank.	106
4.5	Image of the camera configuration used for the scanning experiment.	107
4.6	Side and top view images of the scanning optics.	107
4.7	(a) The fraction of particles dropping out of the measurement volume at every time step. (b) The fraction of particle tracks for a certain length.	110
4.8	Example showing particle tracks from a single set with three different fixed track lengths of (a) $1\tau_\eta$ and (b) $2\tau_\eta$. The particle tracks are color coded with magnitude of velocity normalized by the impeller velocity, $u_{imp} = 166\text{mm/s}$	112
4.9	Spatial distribution of the time averaged mean velocity components (a) u_x (b) u_y (c) u_z and (d) the magnitude of velocity $\sqrt{u_x^2 + u_y^2 + u_z^2}$, normalized by the impeller velocity u_{imp} in a x-y plane at the center z-plane of the measurement volume.	113
4.10	Comparison of pdfs of the Lagrangian velocity components normalized by impeller velocity u_{imp} for a track length of $2\tau_\eta$ using (a) all points along track and (b) middle point of the track.	114
4.11	Spatial variation in rms of fluctuating velocity components normalised by the impeller velocity, in a x-y plane at the center z-plane of the measurement volume.	116
4.12	Comparison of pdfs of the fluctuating velocity components normalized by impeller velocity u_{imp} obtained (a) by subtracting the mean velocity obtained over the entire measurement time window or track length (b) by subtracting the mean at each time step.	117
4.13	Measured velocity variance as a function of normalized track length $\Delta t/\tau_\eta$	118
4.14	(a) Skewness of the velocity fluctuations and (b) flatness of the velocity fluctuations for increasing normalized track length $\Delta t/\tau_\eta$	119
4.15	J-PDF of the continuity equation terms, $-\partial u_i/\partial x_i = \partial u_j/\partial x_j + \partial u_k/\partial x_k$	121
4.16	(a) PDFs of the longitudinal velocity gradients ∂u_i	122
4.17	(a) PDFs of enstrophy production $\omega_i\omega_j s_{ij}$ and strain production $-4/3s_{ij}s_{jk}s_{ki}$ terms. The symbols represent similar result from Lüthi <i>et al.</i> (2005) for a von Karman flow. (b) Logarithmic joint PDF of $\omega_i\omega_j s_{ij}$ and $-4/3s_{ij}s_{jk}s_{ki}$	123
4.18	J-PDF of the acceleration terms from all three velocity components, $Du_i/Dt = \partial u_i/\partial t + u_j\partial u_i/\partial x_j$	125
4.19	PDF of the cosine of the angle between the Lagrangian acceleration vector along trajectories, and the summation of the local acceleration and the advective acceleration (circles). PDF of the cosine of the angle between the local acceleration and advective acceleration (stars).	126
4.20	Measured acceleration variance as a function of normalized track length $\Delta t/\tau_\eta$	126

4.21 PDFs of the three components of acceleration components normalized by rms. The solid line represents a stretched exponential form given by Voth <i>et al.</i> (2002).	127
4.22 The relative contribution to the second ($a_x^2 P(a_x) / \langle a_x^2 \rangle$) and fourth moments ($a_x^4 P(a_x) / \langle a_x^4 \rangle$) of the acceleration components.	128
4.23 Contributions to the (a) second ($a_x^2 P(a_x) / \langle a_x^2 \rangle$) and (b) fourth moments ($a_x^4 P(a_x) / \langle a_x^4 \rangle$) of the acceleration components.	129
4.24 Example of best Mie fit for a particle intensity variation over the scattered angle obtained from the three cameras views.	130
4.25 Sample scattering intensity data and best Mie fits over the scattering intensity from camera 1 and camera 2 for a particle from (a) particles with nominal mean diameter of $80\mu\text{m}$ and (b) particles with nominal mean diameter of $40\mu\text{m}$	131
4.26 Example representing the of scattering intensity data and best Mie fits over the scattering intensity from camera 2 and camera 3 for a particle from (a) particles with nominal mean diameter of $80\mu\text{m}$ and (b) particles with nominal mean diameter of $40\mu\text{m}$	132
4.27 Example representing the of scattering intensity data and best Mie fits over the scattering intensity from camera 1 and camera 3 for a particle from (a) particles with nominal mean diameter of $80\mu\text{m}$ and (b) particles with nominal mean diameter of $40\mu\text{m}$	133
4.28 Number distribution and the corresponding SMD determined using the scanning technique, compared to the distribution obtained by the manufacturer (Microbeads AS), using the Coulter principle, for the first batch of particles with nominal mean diameter of $80\mu\text{m}$ with a least squares difference of 0.09 for the three two-camera combinations (a) 1&2 (b) 2&3 and (c) 1&3. . .	134
4.29 Number distribution and the corresponding SMD determined using the scanning technique, compared to the distribution obtained by the manufacturer (Microbeads AS), using the Coulter principle, for the first batch of particles with nominal mean diameter of $40\mu\text{m}$ with a least squares difference of 0.09 for the three two-camera combinations (a) 1&2 (b) 2&3 and (c) 1&3. . .	135
4.30 Comparison fit from three particle sizes over the intensity data distribution from three two camera combinations; (a) Camera 1 and 2 (b) Camera 2 and 3 (c) Camera 2 and 3. In all the plots, the fit from particle shown in red is the real fit.	137
4.31 Examples of particle tracks and corresponding best Mie fits over the scattering intensity to estimate the particle size for the batch number 3I-080-1771 particles, from three track lengths of (a) - (b) $1.5\tau_\eta$; (c) - (d) $2.5\tau_\eta$ and (e) - (f) $3.5\tau_\eta$	139

4.32	Sauter mean diameter obtained using particle size measurements from increasing track lengths.	140
4.33	Comparison of size distributions from three track length bands.	141
4.34	Number distribution and the corresponding SMD determined using the scanning technique, compared to the distribution obtained by the manufacturer (Microbeads AS), using the Coulter principle, for the first batch of particles with nominal size of $80\mu\text{m}$ with a least squares difference of (a) 0.09 (b) 0.05 and (c) 0.01.	142
4.35	Examples of particle tracks and corresponding best Mie fits over the scattering intensity to estimate the particle size for the particles with nominal size of $40\mu\text{m}$, from two track lengths of (a) - (b) $2.5\tau_\eta$ and (c) - (d) $3.5\tau_\eta$	143
4.36	The number distribution the corresponding SMD determined using the scanning technique, compared to the distribution obtained by the manufacturer (Microbeads AS), using the Coulter principle, for the second batch of particles with nominal size of $40\mu\text{m}$, obtained using two least squares difference tolerance of 0.09 and 0.05.	143
4.37	Number distribution from sizing two different sizes simultaneously, determined using the scanning technique, compared to the distribution obtained by the manufacturer (Microbeads AS), using the Coulter principle, for particles with nominal size of $40\mu\text{m}$ and $80\mu\text{m}$	144
A.1	Mie scattering geometry. Adpated LePera (2012)	157
B.1	Illustration of light scattered from a single particle throughout the course of a scan , and its calculated center position based on a Gaussian fit. (Knutsen <i>et al.</i> (2017)).	159
C.1	Schematic representation of the particle tracking algorithm.	162
C.2	Comparison of acceleration pdfs obtained using (a) the particle tracking technique used in this thesis to (b) the modified particle tracking technique.	163

List of tables

1.1	Three domains of elastic scattering	15
3.1	Nomenclature. $[L]$ is the length and $[T]$ the time unit adopted in the physical experiment or DNS database	48
3.2	Relevant scanning PTV parameters for testing of experimental setup . . .	50
3.3	Parameters for the synthetic experiment. Those not listed here are as in table 3.1	60
3.4	Numerical scanning experiment parameters	71
3.5	Flow parameters	80
3.6	Imaging parameters	80
3.7	Sizing particle parameters	82
3.8	Scanning parameters	82
3.9	Mean inter-particle distance for different seeding densities	89
3.10	Comparison of enstrophy and dissipation rate between different seeding density cases and DNS	93
3.11	Comparison of particle sizing error before and after interpolation	98
4.1	Scanning experiment parameters	104
4.2	Characteristic scales of the flow. f_I is the impeller rotation frequency and Δt is the separation time between subsequent scan volumes.	109
4.3	Velocity statistics calculated at the mid point from tracks with track length $2\tau_\eta$	115
4.4	Flatness value from the experiment.	128
4.5	Comparison of particle size measurement for the three combinations using two different least squares difference tolerance (χ^2).	136
4.6	Comparison of particle size measurement for the particles with nominal size of $80\mu\text{m}$ using different least squares difference tolerance (χ^2).	140
4.7	Comparison of particle size measurement for particles with nominal size of $40\mu\text{m}$ using two different least squares difference tolerance (χ^2).	141

Nomenclature

Roman Symbols

a_i	i th acceleration component
D	Particle image diameter
d_p	Particle diameter
dz	Projection volume
f	Focal length
f_I	Frequency of impeller
f_s	Fractional sheet number
G_j	Intrinsic camera matrix
I_3	Identity matrix
$i_{1,2}$	Intensity functions
I_o	Incident light intensity
I_s	Scattered intensity
l	Integral lengthscale
L_x, L_y, L_z	Measured volume dimensions
l_z	Adjusted scanning depth
M	Magnification
n	Refractive index
N_I	Seeding density
N_s	Number of parallel laser sheets

Nomenclature

n_s	Nominal sheet number
N_v	Volumetric seeding density
ppp	Particles per pixel
ppv	Particles per voxel
\bar{r}_{2D}	Average distance between particles
R	Camera distance from field of view
r_s	Nearest neighbor search radius
Re	Reynolds number
Re_λ	Taylor-scale Reynolds number
R_j	Rotation matrix
R_p	Particle's distance from camera center
t	Time
T_{RET}	Scanner retrace period
U	Characteristic velocity
u, w, v	Transverse and Axial velocities
u_i	i th velocity component
u_s	Laser scan speed
u_{rms}	rms flow velocity
w	Laser sheet width
x, y, z	3D coordinates
$x_{c,j}$	Translation matrix
x_p, y_p, z_p	Particle location

Greek Symbols

α	Particle size parameter
Δt	Scan volume separation time
Δz	Sheet overlap

Δ_z	Tolerance in depth direction
Δ	Coarse-grain filter length
$\Delta\theta$	Mean fringe spacing
Δ	Difference operator
Δ_{disp}	Particle displacement
ϵ	Turbulence kinetic energy dissipation
γ	Tracking parameter
λ	Incident light wavelength
η	Kolmogorov length-scale
ω	Vorticity
Ω	Rotation rate of the flow
ϕ_0	Camera azimuthal angle
ϕ_s	Particle azimuthal angle
ρ	Density
τ	Kolmogorov time-scale
χ^2	Sum of least squares
ν	Kinematic viscosity
θ_0	Camera scattering angle
θ_s	Particle Scattering angle
$\theta_{1,2,3,4}$	Camera angle

Acronyms / Abbreviations

DNS	Direct numerical simulation
LPT	Lagrangian Particle Tracking
PTV	Particle Tracking Velocimetry
J-PDF	Joint probability density function
LDV	Laser Droplet Velocimeter

Nomenclature

PIV	Particle Image Velocimetry
GLMT	Generalized Mie Theory
IPI	Interferometric Particle Imaging
PDF	Probability density function
GPD	Global Phase Doppler
PDA	Phase Doppler Anemometry
SMD	Sauter mean diameter
LSD	Laser Sheet Droplet Sizing
SNR	Signal-to-noise ratio
LIF	Laser Induced Fluorescence

Introduction

0.1 Background, motivation and objectives

A particle can be defined as “a minute quantity or fragment” or “the smallest discrete portion of something” that holds its basic mechanical properties. The use of particle suspensions and particle technologies have a profound application in a variety of industries like coal, electronics, metals and minerals, pharmaceuticals, agriculture, paints etc. In fluid mechanics, the term particle can be interpreted as droplets, bubbles or solid particles suspended in fluids. Measurements of particle/droplet velocity and size are important in research applications, such as the analysis and characterization of sprays, combustion of liquid fuels, mixing in vessels for the chemical industry (Black *et al.*, 1996; Tropea, 2011). Besides these applications, measurement of particle size and velocity is also key to understanding and predicting the response of particles in a turbulent flow (Calzavarini *et al.*, 2009; Mordant *et al.*, 2004; Qureshi *et al.*, 2008; Voth *et al.*, 2002).

Particles suspended in a flow can be also used to understand the physics of the flow, when the particles have the ability to follow the instantaneous motion of the flow over a sequence of time. Such particles are called tracer particles. There are two approaches by which this can be done; an Eulerian approach or a Lagrangian approach. The Lagrangian description of fluid flows is physically more natural than the Eulerian one since it is related most directly to the motion of fluid elements as is done in Newtonian mechanics. The traditional problems for which Lagrangian description is especially appropriate are turbulent diffusion, transport and mixing in a great variety of applications, e.g. geophysical, cloud formation, atmospheric transport, tracers on the ocean surface, combustion systems, Monin and Yaglom (1971, ch. V, pp. 527-693), Tennekes and Lumley (1972), Kim and Stinger (1992), Babiano *et al.* (1987). Another aspect is associated with the dynamics of inviscid fluids, theoretical problems associated with Euler equations, vortex dynamics, dynamics of interfaces and surface waves, Saffman (1991), Moffatt (2000), and Lundgren and Koumoutsakos (1999).

Techniques that provide the Lagrangian description of fluid flows is generally known as Lagrangian particle tracking (LPT). The method is usually based on three steps: the

identification of illuminated tracer particles from multiple camera views, a triangulation step in which the probable 3D location of the particles is calculated, and the linking of subsequent particle locations to form probable particle trajectories. This is commonly implemented as a Particle Tracking Velocimetry (PTV) and it is a well-established measurement technique used for the study of 3D Lagrangian particle motion in turbulent flows (Maas *et al.*, 1993; Virant & Dracos, 1997). The goal of establishing such particle tracks is often to calculate Lagrangian velocities (Nishino *et al.*, 1989) and accelerations (Malik *et al.*, 1993). In all these the basic ingredient is the motion of fluid particles, which is essentially Lagrangian in its nature as contrasted to the Eulerian description in which the observation of the system is made in a fixed frame as the fluid goes by.

To reconstruct particle trajectories, it must be possible to both accurately triangulate the locations of tracer particles, and then unambiguously link particles to form trajectories. At high particle seeding densities, required for the spatial resolution of the fine scales present in high-Reynolds number flows, both of these operations become challenging. The number of potential particle image matches increases non-linearly with seeding density, resulting in ambiguity during the triangulation procedure giving erroneous particle locations. Difficulties also arise in correctly pairing the same particle with its appearance in subsequent images given many nearest-neighbour candidates. There is therefore an inherent tension between the conditions for accurate Lagrangian particle tracking (LPT) and the high particle densities required to capture the fine scales of high-Reynolds number flow.

Recent particle tracking implementations seek to overcome these restrictions, focusing either on accurate tracking in densely-seeded flows, or on the reconstruction of the Eulerian field from sparse Lagrangian data. In the latter category a technique described as ‘pouring time into space’ was recently introduced by Schneiders & Scarano (2016), making use of both the instantaneous velocity and the velocity material derivative to improve the consistency of the reconstructed instantaneous velocity fields within the framework of sparse tracks. Another approach is the so-called ‘FlowFit’ method (Gesemann *et al.*, 2016), which employs a system of smooth B-splines and invokes physical constraints during velocity, acceleration and pressure field reconstruction. The method is thus able to increase the spatial and temporal resolution by ‘supersampling’ the starting scattered data, additionally reducing noise during the process. On the other hand several novel approaches have emerged recently to track particles successfully at higher tracer particle densities. Notable is the ‘Shake-The-Box’ method (Schanz *et al.*, 2016) extending the Iterative Particle Reconstruction (IPR) methodology of Wieneke (2012). Attempts have also been made recently to find 3D particle locations directly from the reconstructed intensity volumes from tomographic PIV, for example the Tomo-3D-PTV of Novara & Scarano (2013), although this approach is susceptible to errors when particle tracking is undertaken since many ghost particles are reconstructed at high seeding densities. The

concept of particle prediction as introduced in the ‘Shake-The-Box’ method (Schanz *et al.*, 2016) is extended into the domain of tomographic PIV by Lynch & Scarano (2015) with an efficient ‘motion-tracking-enhanced’ intensity field reconstruction. The number of ghost particles is thus significantly reduced, and combined with a suitable tracking scheme, such an approach could increase the particle density at which Tomo-3D-PTV could be applied. The present LPT methodology is aimed to increase the accuracy up to an equivalent particle image density similar to the upper particle image density limit tackled by the four-camera setup of Schanz *et al.* (2016), using a scanning laser sheet to illuminating tracer particles.

The case of particles in turbulent flow has been and remains a challenge to the fluid dynamicist. When compared to pure turbulence, the theoretical and experimental studies on particle-turbulence are still in their early stages. The difficulty arises in the interaction of particles of different sizes with the turbulent flow. When the size of the particles are small compared to the smallest turbulent length scale of the flow (Gouesbet & Berlemont, 1999; Maxey & Riley, 1983) or when there is only a vanishing difference between the density of the fluid and the particle, the particles then behave like fluid elements and are called fluid tracers. This property is crucial for several experimental techniques like PIV, PTV etc where these particles are used to resolve the velocity fields (eg:Lawson & Dawson (2015)).

For finite sized or heavy particles, both large scale and small turbulent eddies can contribute to particle dispersion, depending on the local Stokes number (Bachalo (1994)). These interactions can cause the particles to cluster (Wood *et al.* (2005)) or can create a void, which can alter the turbulent characteristics of the continuous medium in which they are immersed. This variation in the flow characteristics are higher for polydisperse particle size distribution as compared to monodisperse case (Sommerfeld (1990)). The range of sizes is important in some studies on the effects of particle interactions with turbulence in a multiphase regime, whilst in others appropriate mean values suffice. The particular mean required is usually determined by the use to which the data is to be put. The most common of these is the volume to surface area mean, D_{32} , the Sauter Mean Diameter (SMD), which is used in mass transfer work where the surface area governs the resistance and the volume determines the concentration. The type of distribution can also be important particularly in the comparison of theory and experiment. Two main types of distributions are temporal (vary with time at one point in space) and spatial (vary in space at one point in time).

Particle size measurement technique is broadly divided into optical and non optical methods (Barth & Flippen, 1995; Black *et al.*, 1996; Hirleman & Bohren, 1991; Tayali & Bates, 1990). Non optical methods, relies on either physical separation of samples such as sieving, sedimentation, impactors etc. Impact devices use a coating of fine material such as magnesium oxide or soot on to which the particles impact, leaving crater-like

impressions. Optical techniques relies on imaging, microscopy or holography. These are relatively simple techniques, where the particles are illuminated by a light source, chosen based on the particle velocity and size. In imaging or microscopy technique, particles are exposed to the illumination, with the exposure time also depending upon the velocity and diameter of the particle. Particles can be imaged perpendicular to the direction of the flow using either back or side illumination. In holography technique, a dynamic three-dimensional distribution of particles is stored in a hologram from which a stationary image can be produced for detailed study of size and relative position of the particles. Typical measurement accuracies from these optical techniques range between 5 – 15% (Black *et al.*, 1996; Tropea, 2011) with measurable sizes ranging between 0.5 – 10000.

The evolution of laser diagnostics has played a profound role in the development of a new kind of method, which was based on the light scattering properties of the particles. The laser based method also allowed for the measurement of velocity of the particle simultaneously. Currently, laser based measurement techniques is considered to be the most popular way of measuring the particle velocity and size. This is purely due to its properties such as its coherence, spectral power and its monochromatic nature.

One major challenge faced by laser based methods, when a Gaussian intensity profile laser is used for sizing is that, the same particle passing through different locations of the laser beam/sheet can scatter different amounts of light. This essentially means that a large particle at the edge of the laser sheet and a small particle at the center of the sheet can scatter same amount of light, and this effect was termed as the “trajectory effect” (Black *et al.* (1996)). This effect is unavoidable even in a top-hat beam intensity profile, as the profile is not uniform over the entire sheet width as their tails are nonetheless similar to a Gaussian profile.

It is therefore required to develop a volumetric technique where either exact particle location within the laser sheet is known for each particle at every instant and a relative correction of the measured intensity is performed or to approximately obtain the particle intensity corresponding to the laser sheet center (Gaussian center). The method should also needs to accurately estimate the 3D location of the particle at each time instant at a higher particle concentration, for the tracking purpose, to simultaneously measure its velocity.

This report focuses in developing a novel laser based experimental technique, to measure the velocity and size of particles in the Mie scattering regime, in a turbulent flow. This is the first known experiment conducted that provides the velocity, acceleration and size of particles in a 3D space. This work aims to take the advantage of volumetric particle tracking methods which samples the same particle several times as it traverses the measurement volume. This provides the possibility of measuring the particle size numerous times, which should in principle increases accuracy. The technique is introduced

through its application on tracer particles in turbulent flows; which could be further used in studying interactions of neutral and heavy particles in turbulence.

0.2 Outline of the thesis

The present work is structured in the following way:

In Chapter 1, a literature review on the fundamentals in particle tracking and Mie scattering theory are presented followed by a discussion on the relevant particle tracking and sizing techniques.

The fundamental principles of the scanning technique are presented in Chapter 2; the working principle is discussed together with the main aspects involved in the experimental setup. The methodology to assess the particle tracks and sizes is explained in detail, following which the steps for data processing is also outlined.

In Chapter 3 a performance assessment by means of computer generated synthetic scanning data for both tracking and sizing are presented. Various parameters that may affect the 3D particle triangulation and tracking within the measurement volume are considered, addressing both controllable and uncontrollable effects. A discussion on the experimental design of the sizing technique, where the limits in the design are derived and the parameters to optimize this limit is also presented. Results from the triangulation, tracking and sizing from the synthetic experiment are also presented.

In Chapter 4, the application of the technique on a real laboratory data set from an rotating turbulent flow (Ekman pumping flow) is given. The tracking technique is validated comparing the measured Lagrangian statistics with Lagrangian statistics in similar turbulent flows. The sizing technique is validated by comparing the measured size distribution to size distribution of the tracer particles provided by the manufacturer, used in the flow for the measurement.

Finally the main results and conclusions of the thesis are summarized in Chapter 5.

0.3 Papers included in the thesis

The results in the first three sections of Chapter 3, described in this thesis regarding scanning Lagrangian particle tracking and their associated parametric testing and numerical simulation were previously published in the journal *Experiments in Fluids*, in an article written in collaboration with Kozul, Worth, and Dawson. Instead of rewriting this article, it is reproduced in the Chapter 3 as it appeared in the journal. The sections 3.2, 3.3 and 3.4, and respective figures in these sections have been adapted to the format of this thesis. Kozul is the first author of this paper. Koothur contributed equally by developing concept of particle tracking and MATLAB scripts for it. The contents and results of sections 3.2

and 3.3 were performed and written by Koothur. Kozul improved the running speed of the triangulation and particle tracking scripts using GPU functions, and contributed by testing the developed scanning particle tracking technique by performing numerical simulation in HIT as discussed in section 3.4. Dawson (main supervisor) and Worth (co-supervisor) have been Koothur's supervisors for the PhD and have contributed to the papers through rigorous technical discussions, suggestions and comments and reviewing the manuscript.

Paper 1

Kozul, M., Koothur, V., Worth, N. A. Dawson, J. R. 2019. A scanning particle tracking velocimetry technique for high-reynolds number turbulent flows. *Experiments in fluids*, **60**, 137.

Chapter 1

Literature review

This chapter provides an overview of the most relevant laser diagnostic techniques that are used to measure the velocity, acceleration and size of particles/droplets statistics in flow. Before discussing/comparing these techniques, the fundamentals behind these techniques which are; the understanding of epipolar geometry required to obtain the 3D location of a particle and the scattering theory knowledge essential in the particle sizing approaches are introduced.

1.1 Particle tracking

Particle image velocimetry and particle tracking velocimetry provides the two most common ways of measuring the velocity in a flow based on the motion of particles (Adrian (1991)). While PIV characterizes the flow in an Eulerian point of view, PTV characterizes them in a Lagrangian point of view. The particle tracking technique can provide the measurements of the flow velocity, when the particles used are tracer particles; or can be used to measure the velocity of the particles itself when the particles are inertial and have their dynamics (Sato & Yamamoto, 1987; Virant & Dracos, 1997; Voth *et al.*, 2002). Particle tracking can be implemented in two ways. In the first method, pair of images are recorded in rapid succession followed by a time interval before next the pair. This method provides a single vector for each particle in the pair. In the second method, a long sequence of images are captured, separated by small equal intervals. Such a measurement provides location, velocity and acceleration of the particle over $n, n-1$ and $n-2$ measurements along a single trajectory.

In general, particle tracking method is usually based on three steps: the identification of illuminated particles from multiple camera views, a triangulation step in which the probable 3D location of the particles is calculated, and the linking of subsequent particle locations to form probable particle trajectories (Maas *et al.*, 1993; Malik *et al.*, 1993;

Novara & Scarano, 2013; Schanz *et al.*, 2016; Wieneke, 2012). Unlike in other methods, particle tracking is based on the coordinate measurement of individual particles, which requires a reliable identification, multi-image matching and coordinate determination.

The particle image position is first obtained in the 2D image-plane, e.g. by a 2D-Gaussian intensity peak fit. The particle image positions, a standard 2D peak finding algorithm first identifies pixels above a prescribed threshold, and then fits two 1D Gaussian functions (Ouellette *et al.* (2006)) to neighbouring pixels. The method was found to retrieve the particle image position at sub-pixel accuracy.

To reconstruct a particle’s 3D location, first a relationship between the multiple cameras, the 3D point and its projections on the camera’s image plane has to be derived. A geometry that relates this relationship is called epipolar geometry (Hartley & Zisserman (2003)). The standard epipolar geometry setup involves two cameras observing the same 3D point P , as shown in figure 1.1. The projection in each of the image planes is located at p and q respectively. The line between the two camera center of projection is referred to as the baseline. The plane defined by the two camera center of projections and P is the epipolar plane. The locations of where the baseline intersects the two image planes are known as the the epipoles e and f . Finally, the lines defined by the intersection of the epipolar plane and the two image planes are known as the epipolar lines. The epipolar lines have the property that they intersect the baseline at the respective epipoles in the image plane.

In real-world situations, however, the exact location of the 3D location P is unknown, but its projection in one of the image planes (eg: I) is known. The camera locations, orientations and camera matrices are also known for both the cameras. With the knowledge of camera locations of C and D and the image point p , the epipolar plane can be defined with which the epipolar line of p . Then by the definition, P ’s projection into the second image q must be located on the epipolar line of p in the second image J .

The projection of P onto the image plane can be modelled in different ways, which includes using; polynomials (Soloff *et al.*, 1997), camera pinhole with distortion (Tsai, 1987; Willert, 2006) and pinhole with Scheimpflug corrections (Fournel *et al.*, 2004; Louhichi *et al.*, 2007). In a pinhole model, the projection of point P onto the image plane is modelled as

$$p \approx G_j R_j [I_3 | -x_{c,j}] P \tag{1.1}$$

I_3 is the 3×3 identity matrix and G_j is a 3×3 upper triangular matrix which represents intrinsic camera parameters, such as focal length and magnification. The variables $x_{c,j}$ and R_j are extrinsic camera parameters which represent the camera’s position in object space and orientation with respect to the object space coordinate system respectively.

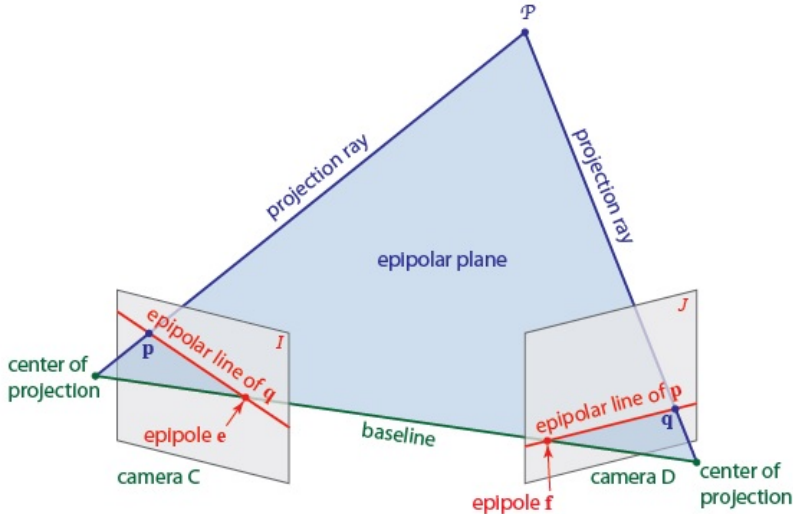


Figure 1.1: The general setup of an epipolar geometry. The shaded gray region represents the epipolar plane and the red lines represents the epipolar lines.

For the identification of particle 3D location, in recent years, two main approaches have been used: Triangulation (Hartley & Zisserman, 2003; Maas *et al.*, 1993) and, more recently, iterative reconstruction (Schanz *et al.*, 2016; Wieneke, 2012). The basic idea behind the triangulation-based algorithms is that a particle is seen along different projection rays when viewed by two cameras at different angles, as explained above. The 3D position is then found from the intersection of these projection rays. The iterative particle reconstruction algorithms work quite differently, compared to the triangulation-based method. Here the triangulation method is used, only for the first few frames, after which the position is predicted using the Kalman-filter approach. The predicted position is then used to generate an artificial image where the particles are modelled as a Gaussian distributed pixel intensity at the particle location and the modelled image is then compared to the measured image for each particle individually. This comparison is then used to optimize the particle position. The particle tracking techniques which follows either one of these 3D particle location-identifying methods and the problems associated with them are discussed in the following section.

1.1.1 Comparison of the relevant particle tracking techniques

Lagrangian particle tracking (LPT) seeks to uncover the physics of a particular fluid flow by following individual particle tracers over a sequence of time-resolved recordings. The goal of establishing such particle tracks is often to calculate Lagrangian velocities (Nishino

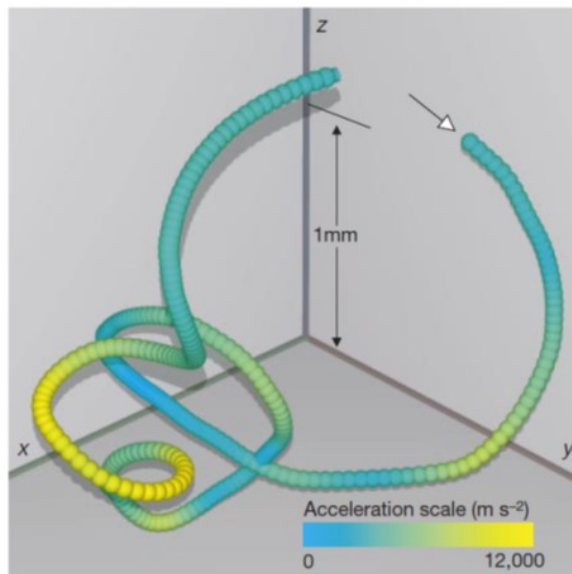


Figure 1.2: Particle track obtained using 3D PTV. The spherical markers represent the particle position and the color code represents the magnitude of acceleration (Porta *et al.* (2001)).

et al., 1989) and accelerations (Malik *et al.*, 1993). Major developments in the field of particle tracking in 3D are discussed below:

3D particle tracking

3D particle tracking by (Maas *et al.*, 1993; Malik *et al.*, 1993; Virant & Dracos, 1997) are early attempts at Lagrangian particle tracking in a 3D space. Their technique was based on gathering the particle positions from projections on few images by triangulation, using epipolar lines. Particle positions for each time-step were then matched in successive time-steps using a search either in the image or in world space. Several studies demonstrated that accurate Lagrangian statistics can be constructed following particles over long trajectories (Porta *et al.*, 2001; Voth *et al.*, 1998); as shown in figure 1.2, using this technique.

The major disadvantage of this technique is its limitation to higher seeding densities, due to the general issue of ambiguities in the triangulation procedure. To reconstruct particle trajectories, it must be possible to both accurately triangulate the locations of tracer particles, and then unambiguously link particles to form trajectories. High particle seeding densities are required for high spatial resolution, for example if aiming to measure the fine scales present in high-Reynolds number flows, both of these operations become challenging. The number of potential particle image matches increases non-linearly with

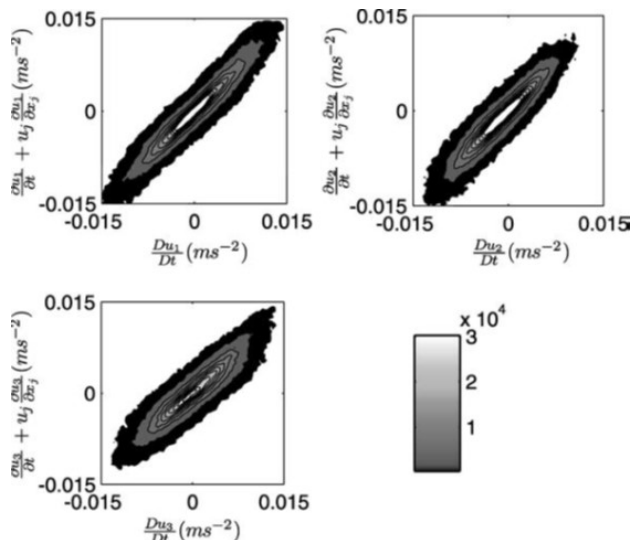


Figure 1.3: Acceleration check to show a better assessment on the accuracy of the velocity derivatives. The x-axis represents the Lagrangian acceleration and the y-axis represents the sum of local and convective acceleration (Hoyer *et al.* (2005)).

seeding density, resulting in ambiguity during the triangulation procedure giving erroneous particle locations. Difficulties also arise in correctly pairing the same particle with its appearance in subsequent images given many nearest-neighbour candidates. There is therefore an inherent tension between the conditions for accurate particle tracking and the high particle densities required to capture the fine scales of high-Reynolds number flow. Implementations of the technique exploiting three-dimensional particle tracking velocimetry (3D-PTV) using three (e.g. Maas *et al.*, 1993) or four (e.g. Lüthi *et al.*, 2005) cameras helps resolve ambiguities to an extent, however these 3D-PTV methods are typically limited to relatively low particle image densities N_I of ≈ 0.005 particles per pixel (ppp) (cf. Maas *et al.*, 1993) in order to maintain confidence in the deduced particle tracks.

3D scanning particle tracking

3D scanning particle tracking technique (Hoyer *et al.* (2005)) expands on the classical 3D particle tracking technique mentioned above. In this technique, the flow field is recorded by sequential tomographic high-speed imaging of the region of interest. The 3D scanning particle tracking technique was developed to predominantly overcome the problem of reduced spatial resolution due to lowered seeding density in the classical 3D particle tracking technique. Better spatial resolution is essential in turbulence studies, to measure higher order velocity gradients accurately.

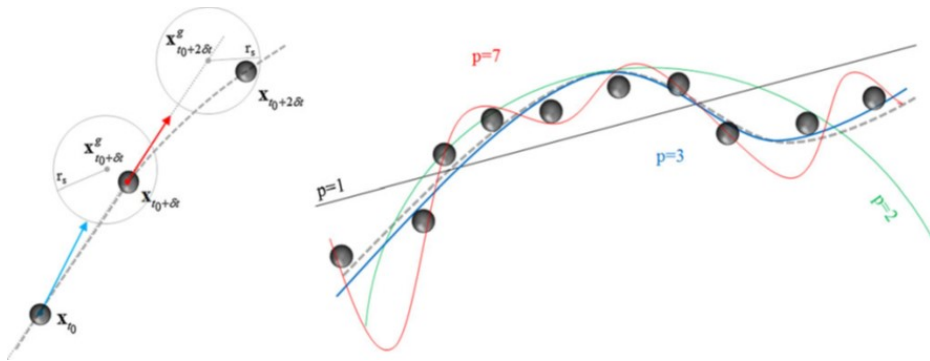


Figure 1.4: (a) Particle linking procedure in TOMO-PTV, using the cross correlated velocity field as the predictor. (b) Polynomial fits of n th orders, to reduce the truncation error for complex trajectories (Novara & Scarano (2013)).

The merits of the 3D scanning particle tracking technique over the classical 3D particle tracking technique in terms of spatial resolution was compared experimentally (Hoyer *et al.*, 2005; Lüthi *et al.*, 2005). Several checks on the spatial resolution, such as the acceleration check as shown in figure 1.3, on a quasi-homogeneous isotropic turbulence (Lüthi *et al.* (2005)), shows that the 3D scanning particle tracking offered Hoyer *et al.* (2005), an enhanced data quality when compared to the classical 3D PTV by Lüthi *et al.* (2005). The 3D scanning particle tracking proves to be an excellent tool for turbulence investigation.

Tomographic particle tracking

Tomographic particle tracking was attempted as an outcome of the advancements in Tomographic PIV (Elsinga *et al.* (2006)). Schröder *et al.* (2008) tracked the particles from the reconstructed tomographic field, to get the material derivative. The concept of 3D PTV was later added to reduce the error in the reconstructed tomographic particle field (Wieneke (2012)). In this method, correlation-based velocity fields are used as the predictor field, which allowed us to evaluate the particle trajectories (Figure 1.4a)). The tomographic particle tracking method was extended by Novara & Scarano (2013) for accurate measurements of material derivatives. The truncation errors for complex trajectories are reduced using polynomial fitting functions that describe the particle position in time with sequences based on several recordings (Figure 1.4 b)). The polynomial regression approach also helped in the reduction of the random errors due to the particle position measurement, leading to accurate acceleration measurements. The limitations of TOMO-PIV are in turn limitations for TOMO-PTV as well, which is the influence of ghost particles, especially when the seeding densities are increased. The Iterative Particle Reconstruction (IPR) technique introduced by Wieneke (2012) when applied to

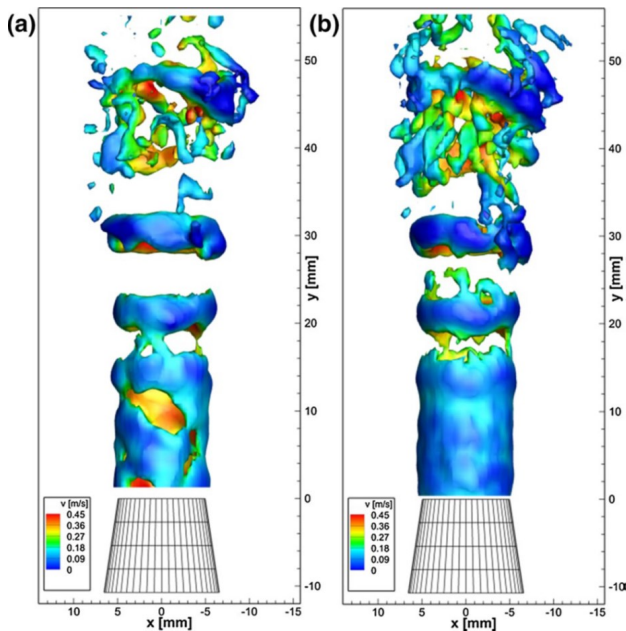


Figure 1.5: A comparison isosurfaces of vortices obtained from (a) TOMO-PIV and (b) combination of STB and 'FlowFit' interpolation scheme. The colorcode represents streamwise velocity (Schanz *et al.* (2016)).

the TOMO-PTV, demonstrated increased position accuracy compared to the reconstructed intensity field from TOMO-PIV, but still, the number of ghost particles was seen rapidly increasing as soon as the particle image density approached 0.05 ppp.

Shake the Box

'Shake-The-Box' (Schanz *et al.*, 2016) method is also an advancement in the tomographic method, where the IPR methodology of Wieneke (2012) is extended. Initialised individual tracks are prolonged to the next time step via extrapolation, where the predicted particle locations are corrected by 'shaking' them in space and image matching in time. Since ghost particles are decorrelated and do not typically generate consistent tracks persisting over several successive recordings, essentially ghost-free, and very accurate, particle tracks are generated for particle image densities of up to ≈ 0.125 ppp. Temporal information is thus exploited in addition to the purely spatial information offered by conventional tomographic PIV (Elsinga *et al.*, 2006). STB offers better spatial coherence when compared to TOMO-PIV, as seen in figure 1.5, where the large structures are more unevenly represented with many small scale structures lacking from TOMO PIV representation when compared to STB representation. The better spatial coherence is due to the combination of ghost-free reconstructions, position accuracy, a lack of spatial filtering induced by a correlation

window and the possibilities of pouring physical constraints, like divergence penalization, into the cost function of the interpolation.

The concept of particle prediction as introduced in the ‘Shake-The-Box’ method (Schanz *et al.*, 2016) is extended into the domain of tomographic PIV by Lynch & Scarano (2015) with an efficient ‘motion-tracking-enhanced’ intensity field reconstruction. The number of ghost particles is thus significantly reduced, and combined with a suitable tracking scheme, such an approach could increase the particle density at which Tomo-3D-PTV could be applied.

Recent particle tracking implementations seek to overcome these restrictions, focusing either on accurate tracking in densely-seeded flows or on the reconstruction of the Eulerian field from sparse Lagrangian data. In the latter category a technique described as ‘pouring time into space’ was recently introduced by Schneiders & Scarano (2016), making use of both the instantaneous velocity and the velocity material derivative to improve the consistency of the reconstructed instantaneous velocity fields within the framework of sparse tracks. Another approach is the so-called ‘FlowFit’ method (Gesemann *et al.*, 2016), which employs a system of smooth B-splines and invokes physical constraints during velocity, acceleration and pressure field reconstruction. The method is thus able to increase the spatial and temporal resolution by ‘supersampling’ the starting scattered data, additionally reducing noise during the process. On the other hand several novel approaches have emerged recently to track particles successfully at higher tracer particle densities.

1.2 Scanning technique

The recent developments in particle tracking are mostly based on a Tomographic approach. Tomographic techniques are much more computationally expensive with a large part of this cost lying in the tomographic reconstruction. An alternative approach to volumetric measurements in flow is to use a scanning technique introduced by Brücker (1995). Scanning technique has been developed over the past two decades, for example as discussed in section 1.1.1. Whilst specific implementations differ, the general concept is similar: one or more cameras capture particle images as a light sheet is quickly moved across a measurement volume. The most common approach has been to perform multiplanar stereo PIV measurements at different depths through the volume, which are then “stacked” together to recover the velocity field (Brücker, 1995; Soodt *et al.*, 2012; Toshio & Jun, 2004). But these approaches suffered the same errors as in stereo PIV and the resolution was constrained by the finite thickness of the laser sheet, with the added complexity of scanning.

A modification to the existing scanning technique was introduced by Lawson & Dawson (2015), with an aim to increase the seeding density of volumetric reconstructions and

reduce the incidence of ghost particles, in order to improve the spatial resolution and reduce the noise of the measurement. The technique has the added benefit that just one or two cameras are required to make volumetric measurements. This made its general application quite attractive as it reduces the number of laser sheets needed to make accurate measurements, which reduces the time needed to complete the scan. Scanning PIV by Lawson & Dawson (2015) was applied to make time-resolved, volumetric measurements at the centre of a large, von-Kármán swirling water flow. This provided access to the full velocity gradient tensor, pressure gradients and pressure Hessian fields in three dimensions.

1.3 Particles sizing in the Mie scattering regime

In the above techniques, the intensity information is discarded which can be used for particle sizing. In this section, the general concept of particle sizing in the Mie scattering regime is discussed. To aid the discussion, the concept of Mie scattering and the interaction of light with particles in a Mie scattering regime, using generalized Mie scattering are discussed. In the last part of this section, a review of the techniques which are based on Mie scattering is done.

Elastic and inelastic scatterings happen when a monochromatic light impinges on a molecule are; elastic and inelastic scattering. Within the elastic scattering mode, Lorenz-Mie theory (Bohren & Huffman, 1983; Kerker, 1969; van de Hulst, 1981) was used to relate particle scattering to its dimensionless diameter α , given as

$$\alpha = \pi d_p / \lambda, \tag{1.2}$$

where d_p is the particle diameter and λ is the wavelength of the incident light. The major assumption was that the illumination was uniform across the particle. Three different regimes are defined, as provided in table 1.1 and shown in figure 1.6.

Table 1.1: Three domains of elastic scattering

$\alpha \ll 1$	Rayleigh: Wavelength large compared to the particle
$\alpha \approx 1$	Mie: Wavelength and particle about the same size
$\alpha \gg 1$	Geometric: Particle large compared to the wavelength

If the size is small in comparison to the incident wavelength, i.e. the Rayleigh regime, the emitted wavelets are in phase and thus the scattered intensity varies marginally for different scattering angles. The elastic scattering magnitude is, however, highly dependent on the diameter of the particle and is proportional to λ^{-4} . In the opposite case, where the wavelength and the particle size are of comparable dimensions, i.e. the Mie regime a

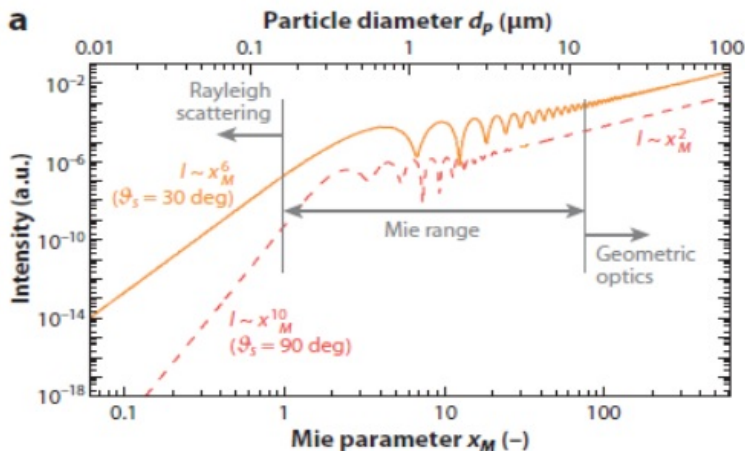


Figure 1.6: Relationship of the scattered intensity with respect to particle diameter, in the three scattering regimes. Adapted (Tropea (2011))

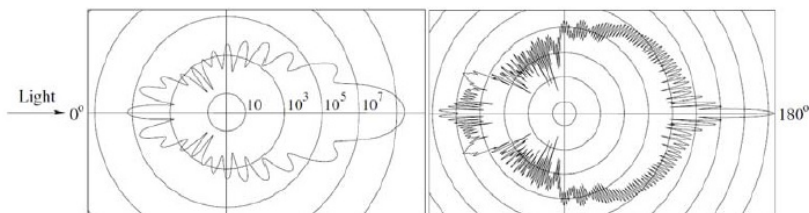


Figure 1.7: Scattered light by a $1\mu\text{m}$ (left) and a $10\mu\text{m}$ oil particle in air. Adapted (Raffel *et al.*, 2018)

phase mismatch develops and the wavelets interfere constructively or destructively. Hence, in contrast to Rayleigh scattering, Mie scattering has a high angular dependency and exhibits preferential scattering directions relative to the illumination direction.

One of the most important results of Lorenz-Mie theory is that the light scattered by a spherical particle is inhomogeneously distributed in space, depending on particle diameter, refractive index and incident light characteristic. Figure 1.7 illustrates how the scattering intensity varies for different (spherical) particle diameters, illuminated by $\lambda = 532\text{ nm}$ (corresponding to the frequency doubled radiation emitted by a Nd:YAG laser source). Noticeable is the increase in the number of scattering lobes as well as the more pronounced forward scattering peak appearing as the particle diameter increases. By using the generalized Lorenz-Mie theory as in (Bohren & Huffman, 1983; van de Hulst, 1981), it can be shown that the scattered light intensity is an oscillating function of the scattering angle.

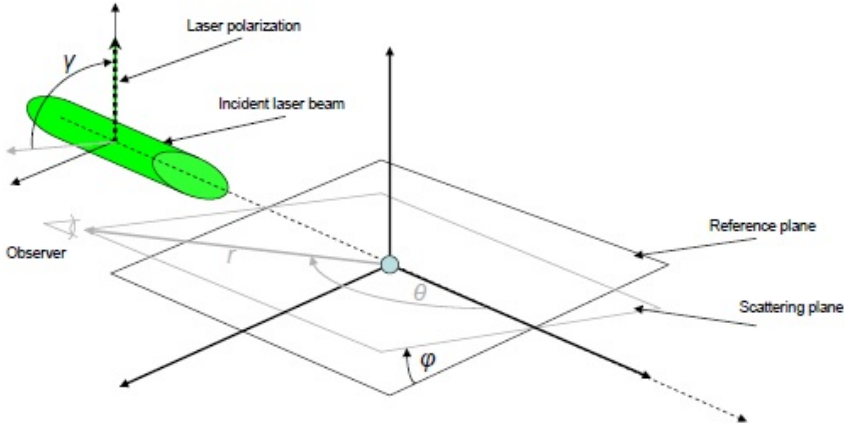


Figure 1.8: Mie scattering geometry. Adpated LePera (2012)

The theory for Mie scattering was explained by Maxwell, Debye and Fourier in different ways, but the theory from Mie became generalized, hence given the name generalized Mie theory (GLMT) (Bohren & Huffman (1983), Kerker (1969), van de Hulst (1981)). Following Bohren and Huffman's notation and development Bohren & Huffman (1983), the geometry of this problem is given in Figure 1.8. The reference plane is denoted in black, the scattering plane in gray. The scattering plane is defined as the plane containing the propagation axis and the observer vector r . The location of the observer is defined in the spherical polar coordinate system (R, θ, ϕ) , where r is the vector distance between the scattering particle and the observer, θ is the angle (on the scattering plane) between the light-propagation-axis and the observation, and ϕ is the angle between the reference plane and the scattering plane. The angle between the scattering plane and the polarization direction is denoted as γ . Scattering near $\theta = 0^\circ$ is often called "forward" scattering while scattering near $\theta = 180^\circ$ may be called "backward" scattering.

Light scattered by a spherical particle is in-homogeneously distributed in space depending upon its size as shown in figure 1.7, characterized by its diameter d_p , refractive index n , incident light of intensity I_o and wavelength λ , at the angle θ_s . The particle size is usually denoted by the size parameter $\alpha = \pi d_p / \lambda$, which takes into account, the size and the wavelength. The flux of scattered light intensity (in Wm^{-2}), in direction θ_s at a distance of R from the scattering sphere is given by

$$I_s\{n, \theta_s\} = \frac{I_o \lambda^2}{4\pi^2 R^2} (i_1\{\alpha, n, \theta_s\} + i_2\{\alpha, n, \theta_s\}), \quad (1.3)$$

where i_1 and i_2 are the intensity functions. The details on how the scattering intensity is obtained is given in the Appendix A

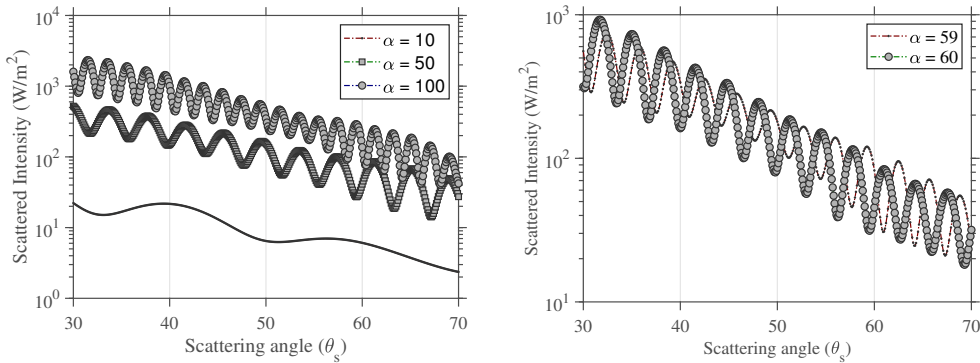


Figure 1.9: Mie theory calculations of scattered intensity as a function of angle for water particles with refractive index n 1.33. The particle size parameters α are (a) 10, 50 and 100 (b) 59 and 60.

Using this theory it can be shown that the scattered light intensity from a spherical particle in a non-absorbing medium is an oscillating function of the angle in the range $0 \leq \theta_s \leq \pi$, as shown in figure 1.7. In the scattering angle range $30 \leq \theta_s \leq 70$, the Mie scattering theory is also valid in cases where the size of the particle is much larger than the incident wavelength ($\alpha \gg 1$) (Mounaïm-Rousselle & Pajot, 1999). Figure 1.9(a) shows the angular variation of scattered intensity for a water particle with refractive index $n = 1.33$ for three different size parameters of 10, 50 and 100, for an incident light wavelength of 532nm, obtained using the equation 1.3. The oscillating pattern is very sensitive and unique to the diameters of particles with the same physical property, as shown in figure 1.9(b) for two water particles with very close size parameters of 59 and 60.

1.3.1 Description of particle diameter

Before discussing different relevant techniques that are used to measure the size of particles in flow, a discussion on various types of particle diameters used to specify particle size in a variety of situations encountered by using particle-size measurement systems, is given. In general, a particle diameter measured from an experiment represented as an equivalent spherical diameter which can be related to some aspect of the particle. If the particle under consideration is spherical, then all diameters become equal. The different variation in particle shape leads the different representations of a diameter such as the volume diameter, surface diameter etc. In volume diameter, the diameter is that of a sphere having the same volume as the actual particle, whereas in surface diameter the diameter is that of a sphere having the same surface area as the actual particle. Each of these diameter definitions stems from the application of one or more methods of size analysis.

Most of the laser-based particle size measurement techniques generally determine the distribution of such equivalent spherical particle sizes. In many applications of particle size measurements, it is convenient to work only with mean or average diameters instead of the complete drop size distributions. The mean particle size of the distribution can then be defined in different ways. Some of the most common are:

1. Arithmetic mean (d_{10}) - the normal average particle diameter of the size distribution.
2. Surface mean (d_{20})- diameter of a sphere with the average surface area of the particles in the size distribution.
3. Volume mean (d_{30})- diameter of a sphere with the average volume of the particles in the size distribution.
4. Sauter mean (SMD or d_{32}) - diameter of a sphere having the surface area of the average particle size in the distribution.
5. Weight mean (d_{43}) - diameter of a sphere having the average weight of all the particles in the size distribution.

Each of these mean diameters is defined to be the most useful or convenient measure to use given the phenomena under investigation. For example, d_{32} is used in combustion-related fields, d_{43} is used in the field of chemical kinetics but the most common mean diameter reported in most of the techniques discussed below is d_{30} .

1.3.2 Comparison of the relevant particle sizing techniques

Techniques that use Mie scattering theory is reviewed. Numerous techniques using Mie scattering have been developed in the field of particle sizing, hence the techniques presented in this review has been limited to only some of them which has some similarity with the technique which is to be presented in this work. Based on the type of measurement it can be classified into

- Techniques that measure individual particles
- Techniques that measure an ensemble of particles

The techniques described below have been grouped in the above way, with the scattering theory used in the technique mentioned accordingly.

Individual particle sizing techniques

Phase Doppler Technique

Phase Doppler technique is an interferometric technique (Bachalo & Houser, 1984) that measures the size and velocity of spherical particles simultaneously, using the spatial

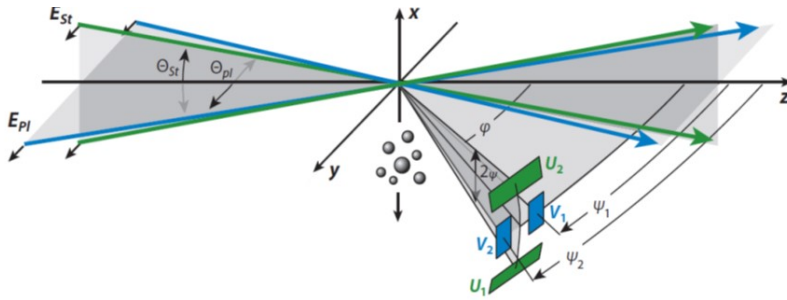


Figure 1.10: Optical schematic of a Phase Doppler Technique (Tropea *et al.*, 1996).

fringe pattern of the light scattered by the particle crossing a laser Doppler probe. It was developed as a point-wise measurement technique. The GLMT is used here; collection of light of a given wavelength at certain scattering angles and building a relationship between the phase difference and particle diameter. The phase Doppler method utilizes an optical system as illustrated in figure 1.10. Particles passing through the intersection of the two laser beams scatter light which forms an interference fringe pattern in the surrounding space. The spatial frequency of the interference fringe pattern is inversely proportional to the particle diameter but also depends upon the laser wavelength, beam intersection angle, particle refractive index and the location of the receiver. Dynamic measurements of the spatial frequency of the interference fringe pattern can be achieved using pairs of detectors placed at appropriate locations and separations. The detector position is chosen at an off-axis scattering angle (ψ) for which one scattering order dominates, as shown in figure 1.10.

Interferometric particle imaging

Interferometric particle imaging (IPI) also known as Mie scattering imaging (MSI) (Graßmann & Peters, 2004) or Global phase Doppler (GPD) technique (Damaschke *et al.*, 2005), is a planar measurement technique using interferometry as in PDA (König *et al.*, 1986). The technique is based on the evaluation of the scattered light, based on geometric optics, in an out of focus plane. In IPI a laser sheet is passed through the measurement volume and the scattered intensity is captured at a defocused plane. Within the aperture image scattered light according to Mie theory is received which appears in terms of interference fringes. Information on the particle diameter and the refractive index can be retrieved in terms of fringe spacing and position. The generation of focused and defocused images from a spherical particle by using an optical system is shown in figure 1.11.

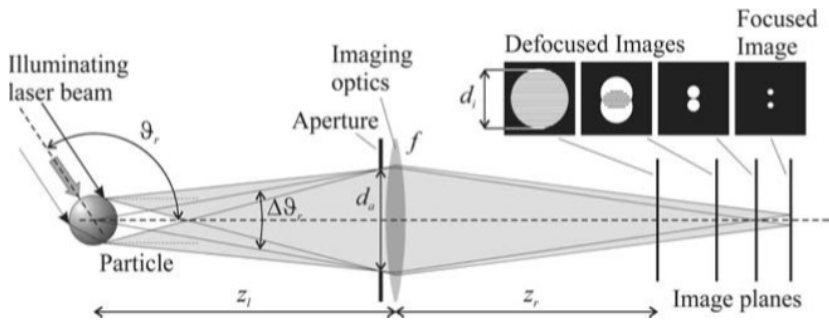


Figure 1.11: Generation of focused and defocused images from a spherical particle by using an optical imaging system (Damaschke *et al.*, 2005).

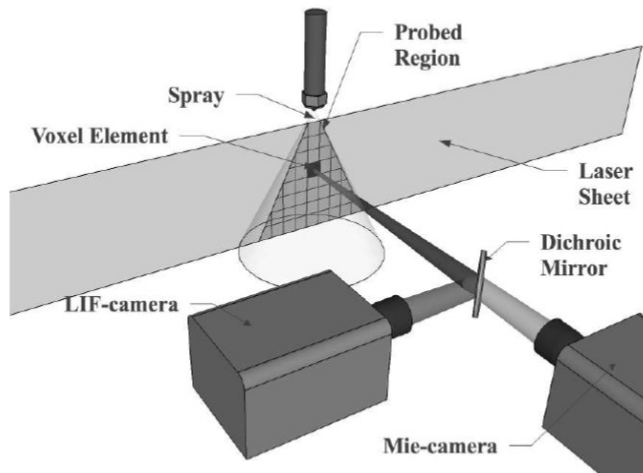


Figure 1.12: Optical Schematic of a Laser sheet droplet sizing.

Laser sheet droplet sizing

Laser sheet droplet sizing (LSD) is also known as Planar droplet sizing (PDS) (Domann & Hardalupas, 2001). In this method, the Mie scattered light is approximated as proportional to the surface area (D^2) and the fluorescence signal to volume (D^3). Hence a ratio between a PLIF and planar Mie scattering image would give an approximate diameter D of the particle (Domann & Hardalupas, 2003). An example of a typical experimental arrangement for the LSD technique is illustrated in Figure 1.12. To explain in more detail, consider a volume element containing an ensemble of N fluorescing droplets with a certain size distribution. The LIF signal detected from this element is given by

$$S_{LIF} = C_{LIF} \sum_{i=1}^N D^3 \quad (1.4)$$

where C_{LIF} is a measurement constant that depends on factors such as collection optics, index of refraction, scattering angle, etc. The corresponding elastically scattered signal can be expressed according to

$$S_{Mie} = C_{Mie} \sum_{i=1}^N D^2 \quad (1.5)$$

If these signals are measured simultaneously, i.e. on the same ensemble of particles, the ratio of these signals is proportional to the Sauter Mean Diameter (SMD), often denoted D_{32} .

$$\frac{S_{LIF}}{S_{Mie}} = K \frac{C_{LIF} \sum_{i=1}^N D^3}{C_{Mie} \sum_{i=1}^N D^2} = K.SMD \quad (1.6)$$

The value of K in the above equation is usually determined from a calibration measurement using a second sizing approach, e.g. Phase Doppler Anemometry (PDA).

Ensemble droplet sizing techniques

Ensemble techniques provide information on the entire population of particles within a measurement volume or area, but no information about individual droplets. By their nature, this type of measurement is either a spatial average, temporal average, or very often both. One of the most popular ensemble droplet sizing technique is a laser diffraction analysis, also known as laser diffraction spectroscopy or low angle laser light scattering (LALLS), developed by Malvern Instruments Ltd. In this technique particle size distributions are measured by measuring the angular variation in the intensity of light scattered as a relatively broad (10mm) collimated laser beam is passed through the spray/aerosols/particles being examined. The scattered light is focused forward on multiple detectors that measure the angular distribution of the intensity of the scattered light. Large particles scatter light at

small angles relative to the laser beam and small particles scatter light at large angles. The angular scattering intensity data is then analyzed to calculate the size of the particles responsible for creating the scattering pattern, using the Mie theory of light scattering. The Fraunhofer pattern of the scattered light, an “Airy disk”-like series of concentric rings of alternating maximum and minimum intensities, contains information on the mean size, shape and width of the distribution, including any shoulders and tails (Dumouchel *et al.* (2009)). Mie theory and diffraction analysis are typically combined to determine the character of the spray. These instruments can analyze across a wide size range, typically as low as $0.1\mu\text{m}$ and up to $2000\mu\text{m}$ and recognize even complicated, bi-modal droplet distributions and high-density sprays. The particle size is reported as a volume equivalent sphere diameter.

1.3.3 Limitations of the existing particle sizing techniques

The most important drawback of a point-wise measurement like PDA is that they are unable to quantify the temporal and spatial fluctuations of the particle concentration and size. The method also relies on looking at reflected or refracted light with an extra requirement that involves avoiding the collection of diffracted light. Even though the IPI technique is not a point wise measurement technique, still the techniques are limited to small cross-sectional areas. Similar to the PDA technique, this method also relies on reflected and refracted light but in a defocused plane. One major disadvantage of an IPI technique is that since the images are captured in an out-of-focus plane, there is always a limitation to maximum particle concentration that could be measured. This is since the imaging is performed in an out of focus plane, the blurring effect caused overlapping of particle images, as a result of which there will be overlapping of the fringe pattern. This would then lead to incorrect sizing of the particles. Laser sheet particle sizing measures the Sauter Mean Diameter (SMD) that does not represent the average particle diameter but is always biased towards larger diameters due to the volume-dependence of the LIF signal. LSD is related to the volume- and area-dependence of the inelastically and elastically scattered light, respectively. With a too high dye concentration, the volume of the particle is not equally illuminated due to absorption, and consequently, the D^3 dependence in Eq. 1.4 is no longer valid. The D^2 relation in Eq. 1.5 is questionable (especially for small particles) due to the appearance of signal oscillations. Another limitation or draw-back of LSD techniques is the need for calibration, which requires the use of additional sizing techniques like a phase Doppler anemometry (PDA). A major limitation of a LDA technique is the range of spatial resolution. This is because the measurement technique is a line-of-site method, so the resulting size characterization is a spatial integration of all the particles within the measurement region of the instrument. All the above technique also suffers from the effect of laser extinction, scattering signal

extinction and most importantly the effect of multiple scattering with increasing particle concentration. But one of the fundamental issues with sizing techniques arises because of the Gaussian nature of light intensity. The issue is related to the trajectory of particle through the Gaussian beam/sheet, hence termed as trajectory effect (Bachalo, 1994; Black *et al.*, 1996; Sankar *et al.*, 1994). Lasers operated in the standard TEM_{00} mode are characterized by a Gaussian intensity profile. Particles in the flow field generally pass through the beam, where scattered light information is collected for particle size analysis. The problem the Gaussian beam creates for particle-size measurement is that the light scattered by a particular particle size passing through different locations in the beam or sheet can scatter different amounts of light. Thus a large particle passing through the edge of the beam or sheet and a small particle passing through the center of the beam or sheet can scatter the same amount of light. This creates a dependence of particle size on its trajectory through the sample volume. In PDA and IPI this would lead to phase difference which is a mixture between that expected for the various scattering orders, again typically involving reflected and first-order refracted light lead to incorrect sizing of the particles. In LSD and LDA, this would lead to measuring inaccurate scattering intensities.

1.4 Summary

The key aspects from the literature review can be summarized as follows:

Particle tracking is achieved through three steps: identifying particle location in 2D, identifying its 3D location and linking them in time. The accuracy of tracking depends on the efficacy of identifying the 3D particle location, which can be achieved through either triangulation or iterative reconstruction. The accuracy of the triangulation method reduces with increasing seeding densities, due to matching ambiguities. Even though the iterative reconstruction method offers better accuracy for increased seeding densities, the number of iterations required to achieve better accuracy increases with increasing seeding densities, making them computationally expensive.

Scattering intensity from particles in the Mie regime shows a high angular dependency, with a noticeable increase in the scattering lobes as the particle diameter increases. In order to produce Mie scattering from a particle, the wavelength of the incident light should be of the same order as the size of the particle. In conventional laser diagnostics, the most common is to use a laser with a wavelength of 532nm, whose beam profile is usually Gaussian in nature. A major problem in the measurement of scattered intensity from a light source with such a profile is commonly termed as ‘trajectory effect’, which causes scattering intensity to be dependent on the particle’s location within the illuminating beam/sheet. The scattered intensity is also a function of the particle location in a laser sheet. This means that the multi-angular intensity measurement for the same particle would be different, as compared to the expected value when using a plane wave.

The aim of this study is to develop a new tracking and sizing technique that:

1. Uses a single wavelength light source exploiting variables in the intensity of particles.
2. Uses a scanning method to minimize the line of sight errors involved in tomographic methods.
3. Uses a novel laser sheet calibration method to increase the accuracy of reconstruction in the scanning method.
4. Uses particle tracking that enables multiple viewing of the particles, that gives information of the scattered intensity with respect to the scattering angle.

Chapter 2

Methodology

As explained in chapter 1, the aim of this work is to use a scanning technique to measure the velocity of the particles in a flow via tracking and size them. A scanning technique to measure the velocity of flows was first introduced by Brücker (1995), as a PIV variant. Since then numerous variations on this technique have been developed (Lawson & Dawson, 2015; Soodt *et al.*, 2012; Toshio & Jun, 2004). The general approach was to reconstruct two-particle 3D fields with small time separation and cross-correlate them to get the velocity fields. A scanning technique offers higher seeding density when compared to a tomographic technique. The advantages, which the scanning technique offers due to the multiple illumination of the same particle, in developing the tracking and sizing, is why the scanning technique has been chosen in this work. The main disadvantage being that the flow speed and timescales are restricted by available scanning speeds. However, this may not be the most stringent constraint, since the finite acquisition rate of cameras or the laser source may play a more significant role.

In this chapter, the first section is dedicated to briefly discuss the design of the scanning technique (Lawson, 2015). The methodology of triangulation, tracking and sizing followed by the post-processing of the particle tracks to estimate the Lagrangian quantities is then discussed. Finally, a brief discussion on procedures to verify the results from the post-processing of the tracks is given.

2.1 Scanning system

The camera configuration in a scanning experiment is similar to a stereo PIV system configuration. The particles are recorded using two or more than two high speed cameras, as illustrated in the figure 2.1a, which view the laser sheet bundle from three angles of θ_1 , θ_2 and θ_3 , with respect to the laser sheet. Each is equipped with lenses, using a high f-number, which could provided sufficient depth of field to keep particle images in focus

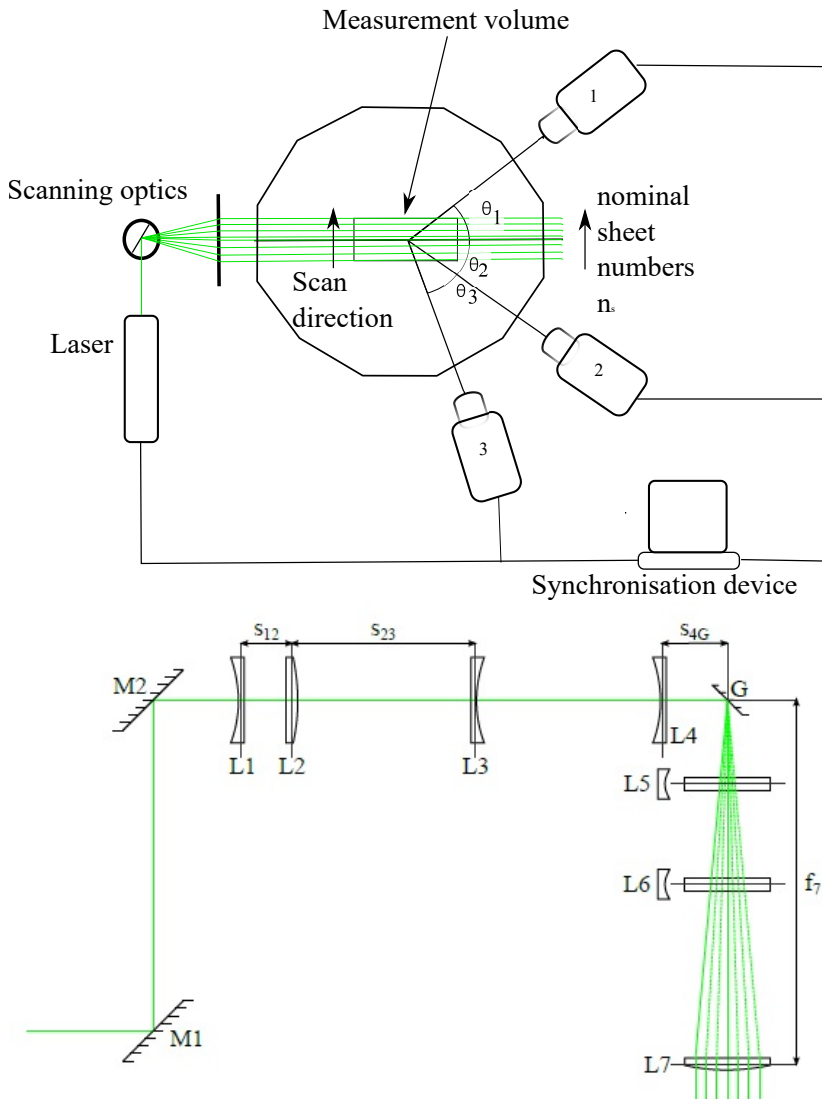


Figure 2.1: **a** Schematic of a typical scanning setup. **b** Schematic of the optics used in a typical scanning experiment (Lawson (2015)).

over the scan depth. The cameras are equipped with Scheimpflug adapters, to make the focal plane parallel to the laser sheet plane.

A set of optics are used in a scanning experiment to generate approximately parallel laser sheets with controlled laser sheet thickness. Figure 2.1b shows a schematic of the standard optical setup used to achieve this (Lawson, 2015). The first pair of lenses (L1 and L2), with variable focal length, act as a convergent compound lens. In combination with the divergent lens L3, the arrangement forms a telescope, which allows the thickness

of the beam to be decreased by up to a factor of six and the collimation to be varied independently.

After passing through a spherical divergent lens (L4), the beam reflects off the galvanometer mirror (dynAXIS XS, Scanlab GmbH) at G. A galvanometer mirror is preferred over a rotating mirror drum, rotating polygon mirrors, a rotating prism as it is free from vibrations, that can cause uncertainty in the laser sheet position. After reflecting from the galvanometer mirror the beam passes through a pair of cylindrical lenses (L5 and L6), which expand it to a sheet. Finally, a convergent lens L7 acts to make the laser sheets parallel, since the mirror surface (G) is placed one focal length away from L7. The divergent lens (L4) was introduced to control the position of the beam waist induced by L7. By coordinating the steady rotation of the mirror with the laser triggering, parallel laser sheets can be generated which traverse the measurement volume at a constant rate.

A number of parallel laser sheets, N_s , of thickness w , generated from the scanning optics, travel across the volume at a constant rate over the course of which N_s images are acquired by each of the cameras, at a frame rate $1/T_F$. At the end of a scan, there is a “retrace period” of duration T_{RET} where the mirror returns to its starting position. The timing of the displacement generated by the scanning optics is synchronised with the pulsed laser such that the spacing between subsequent laser sheets is Δz . Figure 2.2 illustrates a typical timing diagram for a scanning acquisition.

The interval between subsequent acquisitions is $\Delta T \approx N_s T_F + T_{RET}$, which specifies the time separation between subsequent volumes. In order to “freeze” the flow, the ratio of ΔT and $w/\Delta z T_F$ is kept large (Brücker *et al.*, 2012).

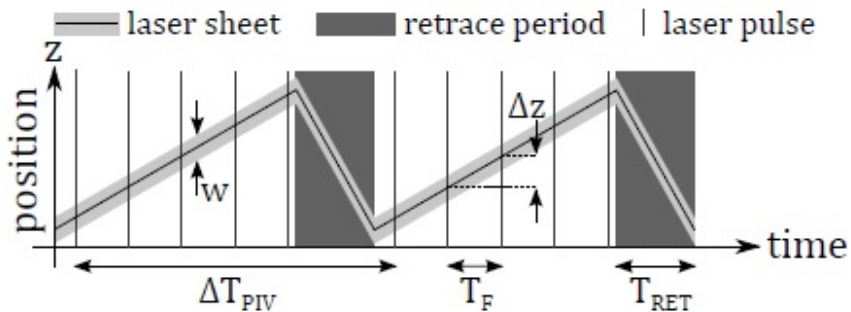


Figure 2.2: Typical timing diagram of a scanning acquisition (Lawson, 2015).

2.2 Calibration

In this section, the basis for the camera model and the calibration procedure for the camera and the laser is discussed.

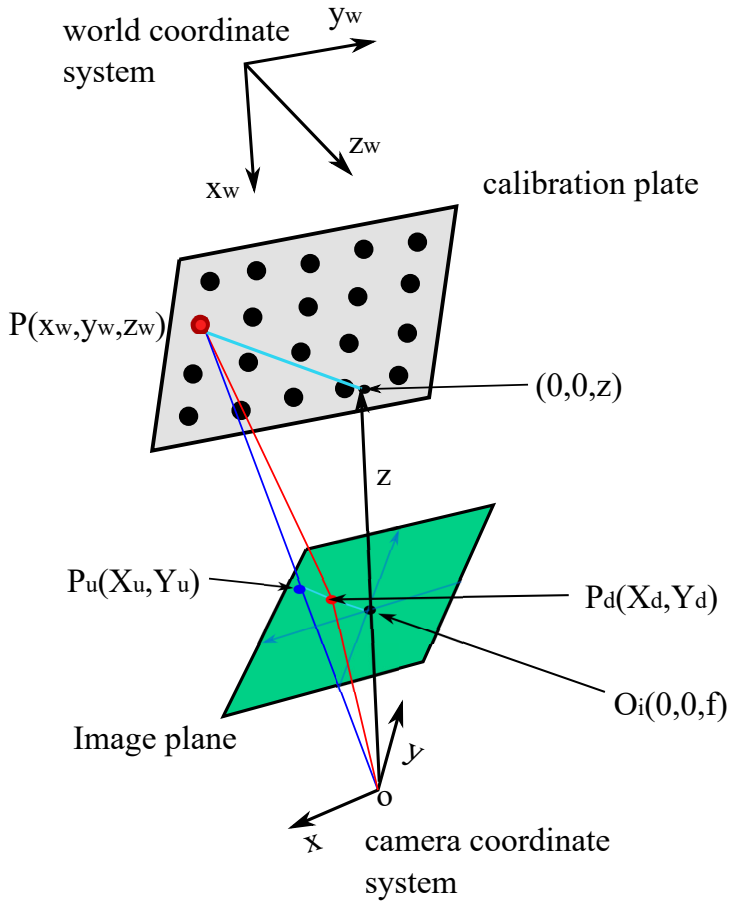


Figure 2.3: Schematic of a pinhole camera model (Tsai (1987)).

2.2.1 Camera model

A pinhole model is chosen for the camera calibration. The projection of a point in 3D to 2D can be done in four steps Tsai (1987). In figure 2.3, in order to project the 3D coordinate (x_w, y_w, z_w) , it has to first converted from the world coordinate system to the camera coordinate system (x, y, z) . This is done by the rotation R_j and the translation matrix T_j as,

$$\begin{pmatrix} x \\ y \\ z \end{pmatrix} = R_j \begin{pmatrix} x_w \\ y_w \\ z_w \end{pmatrix} + T_j \quad (2.1)$$

Next, the point in the camera coordinate is converted to the image coordinate as,

$$X_u = f \frac{x}{z} \quad \text{and} \quad Y_u = f \frac{y}{z}, \quad (2.2)$$

where f is the focal length. A correction for the radial distortion has to be applied, which is given by

$$X_d = X_u + X_u(k_1 r^2 + k_2 r^4 + \dots) \quad \text{and} \quad Y_d = Y_u + Y_u(k_1 r^2 + k_2 r^4 + \dots) \quad (2.3)$$

with $r = \sqrt{X_d^2 + Y_d^2}$.

Finally, the image coordinate is transformed to the pixel coordinate as

$$X = \frac{s_x X_d}{d_x} \quad \text{and} \quad Y = \frac{X_d}{d_y} \quad (2.4)$$

where d_x and d_y are the number of pixels in x and y , and s_x is the skew parameter that represents the scale factor of the pixel array.

2.2.2 Camera calibration

The objective of the camera calibration procedure is to get the camera rotation, translation and camera matrix, which can be used to map the object space to the image space. A bundle calibration technique similar to Brücker *et al.* (2012), is used to calibrate the cameras.

To calibrate the cameras, images of a calibration plate are captured as the plate is moved across the measurement volume. The spacing of markers on the calibration plate, the position of the calibration plate and the orientation of the plate must be known to calibrate the cameras. With knowledge of the orientation of the calibration plate, simple geometry can be used to calculate object space coordinates of calibration markers (x, y, z) , whilst their image space counterparts (X, Y) can be identified using pattern matching. Using points from these two coordinate systems a pinhole camera model fit is applied.

There will be some residual error after the pinhole model has been fit. A bundle adjustment procedure which is as an iterative algorithm Triggs *et al.* (2000), is applied to minimize the residual error. Each iteration consists of two steps: resection and intersection. In the resection step, a camera pinhole model is fitted to the object space coordinates of the calibration markers, calculated from the internal model of the plate position and orientation. Then, it is supposed that knowledge of the plate position and orientation is wrong. The intersection step is a least-squares optimization which minimizes the residual error between the marker positions projected in image space and their measured positions. This creates an update of the position and orientation of the plate in each pose, which is

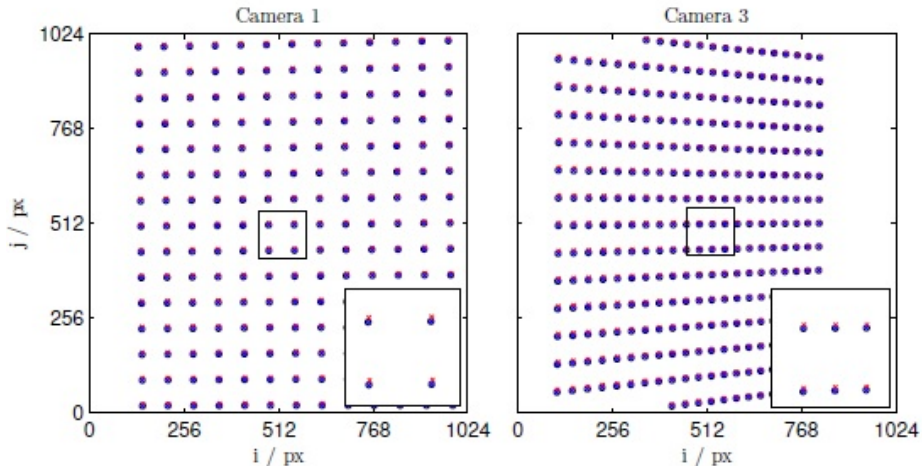


Figure 2.4: Measured (o) and re-projected (x) measured marker positions for one position of the calibration plate, before (red) and after (blue) bundle calibration. The inset shows a zoomed in version of the marked region in either sub figure (Lawson, 2015).

used for the next iteration. The algorithm converges to a solution in under five iterations. Figure 2.4 shows the difference between the model before and after a bundle adjustment procedure and measured marker positions re-projected marker positions after bundle calibration (in blue). After bundle calibration, the re-projected (modeled) markers agree much more closely with the measured marker positions, which indicates that the systematic disparity has been eliminated.

2.2.3 Laser sheet calibration

Calibration of the laser sheet is performed, to get the position, orientation and width of all the parallel scanned laser sheets across the measurement volume. A self-calibration method described by Knutsen *et al.* (2017) is used due to its simplified approach. Here the position of the particles in the 3D space obtained by triangulation is related to its corresponding fractional sheet number f_s , which describes a particle's position relative to laser sheet and a laser sheet model is then fit this data. The concept of fractional sheet number will be described in detail in section 2.3.2. The details of the laser sheet calibration are given in Appendix B.

2.3 Data processing

In this section, the principles and steps of the new method for simultaneous particle tracking and sizing based on a scanning laser light source introduced and described. The

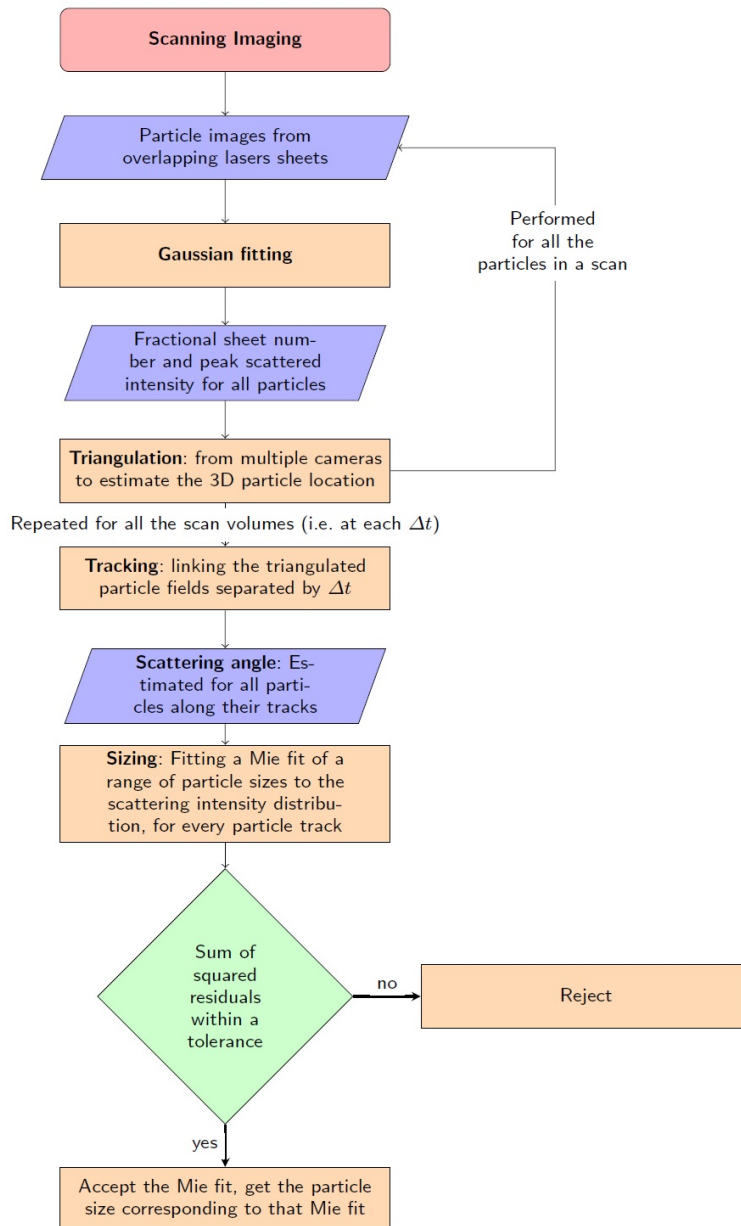


Figure 2.5: Flow chart for scanning particle tracking and sizing.

steps involved in the scanning particle tracking and sizing routine is depicted as a flow chart, in figure 2.5.

2.3.1 Detection of particle image locations

Laser light scattered from seeding particles is collected via the cameras' optics in the form of particle images. To reduce the impact of noise, image preprocessing is applied. Importantly the preprocessing is chosen in such a way that the intensity information of each particle over the course of a scan is preserved. Image noise is then reduced by using a Gaussian low-pass filter, with 3×3 pixel (px) window size and a standard deviation of 0.5 px, which also reduces the incidence of false particle detection. To identify particle image locations at sub-pixel accuracy, a standard 2D peak-finding algorithm is applied, which first identifies pixels above a prescribed threshold (presently based on the average of the 10 brightest pixels), and then fits two 1D Gaussian functions (Ouellette *et al.*, 2006) to neighbouring pixels.

One of the challenges of higher seeding densities is the effect of overlapping particles within images. Cierpka *et al.* (2013) shows that with increasing particle density, the percentage of particles overlapping also increases, which could lead to a shift in 2D peak identification, possibly resulting in significant positional errors. In scanning PIV, since the whole volume is subdivided into many smaller volumes (i.e. laser sheet thicknesses), the incidence of overlapping particle images is significantly reduced when compared to methods that illuminate the entire volume simultaneously for image taking. The present sub-pixel identification method attempts to avoid erroneous particle identification due to the remaining overlapping particles by rejecting particle locations if more than one peak is identified within a radius of 2-3 px.

2.3.2 Triangulation

Once the 2D locations in both camera views are identified, starting from an identified particle location in one camera image, an epipolar line in the other camera images can be calculated based on existing knowledge of the camera calibrations. Particle images in the second camera image coinciding with the epipolar line are candidates to be the particle's match in the second view. The length of this epipolar line is determined by the estimated depth range of the particle in the object space coordinate. In typical triangulation procedures (Maas *et al.*, 1993) this depth is chosen to be that of the illuminated measurement volume, classically the entire volume of interest. At high seeding densities, there can be many possible particle matches from the other view(s), the number being linearly proportional to the length of the epipolar line (Maas *et al.*, 1993). A better estimate of the particle's location along the depth coordinate z in object space will restrict the length of the epipolar line and thus reduce the number of possible matches.

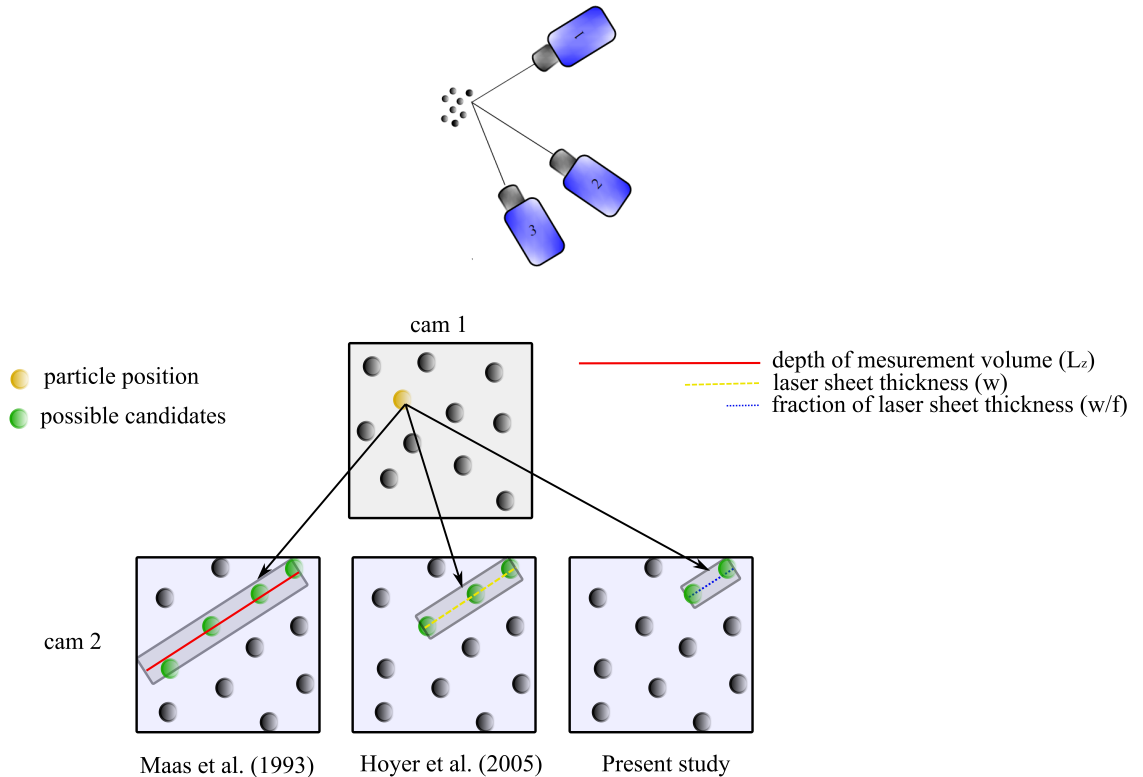


Figure 2.6: Schematic comparison of particle matching in classical triangulation used by Maas *et al.* (1993), in scanning technique used by Hoyer *et al.* (2005) and in the present study

Using a scanning technique (Hoyer *et al.*, 2005) reduces this depth to a fraction of the entire measurement volume. Having restricted the particle's location to the known z position of a nominal laser sheet n_s , Hoyer *et al.* (2005) used the thickness of the laser sheet as the length of the epipolar line for triangulation of individual particles. Such a scheme represents a great improvement in comparison to using the whole measurement volume depth, since the triangulation process begins with a much better estimate of the particle's location along the scan direction z , reducing ambiguous matching to other particles. Yet the chances of incorrect matching between camera images remains an issue, especially when seeding density increases for better spatial resolution of high-Reynolds number flows.

Figure 2.6, shows a comparison of the length of the epipolar lines used for particle matching, in the above mentioned two cases and that intended in this study. The present method seeks to improve this scanning setup by further tightening the particle's location

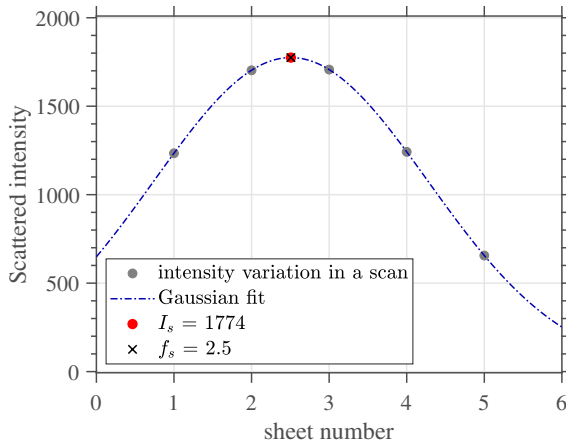


Figure 2.7: Variation in intensity of a particle as a function of nominal sheet number. A Gaussian fit gives the fractional sheet number and peak intensity at that fitted sheet number for the particle in the scan.

along the scan direction. In addition to the nominal sheet number n_s introduced above, a fitted fractional sheet number f_s is central to the current triangulation method. The nominal sheet number corresponds to the sheet number in which the particle is identified, changing value as the particle is illuminated by subsequent (overlapping) laser sheets as the laser sheet scans through the volume. The fractional sheet number f_s indicates the hypothetical sheet number where the particle location would coincide with the center of the laser sheet (location of peak intensity, assuming a Gaussian intensity distribution) as the laser sheet scans over it. To find f_s , instances of the same particle being illuminated by successive, overlapped sheets are grouped using a nearest neighbour approach. A search region of only 1-2 px is used as particle displacement during a scan is minimal given high scanning speeds. This is considerably larger than the expected displacement of the particles during image taking for the neighbouring sheets, however a slightly relaxed search radius may account for error during the peak finding step. This search region remains well below the average distance between particles, which can be estimated by $\bar{r}_{2D} = 0.5 N_{I,s}^{-1/2}$ (Adrian, 1991).

Once the particle's appearance in successive scan images is identified, the variation in its intensity during the scan is collated. Given a laser sheet whose intensity varies approximately as a Gaussian across its thickness, the fractional sheet number f_s of the particle is then estimated by fitting a Gaussian curve to these intensities and nominal sheet numbers n_s . The peak of the fitted Gaussian, as shown in figure 2.7, corresponds to the estimated fractional sheet number, which we assume corresponds accurately to the particle's location along the scan direction. This technique was originally intended for

laser sheet self-calibration (Knutsen *et al.*, 2017) discussed in section 2.2.3, but is here repurposed for finding the particle locations themselves along the scan direction.

The triangulation algorithm then follows that used by Maas *et al.* (1993), but now using a reduced search depth giving a shortened epipolar line. The first and last sheet images are excluded since they contain many particles at the edge of the measurement volume not illuminated more than once (obtaining a reasonably accurate f_s requires at least three readings of a particle's intensity). A schematic representation of a three-camera

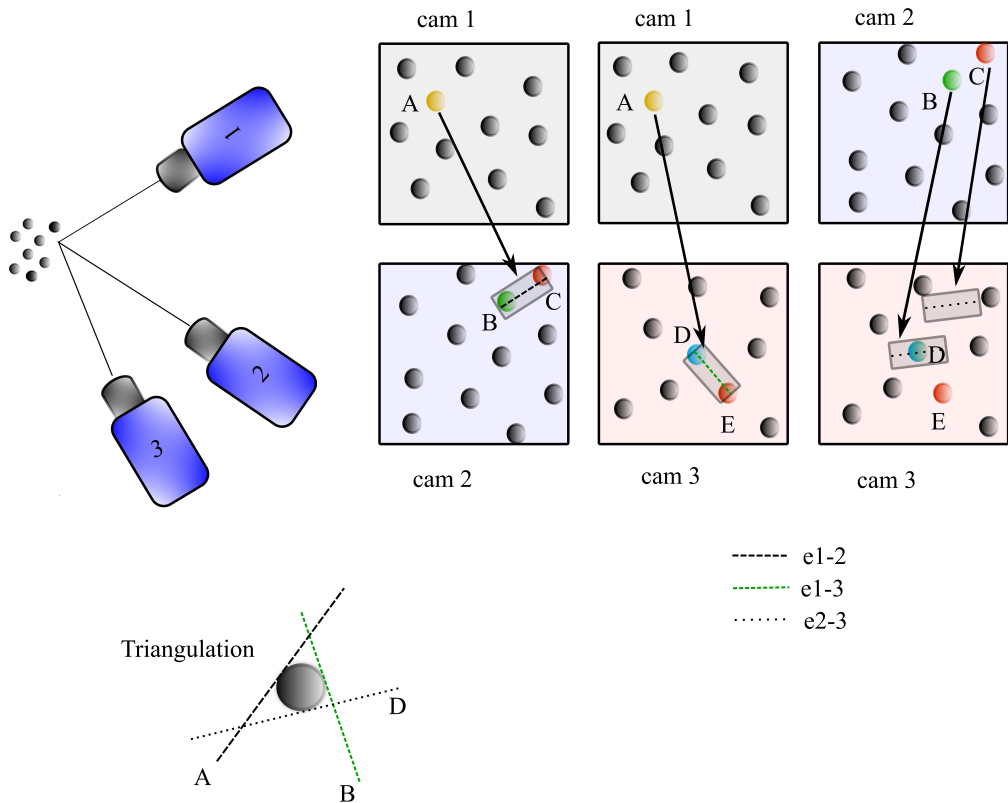


Figure 2.8: Schematic representation of three camera triangulation in the scanning technique. The epipolar lines of view a in view b is represented as e_{a-b}

triangulation is shown in figure 2.8. Starting with a particle A in camera 1, its f_s is used to fix a projection volume $dz = z(f_s) \pm \Delta_z$, where in practice a small tolerance Δ_z about the z location corresponding to the deduced f_s is used. This line of sight is then projected onto the image plane of the other cameras. Any particle image that is within a tolerance away from the projection of the line of sight is then added into a list. Such a list is created for each combination of two cameras. These lists are checked for closed paths which then contain the particle images belonging to a particle. In figure 2.8, the path is $1A \rightarrow 2B \rightarrow 3D \rightarrow 1A$. The estimated 3D locations are projected to all the camera views

to estimate the re-projection error, which is the difference between the actual location of the particle in the original image to that in its projected image from the candidate triangulation location. The 3D location is only retained as a triangulated particle if the re-projection error is below a certain threshold.

Finally, particles triangulated in a current sheet are removed from particle lists in subsequent sheets where they were identified during the calculation of their f_s . That is, when a particle is triangulated in sheet n_s , it is removed as a potential particle from sheets $n_s + 1$ and so on. Doing so means subsequent sheets have comparatively fewer particles on which a triangulation is attempted, accelerating the procedure along the scan direction z . In addition, an iterative triangulation for the whole volume may be attempted by using residual images. These are formed by subtracting the projected image of triangulated particles from the original image. For example, a 2 px radius about the projected location is identified within the original image, and this intensity distribution is subtracted to form the residual image for that sheet. If needed, it is possible to use a more sophisticated method for subtracting projected images of triangulated particle locations exploiting a calibrated optical transfer function (Schanz *et al.*, 2013), since overlapping images of particles not yet triangulated is also deleted in such a process. However, in this instance, a small fraction of particle images are overlapped due to the division of the volume into thin slices via scanning. Hence such a method is not expected to greatly improve upon a simpler subtraction of all intensity in the proximity of the projected image location.

2.3.3 Estimating the scattered intensity (I_s) of the particles

Scanning a laser sheet with increased overlap will measure the scattered intensity from the same particle multiple times, recording its intensity variation across a laser sheet. The effect of scanning a laser sheet with a Gaussian profile is shown in figure 2.7. The Gaussian fitting procedure explained in the previous section not only gives us the fractional sheet number (f_s), but also the fitted peak intensity corresponding to f_s . Since the fractional sheet number is the best approximation to particle location based on laser sheet center, the fitted peak intensity (I_s) at the fractional sheet number (f_s) should be the closest approximation to the scattered intensity at the centre of the laser sheet. This procedure helps us to avoid the trajectory effect reported in Chapter 1.

2.3.4 Building the trajectories

Estimated 3D locations in sets separated by the time interval Δt , now allows linking particles in time. The tracking procedure aims to correctly link the same particle between subsequent time steps. For particle tracking, the scheme of Malik *et al.* (1993) as shown in figure 2.9, was used. This algorithm was implemented in Matlab. The linking process is guided by three heuristic criteria:

1. *Nearest neighbour*: Here particle displacement is limited in all directions. For a particle $x_p(t)$, every particle in the next time step, within a maximum distance $\|x_p(t) - x_p(t + \Delta t)\| \leq x_{max}$ can be considered as a link. The location $x_p(t + \Delta t)$ closest to $x_p(t) + x_{max}$ is considered as the link. The success of linking particles in tracking depends upon the tracking parameter γ , which is the probability of finding only one or a small number of particles within the search volume. Based on the maximum radius r_s of the search volume, Malik *et al.* (1993) defined it as

$$\gamma = \frac{d_o}{r_s} \quad (2.5)$$

where d_o is the mean inter-particle distance. An equivalent to this, in terms of the maximum possible displacement of a particle in a flow $|x_{max}|$, was given by Pereira *et al.* (2006) as

$$\gamma = \frac{d_o}{|x_{max}|} \quad (2.6)$$

2. *Minimum acceleration*: Here the Lagrangian acceleration of a particle is limited. Using the particle positions at $t - \Delta t$ and $t - 2\Delta t$ and the one at the current frame t , the velocity is calculated and the position at $\hat{x}_p(t + 1\Delta t)$ can be predicted. For all particles in the search radius around the estimate, the acceleration can be calculated. The trajectory showing minimal acceleration is considered to be more likely to be physically correct.
3. *Least change in acceleration*: The position, velocity \hat{v}_p , and acceleration \hat{a}_p , of the particle in frame $n + 1$ is estimated using the step described above. The position in frame $n + 2$ can be estimated as $\hat{x}_p(t + 2\Delta t) = \hat{x}_p(t) + \hat{v}_p(2\Delta t) + \hat{a}_p(2\Delta t)$. For all points in a search region around $\hat{x}_p(t + 2\Delta t)$ the change in acceleration, is calculated. The best match for the frame $n + 1$ is the particle showing the minimum change in acceleration from the prediction in frame $n + 2$. In cases of multiple choices, the trajectory resulting in the smallest change in acceleration is deemed the most likely one.

2.3.5 Particle trajectory processing

A detailed description of the particle tracking methodology is given in the next chapter. In this section, the steps involved in estimating the Lagrangian velocity, acceleration, spatial and temporal derivatives from the tracks are explained.

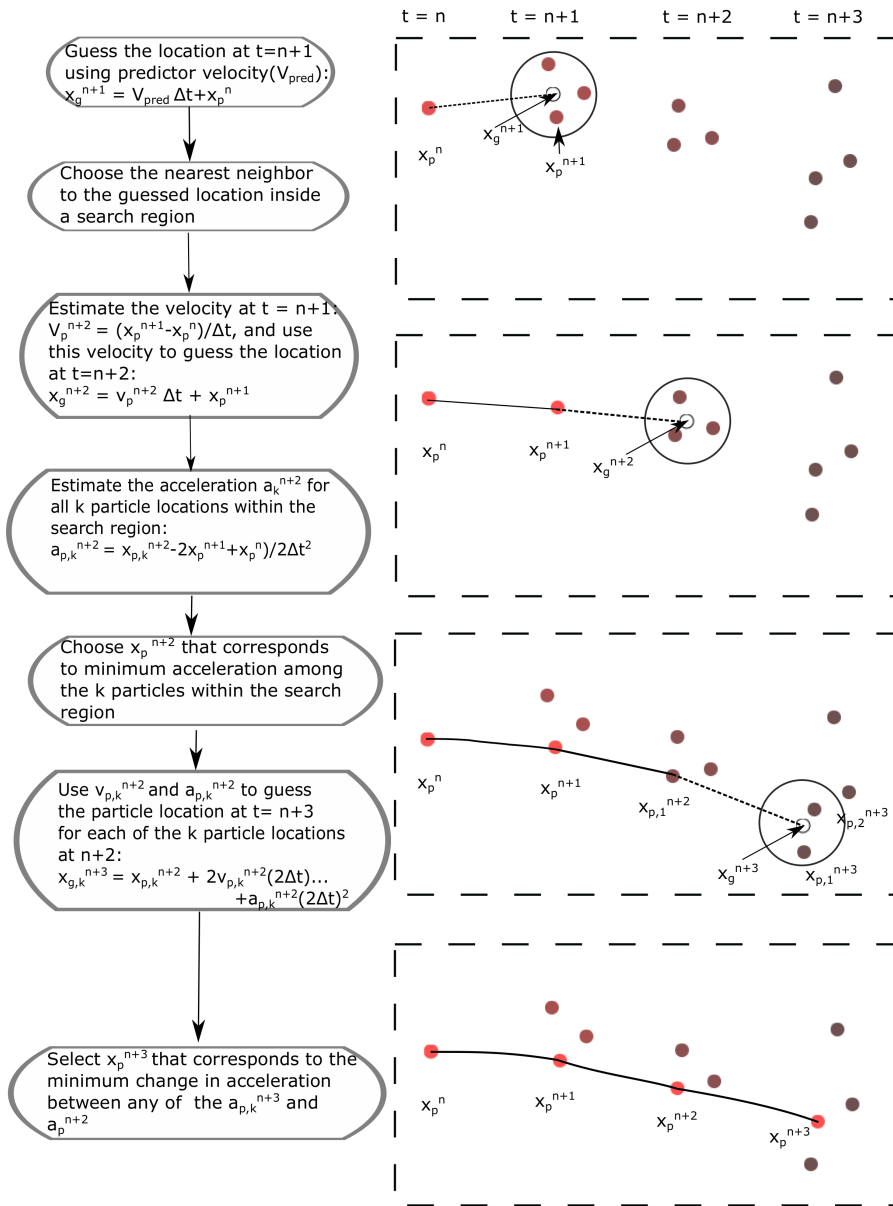


Figure 2.9: Schematic representation of the particle tracking algorithm.

The Lagrangian velocity u_i at a time step t is obtained as

$$u_i(t) = \frac{1}{2} \left(\frac{x_i(t + \Delta t)}{\Delta t} - \frac{x_i(t - \Delta t)}{\Delta t} \right) \quad (2.7)$$

and the Lagrangian acceleration a_i can be obtained using

$$a_i(t) = \frac{1}{2\Delta t} \left(\frac{x_i(t + \Delta t)}{\Delta t} - 2\frac{x_i(t)}{\Delta t} + \frac{x_i(t - \Delta t)}{\Delta t} \right) \quad (2.8)$$

Lüthi *et al.* (2005) presented a method that yielded filtered Lagrangian velocities and accelerations from the trajectories using a moving-spline interpolation scheme, since the velocities and especially the accelerations obtained from a simple central difference of position data showed significant noise, caused mainly by positioning errors. The interpolated positions were derived from a third-order polynomial moving-spline function fitted from an over-determined set of ten points prior and post the current point along the trajectory ($(t - 10\Delta t)$ and $(t + 10\Delta t)$). The position, velocity and acceleration, \hat{x}_i , \hat{u}_i and \hat{a}_i , after filtering is obtained as

$$\hat{x}_i(t) = c_{i,0} + c_{i,1}t + c_{i,2}t^2 + c_{i,3}t^3 \quad (2.9)$$

$$\hat{u}_i(t) = c_{i,1} + 2c_{i,2}t + 3c_{i,3}t^2 \quad (2.10)$$

$$\hat{a}_i(t) = 2c_{i,2} + 6c_{i,3}t \quad (2.11)$$

The filtered velocities obtained from the above step, the spatial ($\partial u_i / \partial x_j$) and temporal velocity derivatives ($\partial u_i / \partial t$), are interpolated for every particle trajectory point. The procedure involves two steps: a local linear interpolation of the velocity field and a weighted polynomial fit to the derivatives along particle trajectories, making use of the auto-correlations of the Lagrangian derivatives.

Spatial velocity derivatives

Assuming that to a good approximation the velocity field in the proximity of position x_0 is linear, for $\hat{u}_i(x_0)$, $i = 1, 2, 3$, the linear ansatz

$$\hat{u}_i(x_0) = c_{i,0} + c_{i,1}x_1 + c_{i,2}x_2 + c_{i,3}x_3 \quad (2.12)$$

with,

$$c_{i,1} = \frac{\partial u_i}{\partial x_1}, c_{i,2} = \frac{\partial u_i}{\partial x_2}, c_{i,3} = \frac{\partial u_i}{\partial x_3} \quad (2.13)$$

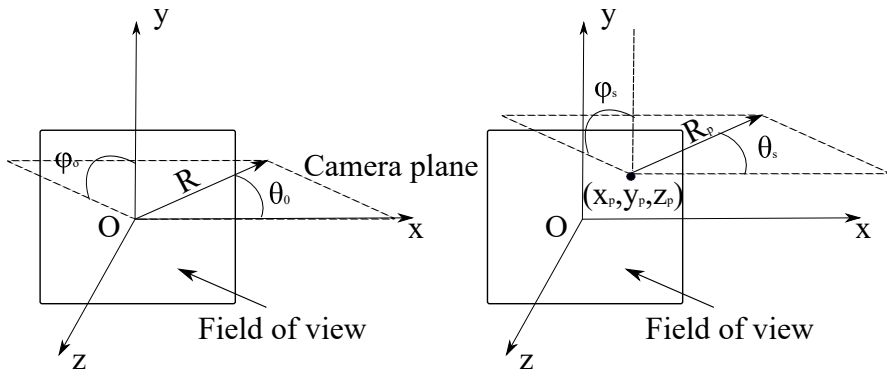


Figure 2.10: Schematic definition of (a) camera angle θ_0 and azimuthal angle ϕ_0 (b) scattering angle θ_s and the corresponding azimuthal angle ϕ_s of particle in the field of view.

Information from $n = 4$ points are enough to solve the expression 2.13, but as the sensitivity of $c_{i,j}$ to errors of \hat{u}_i are high, it will therefore be used to determine the weights of individual equations of $\mathbf{A}\mathbf{c}_i = \mathbf{v}_i$, with information from $n \gg 4$, is used to obtain c_i , as

$$\mathbf{c}_i = (\mathbf{A}^T \mathbf{v}_i)(\mathbf{A}^T \mathbf{A})^{-1}, \quad (2.14)$$

where \mathbf{A}_i is the position vector and \mathbf{v}_i is the velocity vector.

Temporal velocity derivatives

For $\hat{u}_i(x_0)$, $i = 1, 2, 3$, the linear ansatz

$$\hat{u}_i(x_0) = c_{i,0} + c_{i,1}x_1 + c_{i,2}x_2 + c_{i,3}x_3 + c_{i,4}t \quad (2.15)$$

with,

$$c_{i,1} = \frac{\partial u_i}{\partial x_1}, c_{i,2} = \frac{\partial u_i}{\partial x_2}, c_{i,3} = \frac{\partial u_i}{\partial x_3}, c_{i,4} = \frac{\partial u_i}{\partial t} \quad (2.16)$$

Again, a system of weighted linear equations is used to obtain c_i (expression 2.15) with the weighted information of n points that are in the proximity of x_0 .

2.3.6 Estimating the scattering angle (θ_s) of the particles

The scattering angles of a particle along its track has to be estimated for the sizing step. To estimate this, the parameters of the camera projection function from 3D to 2D for the cameras involved, represented by the camera matrices are used. The positions of the cameras are determined by the scattering angle θ_o , azimuthal angle ϕ_o and the distance R to the cameras, with respect to the center of the cameras field of view as shown in figure

2.10. The scattering angle and the azimuthal angle for any particle located at (x_p, y_p, z_p) in the field of view can be derived as

$$\tan\theta_s = \frac{(R_p^2 \sin^2\theta_o + y_p^2 - 2y_p R_p \sin\theta_o \cos\phi_o)^{1/2}}{R_p \cos\theta_o - x_p}, \quad (2.17)$$

$$\sin\phi_s = \frac{(R_p \sin\theta_o \sin\phi_o)}{(R_p \cos\theta_o - x_p) \tan\theta_s} \quad (2.18)$$

where $R_p = R + z_p$.

2.3.7 Estimating particle sizes

As explained in section 1.3, the scattered light intensity is an oscillating function of the scattering angle. The angular distribution of the scattered intensity of a particle in a fringe changes rapidly with its size, due to the increase in oscillations with an increase in particle size. This increase in oscillations has a nearly linear relationship with the size of the particle, as shown in figure 2.11a, for a polystyrene particle with refractive index 1.586. This demonstrates that the angular distribution of scattered light in any fringe should be unique for any particle size, for a given refractive index. A measurement of scattered intensity distribution at convenient angles within a fringe can thus give a useful estimate of the size of the particle.

In addition, the positions of the fringe maxima are linear with the number of maxima, as shown in figure 2.11b. The slopes represent the average width $\Delta\theta$, between these maxima in the oscillations. The slope values decrease with particle size, whereas the linear correlation coefficients are always greater than 0.99, for all the sizes, which means that this width $\Delta\theta$ changes minimally with the scattering angles. This also means that the half the width $\Delta\theta/2$, can represent the average width.

The particle tracks for each particle in the volume gives us the variation of fitted scattering intensity with respect to the scattering angle obtained using the 3D location of the particle along the track. We apply a fit using appropriate theoretical curves, on this data. The theoretical scattering intensities were calculated using the equations in Append. A. It is difficult, if not impossible, to calculate the absolute theoretical scattering intensity with any real accuracy, because it depends on many factors, such as the density of the particle in the medium and the absolute intensity of the incoming beam. Therefore, we decided to have our fitting routine applied to the normalized data. The intensities are normalized by the highest intensity along the scattering angle for each particle. All initial scattering intensities were calculated using an in-house MATLAB program, which generates angular scattering distributions for some scaling factor, given a size parameter (α). The program was used to generate tables of scattering intensities over relevant ranges of angles and size parameters in increments of 0.001 deg and 0.12, respectively.

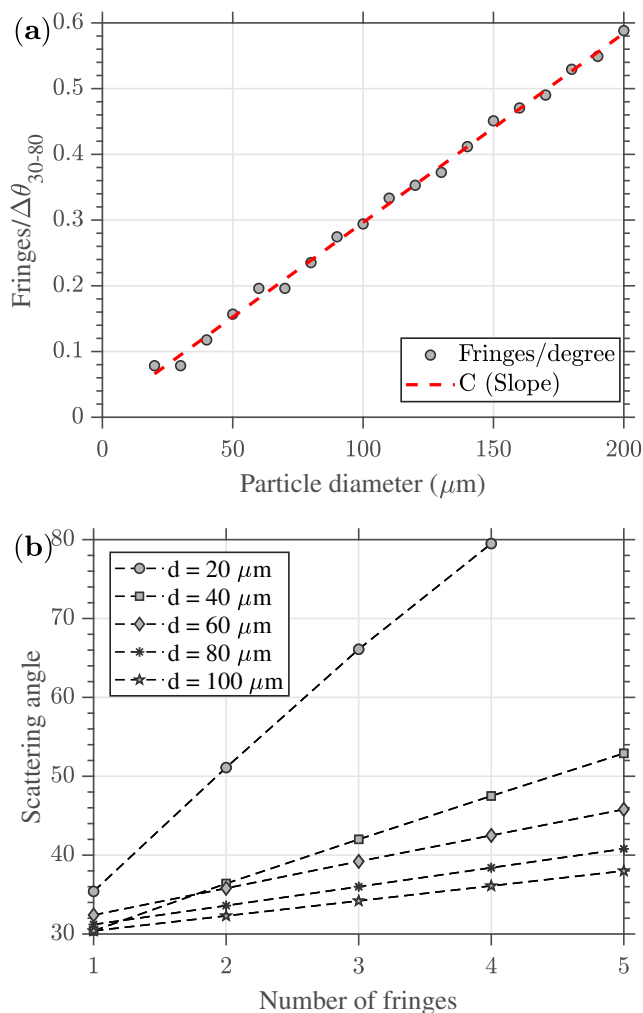


Figure 2.11: (a) Number of peaks in the oscillation of scattering intensity per unit scattering angle, for increasing particle size (b) Relationship between the number of fringes to the fringe position in the Mie pattern for increasing particle size.

The fitting program takes as input the theoretical scattering tables and the measured angular scattering data. To the given measured angular scattering data, the best-fitting curve from the theoretical scattering tables is obtained by minimizing the sum of the squares of the offsets (χ^2) of the points from the curve. The sum of the squares of the offsets is used instead of the offset absolute values because this allows the residuals to be treated as a continuous differentiable quantity. The accuracy of the fit is in principle only limited by the spacing of the size parameters in the theory table constructed. Figure 2.12(a) and (b), markers in the plot shows the scattered intensity for the selected scattering angle

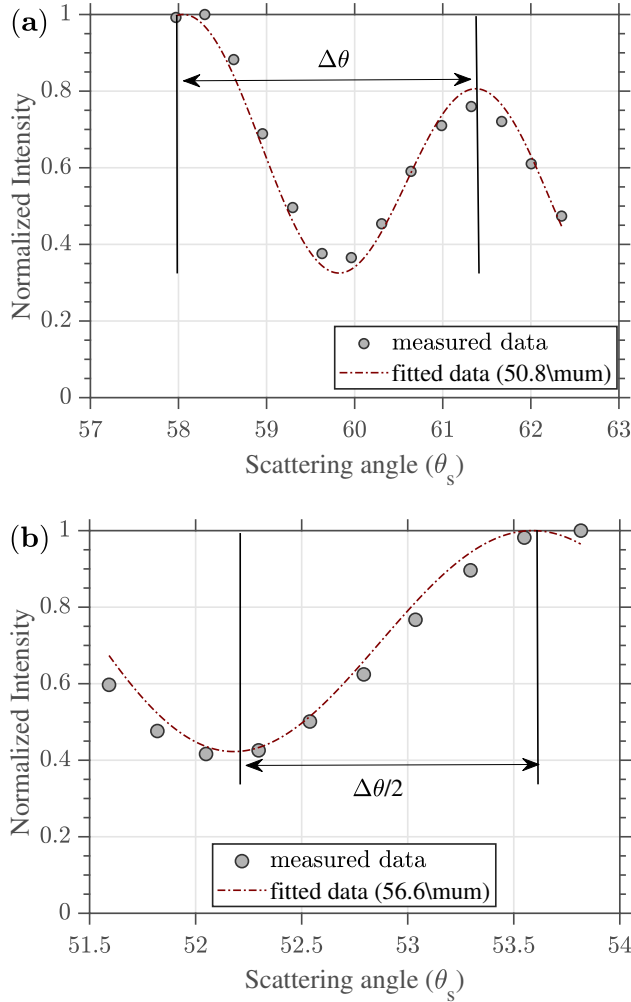


Figure 2.12: Scattering data for particles with (a) $50.4 \mu\text{m}$ diameter ($\alpha = 59.5$) and (b) $56.2 \mu\text{m}$ diameter ($\alpha = 66.4$); incident laser light ($\lambda = 532 \text{nm}$). The best fit is to particles with $50.4 \mu\text{m}$ and $56.6 \mu\text{m}$.

in the x-axis for two closely sized, numerically generated polystyrene particles with of size $50.4 \mu\text{m}$ and $56.2 \mu\text{m}$, with small jitter in the real intensity values for these particle sizes. The solid line shows the application of the scattering intensity variation (best fit) obtained after applying the Mie fitting procedure explained above. The best fit retrieves the sizes of these particles with an accuracy level within $0.5 \mu\text{m}$.

2.4 Data verification

Estimation of the quantities described above from the particle tracks involves a lot of steps including measurements, image processing, polynomial fittings etc. It is therefore essential to check the final accuracy of these measured quantities.

The incompressibility of water, naturally helps to check with divergence criteria, where the trace of $\partial u_i/\partial x_j$ should be zero i.e.:

$$\frac{\partial u_i}{\partial x_i} + \frac{\partial u_j}{\partial x_j} + \frac{\partial u_k}{\partial x_k} = 0 \quad (2.19)$$

Numerous variations on these tests exist. Examples include measuring the root mean square (RMS) divergence, the correlation coefficient between longitudinal velocity gradients, and examining single and joint PDFs of normalised and unnormalised longitudinal velocity gradients. These provide a rough estimate of the error in velocity gradients.

Another check, involves everything that could be measured, namely, Lagrangian accelerations, $a_i = \frac{Du_i}{Dt}$, local accelerations, $a_{l,i} = \frac{\partial u_i}{\partial t}$ and convective accelerations, $a_{c,i} = u_j \frac{\partial u_j}{\partial x_j}$. An approach, similar to divergence check can be used as an overall check of the applied procedures, i.e.:

$$\frac{Du_i}{Dt} = \frac{\partial u_i}{\partial t} + u_j \frac{\partial u_j}{\partial x_j} \quad (2.20)$$

The left-hand side of the equation is derived from the trajectory of a single particle, whereas the right-hand terms need common information from neighboring particles. In a spatially under-resolved low-pass-filtered flow field, the divergence check might still be satisfactory with underestimated velocity gradients. The acceleration check provides a better assessment of the accuracy of velocity derivatives, because a_i , compared to the other two quantities, is obtained in a more straightforward manner.

2.5 Summary

The general setup of a scanning system is described with a detailed description of the scanning optics and timing in the scanning acquisition are given. the calibration procedure for the camera and the laser sheets have also been discussed.

The methodology of the scanning particle tracking and sizing have been described. The present scanning technique permits to extend the seeding density at which a ‘classic’ LPT methodology such as that of Maas *et al.* (1993), where sequential particle fields are triangulated following which particles are linked to form tracks, can be used. 3D particle field reconstruction is completed for each individual sheet location along the scan, permitting higher particle densities and more accurate triangulation by restricting individual particle locations to the thin illuminated volume where the particle was imaged.

The triangulation process is improved by using a fitted sheet number (Knutsen *et al.*, 2017) as opposed to the nominal sheet number for particles identified in each image.

The size of the particle is estimated by minimizing the squared difference between normalized intensity along a track and normalized theoretical intensity along the same track obtained from GLMT, over a range of particle sizes.

Chapter 3

Validation of the scanning particle tracking and sizing technique via numerical simulation

3.1 Introduction

In this Chapter, the scanning particle tracking and sizing technique are validated using synthetic experiments. Before validating the technique, a study of the effect of experimental parameters on the tracking technique is studied. The present work mainly aims in improving the triangulation part of the full tracking scheme, hence the influence of various scanning parameters upon the performances of the proposed triangulation method for instantaneous 3D particle fields is studied. Particles triangulated within fields at subsequent times are then linked to form tracks according to the scheme of Malik *et al.* (1993).

Section 3.2 describes the procedure to generate synthetic images for a scanning setup. In section 3.3, different experimental parameters for particle tracking, with the effect of controllable experimental parameters such as the seeding particle density, laser sheet overlap, sheet thickness and scanning laser sheet speed, all being set prior to performing an experiment, and uncontrollable factors such as the effect of noise in the images and deviations of the laser sheet intensity profile from an assumed ideal Gaussian one, are studied. For the study of controllable experimental parameters, ideal noise-free images were used. The results are quantified in terms of both accuracy (mean error in the triangulated particle locations with respect to ‘ground truth’ particle locations) and efficacy (fraction

Numerical simulation

Table 3.1: Nomenclature. $[L]$ is the length and $[T]$ the time unit adopted in the physical experiment or DNS database

Parameter	Symbol	Unit
Nominal sheet number	n_s	
Fitted sheet number	f_s	
Number of laser sheets	N_s	
Sheet e^{-1} width	w	$[L]$
Sheet overlap	Δz	$[L]$
Meas. volume dimensions	L_x, L_y, L_z	$[L]$
Particle density (3D)	N_V	ppv
Equiv. particle image density	N_I	ppp
Particle image density, per sheet	$N_{I,s}$	ppp
Particle image diameter	D	$[L]$
Number of particles	N	
Number in a single sheet	N_{ps}	
Number of overlapping particles in a single sheet	N_{os}	
Magnification	M	px/ $[L]$
Sheet speed	u_s	$[L]/[T]$
rms turbulent velocity	u'_{rms}	$[L]/[T]$
Kolmogorov lengthscale	η	$[L]$
Kolmogorov timescale	τ_η	$[T]$

of ‘ground truth’ particles triangulated) of the triangulation procedure. In section 3.4 results of a synthetic tracking experiment are presented. The accuracy of the tracking for a high seeding density case is presented and discussed.

In section 3.5, the experimental design considerations for the particle sizing routine is detailed. This includes the measurement area, minimum and maximum measurable diameter for a given configuration, effect of camera angle, camera solid angle and finally the number of cameras required for efficient sizing. Before concluding this chapter, the results from a numerical experiment with known sizes with effects of noise in scattering intensity and scattering angles is given in section 3.6.

3.2 Synthetic particle image generation for the scanning setup

Synthetic images were generated for a simulation of the scanning configuration, which was set up to mimic the previously-realised experiment of Lawson & Dawson (2014). The scanning parameters were chosen based on the dimensions of the simulated volume. Two cameras were simulated at angles $\theta = 30^\circ$ and -30° , whose sensor sizes were set to 1024×1024 px. Particles were randomly distributed within the volume, based on the required volumetric seeding density N_V in particles per voxel (ppv). The laser sheet positions along the scan were set based on a laser sheet thickness w , sheet spacing Δz and number of sheets N_s , required to scan the depth along the scanning direction L_z . Particles located within the sheet thickness at each sheet position were then projected to image coordinates using a pinhole camera model (Hartley & Zisserman, 2003).

The intensity $I(z)$ of a particle as a function of its z -position within a laser sheet follows the form (Scharnowski & Kähler, 2016):

$$I(z) = I_{max} \cdot \exp \left[- \left| \left(\frac{2z}{\Delta z_0} \right)^s \right| \right], \quad (3.1)$$

where $\Delta z_0 = w$ is the width at which $I(z)$ drops to I_{max}/e , and s is the shape factor, $s = 2$ being presently used to yield a Gaussian beam profile. The maximum intensity at the light sheet centre, I_{max} , at a scattering angle of $(\pi/2 - \theta)$ is modelled as

$$I_{max} = \frac{4}{\pi k^2 R^2} I_\lambda i(\theta)^2, \quad (3.2)$$

where I_λ is the input light energy density (set to 2.546×10^4 J/m²), $i(\theta)$ is the Mie scattering coefficient, R is the distance of the particles from the camera sensor and $k = 2\pi/\lambda$ is the wave number for wavelength $\lambda = 532$ nm.

Random background white noise was added to the images at a range of levels (section 3.3.2) with the mean of each noise level set as a percentage of the maximum intensity in the original noise-free image.

Table 3.2: Relevant scanning PTV parameters for testing of experimental setup

Parameter	Symbol	Value
Taylor microscale Re	Re_λ	418
Measured volume width	L_x/η	128
Measured volume height	L_y/η	128
Measured volume depth	L_z/η	32
Camera 1 viewing angle	θ_1	30°
Camera 2 viewing angle	θ_2	-30°
Image resolution (px)	–	1024×1024
Particle image diameter	D/η	0.02
Laser sheet thickness	L_z/w	variable
Laser sheet spacing	$M\Delta z$	variable
Laser sheet overlap	$w/\Delta z$	variable
Laser sheet speed	u_s/u'_{rms}	variable

3.3 Study of experimental parameters for particle tracking

3.3.1 Controllable experimental parameters

Seeding density

To study the effect of increasing seeding density on the efficacy and accuracy of the triangulation method, six seeding densities N_V (in ppv) ranging $N_V = 1.8 \times 10^{-5} - 4.4 \times 10^{-4}$ ppv were considered. An approximate particle image density N_I (in ppp), representing the equivalent particle image density assuming full-field illumination so as to permit comparison with volumetric 3D-PTV methods, is found by conversion of N_V using an adjusted scanning depth ℓ_z (in px) accounting for the viewing angle:

$$N_I \approx N_V \ell_z = N_V \frac{L_z}{\cos \theta}, \quad (3.3)$$

such that our tested range corresponds to $N_I \approx 0.05 - 0.125$ ppp. The Iterative Particle Reconstruction (IPR) of Wieneke (2012) is able to reconstruct particle fields from single recordings up to around $N_I \approx 0.05$ ppp. Building upon IPR by additionally exploiting time information yielded from a sequence of recordings, the ‘Shake-The-Box’ method (Schanz *et al.*, 2016) was shown to be highly effective in creating accurate and virtually ghost-free particle tracks over the range $N_I = 0.01 - 0.125$ ppp. With regards to the sheets, $L_z/w = 12$, $w/\Delta z = 5$ were set for this section. Setting $L_z/w = 12$ means

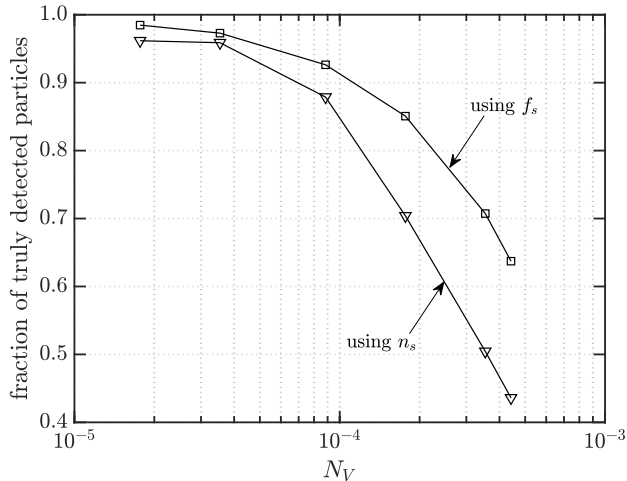


Figure 3.1: Fraction of successfully triangulated particles, given the known ‘ground truth’ locations: the nominal sheet number n_s as in Hoyer *et al.* (2005), and the fitted sheet number f_s

the actual particle image densities tackled by the present method corresponds to $\approx N_I/(L_z/w) = N_{I,s} \approx 0.0034 - 0.010$ ppp. That the actual particle image densities faced by the triangulation algorithm are so reduced via partition of the volume using scanning means the ‘classic’ triangulation of Maas *et al.* (1993), improved using a fitted sheet number f_s , performs satisfactorily. These two sheet parameters are shown in figure 3.3(b) below to maximise the fraction, for a modest number of sheets, of ‘fitted’ particles, denoting those particles viewed three or more times such that their position along the scan direction z is estimated accurately by calculating their fitted sheet number f_s via Gaussian curve fitting. In addition $u_s/u'_{rms} = \infty$ was used for this section, such that all images are taken at the same time. In the present method, particle triangulation is aided by tightly fixing the location of each particle along the scan direction z via use of the fitted sheet number f_s . A tolerance of 1/4 th of the sheet thickness w about the estimated z location (from f_s) is used for triangulation.

If a triangulated particle is found within a 1 px radius of a known ‘ground truth’ particle location then the particle is deemed to be correctly ‘detected’, this being the same threshold used by Schanz *et al.* (2016). We note that increasing the search range would increase the number of ‘found’ particles, at the expense of triangulation accuracy. For the purposes of analysis, it is however necessary to define a threshold. Figure 3.1 shows the fraction of particles successfully triangulated over a range of N_V via the present scanning technique. Triangulation where the search depth is the entire volume generally becomes unfeasible (i.e. returns a larger fraction of ghost particles than ‘true’ particles) at particle

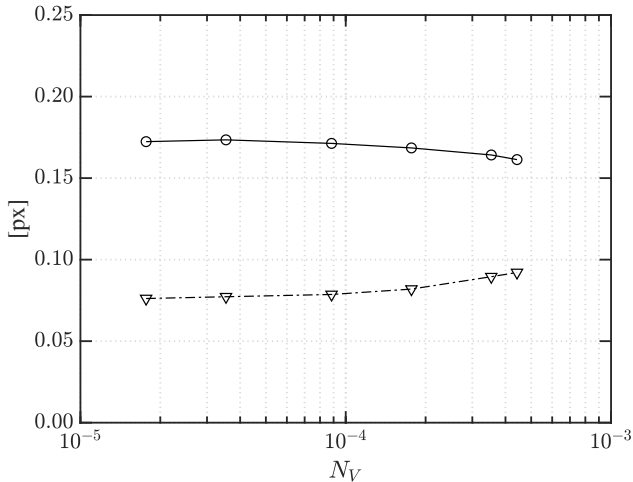


Figure 3.2: Positional error in ‘truly’ detected triangulated particle location for the current scanning PTV: ○, mean error and ▽, standard deviation in error

image densities of $N_I \approx 0.005$ ppp (for the present synthetic setup this corresponds to a volumetric density of $N_V \approx 1.8 \times 10^{-5}$ ppv using (3.3)). A significant improvement is found over the method of Hoyer *et al.* (2005), which used n_s , as the particle density increases. The vast majority of successfully triangulated particles are fitted with a f_s prior to triangulation; in those cases which they have not the particles’ nominal sheet number n_s may be used. The fraction of detected particles decreases rapidly with increasing seeding density for high N_V . At the highest seeding density considered ($N_V = 4.4 \times 10^{-4}$ ppv), the fraction of particles found is only around 0.6.

Figure 3.2 plots the mean and standard deviation of the positional error between the correctly triangulated (‘detected’) and ground truth particle locations. It is seen that as N_V increases, the fraction of successfully detected particles decreases as per figure 3.1. Interestingly, the positional error does not increase with increasing N_V for successfully detected particles, in fact decreasing slightly, however this is at least partially due to the criterion used for deciding on which particles are ‘detected’, currently set to be those within a 1 px radius of a ‘ground truth’ particle (i.e. there is an upper bound on the value that the error in figure 3.2 may take). That the mean positional error is ≈ 0.17 px then suggests that most correctly detected particles are in fact closer than 1 px to the ‘ground truth’ particle location. However, the percentage of ghost particles increases with increasing N_V . For the tested equivalent particle image densities $N_I \approx \{0.005, 0.01, 0.025, 0.05, 0.1, 0.125\}$ ppp (assuming full-volume illumination) the percentage of ghost particles detected is $\{0.23, 0.38, 1.7, 4.4, 12, 17.3\}\%$ (as a percentage of the total number of particles triangulated). Although out-performed on positional error by the iterative ‘Shake-The-Box’ method,

which is also able to effectively eliminate ghost particles at the densities considered here, the mean positional error with the current two-camera method compares favourably to that incurred with the iterative MLOS-SMART tomographic reconstruction method, which increases with increasing N_V . Additionally, the percentage of ghost particles reconstructed is much smaller, which with MLOS-SMART exceeds 250% at $N_I \approx 0.125$ ppp (Schanz *et al.*, 2016).

Sheet overlap

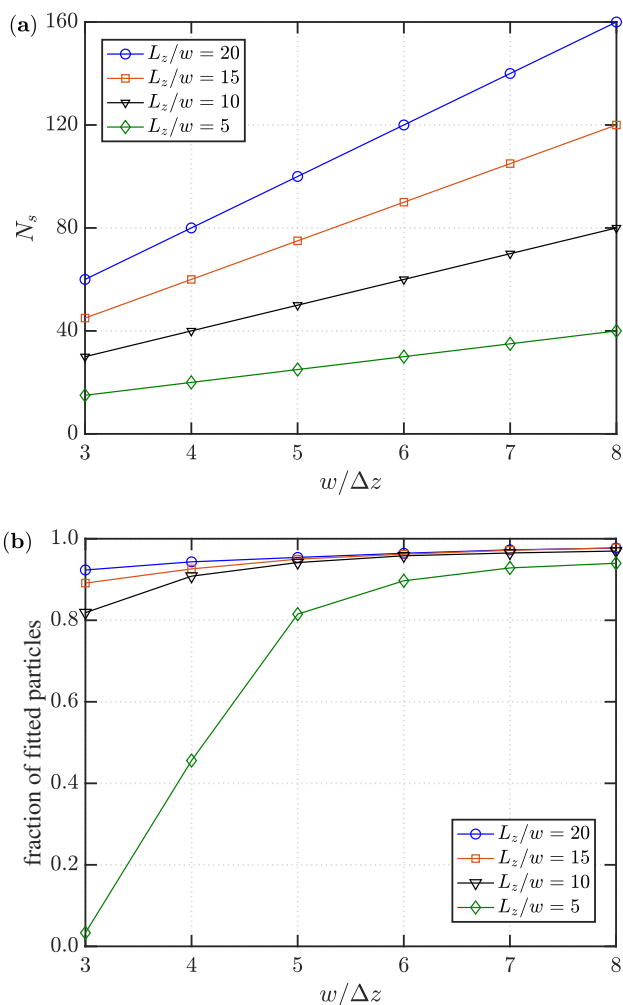


Figure 3.3: (a) Number of sheets N_s required as a function of sheet overlap $w/\Delta z$ for different sheet thicknesses L_z/w ; (b) fraction of particles successfully fitted

Here the effect of sheet overlaps $w/\Delta z$ and thickness L_z/w is considered. The triangulation efficacy of our method is directly dependent on the percentage of particles illuminated multiple times over the course of a scan. In order to fit a Gaussian profile, the particle's intensity must be measured at least three times. Hence it is necessary to understand how the fraction of successfully fitted particles depends on these parameters.

Figure 3.3 shows the result of this parametric study. Sheet overlap ratios of $w/\Delta z = \{3, 4, 5, 6, 7, 8\}$ are considered, corresponding to overlap percentages $\{66, 75, 80, 83, 85, 87.5\}\%$. For a fixed L_z , sheet thicknesses $L_z/w = \{5, 10, 15, 20\}$ are considered. Figure 3.3a shows how many sheets (N_s) are required for a fixed L_z as a function of sheet thickness L_z/w and sheet overlap $w/\Delta z$. For higher N_s , the image acquisition rate would need to be increased such that the flow remains 'frozen' as the scan is carried out. For the purposes of this section, sheet speed $u_s/u'_{rms} = \infty$ was used. Figure 3.3b shows how increasing sheet overlap but decreasing sheet thickness (increasing L_z/w) improves the fraction of fitted particles. The large increase for lower $w/\Delta z$ is expected since more particles will be identified the minimum three times required in order to deduce f_s from a Gaussian fit. The further slow increase at higher $w/\Delta z$ is attributable to more measurements giving a better estimate of f_s (higher N_s for increasing L_z/w and increasing $w/\Delta z$ as shown in figure 3.3a), and also possibly due to a lower effective seeding density with higher N_s as the scan progresses due to the residual triangulation method (i.e. where a particle, identified over multiple neighbouring sheets during the calculation of f_s , is removed from the particle lists of subsequent sheets where it appears if successfully triangulated in a previous sheet). However gains beyond $w/\Delta z = 5$ and $L_z/w = 10$ are marginal yet further increasing these requires more sheets. The values $w/\Delta z = 5$ and $L_z/w = 12$ were thus selected for the density study above in section 3.3.1 and for the synthetic particle tracking experiment in section 3.4.

Overlapping particle images

To study the effect of sheet width and particle density on the incidence of overlapping particle images, all N_V as considered in section 3.3.1 and the four sheet widths (L_z/w) from section 3.3.1 are investigated. The extent of overlapping particles directly affects peak-finding within the camera images and thus the correct identification of individual particles. The number of particles N_{ps} within a single image (i.e. the slice illuminated by the laser sheet) is calculated based on the sheet width as

$$N_{ps} = N \times \frac{w}{L_z}. \quad (3.4)$$

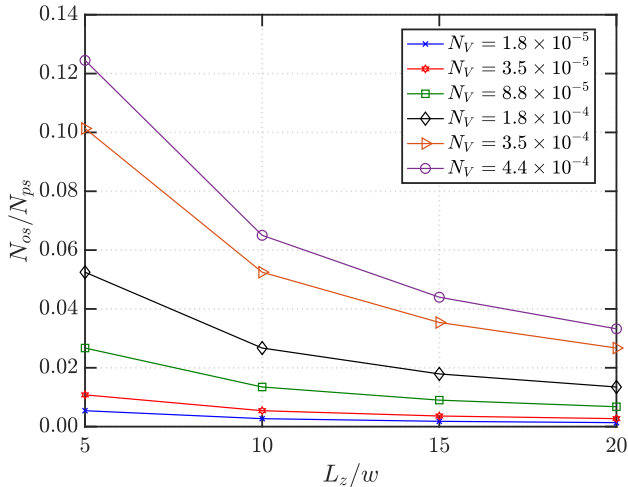


Figure 3.4: Fraction of overlapping particles for different sheet thicknesses L_z/w

The number of overlapping particles N_{os} in each sheet image of area $A = L_x \times L_y$ is then given by (Cierpka *et al.*, 2013)

$$N_{os} = (N_{ps} - 1) + \frac{A}{A_{crit}} \left(\exp \left[\frac{-(N_{ps} - 1)A_{crit}}{A} \right] - 1 \right), \quad (3.5)$$

where $A_{crit} = \pi(D/2)^2$ for particle image diameter D .

Figure 3.4 shows the percentage of overlapping particles for different sheet widths at the seeding densities studied. A high fraction of overlapping particles will degrade the efficacy of individual particle identification in images for the ensuing triangulation. The fraction of overlapping particle images is essentially zero for the lowest density case $N_V = 1.8 \times 10^{-5}$ ppv ($N_I \approx 0.005$ ppp) at all sheet thicknesses. For the higher density cases, a substantial reduction from around 10% overlapping particle images to around 5% is achieved with $L_z/w = 10 - 15$.

Finite sheet speed

A source of error specific to a scanning setup is the effect of a finite scanning laser sheet speed. Where figure 3.1 considers an infinite sheet speed, figure 3.5 considers a range to better understand the effect of finite sheet speed on triangulation accuracy. For both the present parameter assessment and the synthetic experiment presented in section 3.4, velocity fields from the forced homogeneous isotropic box turbulence case are sourced from the Johns Hopkins Turbulence Database (JHTDB) (Li *et al.*, 2008a), with rms velocity u'_{rms} , and are used to advect the particles. Subsequent scans of the measurement volume are separated by a time Δt during which the particles are advected by the local fluid

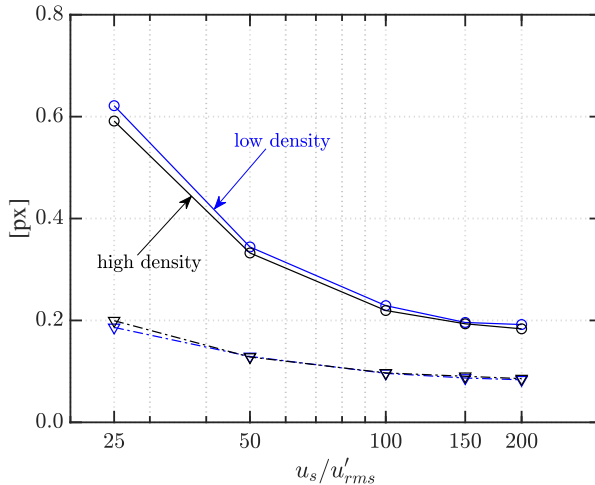


Figure 3.5: Error in linearly-corrected triangulated particle locations for different sheet speeds u_s/u'_{rms} ; \circ , mean error and ∇ , standard deviation in error; curves in black, $N_V = 1.8 \times 10^{-4}$ ppv ($N_I \approx 0.05$ ppp); curves in blue, $N_V = 1.8 \times 10^{-5}$ ppv ($N_I \approx 0.005$ ppp)

velocity. For a finite sheet speed, requiring a finite time to scan the volume, the particles are also advected *during* the scan. In an experiment, this time is determined by the frame rate f_{scan} and the number of sheets N_s . A decreasing u_s/u'_{rms} means that the particles move increasingly during the scan, giving triangulated locations for a single scan that correspond to an increasing spread of times between particles in the first and last sheets.

Sheet speed ratios of $u_s/u'_{rms} \approx \{25, 50, 100, 150, 200\}$ were considered to study the effect of finite sheet speed. Following 3D particle reconstruction, a linear (i.e. first-order) positional correction is applied to all particles using their fitted sheet numbers to recover their approximate locations at a simultaneous time corresponding to the end of the scan. That is, particles in the final sheet will be subject to no correction, whereas particles in the first sheet will have a 3D positional correction applied by adding $\Delta x = t_{scan} u_{loc}$ to their triangulated positions, where t_{scan} is the time taken to complete the scan, and u_{loc} is the local velocity vector at the beginning of the scan.

In the step where triangulation/Gaussian fitting is performed as explained in section 2.3.2, when the same particle within the scan is identified in successive images, and are grouped together to fit a Gaussian and identify its relative position at the center of the sheet, the local velocity of the particle is estimated using their displacement within these successive sheets and the time for which the particle was found, which is determined by the frame rate f_{scan} and the number of sheets $N_{s_{loc}}$ for which the particle was found. Thus

$$u_{loc} = \frac{\delta_z}{N_{s_{loc}} f_{scan}} \quad (3.6)$$

Figure 3.5 shows the mean error in pixels between the ‘ground truth’ particle locations (recorded at the end of the scan) and the corrected particle locations for the different sheet speed ratios. When the sheet speed is $u_s/u'_{rms} \gtrsim 100$, the mean error in the corrected particle locations is ≈ 0.2 px for both low ($N_V = 1.8 \times 10^{-5}$ ppv, $N_I \approx 0.005$ ppp) and higher ($N_V = 1.8 \times 10^{-4}$ ppv, $N_I \approx 0.05$ ppp) seeding density cases. These values are only ≈ 0.03 px greater than the positional error shown for the infinite- u_s study in figure 3.2 in section 3.3.1. All other things being equal, the error will likely increase with a larger L_z (i.e. more sheets) since particles in latter sheets have more time to move during the scan, possibly eventually exceeding that which can be corrected linearly as herein.

3.3.2 Uncontrollable experimental parameters

Noise

Four levels of random noise are introduced to the ideal images in order to study its impact on the triangulation procedure, being 5, 10, 15 and 20% of the maximum illumination in the noise-free image, with a variance/RMS value of 0.25 times the mean values respectively. This was applied to all seeding densities considered in section 3.3.1. Prior to the triangulation step, 2D intensity peaks must be located within the images, presently carried out using the peak-finding algorithm described in section 2.3.1. Figure 3.6a shows the mean error in the 2D peak location estimation when images are subject to these varying levels of noise. A higher intensity threshold for peak-identification was used in this section than for others so that particles for the 20% noise case could be better distinguished. This in general results in fewer triangulated particles as weaker intensity spots are disregarded. The mean error in 2D intensity peak location was < 0.3 px for all cases and all noise levels investigated. The error appears to grow in a fairly steady manner both with the noise level and particle density for the ranges considered, except for the highest N_V where it increases rather more rapidly. This is presumably due to the intensity peaks becoming more difficult to distinguish with high levels of background noise when there are many closely-spaced particle images. Figure 3.6b shows the fraction of successfully triangulated particles (using the same criterion used for figure 3.1, i.e. if a triangulated location is within a 1 px radius of a known ‘ground truth’ particle location, the particle is considered ‘found’) for the studied range of seeding densities. The performance of the present triangulation procedure is shown to be robust in the presence of mild to moderate noise. However above noise levels of $\approx 15\%$ and particle densities $N_V \approx 3.5 \times 10^{-4}$ ppv, the method triangulates $< 50\%$ of ground-truth particle locations.

Deviation of the laser sheet profile from an ideal Gaussian

The shape of the laser sheet profile is determined by shape factor s in (3.1), which when set to $s = 2$ gives a Gaussian profile. Accurate sheet fitting requires some variation of the

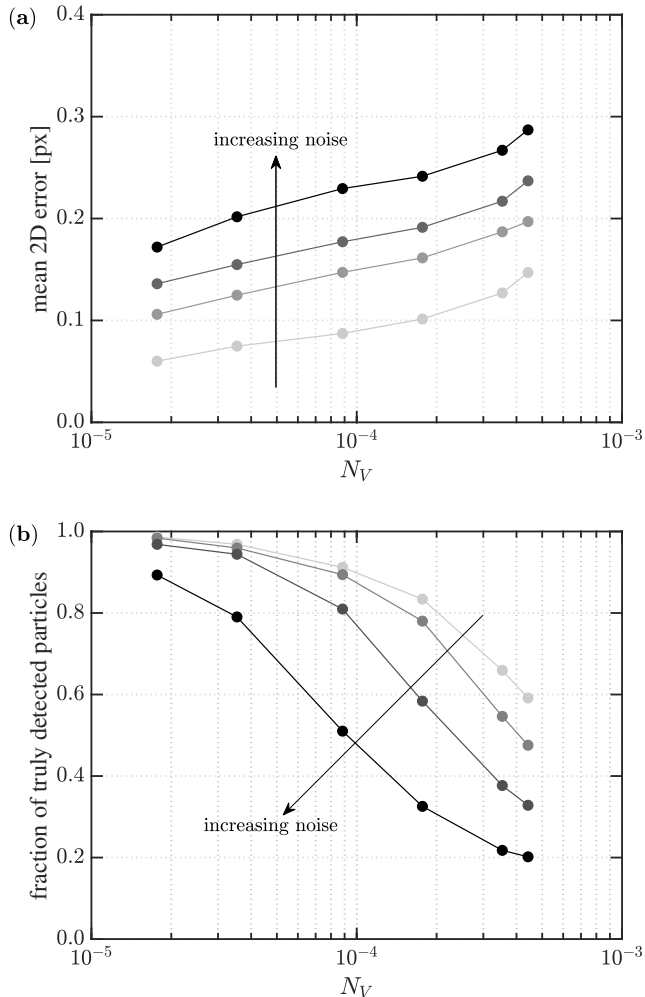


Figure 3.6: (a) Mean error in 2D particle image detection as a function of particle density N_V for four different random noise levels $\{5\%, 10\%, 15\%, 20\%\}$, curves darkening with increasing noise level; (b) fraction of successfully triangulated particles, given the known ‘ground truth’ locations; curves and N_V range same as in (a)

laser’s intensity over the range of nominal sheet number n_s being used to find f_s . This is now varied to $s = \{2, 4, 10\}$ for the seeding density $N_V = 1.8 \times 10^{-4}$ ppv ($N_I \approx 0.05$ ppp). As s increases the profile approaches a top-hat profile. Figure 3.7a shows the intensity variation of a particle over five sheets, demonstrating how the shape of the laser beam profile changes with s . For a single particle, the fitted sheet numbers (f_s) obtained for $s = \{2, 4, 10\}$ within (3.1) are essentially exactly the same. The mean error is shown in figure 3.7b also doesn’t vary significantly for the different profile shapes considered

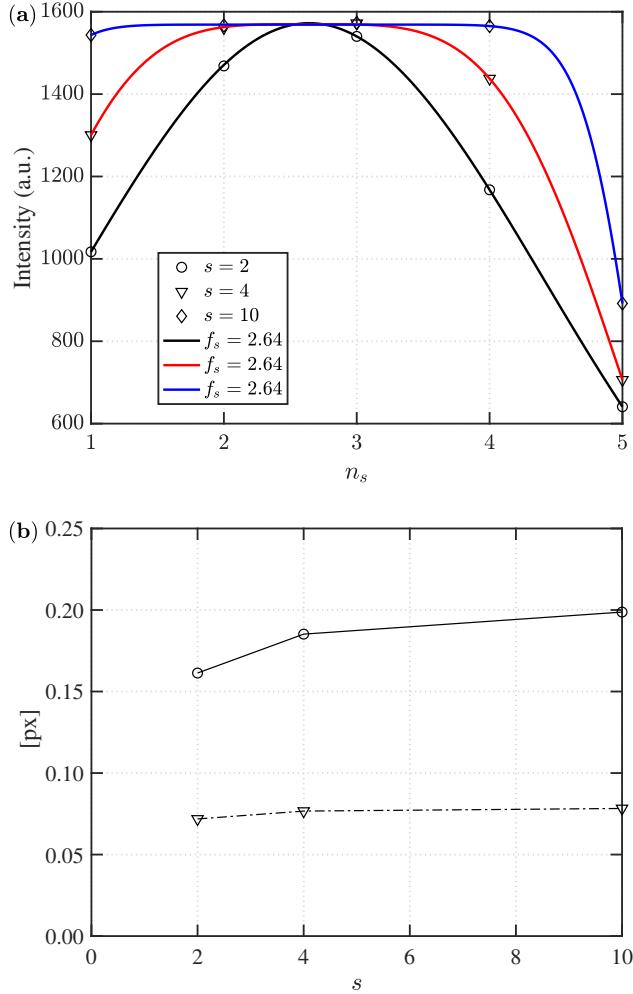


Figure 3.7: **(a)** Intensity variation of a single particle over five sheets within a scan, for three different sheet shape factors s ; **(b)** error in triangulated particle location for the different shape factors for the medium-density case with $N_V = 1.8 \times 10^{-4}$ ppv ($N_I \approx 0.05$ ppp): \circ , mean positional error; ∇ , standard deviation of positional error

presently. Therefore the actual profile of the laser sheet found doesn't significantly affect the efficacy of the triangulation method for the values of s considered here, as long as there is some intensity variation over the laser sheet's thickness, and it is correctly characterized prior to the experiment.

3.4 Verification of tracking via synthetic experiment

The JHTDB was used for a synthetic experiment on which the present methodology has been tested thus far. The initially random distribution of particles is advected in time subject to the time-evolving velocities from the forced and isotropic DNS fields. For this purpose, the Lagrangian tracking ‘GetPosition’ function as supplied in the JHTDB toolbox (Yu *et al.*, 2012) is used. Scanning PIV images for two camera angles were created using a code based on the EUROPIV Synthetic Image Generator (Lecordier & Westerweel, 2004). The main details of the synthetic experiment may be found in table 3.3. An image resolution of 1024×1024 px was used. Parameters were chosen such as to be dynamically similar to the scanning PIV experiment of Lawson & Dawson (2014). Aside from the sheet overlap, which has been increased slightly for the synthetic experiment in order to deduce the fitted sheet number f_s for individual particles, the remaining parameters are also chosen to be similar, so that our synthetic experiment represents a setup realisable in the laboratory (i.e. feasible sheet speed u_s/u'_{rms}). The present scanning PTV setup places specific demands upon laser sheet speed and sheet overlap for the triangulation to be effective, which may impose practical restrictions upon laboratory experiments. The sheet overlap must be higher than in previous similar setups (Lawson & Dawson, 2014, 2015) such that f_s may be calculated for a majority of particles. Both the sheet overlap and sheet speed requirements of the current methodology are met in the recent experiments in water presented in Lawson *et al.* (2019) for a Taylor microscale Reynolds number of $Re_\lambda \approx 315$. Samples from within the JHTDB are separated in time by the large eddy turnover time $T_L = L/u'_{rms}$, where L is the integral scale, and in space by a distance $\approx 1.5L$ within the computational domain, such that the samples may be considered independent.

Table 3.3: Parameters for the synthetic experiment. Those not listed here are as in table 3.1

$N_{samples}$	N_s	N_V	N_I
15	62	1.8×10^{-4} ppv	0.05 ppp
$\Delta t/\tau_\eta$	u_s/u'_{rms}	$w/\Delta z$	L_z/w
0.094	157	5.0	12

3.4.1 Lagrangian statistics

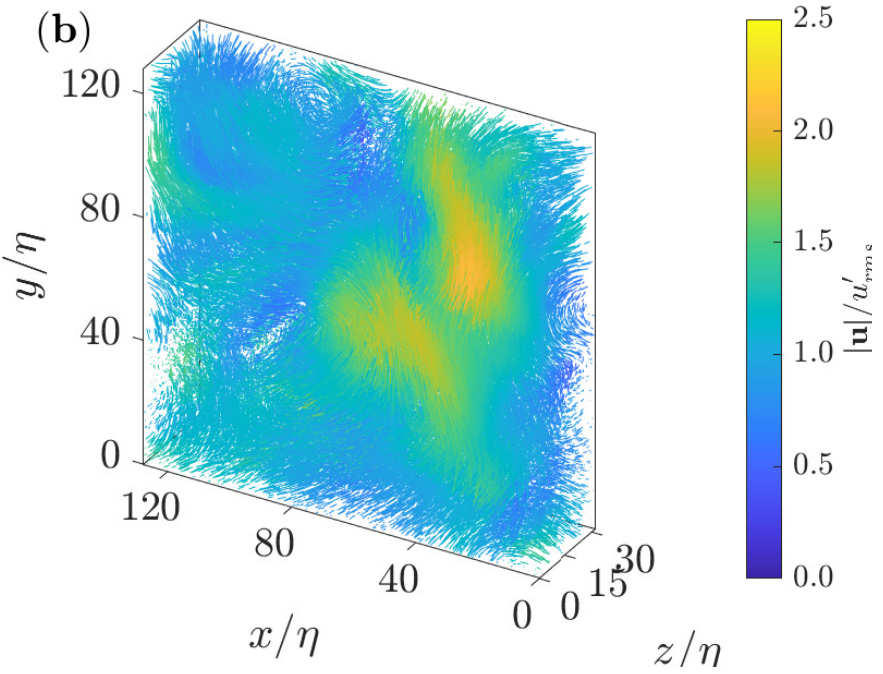
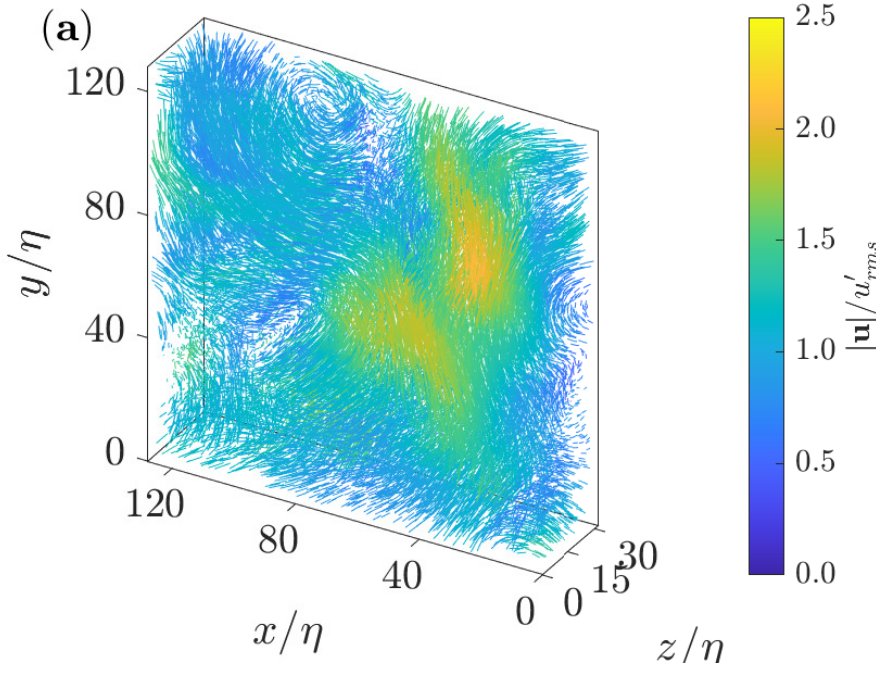
The present experimental scanning method as used by Lawson & Dawson (2014) was first developed to yield Eulerian statistics on a regular grid via PIV cross-correlation. Lagrangian statistics are the goal of the present technique. The present method tracks

a single particle for over $20 \Delta t$ ($\approx 2 \tau_\eta$) to an accuracy of < 1 px when compared to the final location found using pseudo-tracking directly within the time-evolving DNS. Particle movement during the scan (due to the finite sheet speed) remains small enough such that a linear positional correction using the local velocity is adequate to interpolate their position to that corresponding to a simultaneous time for the whole domain before the tracking algorithm is applied, as was done in section 3.3.1. The search region about a predicted location is presently set to a radius of approximately $1/3$ of the mean inter-particle distance. Once tracks of the desired length are established via the particle tracking algorithm, the cubic spline interpolation scheme of Lüthi *et al.* (2005) explained in section 2.3.5 is used. All components of the particle velocities and accelerations may then be calculated at any point along these trajectories.

Figure 3.8a and c shows tracks for two samples of the synthetic experiment with a comparison to the “true” tracks in figure 3.8b and d. Figure 3.8a shows a larger number of smaller eddies whereas the sample of figure 3.8c is seemingly dominated by a single larger structure on the order of the measurement volume itself.

Accelerations

Tracks of length of $tr_l \approx 0.75 \tau_\eta$ in time are used to calculate accelerations as in Voth *et al.* (2002). Components of Lagrangian acceleration $a = (a_x, a_y, a_z)$, the distributions of which are shown in figure 3.9. As demonstrated in Voth *et al.* (2002), the presence of large accelerations signalling extreme events is characteristic of turbulence. For reference the curve fit of Voth *et al.* (2002) is plotted, although their data was taken in a sparsely-seeded flow. For the present high-density synthetic experiment ($N_I \approx 0.05$ ppp), find the tails to be considerably narrower than that suggested by Voth *et al.* (2002). However wider tails are recovered if the experiment is repeated at a lower density ($N_I \approx 0.005$ ppp). To avoid ambiguity in the particle matching, the search radius about a predicted location in a subsequent time step is restricted to $1/3$ of the inter-particle distance as mentioned above. Hence the sparse case will permit larger accelerations to be recorded since the algorithm in the dense case is unable to distinguish one potential track from another if the particle’s actual location differs from the predicted location by an amount on the order of the inter-particle spacing. The sparse case, with a larger inter-particle spacing, therefore admits larger ‘deviations’ from a predicted path, and hence more extreme accelerations. The difference in the acceleration PDFs is therefore not the result of a difference in spatial or temporal resolution, but rather exposes an inherent limit on the magnitude of acceleration measurable in dense fields. Presently, the particle tracking algorithm proposed by Malik *et al.* (1993) is used unaltered with a conservative search radius such as to avoid ambiguous particle matching. However, it is possible that a more sophisticated tracking



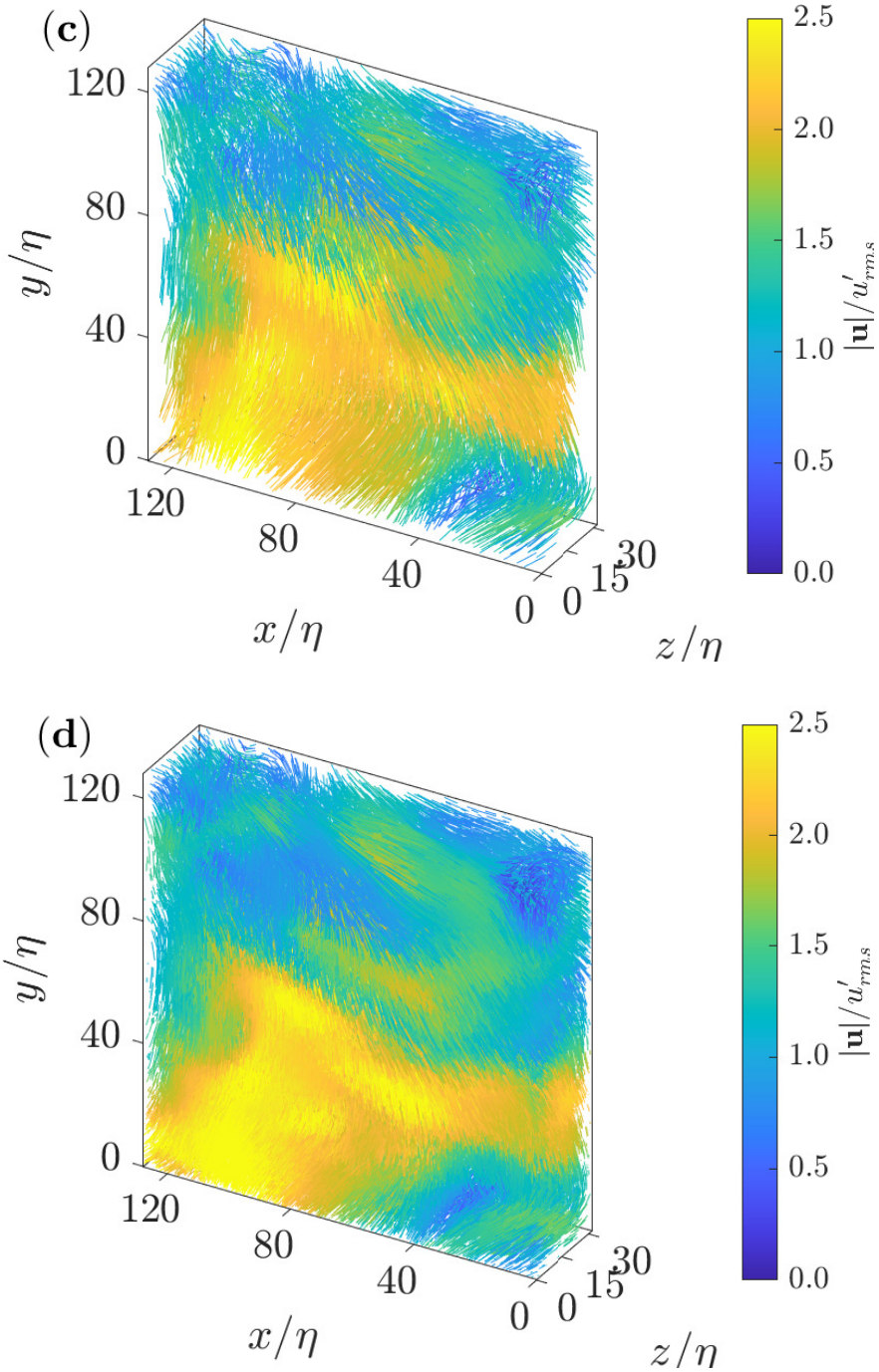


Figure 3.8: Particle tracks for two different samples, demonstrating variations in structures for the selected ‘slab’ of turbulence. Tracks are coloured by the magnitude of the velocity vector $\mathbf{u} = (u, v, w)$ along each track at each point in time. Subfigures a) and c) are the tracks obtained from measurement and subfigures b) and d) are their respective “true” tracks.

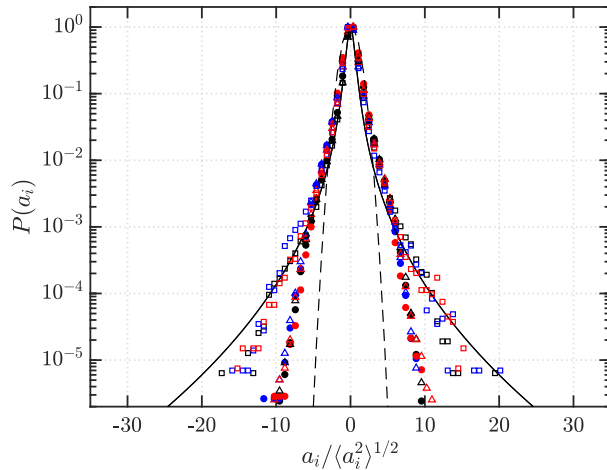


Figure 3.9: Probability density function (PDF) of the components of Lagrangian acceleration normalized by the standard deviation for each component: for the present LPT methodology: \bullet a_x , \bullet a_y , \bullet a_z ; from pseudo-tracking directly within the DNS fields: \triangle a_x , \triangle a_y , \triangle a_z ; repeating the synthetic experiment with a lower equivalent particle image density $N_I \approx 0.005$ ppp: a_x , a_y , a_z . Accelerations are computed from tracks of length $\approx 0.75 \tau_\eta$ in time from which measurements are bootstrapped along the lengths to increase statistical convergence; 201, fit from Voth *et al.* (2002): $P(a) = C \exp(-a^2 / ((1 + |a\beta/\sigma|^\gamma)\sigma^2))$, where $\beta = 0.539$, $\gamma = 1.588$, and $\sigma = 0.508$; , Gaussian distribution with the same standard deviation as $P(a_x)$

scheme, perhaps involving a multi-pass approach for ‘unclaimed’ particles, could admit larger particle accelerations in dense fields.

In general, long tracks formed over a time corresponding to at least $\approx 2\tau_\eta$ are necessary in order to yield smooth Lagrangian statistics (Lüthi *et al.*, 2005), particularly spatial velocity derivatives. Tracks of this length are used to reproduce the acceleration ‘test’ as in Hoyer *et al.* (2005). The Lagrangian accelerations ($a_i = Du_i/Dt$) are related to the local accelerations ($a_{l,i} = \partial u_i/\partial t$) and convective accelerations ($a_{c,i} = u_j \partial u_i/\partial x_j$) via the following relation:

$$\frac{Du_i}{Dt} = \frac{\partial u_i}{\partial t} + u_j \frac{\partial u_i}{\partial x_j}. \quad (3.7)$$

Spatial derivatives for the convective accelerations require information from neighbouring particles. At present, the scheme of Lüthi *et al.* (2005) is used with information from the closest 20 particles to the point in space where the spatial derivative is obtained, along with information from times t and $t \pm 2\Delta t$. The average inter-particle distance in the present fields (at the time of initial seeding) is approximately 1.3η , whereas for Lüthi *et al.* (2005) it was around 4.2η , and Hoyer *et al.* (2005) used particle fields with

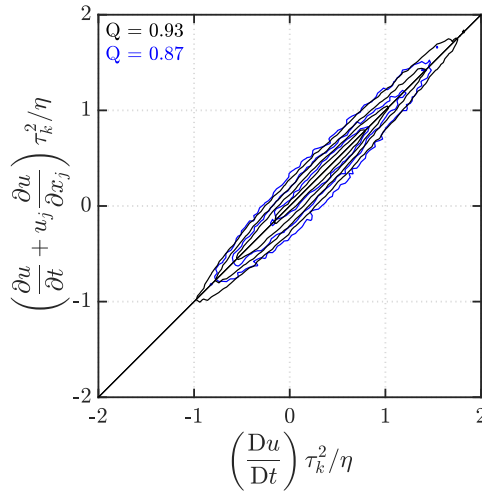


Figure 3.10: Acceleration check (joint PDF) relating Lagrangian, local and convective accelerations; in black, for the high density ($N_I \approx 0.05$ ppp) case; in blue, for the low density ($N_I \approx 0.005$ ppp) case. The high correlation coefficient (value of Q) between the two sides of (3.7) for the high density case demonstrates good spatial resolution

average particle separations of 2.4η . As detailed by Hoyer *et al.* (2005), relation (3.7) is a strict test of spatial resolution. In figure 3.10 there is a very high correlation between the left- and right-hand sides of (3.7) for the a_x component by considering their joint PDFs, confirming the adequate spatial resolution of the present high density ($N_I \approx 0.05$ ppp) synthetic experiment. The value of the correlation is somewhat decreased for the lower density ($N_I \approx 0.005$ ppp) case. Some degradation is to be expected since the fidelity of the velocity gradient tensor, terms of which appear in (3.7), is reduced at lower seeding density. However, for the same number of independent samples, the lower density case represents a smaller number of measurements, meaning the results are less converged. Similar results are found for the other two spatial dimensions.

3.5 Experimental design for particle sizing

Several assumptions were needed to implement this technique. The particles are assumed to be spherical in shape and homogeneous. Homogeneity refers to no change in the refractive index within the particle or other properties of the particle with time. Since the measurement technique developed is based on scattering intensity variation of particles at different scattering angles, the application of this technique in cases where the particle size changes throughout of measurement mainly due to evaporation or due to shear are not considered in this study.

3.5.1 Measurement area and configuration

The measurement area required to measure the size distribution in the flow is directly related to the smallest particle size in the flow. The basic criteria to fix the measurement area dimensions is that it should be greater than the distance between two scattering peaks of the smallest particle, to fit a curve. The imaging resolution M , plays an important role in determining the distance between two scattering peaks from a particle in the measurement.

Figure 3.11a, shows the displacement in pixels Δ_{disp} , required to cover two scattering peaks $\Delta\theta$, for increasing particle size. The three lenses of focal lengths: 18, 50 and 100 mm were chosen to vary the camera distance R , but maintaining a fixed magnification M , at a fixed camera resolution of 512×512 pixels and imaging area of $100 \times 100mm^2$. The displacement Δ_{disp} can be calculated by modifying equation 2.17, to get

$$\Delta_{disp} = MR \tan \Delta\theta \quad (3.8)$$

The figure 3.11a, implies that decreasing the focal length increases the possibility to measure smaller sized particle. This is because the relative displacement required to cover two scattering peaks is directly proportional to the distance R of the particle from the imaging source. For a fixed magnification M , this is lower for a lens with a smaller focal length.

3.5.2 Camera angle

The effect of camera angle can be directly related to the minimum required displacement Δ_{disp} , required to cover two scattering peaks. As the camera angle with respect to the laser sheet increases, the effective distance of the camera from the measurement volume also increases. The displacement Δ_{disp} , is directly proportional to the distance of the particle R , from the camera, hence as the camera angle with respect to the laser sheet increases, the Δ_{disp} required also increases. Figure 3.11b shows the displacement required for the same particle from three camera angles of 30, 45 and 60 degree with respect to the laser sheet, increases with increasing angle.

3.5.3 Measurable size range

Theoretically, the measurement technique can be applied for a wide range of size, starting from particles whose size are above the Rayleigh regime to particles whose size is of the order of a millimetre, as the Mie theory is still applicable even at this upper size range. However, the size range that could be measured is also directly related to the number of measurements that can be made successfully for each particle size or the measurement angular range $\Delta\theta_s$.

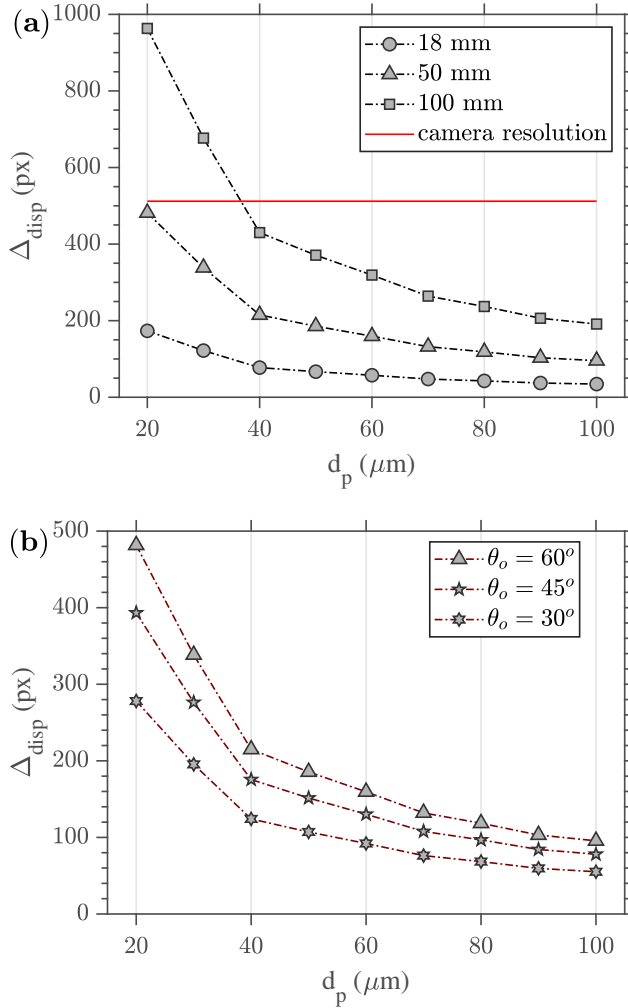


Figure 3.11: (a) The effect of increasing distance of imaging, on the minimum particle displacement required to cover two scattering peaks, for increasing water particle diameters (b) The minimum particle displacement required to cover two scattering peaks for three different angles with respect to the laser sheet.

The number of peaks N_{pks} for a given angular range $\Delta\Theta_s$ is directly proportional to particle size d_p , thus

$$N_{pks} = C \cdot d_p \cdot \Delta\Theta_s, \quad (3.9)$$

where the constant C can be estimated for a given imaging configuration and particle size.

In the lower size ranges as the angular separation between two peaks is larger, the particle displacement or the angular measurement $\Delta\Theta$ must be larger. For example, in

the figure 3.11a and b, $\Delta\theta$ is the angular spacing between two peaks. Using a Nyquist like criteria (Damaschke *et al.* (2002)), the minimum diameter that can be measured for a given resolution M can be estimated. If one considers a Nyquist criterion such that there is at least one peak within the total scattering angle range within the measurement area, $N_{pks} > 1$, which then gives the minimum measurable diameter as

$$d_{p,min} = \frac{1}{\Delta\Theta_s C}. \quad (3.10)$$

As the particle size increases, the frequency of the peaks increases. This means that the measurement angular resolution (θ_m) required to resolve between two peaks must increase as the size of the particle increases. Again a similar Nyquist like criteria would help to decide the maximum particle size that can be measured for a given resolution of M . If one considers a Nyquist criterion such that spacing between two peaks must cover at least 5 pixels, then this results in

$$R \tan \Delta\theta_m M > 5. \quad (3.11)$$

The measured scattering angle range ($\Delta\theta_m$) can be related to the number of peaks N_{pks} , as

$$\frac{N_{pks}}{\Delta\Theta_s} \times \Delta\theta_m = 1, \quad (3.12)$$

and combining 3.9 and 3.11, and substituting in 3.12, the maximum diameter, for a given configuration is

$$d_{p,max} = \frac{1}{C \tan^{-1}\left(\frac{5}{MR}\right)}. \quad (3.13)$$

3.5.4 Camera aperture

A camera aperture is treated as a section of a sphere. The aperture's solid angle, and area in steradians, controls the particle intensity at the focus. The scattered intensity $I_{s_{av}}$ received by a camera at (R, θ_s, ϕ_s) with solid angle averaging can be expressed as

$$I_{s_{av}} = \int I_s(\theta_s, \phi_s) d\Omega \quad (3.14)$$

where $d\Omega = \sin\theta_s d\theta_s d\phi_s$ is the solid angle subtended by the detector aperture at the origin and the integration is performed over the aperture.

Figure 3.12 shows the effect of increasing the solid angle on the amplitude of the variation, for a particle of size $50 \mu m$ and refractive index of 1.586. The effect of angular integration over a solid angle of the collecting lens is to smooth out the scattered intensities. In the Scanning method, since the depth of field has to be increased to keep the particle

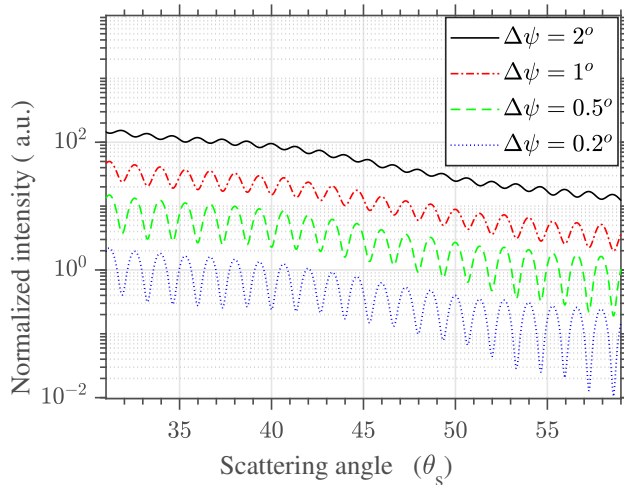


Figure 3.12: The effect of increasing solid angle on the amplitude of the scattering intensity variation with scattering angles for a particle of size $50\mu m$.

images in focus inside the volume, the camera aperture is somewhere between the mid to smallest opening, which as a result would restrict the solid angle from higher values. This prevents the flattening of the angular distribution of the scattered intensity.

3.5.5 Number of Cameras

The minimum number of cameras required to perform triangulation is two. The fraction of particles that could be sized directly depends on the fraction of particles that get tracked successfully. The successful tracking of particles depends upon the fraction of particles that are successfully triangulated. The higher the fraction of successfully triangulated particles, the higher the number of tracked and finally sized particles. For the measurement volume chosen to study the effect of increasing seeding density in section 3.3.1, it can be seen that as N_V is increased the fraction of correctly determined particles falls off. Hence a general question will be: Is there a payoff to be made here if we want to increase the spatial resolution of our measurements, i.e. increase the seeding density?. The number of particles within the measurement volume for the given examples of seeding densities i.e. for $N_V = 4 \times 10^{-4}$ and 2×10^{-4} were 107370 and 53687 respectively. Considering the percentage of successfully triangulated particles for these seeding densities, 70% of 107370 (75159) is obviously greater than 80% of 53687 (42855), which holds true for a single time step. But when considering the tracking process or linking particles from one time step to another, since lower percentage of particles are lost in triangulation for a lower seeding density case the probability of more longer tracks is high for a seeding density of N_V

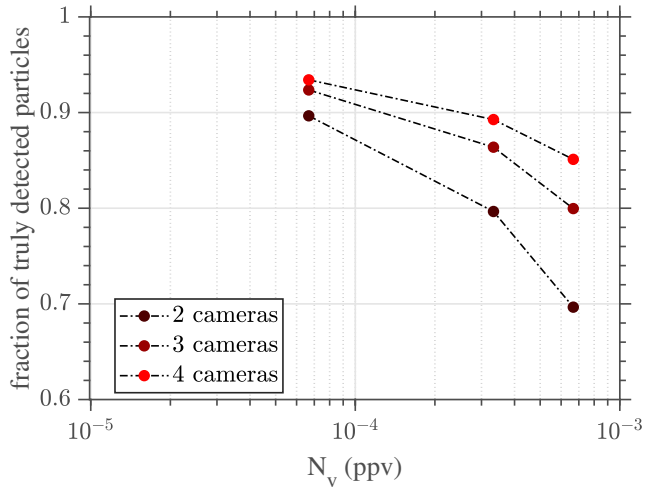


Figure 3.13: Comparison of the fraction of successfully triangulated particles using two camera, three and four camera views, at a seeding density of 0.05ppp.

2×10^{-4} than for $N_V = 4 \times 10^{-4}$. So yes there is a payoff of less longer tracks for higher seeding density (spatial resolution) than for lower seeding density.

Similarly, in the triangulation step, the difficulty in triangulating a high fraction of particles in the volume arises with increasing seeding density. One of the problems with higher seeding density is the effect of particles overlapping in the images. Section 3.3.1 shows that with an increase in particle density, the percentage of particles overlapping also increases, which could lead to a shift in the 2D peak identification, resulting in significant positional errors.

A mitigation to these problems is the use of three or more cameras in a setup. This modification did improve the percentage of truly triangulated particle, as particles overlapped in one view may not be overlapped in the other views, which could be triangulated successfully from the non-overlapped views. Nevertheless, if a particle is overlapped in all the views along the scan, it is discarded. Albeit, the payoff mentioned above still holds true.

The triangulation efficiency using two cameras was compared to a three-camera and four-camera triangulation method. We place a third camera at an angle θ_{c3} , and the fourth camera at an angle θ_{c4} with respect to the laser sheet. Three cases in an increasing 3D seeding density in particles per voxel(ppv) of $\{6.6 \times 10^{-5}, 3.3 \times 10^{-4}, 6.6 \times 10^{-4}\}$ were selected for this study, to compare the fraction of successfully triangulated particles using two, three and four cameras. The corresponding seeding density in particles per pixel(ppp) is $\{0.01, 0.05, 0.1\}$. As shown in figure 3.13, it is quite evident that as the number of camera views increases, the fraction of particles triangulated increases.

The result plotted in Fig. 3.1 were the result of two camera triangulation. In the later stages of development of the technique this issue of losing more particle with increasing seeding density was resolved to an extent by introducing more than two camera views and hence performing 3 or 4 camera triangulation. Section 3.6.5 and figure 3.13 discusses this improvement.

3.6 Synthetic experiments with known sizes

A synthetic scanning experiment was performed, in order to simulate a particle sizing experiment. The synthetic experiment is designed in such a way that it mimics a real scanning experiment by Lawson & Dawson (2014). A forced homogeneous isotropic box turbulence from the Johns Hopkins Turbulence Database (JHTDB) (Li *et al.*, 2008a), with $Re_\lambda = 418$ and $\eta = 0.0028$, were used to advect the particles.

Table 3.4: Numerical scanning experiment parameters

Parameter	Symbol	Value
Camera distance from the volume	D_o/η	600
Focal length of the lens	D_i/η	50
Image resolution	px	512×512
Camera 1 viewing angle	θ_1	35°
Camera 2 viewing angle	θ_2	-30°
Camera 3 viewing angle	θ_3	-40°
Camera 4 viewing angle	θ_4	45°
Camera pixel spacing	size/ η	0.02
Volume width	L_x/η	175
Volume height	L_y/η	175
Volume depth	L_z/η	44
Number of sheets	N_s	60
Laser sheet thickness	w/η	3.64

The camera and scanning parameters were normalized using η , such that they are dimensionally similar to the normalized values from the laboratory scanning experiment by Lawson & Dawson (2014). The size of the imaging volume was changed when compared to the one used in the actual experiment. This was done based on the particle size and corresponding imaging area required to size them, estimated using 3.8, for a resolution of D_i/D_o from the table 3.4. Table 3.4 shows the scanning experiment parameters chosen in this study.

The particles in the volume were assigned a diameter values of $0.02 < d_p < 0.08$, in equal amounts, with an increment of $d_p = 0.01$. The particle diameter is also normalized, $d_p = d_{dns}/\eta$. Properties of PMMA micro spheres with a specific gravity of 1.22 and refractive index $n = 1.49$, was assigned to every particle in the volume. The Stokes number for the biggest normalized diameter chosen in this study was 0.105, which follows the flow. The synthetic particle generation for the scanning setup, described in section 3.2, has been followed here as well. Particles were randomly distributed within the volume, with a relatively high particle image density of 0.05 particles per pixel. For all the scanning numerical experiment performed in this study, a sheet overlap ratio of $w/\Delta_z = 5$ and sheet thickness $L_z/w = 12$. These were found to be a good choice of values that could increase the fraction of fitted particles while reducing the percentage of overlapping particles and maintaining a smaller number of sheets required in the scan.

The accuracy of the sizing method proposed is dependent on the triangulation and tracking in the scanning method. In this section, since the best scanning configuration for better triangulation and tracking accuracy is chosen, only the effect of parameters, that could influence the sizing method.

3.6.1 Effect of noise in scattered intensity

In section 3.3.2, the effect of random noise on triangulation was studied. In this section, two common types of noise sources in digital cameras, photon shot noise and Gaussian background noises is considered. The photon shot noise was modeled using a Poisson distribution, where a random realization from the Poisson distribution with a mean equal to the intensity of the noise-free image, was set as the intensity for every pixel. Gaussian background noise is modeled with a specified mean intensity μ_g , and variance σ_g , and were added to the noise-free images. Four mean intensity values 2, 5, 7 and 10% of the maximum intensity count I_{max} (4096 in this study), with variance σ_g of 0.25 times μ_g , were taken respectively. Figure 3.14 shows examples of particle image with added noise using a uniform distribution and Gaussian distribution.

Before discussing the results of the effect of noise on sizing, it should be noted that increasing noise also affects the fraction of truly triangulated particles, which in turn reduces the track lengths when compared to the ideal case. Figure 3.15 shows that how the fraction of the successfully tracked (track length, $tr_l > 10$) and sized particles, for increasing noise. One can notice that, even for the ideal case, the number of successfully tracked particles is only around 80% of the actual number assigned in the volume. This effect, also known as *particle dropout* happens because, the number of particles that are tracked across a specific time interval is always finite in a fixed volume and decays exponentially as the track length is increased. This decreasing trend escalates drastically with increasing noise. In the following assessment on the effect of noise on sizing accuracy,

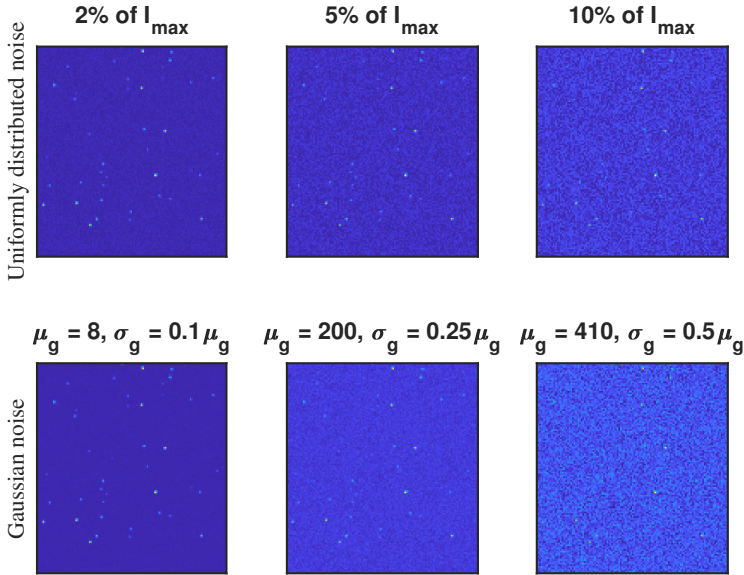


Figure 3.14: Examples of particle images with added noise.

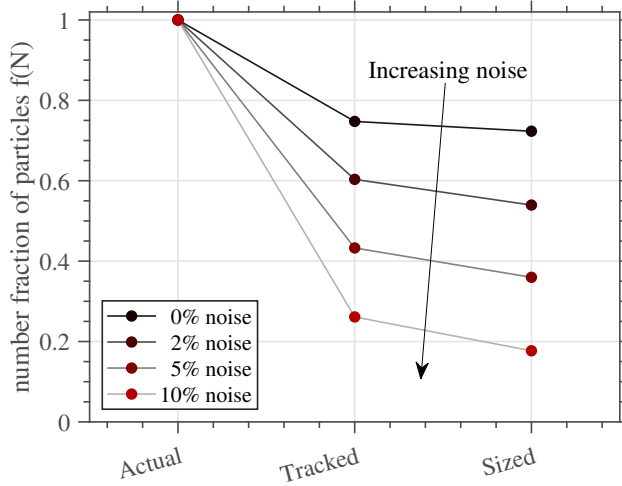


Figure 3.15: Number fraction of truly sized particles, for noise levels of 0, 2, 5 and 10 %.

the expected size distributions are hence from those particles which have been successfully tracked ($tr_l > 10$) and not based on the initial size distribution, assigned in the volume.

An example of the particle tracks ($tr_l = 13$) obtained from all the noise cases for a particle is shown in figure 3.16a. The maximum track length obtained for the highest

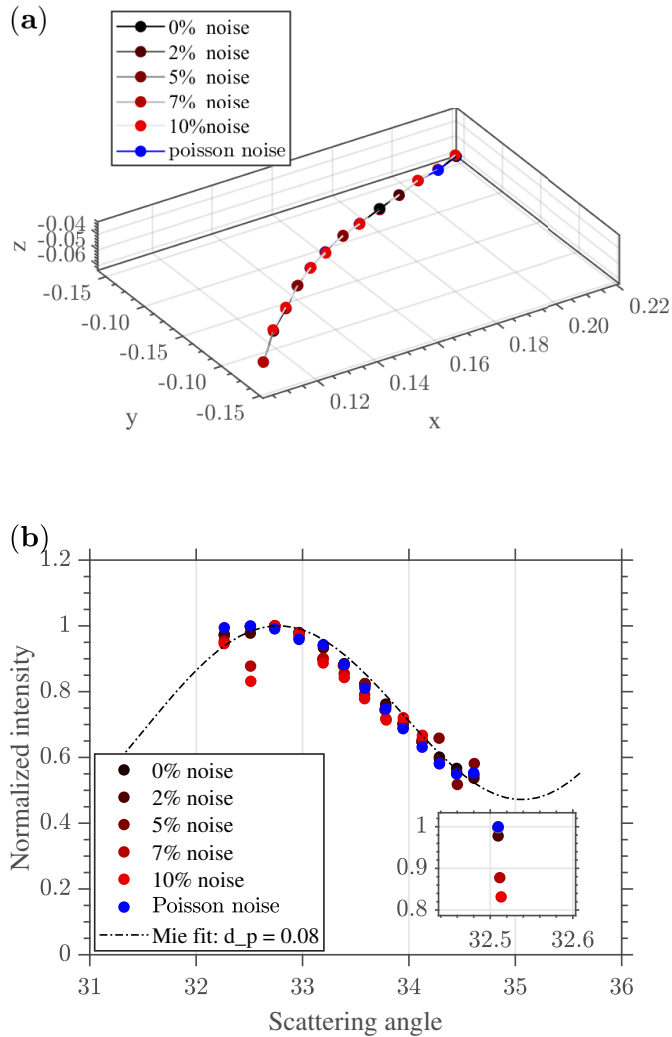


Figure 3.16: Comparison of: (a) Lagrangian track of a particle for different noise cases; (b) scattering intensity distribution w.r.t scattering angle of the corresponding particle with the best Mie fit, for the different noise cases.

noise case is $tr_l = 13$. The scattered intensity distribution with respect to the scattering angles obtained from the track locations for all the noise cases, along with the best Mie fit for the corresponding particle is shown in figure 3.16b. In general, the scattered intensity distribution for all the cases agrees well with the Mie fit, with a small percentage of jitter in the intensity values with respect to the expected intensity. The jitter in the scattered intensity at a scattering angle for all the cases is shown in an inset of figure 3.16b. As expected, at higher noise levels besides the deviation in the scattered intensity, there is also a slight deviation in the scattering angle, which arises due to the 2D location detection

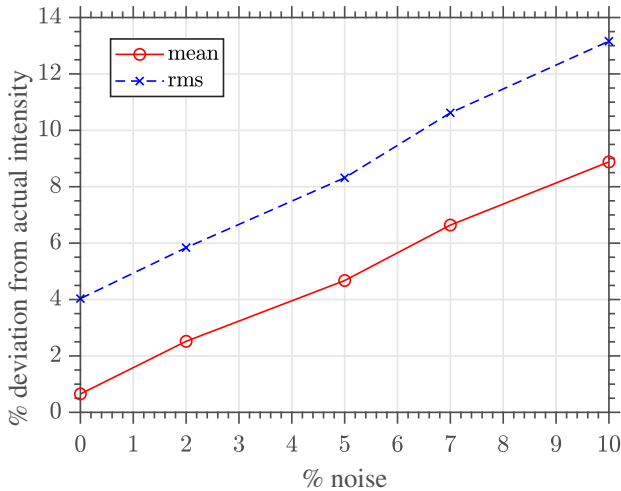


Figure 3.17: Percentage deviation in the measured scattered intensity from the actual scattered intensity for increasing noise.

step. The percentage deviation in the measured scattered intensity from all samples, for the different noise cases, is quantified and plotted in terms of mean and standard deviation, in figure 3.17.

The influence of noise in the scattered intensity on the sizing measurement accuracy is shown in the plot in figure 3.18a for the different noise levels chosen in this study. We have plotted the comparison of the fraction successfully tracked and sized particles to the actual number for each of the noise levels. The trend of decreasing fractions of both tracked and sized particles with noise for each particle size range is similar to that in figure 3.15. Albeit, both tracked and sized numbers has a decreasing trend with decreasing particle size, for all the noise cases. This trend is clearly due to the effect of noise on smaller intensities of the smaller particles. As the background noise increases, the signal to noise ratio of the smaller particles decreases, as a result of which the weaker intensities from the smaller particles are not identified and triangulated.

Figure 3.18b shows the mean and RMS error in the measured particle sizes, obtained using the particle sizing algorithm. A higher prediction interval of 97% on the fit, to estimate the residual χ^2 , was used in this section, so that irregularities in intensities from particles for the higher noise case could also be accounted for within the prediction interval. The mean error was less than $0.005/\eta$ for all the cases of noise levels simulated. The error appears to grow in a fairly steady manner. The RMS error also shows a fairly steady growth between $0.015/\eta$ and $0.02/\eta$ across the increasing noise levels.

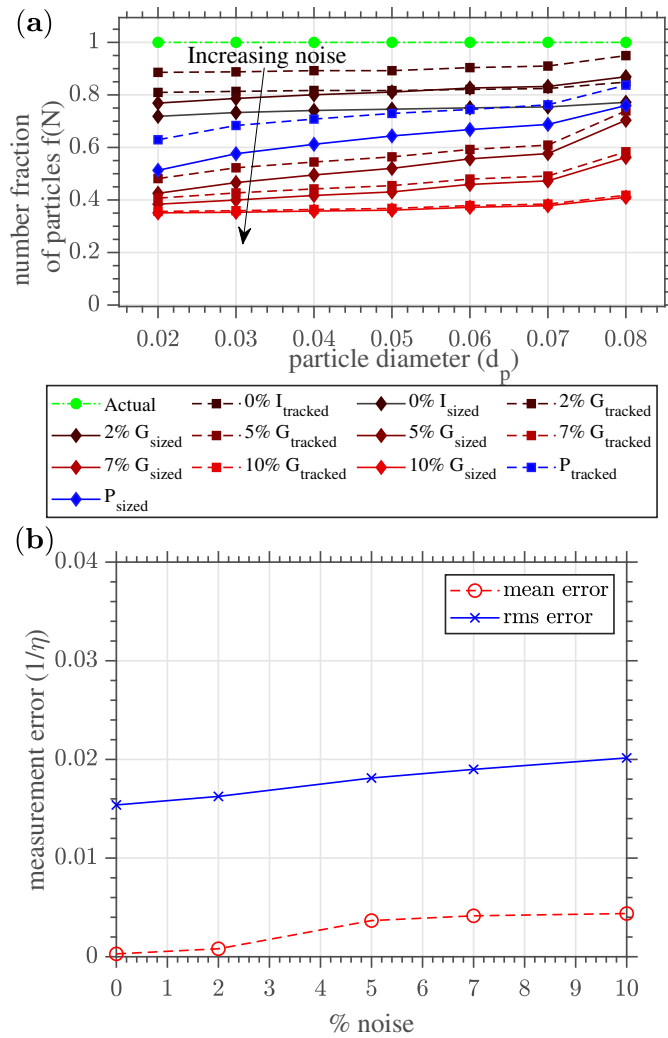


Figure 3.18: (a) Comparison of fraction of successfully tracked and sized particles for increasing noise cases. Here I,G,P stands for ideal case, Gaussian noise and Poisson noise cases respectively. (b) Mean and rms error, normalized by η , for different levels of noise.

3.6.2 Effect of noise in scattering angle

The fitting algorithm in the proposed particle sizing approach is dependent on the scattering angles, which are calculated using the camera calibration model. In a laboratory experiment, camera calibration may also suffer from inaccuracies, so a parametric test on the effect of the camera misalignment can be used to study the effect of jitter in scattering angles on the measured particle diameters is performed. To study this effect, two sets of camera calibrations are generated. In the first set true camera calibration is generated using which the particle images are generated. The second set of camera calibration was generated

by shifting the camera angle in the first set to an expected misalignment in pixels. We chose four sets of misalignment; 0.25° , 0.5° , 0.75° and 1° , which corresponds to 0.6, 1.2, 1.8 and 2.4 px respectively, for the chosen camera configuration in this study. The misaligned camera calibration models were used for triangulation, tracking and sizing. In the triangulation step, to account for the shift due to misalignment, the threshold on the re-projection error is increased with increasing misalignment case.

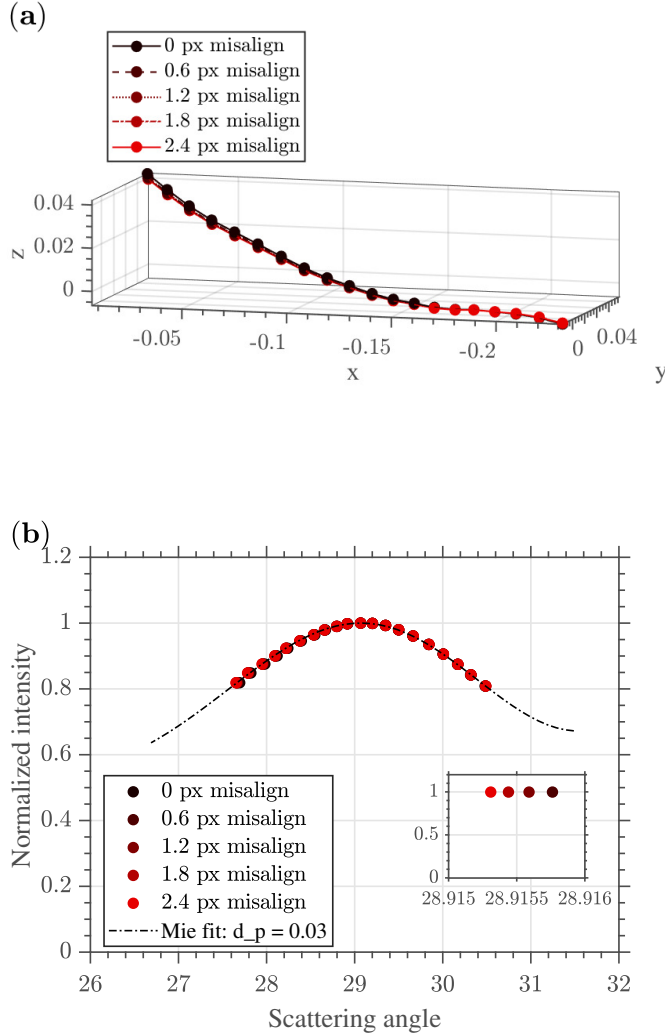


Figure 3.19: Comparison of: (a) Lagrangian track of a particle for different misalignment cases; (b) scattering intensity distribution w.r.t scattering angle of the corresponding particle with the best Mie fit, for the different camera misalignment cases.

An example of the particle tracks ($tr_l = 20$) obtained from all the noise cases for a particle is shown in figure 3.19a. As compared to figure 3.16a the maximum track length

Numerical simulation

obtained here for all the cases are the same hence one of the particles with the highest track length of $tr_l = 20$ is shown in figure 3.19a. The scattered intensity distribution with respect to the scattering angles obtained from the track locations for all the misalignment cases, along with the best Mie fit for the corresponding particle is shown in figure 3.19b. The scattered intensity distribution for all the cases agrees very well with the Mie fit, with a small percentage of jitter in the scattering angle values. There is no jitter in the scattered intensity at a scattering angle for all the cases is shown in an inset of figure 3.19b.

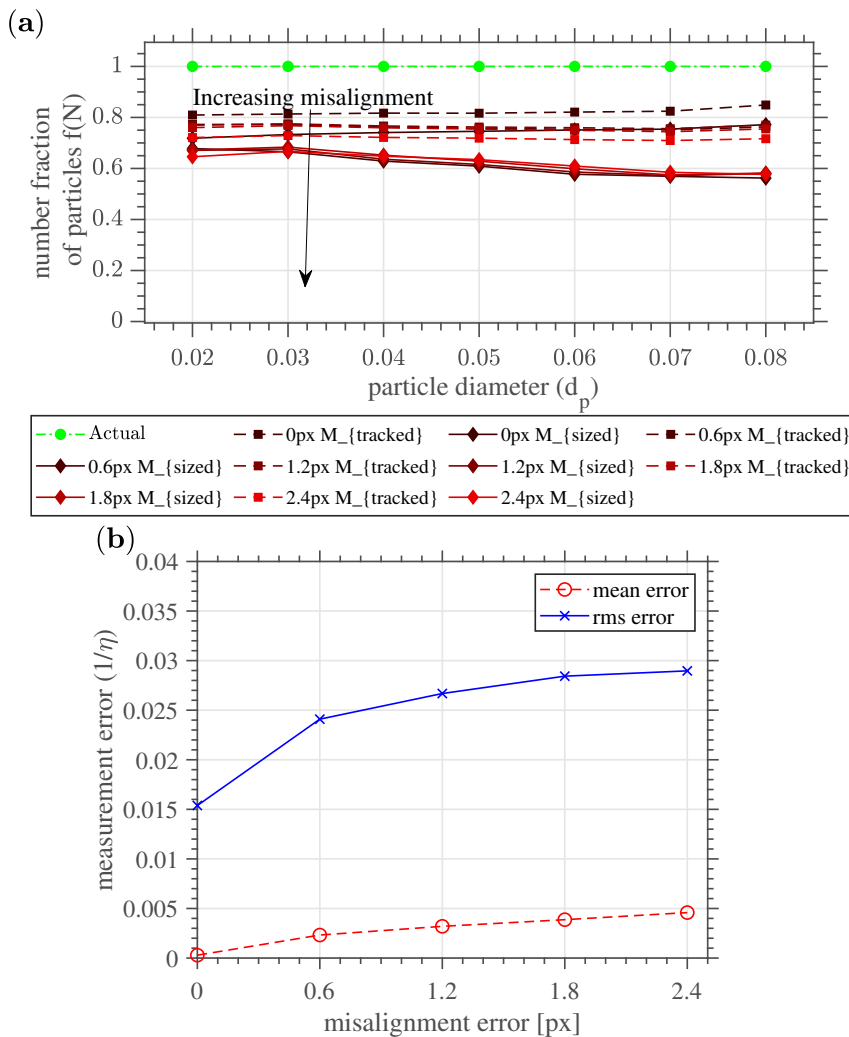


Figure 3.20: **a** Comparison of fraction of successfully tracked and sized particles for increasing misalignment cases. Here M stands for misalignment. **b** Mean and rms error, normalized by η , for different levels of camera misalignment.

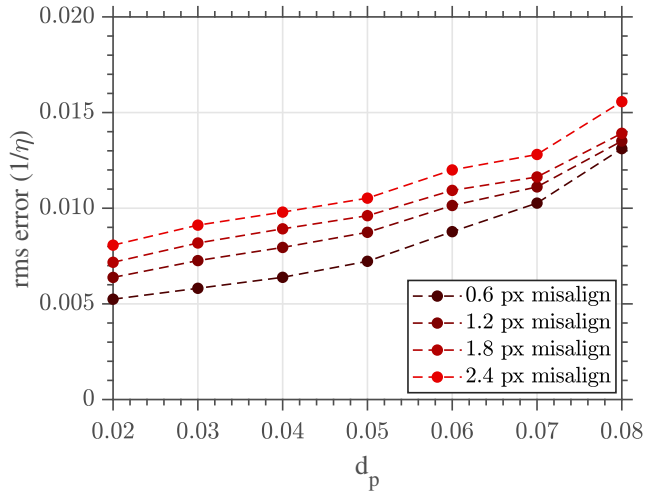


Figure 3.21: Rms error in the measured sizes for the varying size ranges, at different camera misalignment cases.

The influence of noise in the scattering angle on the sizing measurement accuracy is shown in the plot in figure 3.20a for the different misalignment cases chosen in this study. We have plotted the comparison of the fraction successfully tracked and sized particles to the actual number for each of the noise levels, similar to figure 3.18a. Here, the fraction of successfully tracked particles shows a decreasing trend with increasing misalignment. As discussed in the previous section, in this case also a higher prediction interval of 97% is used to account for the shift in the scattering intensity distribution due to the shift in the scattered angle obtained from the camera calibration values for the misaligned case. The mean and the corresponding RMS errors for different camera misalignment are shown in figure 3.20b. There is a steady increase in the variation between the expected and measured sizes with increasing misalignment; the mean error value is less than $0.005/\eta$ for all the cases. The RMS error, in this case, is somewhat higher than in the case of image noise. To understand this we have plotted the RMS error from each size ranges chosen in this study, as shown in figure 3.20b. An interesting observation from figure 3.21 is that, for a given misalignment, the RMS error increases with increasing particle size. The increase in error with increasing particle size can be related to the increasing scattering peaks with increasing particle size where, along the same track the bigger particle has more scattering peaks when compared to smaller particles. When there are more scattering patterns, a misalignment in the camera can increase the chances of a mismatch, during the fitting procedure.

3.7 Numerical experiment in a turbulent channel flow

The suitability of the particle tracking and sizing technique developed is tested by performing a synthetic scanning experiment. To do this, the DNS dataset of a turbulent channel flow at a friction velocity Reynold number $Re_\tau = 1000$, from the John Hopkins Turbulence Database (Graham *et al.* (2016); Li *et al.* (2008b)), were used to advect the particles.

Table 3.5: Flow parameters

Parameter	Symbol	Value
Friction velocity	u_τ	4.99×10^{-2}
Viscosity	ν	5×10^{-5}
Viscous length scale (ν/u_τ)	δ_ν	1.0006×10^{-3}
Friction velocity Reynolds number	Re_τ	9.9935×10^2
Channel half-width	h	1

The database for the turbulent channel flow in the JHTDB was produced from a DNS of wall-bounded flow with periodic boundary conditions in the longitudinal and transverse directions (stream-wise and span-wise directions) and no-slip conditions at the top and bottom walls. The details of the flow parameters can be found in table 3.5. The DNS domain length is $8\pi h \times 2h \times 3\pi h$.

3.7.1 Numerical experiment parameters

The camera and scanning parameters were normalized using h . The scanning particle tracking and sizing experiment is performed in a measurement volume of $2\pi h \times 2h \times 0.5\pi h$. The measurement volume is long enough in the stream-wise direction for a sufficiently long time of particle tracking and also long enough to capture two scattering peaks of the particle sizes chosen in this study, as discussed in section 3.5.1, estimated using 3.7, for a resolution of Di/Do from the table 3.6. Table 3.6 shows the imaging parameters chosen in this simulation.

Three particle sizes with mean diameters $d_p = 23, 42 \& 80$ and standard deviation $sd = 4, 6.9 \& 9.3$ respectively were chosen in the volume, in equal amounts, as shown in figure 3.23. These three sizes were chosen such as to be similar to the experiment performed in this study, detailed in the next Chapter. The Microbeads AS particles used in the experiment had diameters of 23, 42 and 80 μm with standard deviations of 4.03, 6.902 and 9.3 respectively. The particle diameter is also normalized, $d_p = d_{dns}/h$ and the particle diameter and their standard deviations are in μ DNS units. Properties of PMMA micro spheres with a specific gravity of 1.22 and refractive index $n = 1.49$, was assigned

Table 3.6: Imaging parameters

Parameter	Symbol	Value
Camera distance from the volume	D_o/h	200
Focal length of the lens	D_i/h	18
Camera 1 viewing angle	θ_1	35°
Camera 2 viewing angle	θ_2	-30°
Camera 3 viewing angle	θ_3	-40°
Camera 4 viewing angle	θ_3	45°
Image resolution	px	1536×512
Volume width	L_x/h	2π
Volume height	L_y/h	2
Volume depth	L_z/h	$\pi/2$

to every particle in the volume. The Stokes number for the biggest normalized diameter chosen in this study was 0.14, which follows the flow. The synthetic particle generation for the scanning setup, described in section 3.2, has been followed here as well. Particles were randomly distributed within the volume, with a relatively high particle image density of 0.05 particles per pixel, as shown in figure 3.22.

Table 3.7: Sizing particle parameters

Parameter	Symbol	Value
Mean diameter (particle size 1)	d_p/h	0.023
Mean diameter (particle size 2)	d_p/h	0.042
Mean diameter (particle size 3)	d_p/h	0.08
Standard deviation (size 1)		0.004
Standard deviation (size 2)		0.0069
Standard deviation (size 3)		0.0093
Seeding density	ppp	0.05
Stokes number(size 1)	St	9.2×10^{-3}
Stokes number(size 2)	St	3.6×10^{-2}
Stokes number(size 3)	St	1.4×10^{-1}
Specific gravity(all particles)		1.22
Refractive index(all particles)	n	1.49

The 'GetPosition' function as supplied in the JHTDB toolbox is used to advect the particles forward in time using their Lagrangian velocities. Particles are advected for 40 time-steps, again long enough to get the Lagrangian stats and get the size of the particles.

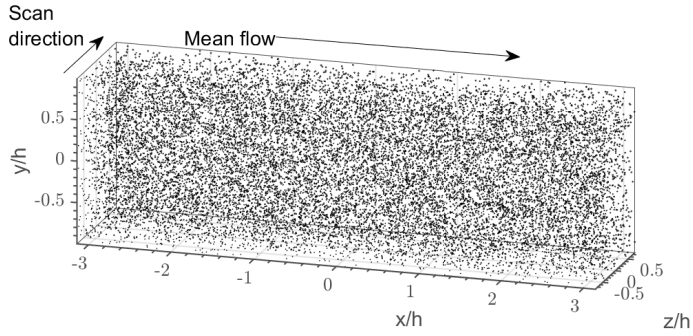


Figure 3.22: Measurement domain chosen for the numerical experiment for the turbulent channel flow with particle seeding density of 0.05 ppp (around 35000 particles).

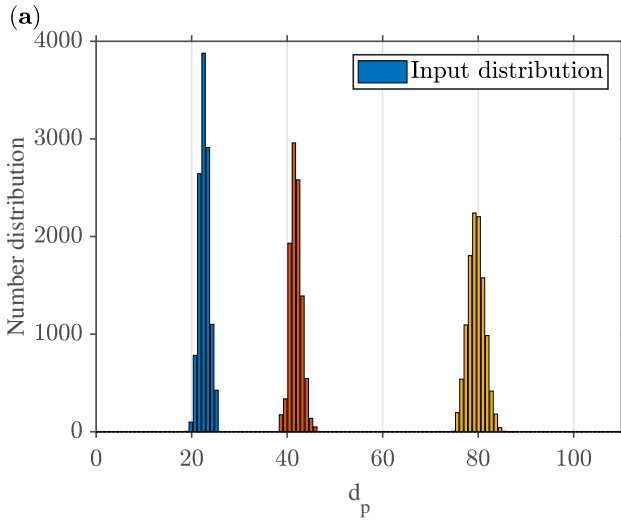


Figure 3.23: Particle size distribution inserted in a sample of volume.

Particles do leave the volume and new particles enter the measurement volume over this period. The tracking time step $\Delta t = 0.032$.

For all the scanning numerical experiment performed in this study, a sheet overlap ratio of $w/\Delta z = 5$ and sheet thickness $L_z/w = 12$. These were found to be a good choice of values that could increase the fraction of fitted particles while reducing the percentage of overlapping particles and maintaining a smaller number of sheets required in the scan.

Table 3.8: Scanning parameters

Number of sheets	N_s	60
Sheet overlap ratio	$w/\Delta z$	5
Mean laser sheet thickness	L_z/w	8
Sheet speed	u_s/u_{rms}	150
Δt		0.032

A total of 10 samples separated in time by one channel flow through time and in space by a distance of πh within the computational domain were chosen, such that they can be considered independent.

The synthetic particle images are generated as explained in section 3.2. To make the numerical experiment conditions closest to a real experiment, 3% noise were added to the particle images and a small misalignment 0.6 px to the camera calibration, as explained in section 3.6.

3.7.2 Results from particle tracking

In the particle tracking algorithm, a central difference scheme was used to estimate the velocity and acceleration at each time step and guess the particle location for the next time step. Linear approximation for velocity and acceleration was used in the post-processing step only to filter the data against any sort of measurement error or error in the identified particle location. A comparison between the velocity and acceleration estimated using the linear approximation method and that estimated using a central difference scheme is performed to check if the similarity of the results from these two schemes. Velocity is estimated using the first-order central difference scheme and acceleration using the second-order difference scheme. For the particle location at the two edges of the tracks forwards and backwards difference schemes were used.

Figure 3.24 compares the pdfs of velocity and acceleration components estimated using linear approximation method and central difference scheme. The general trend shows a very good match between the velocity components estimated using linear approximation and first-order central difference scheme. It is well known that the central difference gives a much more accurate approximation of the derivative compared to the forward and backward differences. Along a track, only apart from the first and the last points, since the derivative along all the other points are estimated using central difference scheme any deviation in the derivative estimated from that estimated using linear approximation could be mainly from the points at the edges of the track. For the velocity estimated this is low as there is a very good match between the velocity estimated by the two methods. This is not true for the acceleration calculated as shown in fig 3.24(b). The acceleration

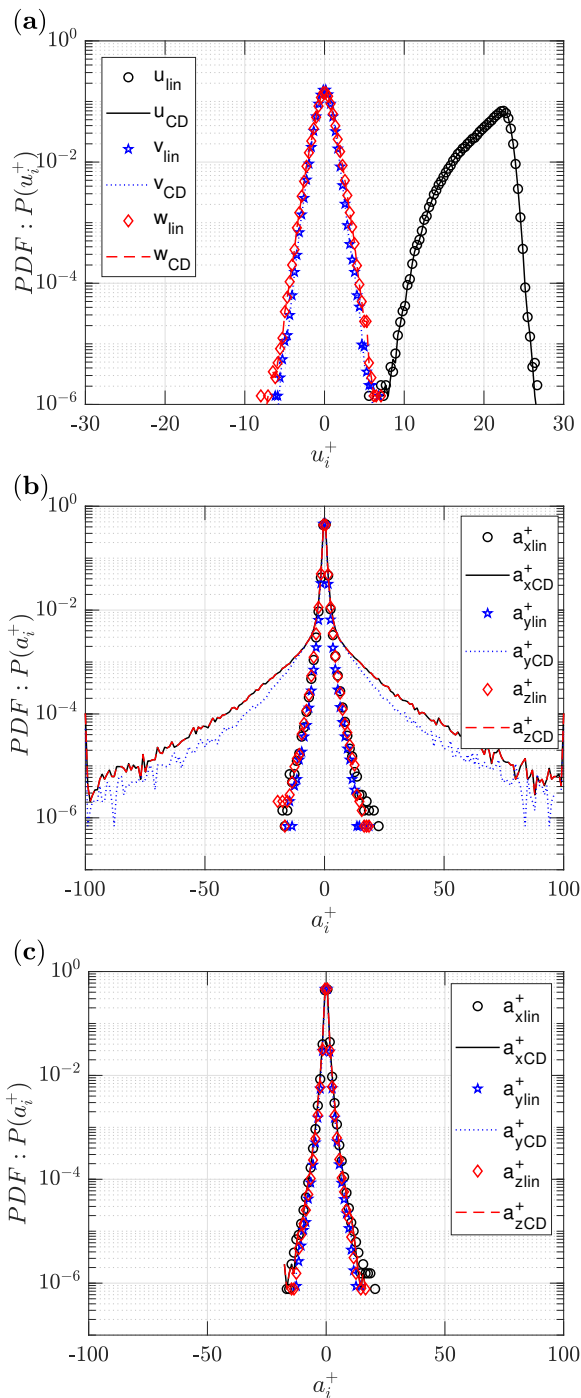


Figure 3.24: Comparison of the two schemes of linear approximation and central difference in estimating (a) velocity components (b) acceleration components for all points along a track and (c) acceleration components excluding the two end points of a track. The markers represent those calculated using linear approximation and solid lines represents values calculated using central difference scheme.

estimated using the forward and backward difference scheme at the edges of the track varies considerably from that estimated using the linear approximation scheme discussed in the section 2.3.5. This is proved by plotting the acceleration omitting the two edges of the tracks where forward and backward difference scheme was used. Hence the approach of using the linear approximation method to estimate the derivatives is justified as this method helps in estimating the values of the flow even at the edges of the tracks.

To show that the measured velocity using linear approximation was compared to the true velocity at those locations using the 'GetVelocity' function provided in the JHTDB toolbox. The Lagrangian velocities measured ($u_i^+{}_{lag}$) at every time step was compared to the actual DNS Lagrangian velocities ($u_i^+{}_{DNS}$). Figure 3.25 (a) and (b) shows the mean and standard deviation of their differences for every time step. Both the plots show the accuracy and suitability of using the linear approximation method to estimate the derivatives for the tracking technique in this study.

Mean velocity

A simple interpolation procedure introduced by Agui & Jimenez (1987) is used to interpolate the velocities to uniformly distributed grid points in the measurement volume, to perform a qualitative comparison of the Eulerian field with the Lagrangian particle track. The Agui & Jimenez (1987) method was to use simple convolution with an adaptive Gaussian window, to estimate the velocity u_{eul} at a location x , as

$$u_{eul}(x) = \frac{\sum_i \alpha_i u_i}{\sum_i \alpha_i} \quad (3.15)$$

where u_i are the measured Lagrangian velocities at points x_i and

$$\alpha_i = \exp\left(\frac{-|x - x_i|^2}{d_o^2}\right). \quad (3.16)$$

H is the grid spacing, which is chosen based on the mean inter-particle distance for a particle concentration C , calculated as

$$d_o = \frac{1}{4} C^{-1/3} \quad (3.17)$$

Figure 3.26(a) and (b) shows tracks and snapshot of an instantaneous 3D velocity field obtained by such an interpolation method, from one of the samples. The grid spacing in-terms of wall units was $d_o^+ = 20$. The track-length of the tracks shown in figure 3.26 (a) is $t^+ = 1$ and the velocity field snapshot is at time $t^+ = 0.5$. A qualitative comparison shows a good match between the particle tracks and the interpolated velocity field with the features of flow captured as it is.

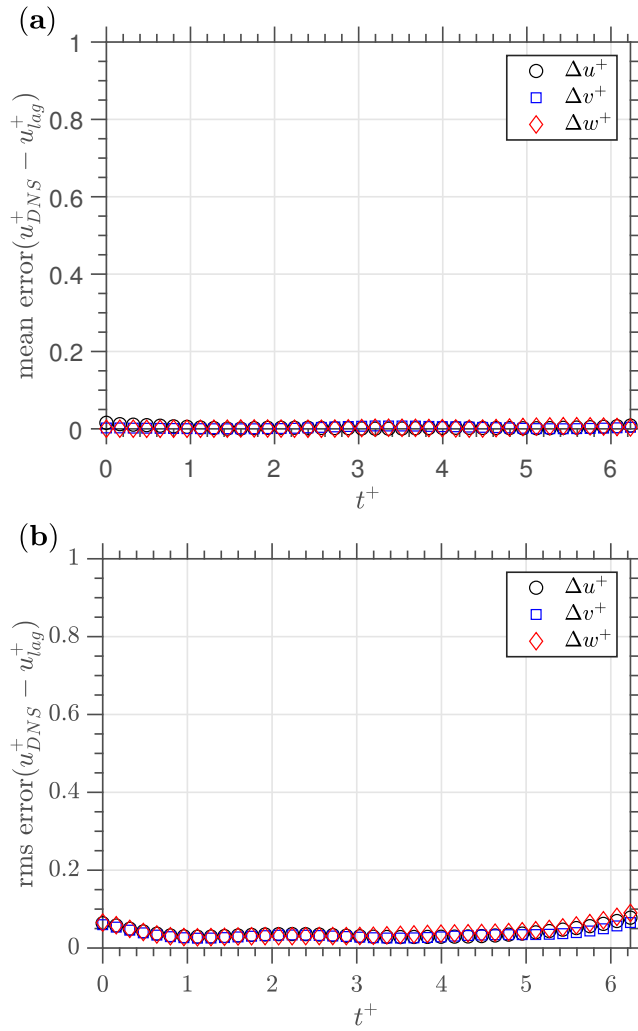


Figure 3.25: (a) Mean of the difference between measured and real DNS velocity; (b) rms of difference between measured and DNS velocity.

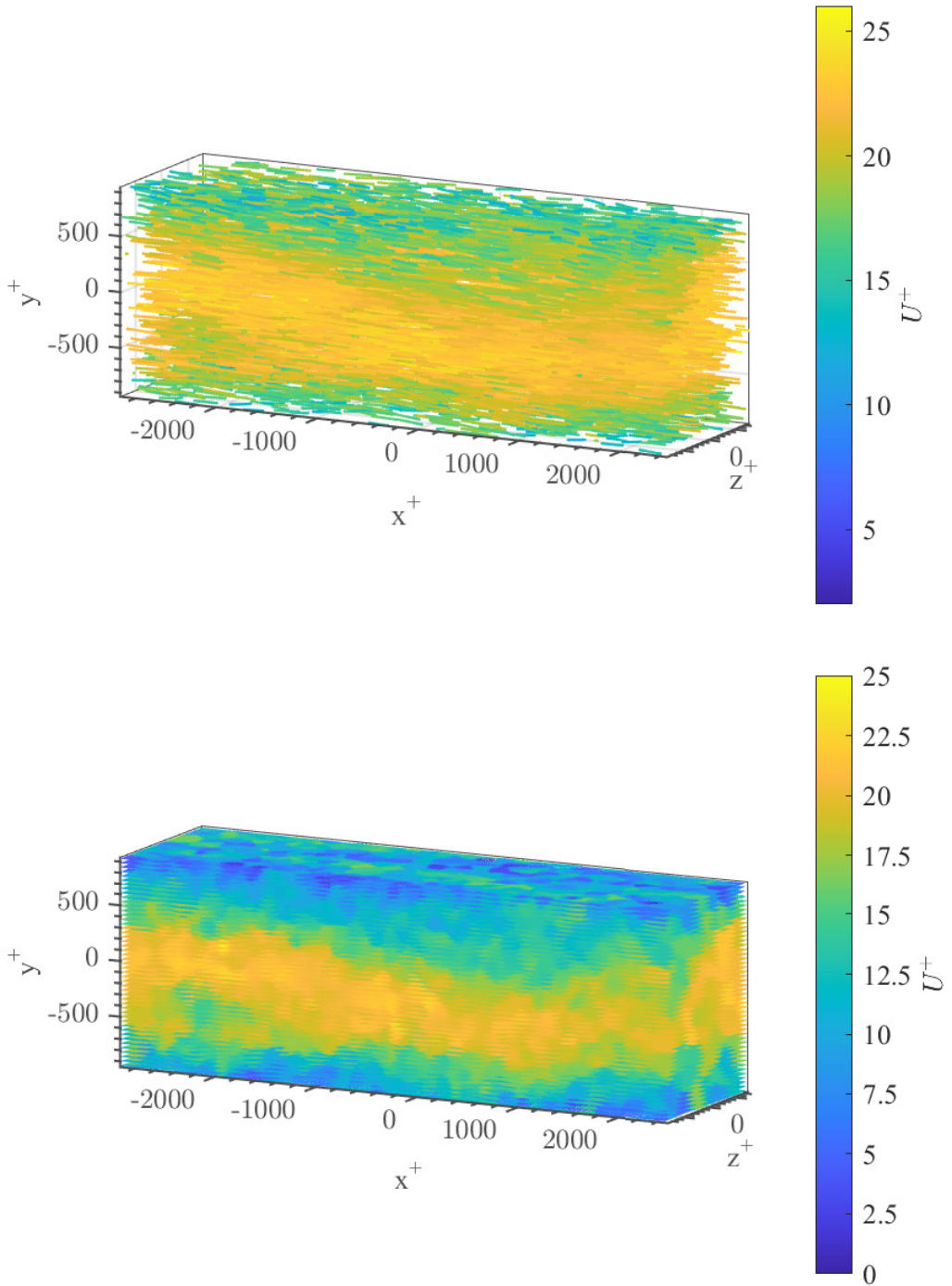


Figure 3.26: (a) Lagrangian tracks of the turbulent channel flow obtained from scanning particle tracking and (b) a snapshot of an instantaneous 3D velocity field obtained by interpolating the Lagrangian velocities to grid points.

To check the accuracy of the measurement, the mean velocity profile obtained from both the Lagrangian and the interpolated Eulerian field was compared to the mean velocity profile obtained from DNS (Graham *et al.* (2016)) . For the Lagrangian measurement, binning of the trajectories based on their distance from the wall was done, to estimate the mean in each of the bins. Since the number of trajectories was very less, close to the wall as compared to the buffer layer, as compared in figure 3.27, a width of the wall distance bins was chosen as 2 wall-units so that bins include more trajectories and are thus more statistically converged, but at the expense of increasingly unjustified spatial "smoothing", as reflected at $y^+ = 2$ in figure 3.28. The mean velocity profile obtained from the Eulerian grided velocity fields is also compared in figure 3.26 (a). The spatial resolution of the Eulerian velocity fields is limited to $y^+ = 20$ when compared to a higher spatial resolution of $y^+ = 2$ obtained from the Lagrangian tracks. The mean stream-wise velocity profile from DNS is plotted in figure 3.28 (a). This result also supports the conclusion that the scanning tracking measurement is very well suited for measurements in a turbulent channel flow.

Spatial velocity gradients

The spatial velocity gradient and the convective acceleration were estimated using the information from neighboring particles, for which the scheme of Lüthi *et al.* (2005) was used with information from the closest ' n ' particles to the point in space where the spatial derivative is to be estimated. To check the effect of mean filtering, the pdfs of the estimated diagonal components of the velocity gradients calculated using information from four choices of distance from the point of calculation; $3d_o$, $4d_o$, $5d_o$ and $6d_o$, were compared to reference case velocity gradients from DNS. Since the spatial resolution is directly related to seeding density, to study this three different seeding density were considered. Apart from the seeding density given in table 3.7 a lower seeding density and a higher seeding density cases were also generated as given in table 3.11. The respective inter-particle distance d_o obtained from the tracks at these seeding densities are also provided in table 3.11. The choice of $3d_o$ was purely due to the need for a minimum of 4 particles within the distance chosen to estimate the velocity gradients using the methodology discussed in the section 2.3.5. For a distance of $2d_o$ the average number of particles closer to the point of calculation within $2d_o$ was approximately 3 which was not enough to estimate the spatial derivatives.

Table 3.9: Mean inter-particle distance for different seeding densities

Seeding density(ppp)	0.025	0.05	0.1
Inter-particle distance (d_o^+)	25	20	15

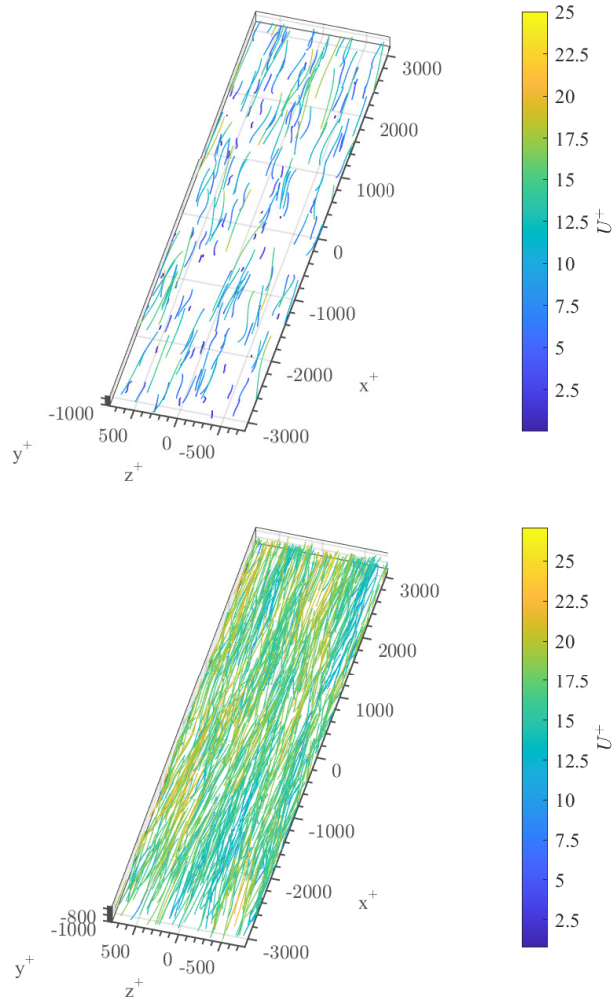


Figure 3.27: (a) Measured particle tracks within the viscous sub-layer ($y^+ < 10^1$) and (b) buffer layer ($10^1 < y^+ < 10^2$).

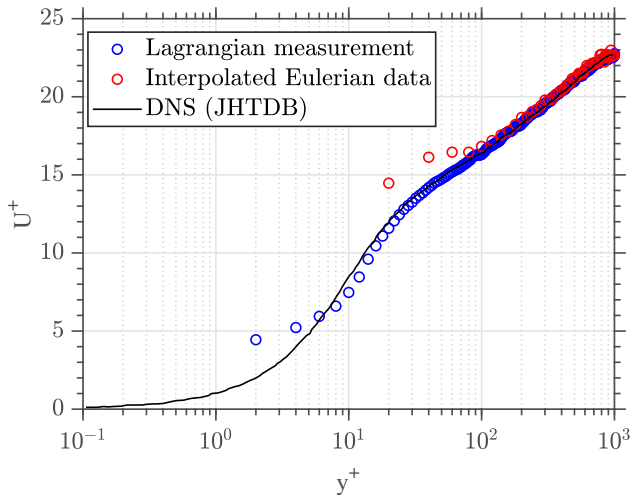


Figure 3.28: Mean velocity profile from Lagrangian and interpolated Eulerian fields, plotted with the DNS of equal Reynolds number.

The 'GetVelocitygradient' function as supplied in the JHTDB toolbox (Li *et al.* (2008b)) is used to estimate the velocity gradients at the measurement points for the reference DNS. Figures 3.29-3.31 shows the comparison of pdfs of the estimated diagonal components of velocity gradients to the reference DNS velocity gradients for the four chosen distance from the measurement point. The tails of the pdfs become successively narrower as the radius of choosing the nearby particles is increased (a)–(d). The figure shows the average number of particles within the search radius for each case. On average around 12 particles are present within a search radius of $3d_o$ for all the seeding density, as shown in figure 3.32.

To check the effect of mean filtering on the measured velocity gradients using the best possible choice of distance $3d_o$, the enstrophy $\langle \omega^2 \rangle^+ = (\langle \omega_x^2 \rangle^+ + \langle \omega_y^2 \rangle^+ + \langle \omega_z^2 \rangle^+)$ and dissipation rates $\langle \epsilon \rangle^+ = 2\langle s_{ij}s_{ij} \rangle$ terms, whose calculation depends on the quality of the velocity gradients estimated is compared with that obtained from DNS. The respective values obtained using $3d_o$ for all three cases of seeding densities are compared with their reference values from DNS as shown in table 3.10. The comparison shows that the percentage deviation with the reference values decreases with seeding density but has the effect of mean filtering in the estimation of velocity gradients.

Mean acceleration profile

The mean acceleration profile from the measurement was estimated using the binning method used to get the mean velocity profile. The measured mean acceleration profile is compared to the mean profile obtained from DNS at $Re_\tau = 1440$ (Nickolas *et al.* (2017)).

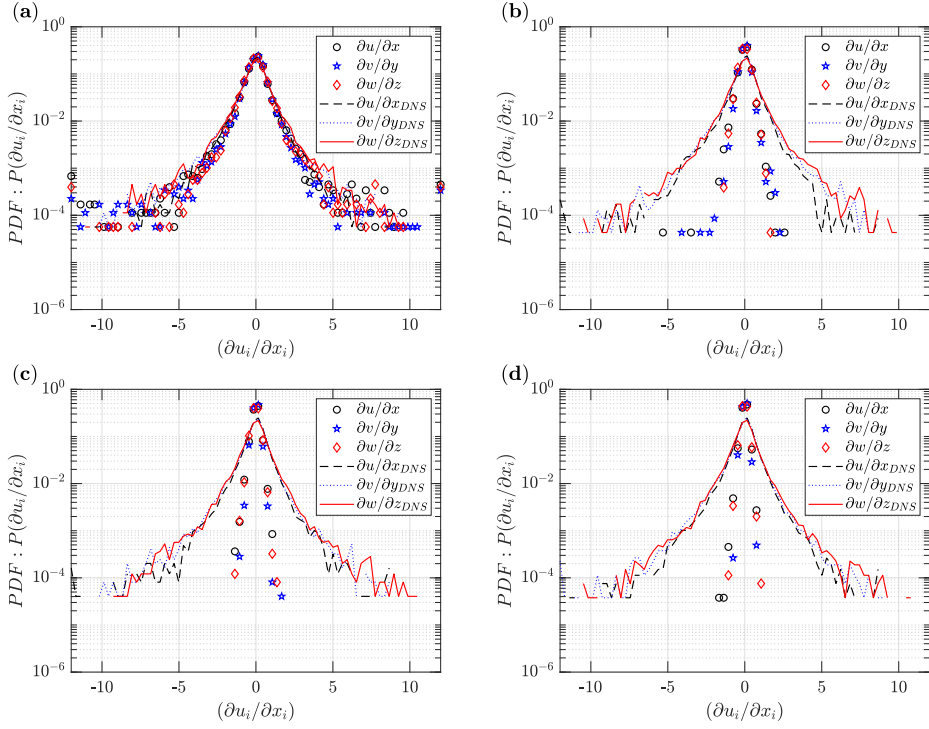


Figure 3.29: Comparison of probability density functions for the diagonal components of the velocity gradient tensor from the reference DNS to that calculated using 'n' nearest particles within a distance of (a) $3d_o$, (b) $4d_o$, (c) $5d_o$ and (d) $6d_o$, from the point of estimation for a seeding density of 0.025 ppp.

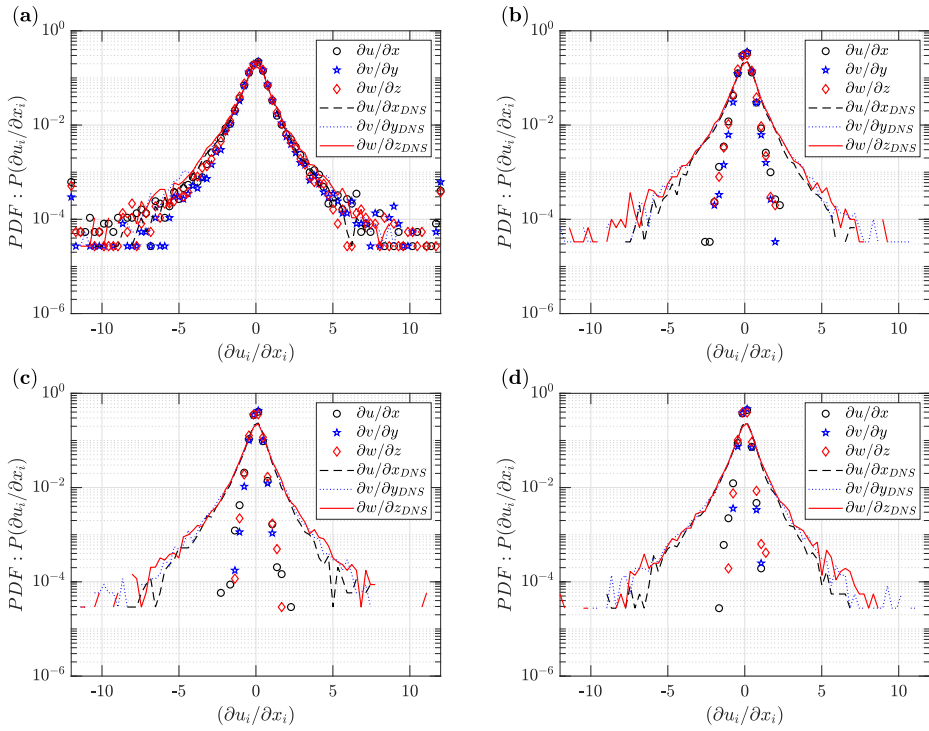


Figure 3.30: Comparison of probability density functions for the diagonal components of the velocity gradient tensor from the reference DNS to that calculated using 'n' nearest particles within a distance of (a) $3d_o$, (b) $4d_o$, (c) $5d_o$ and (d) $6d_o$, from the point of estimation for a seeding density of 0.05 ppp.

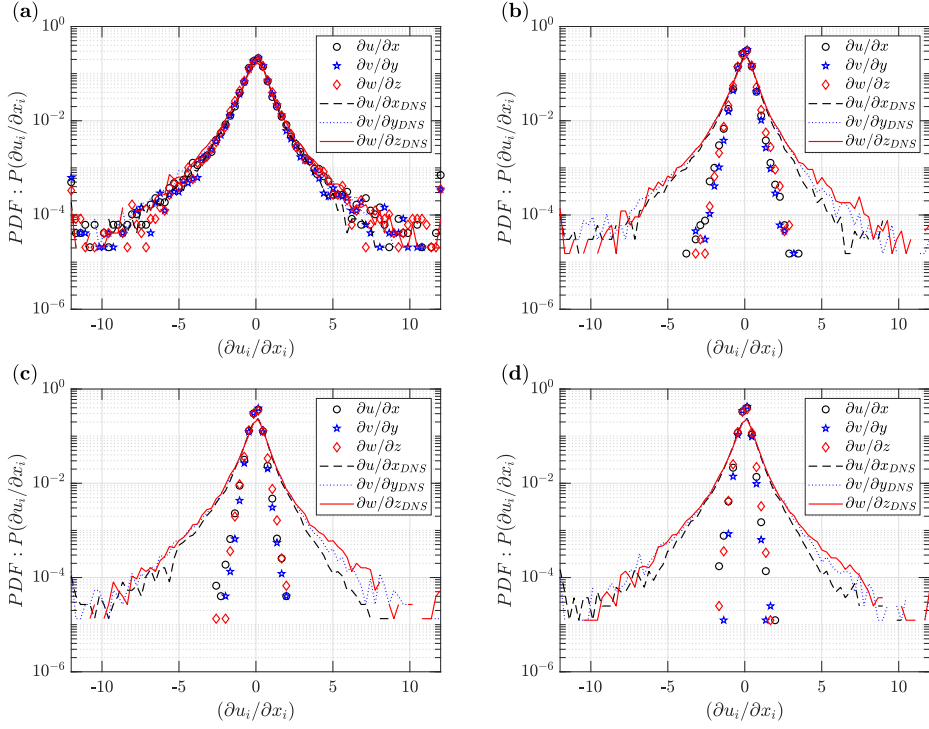


Figure 3.31: Comparison of probability density functions for the diagonal components of the velocity gradient tensor from the reference DNS to that calculated using 'n' nearestst particles within a distance of (a) $3d_o$, (b) $4d_o$, (c) $5d_o$ and (d) $6d_o$, from the point of estimation for a seeding density of 0.1 ppp.

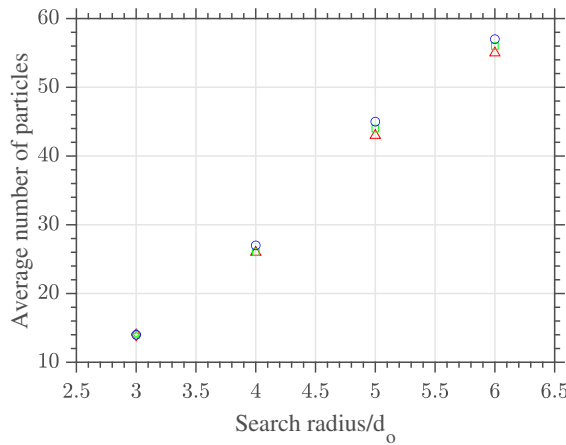
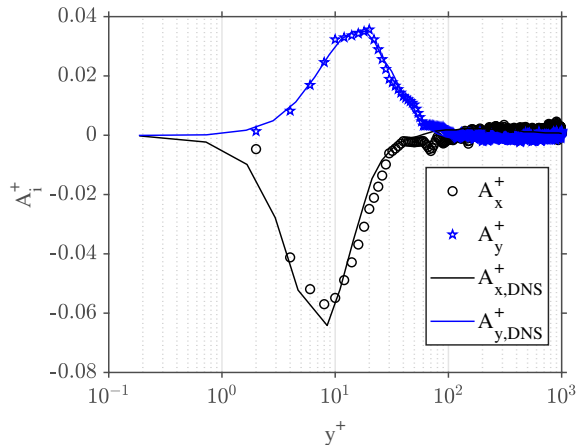


Figure 3.32: Average number of particles within the selected search radius for nearby particle for different seeding densities: \triangle $ppp = 0.025$, \square $ppp = 0.05$, \circ $ppp = 0.1$.

Table 3.10: Comparison of enstrophy and dissipation rate between different seeding density cases and DNS

Quantity	Reference DNS case	ppp = 0.025	ppp = 0.05	ppp = 0.1
$\langle \omega^2 \rangle^+$	0.0017	0.0010	0.0013	0.0015
$\langle \epsilon \rangle^+$	0.0018	0.0012	0.0014	0.0016


 Figure 3.33: Mean acceleration profile obtained from the tracking measurement compared to the profile obtained from DNS at $Re_\tau = 1440$ by Nickolas *et al.* (2017).

The profile of the normalized mean acceleration $\langle A_i^+ \rangle = \langle A_i \rangle / u_\tau^3 / \nu$ in figure 3.33 shows to be in good agreement with the DNS profile. The contributions towards the mean stream-wise ($\langle A_x \rangle$) and wall-normal ($\langle A_y \rangle$) acceleration given as

$$\langle A_x \rangle = \frac{-1}{\rho} \frac{\partial \langle P \rangle}{\partial x} + \nu \frac{d^2 \langle U_x \rangle}{dy^2} \quad \text{and} \quad \langle A_y \rangle = \frac{-1}{\rho} \frac{\partial \langle P \rangle}{\partial y} \quad (3.18)$$

A negative dip in the mean stream-wise acceleration profile close to the wall, due to the $d^2 \langle U_x \rangle / dy^2$ is captured in the mean profile of the measured stream-wise acceleration. Similarly, positive values in the middle of the channel are also obtained in the measured profile, the major contributor being the mean stream-wise pressure gradient term.

The large wall-normal pressure gradient compared to stream-wise pressure gradient is also clearly captured from the measurement, seen in the positive mean wall-normal acceleration component profile.

3.7.3 Results from particle sizing

The novelty of the technique lies in the fact that the discarded intensity information can be used to get the size information of the particles from their measured tracks. For the range

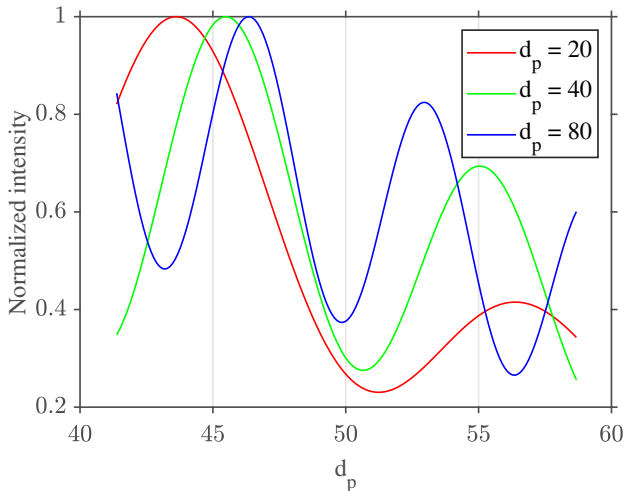


Figure 3.34: (a) Example of scattering peaks within the measurement domain for particles of size $d_p = 20, 40$ & 80 .

of particle sizes chosen in this simulation i.e. $18 < d_p < 85$, the displacement required to distinguish between the Mie fits of each particle sizes in this range is estimated based on the camera configuration. The displacement required is estimated as

$$\Delta_{disp} = MR \times \tan(\Delta\theta/2) \quad (3.19)$$

where $\Delta\theta$ is the average distance between two scattering peaks for each particle sizes. The reason for choosing half of $\Delta\theta$ is discussed in section 2.3.7. R is the camera distance from the particle location. $\Delta\theta$ is estimated by calculating the mean of the difference between scattering peak locations for each particle size, assuming they have travelled across the measurement volume. M is the magnification of the lens ($M = 0.1$, in this simulation). In this simulation, the diagonal length of the measurement volume is the maximum distance a particle can travel. This corresponds to a minimum scattering angle of 40° and a maximum angle of 58° , when combining all the four camera views. Hence the mean of the difference between possible subsequent scattering peaks between the possible minimum and maximum scattering angle for each particle size is taken as $\Delta\theta$.

Figure 3.35 (a), shows the minimum displacement required to apply the Mie fit for each of the particle sizes chosen in this simulation, for the chosen configuration, estimated using equation 3.19.

To estimate the track length required to perform the fitting procedure for particle sizing, the mean displacement for each track length based on Δt and the mean velocity $U_c = 1$ is calculated and plotted as shown in figure 3.35 (b). Based on the mean displacement for

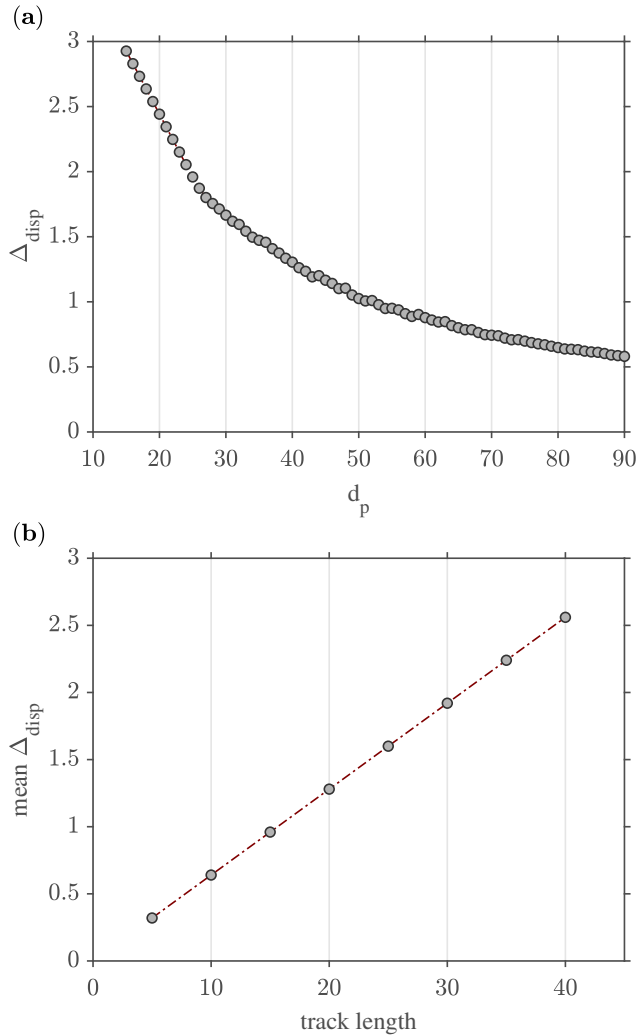


Figure 3.35: (a) Minimum displacement required for each particle sizes to apply the mie fit, to retrieve their sizes. (b) Mean displacement estimated for each track length using the mean flow velocity $U_c = 1$.

each track length from figure 3.35 (b), the ideal track length that satisfies the minimum displacement requirement are tracks with track length greater than 15, but since a track length of 10 satisfies the minimum displacement for larger sized particles, in this study to see the effect of smaller track lengths on the accuracy of the measured sizes, tracks with track length greater than 10 ($t^+ = 1$) is taken.

Using all measured tracks with track length greater than 10, the distribution of the expected (true) and the measured sizes is compared in figure 3.36 (a) and (b). The measured size distribution does not represent the expected size distribution completely, the measure size distribution shows extending tail for all the three size groups.

To find out the reason for the differences between the measured and expected size distribution, various parameters like track length, minimum displacement and missing intensities on the wrongly sized particles were examined. The wrongly sized particles were estimated by choosing all the measured particles (and their tracks), whose magnitude of difference with the true size was more than 1. Around 34% of the total measured sizes are wrongly measured sizes. Figure 3.37 (a) and (b) shows the difference between the expected distribution of those wrongly sized particles to their measured distribution.

Effect of track length

Figure 3.37, shows the number distribution of wrongly sized particles for each track length. Even though the number reduces as the track length increases, this does not truly represent the reason for the error in these measured sizes, as only around 40% of these particles have track length less than 15. Hence the notion of shorter tracks leading to wrongly sized particles does not complete the reason for wrong fits (wrongly sized particles).

Effect of missing intensities

The track data set mainly consist of the 3D location, scattering angle from each camera based on the 3D location and the Gaussian fitted scattering intensities from each camera views. In the triangulation process (four-camera triangulation), in some cases, 2D particle locations (intensities) from one or two camera views will be missing, wherein in such cases, three or two camera triangulation are performed. The reason for the missing 2D particle location is due to the effect of overlapping particles within images as discussed in section 2.3.1. During the triangulation step also there are chances of missing avoiding a 2D particle location from one or two camera views as the re-projection error from those views could be above a certain re-projection error threshold (as discussed in section 2.3.2).

Effect of particle displacement

The third parameter that was examined was the total displacement of each of the wrongly sized particle along their tracks is calculated. The calculated displacement for each wrong

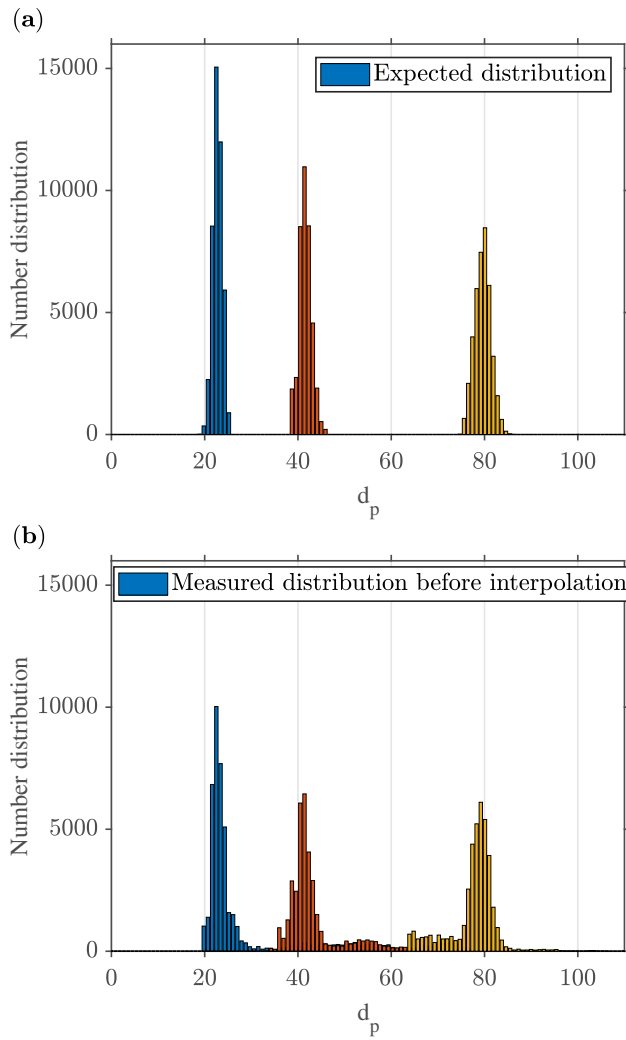


Figure 3.36: A comparison between the (a) expected size distribution from the measured tracks and (b) measured size distribution using the Mie fitting routine.

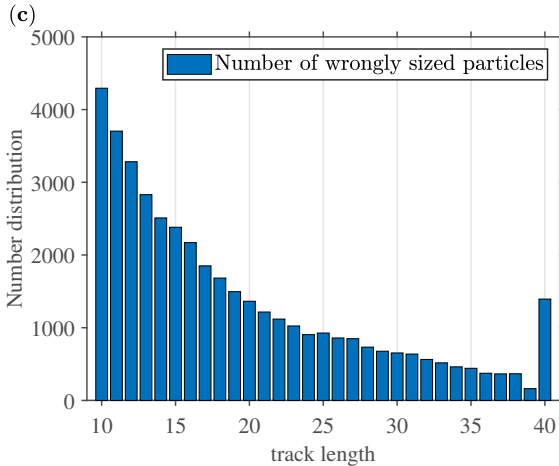


Figure 3.37: Number distribution of wrongly sized particles for the chosen track lengths.

particle is then compared to the minimum displacement required by the real particle size for the Mie fitting step. All the particles that were wrongly sized did not fulfill the minimum displacement required for Mie fitting as shown by the number distribution in figure 3.38 (a). A similar number distribution plotted for the rightly sized particles clearly in figure 3.38 (b) shows that all the rightly sized particles had fulfilled the criteria of minimum displacement for Mie fitting.

Table 3.11: Comparison of particle sizing error before and after interpolation

	Error within ± 1	Error $> \pm 1$
before interpolation	59085	63985
after interpolation	86886	36184
	mean error	rms error
before interpolation	7.478	21.308
after interpolation	0.7829	10.44

The missing intensity and displacement information was interpolated using a spline interpolation method and the Mie fitting routine was applied. Table 3.11 compares the sizing error before and after interpolation of the missing intensity information. Figure 3.39(a) and (b) shows a comparison of the expected size distribution particle with the size distribution obtained after interpolating the missing intensity and displacement information.

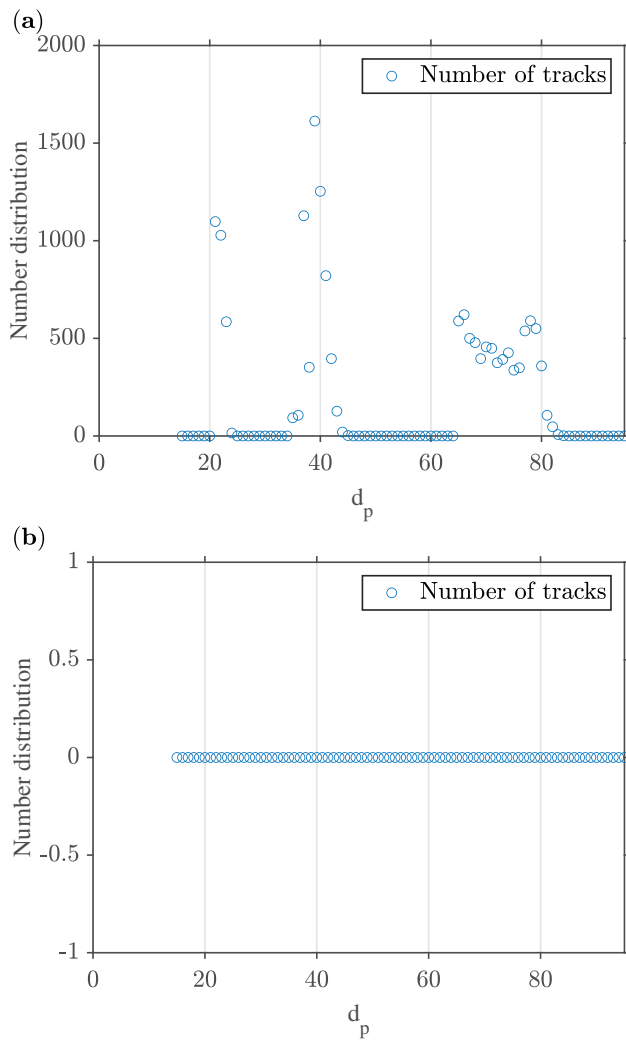


Figure 3.38: A comparison between the (a) number distribution of the wrongly sized particle that did not fulfill the minimum displacement criteria for Mie fitting and (b) that in the case of the rightly sized particles.

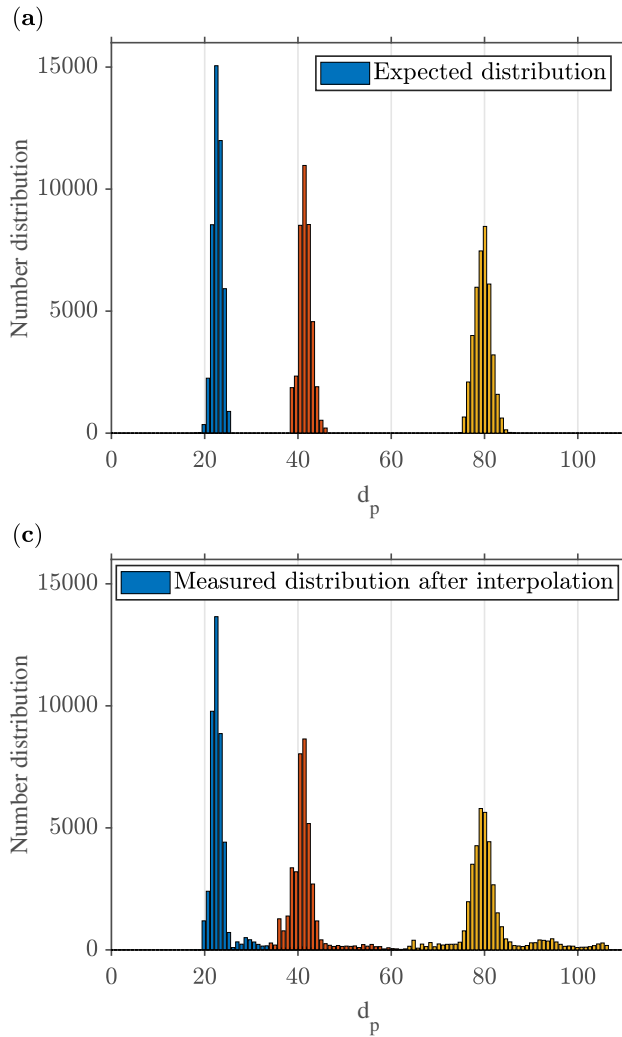


Figure 3.39: A comparison between the (a) expected size distribution from the measured tracks and (b) measured size distribution using the Mie fitting routine on interpolated data.

3.8 Summary

A novel method for Lagrangian particle tracking based on a scanning laser technique. Particles are first triangulated in the 3D measurement domain and then linked in subsequent volumes in time to form tracks from which Lagrangian velocities and accelerations can be calculated. The main contribution of the present work is to improve the particle triangulation efficacy. We demonstrated the use of a fitted sheet space number, which serves to further restrict the particle search depth in the scanning direction. The new

method accurately triangulates a large fraction of true particle locations for very high particle densities, up to an equivalent particle image density $N_I \approx 0.125$ ppp, where typical volumetric triangulation typically suffers from large fractions of falsely detected particles when $N_I \approx 0.005$ ppp. The fraction of successfully triangulated particles remains high in the presence of mild to moderate noise, and particle movement during the scan for finite scanning laser sheet speeds can be corrected if the sheet speed is at least two orders of magnitude larger than the characteristic velocity scale of the flow. The technique was tested via synthetic experiment using a DNS database, mimicking the conditions of a previous scanning setup, for which we were able to calculate Lagrangian velocities and accelerations. Spatial resolution was demonstrated by a very good correlation of the Lagrangian acceleration with the local and convective accelerations. An inherent upper limit on the magnitude of accelerations measurable was found for very dense fields using the current tracking algorithm due to a reduced mean inter-particle distance. To avoid ambiguity when forming particle tracks, the more dense a particle field is, the smaller the permissible search radius about a particle's predicted location at a subsequent time step. A more advanced particle tracking algorithm could possibly permit larger accelerations to be detected at higher densities.

The new scanning PTV method presents a robust technique for obtaining Lagrangian statistics in densely-seeded measurement volumes, required for the adequate spatial resolution of flows with high Reynolds number.

The experimental design consideration for particle sizing, such as the measurement area, camera angle, measurable size ranges, camera aperture and the number of cameras have been discussed. The scanning sizing technique was applied to synthetic data, with known sizes, to demonstrate the ability of the technique to retrieve the particle sizes accurately. The addition of noise did not reduce the accuracy of the sizing technique drastically. The error increases with decreasing particle size, due to the dominating influence of the noise on their scattered intensity. Whereas, misalignment in the cameras showed an opposite trend, where the error increases for larger particles, due to the mismatch arising due to the increasing scattering patterns. The numerical assessment shows that serious errors can occur when the signal to noise ratio decreases but the size measured are not affected seriously when the is calibration error is within 2.4 px. Finally, the suitability of the current technique for different types of flows was shown by conducting numerical simulations on HIT and turbulent channel flows. The particle sizing technique showed its suitability in retrieving back the sizes from a flow mixed with multiple size distributions.

Chapter 4

Validation of the scanning particle tracking and sizing technique via laboratory experiment

4.1 Introduction

Having introduced the experimental methodology in Chapter 2, and its optimisation and validation via numerical tests in Chapter 3, the technique is implemented in a laboratory experiment, the details and results of which are covered in this Chapter. The chapter begins by introducing the experimental set-up, before presenting the results from both Lagrangian tracking and the novel particle sizing technique.

4.2 Experimental setup

Figure 4.1 shows a diagram of the setup used for the scanning tracking and sizing experiment. The measurement volume is located at the mid-plane. Nearly neutrally buoyant seeding particles are recorded with three cameras. Illumination is provided by a Photonics Industries DM Green series Nd-YAG laser, whose beam is steered into a set of optics that expand the beam into a sheet and scan it across the measurement volume. The entire process is coordinated by Davis software provided by LaVision GmbH, which generates trigger signals for the cameras as well as for the scanning optics. The parameters of the cameras and the scanning experiment are provided in table 4.1. The recorded

Experimental Results

single time series measurement consists of 600 scan volumes separated by $dt = 20\text{ms}$. A total of 8-time series measurements were taken in order to increase the data sample for convergence, with each time series measurement separated by a data transfer and storage time of approx 15 minutes.

Table 4.1: Scanning experiment parameters

Parameter	Symbol	Value
Camera distance from the volume	D_o (mm)	800
Focal length of the lens	D_i (mm)	105
Image resolution	px	728×728
Camera 1 viewing angle	θ_1	$\approx 32^\circ$
Camera 2 viewing angle	θ_2	$\approx 34^\circ$
Camera 3 viewing angle	θ_3	$\approx 48^\circ$
Volume width	L_x (mm)	128
Volume height	L_y (mm)	128
Volume depth	L_z (mm)	26
Number of sheets	N_s	66
Mean laser sheet thickness	w (mm)	2.4

This section now details the experimental setup, specifically, the flow facility, scanning optics and seeding.

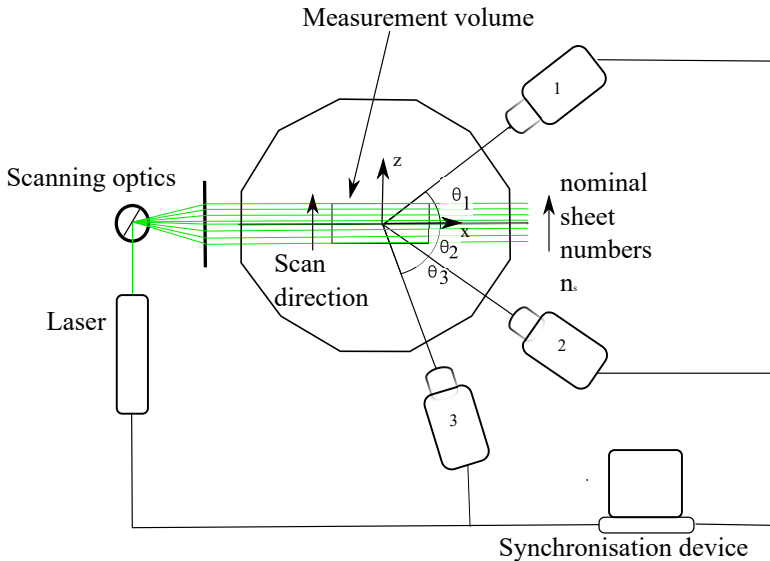


Figure 4.1: Schematic of the experimental setup.

4.2.1 Flow facility

The flow between two counter-rotating disks or impeller has been measured in a large number of experimental studies in order to investigate small scale turbulent structures (Lawson & Dawson, 2015; Worth & Nickels, 2011). Rotating the disks in opposite directions at equal velocities causes the fluid nearest the impellers to spin in opposite directions, establishing a strong shear plane in the centre of the tank, which creates the majority of the turbulence. The accelerated flow nearest to the impeller is expelled at the walls, which provides energy injection in the centre mixing layer of the tank. The energy is then advected towards the impeller via Ekman pumping for further reinjection (Kuzzay *et al.*, 2015). As a result of this, two secondary toroidal recirculation regions are formed, stretching the flow in the central region. The flow has been shown to be anisotropic even at fine scales (Lawson & Dawson, 2015).

Globally inhomogeneous phenomena emerge when one varies the speed of one impeller with respect to the other. Figure 4.2 (Poncet *et al.*, 2008) shows the flow structures for varying ratios of speeds between the impellers in a plane parallel to the axis of rotation. In the exact counter-rotating regime, the flow is symmetric and two cells with the same size coexist, with a shear plane in the center (figure 4.2(a)). For small rotating speed differences, the structure of the mean flow is strongly dominated by the faster disk as seen in figure 4.2(b). Varying the ratio of speed displaces the shear layer towards the slower disk as seen in figures 4.2(c) and (d). The present flow structure resembles that observed in the rotor-stator configuration with streamline patterns parallel to the rotating axis towards the rotating impeller, when the other impeller is stationary, as shown in figure 4.2(e).

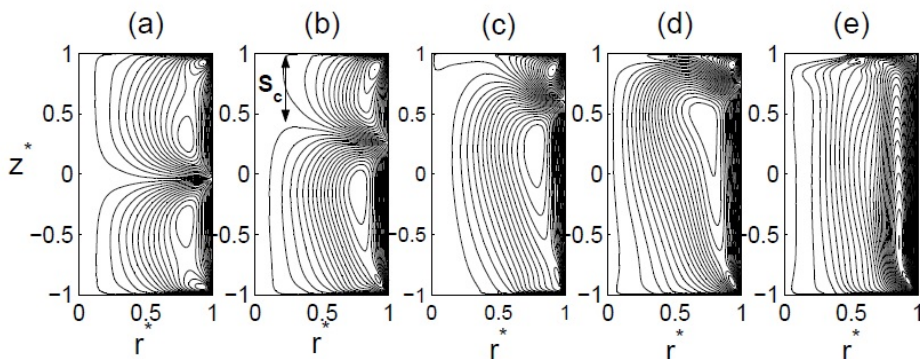


Figure 4.2: Flow structures seen when the impeller speed ratio is varied (Poncet *et al.*, 2008).

Experimental Results

The contribution of Ekman pumping in the generation of von-Karman mixing thus can be studied by making one of the impellers stationary. This leads to an Ekman pumping flow to the rotating impeller from the non-rotating impeller instead of that from the center of the tank, which creates a mean upwelling flow in the tank center. Such a flow is chosen for this study for the following reasons; 1) using a known flow to test the technique 2) the central region of the flow has mean velocity as compared to the case of two counter-rotating impellers. This is ideal for the particle sizing part of the measurement technique, as particles must move a certain minimum distance across the measurement region to provide the scattering peaks as discussed in section 3.5.1. Also, the simple 2D nature of the flow, makes it easier to track the particles in order to demonstrate and validate the current scanning tracking and sizing technique.

Figure 4.3 illustrates the large mixing tank facility. It is a dodecagonal perspex tank which is 2m in height and has a diameter of 2m. To generate an Ekman flow, the water in the tank is stirred by a rotating impeller fixed at the top of the tank, which is equipped with eight vanes. The radius of the impeller R_{imp} is 0.8m. The bottom impeller is kept stationary. Baffles at each of the twelve corners of the tank damp net rotation and contribute to the generation of turbulence. A stepper motor drives the impellers at the rate of $\Omega_I = 2$ rpm. The impeller velocity u_{imp} is the tip velocity calculated based on the impeller radius and the impeller rotation rate.

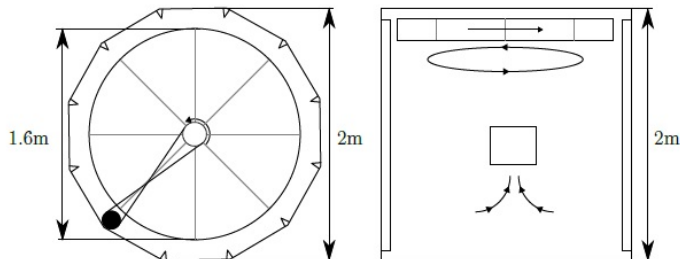


Figure 4.3: Schematic of large mixing tank facility.

4.2.2 Camera configuration

Imaging is performed using three Phantom v2012 cameras, as illustrated in figure 4.5. A three-camera setup has been used for the laboratory experiment owing to its advantages in improved triangulation efficacy, as discussed in section 3.5.5. The cameras are equipped with Sigma 105 mm macro-lenses, using $f = 22$ which provided sufficient depth of field to keep particle images in focus over the scan depth. Scheimpflug adapters are used and the measurement volume is offset 200 mm from the centre of the tank. A cropped resolution



Figure 4.4: Image of the impeller used to rotate the water in the mixing tank.

of 728×728 pixels is used in order to increase the magnification required for the sizing approach, as discussed in section 3.5.1.

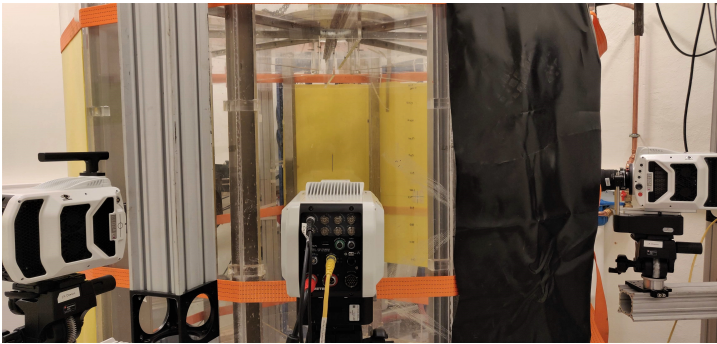


Figure 4.5: Image of the camera configuration used for the scanning experiment.

4.2.3 Scanning optics

To generate approximately parallel laser sheets with control over the laser sheet thickness, an optical set-up similar to Lawson & Dawson (2014) is used, schematically shown in figure 2.1. An image is shown in figure 4.6. The set of optics used to generate the parallel sheets followed the same configuration as that detailed in section 2.1. A total of 66 parallel laser sheets with a mean thickness of 2.4mm was generated using this configuration.

4.2.4 Seeding and water temperature

Two different mean sizes of polystyrene particles are used in the experiment. The specific products are TS-80 Microbeads AS and TS-40 Microbeads AS, with batch numbers, 3I-080-1771 and 2B-040-1518, and mean diameters of $80\mu\text{m}$ and $40\mu\text{m}$ respectively. The density



Figure 4.6: Side and top view images of the scanning optics.

of the particles is 1.05kg/L. Two different particle sizes were chosen for the validation of the particle sizing approach.

4.2.5 Characteristic scales of the flow

The characteristic scales of the flow are given in table 4.2. The Kolmogorov length scale η is defined as

$$\eta = \left(\frac{\nu^3}{\epsilon} \right)^{1/4}, \quad (4.1)$$

and the corresponding Kolmogorov timescale τ_η is defined as

$$\tau_\eta = \left(\frac{\nu}{\epsilon} \right)^{1/2}. \quad (4.2)$$

The dissipation rate ϵ was estimated using the simplest method of calculating it directly from the relation

$$\epsilon = 2\nu \overline{s_{ij}s_{ij}} \quad (4.3)$$

where s_{ij} is the strain rate tensor and ν is the kinematic viscosity of water at 20°C. The Taylor Reynolds number Re_λ is obtained as

$$Re_\lambda = \frac{\sqrt{\overline{u^2}}\lambda}{\nu} \quad (4.4)$$

with

$$\sqrt{\overline{u^2}} = \sqrt{\overline{u_x^2} + \overline{u_y^2} + \overline{u_z^2}} \quad (4.5)$$

and the Taylor microscale length λ_i is estimated as

$$\lambda_i = \sqrt{\frac{\overline{u_i^2}}{(\partial u_i / \partial x_i)^2}}. \quad (4.6)$$

Table 4.2: Characteristic scales of the flow. f_I is the impeller rotation frequency and Δt is the separation time between subsequent scan volumes.

f_{imp}	ϵ	τ_n	η	Re_λ	$\tau_\eta/\Delta t$
(Hz)	(mm ² /s ³)	(s)	(mm)		
0.03	22.09	0.2	0.45	575	10

4.3 Particle tracks

4.3.1 Algorithm parameters for tracking

Three-camera triangulation was performed to get the 3D locations of the particle. To estimate the camera background noise, camera dark images with no particles were recorded. The recorded dark image had a Gaussian profile with a mean intensity value $\approx 2\%$ of the maximum intensity count of 4096. Hence a particle intensity threshold of 0.02 times the maximum intensity from each of the sheet images from all three views, was used to identify the 2D particle location. In order to deduce the fitted sheet number f_s and the peak particle intensity to be used in particle sizing, repeated images of the same particle in adjacent (overlapping) laser sheets must be grouped as being measurements of the same particle. For this purpose, a tolerance of 1 px was used for the displacement of the particle during the scan, but it should be noted that this is much smaller than the expected displacement of the particle over that time and much smaller than the average inter-particle distance. This tolerance accounts for small measurement errors and the small particle movements during the time adjacent images are taken. At infinite scanning speed, the particle would not move during the scan for example. The triangulation was iterated 3 times, to triangulate the particles from the residual images. The RMS fit error from the camera calibration was 0.5, 0.56 and 0.57 px for the three cameras respectively. The maximum allowed triangulation error was hence set to 2px, in order to account for misalignment errors.

To track the particles in time, a predictor velocity field was used. The predictor velocity field was calculated by cross-correlating the 2 camera reconstructed intensity fields, using in-house code as detailed in Lawson (2015). A search radius of 5vx was used to link the particles in consecutive volume.

4.3.2 Track length

Particle trajectories which are longer than the relevant Kolmogorov scales, η , and τ_n , are the key prerequisite for Lagrangian flow analysis and, as will be shown in the later sections,

Experimental Results

they also significantly enhance the accuracy of the applied processing to obtain velocity derivatives.

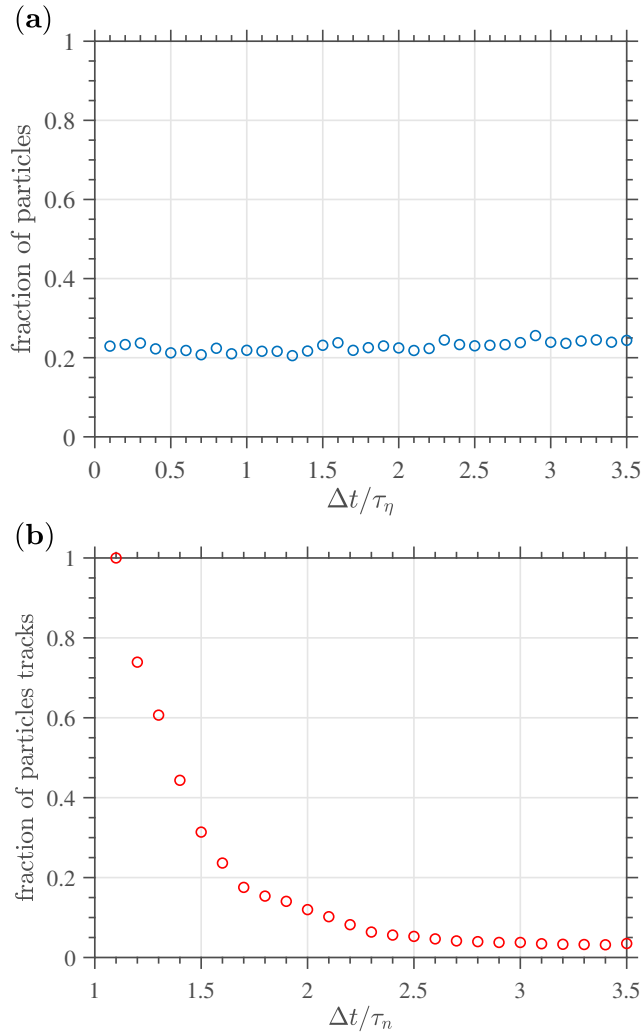


Figure 4.7: **(a)** The fraction of particles dropping out of the measurement volume at every time step. **(b)** The fraction of particle tracks for a certain length.

Since the flow in the center of the tank has a mean component, the particles do not stay in the measurement volume for a long duration. This effect is known as particle dropout. This is reflected in the measured tracks, as the number of particle tracks at increasing track lengths diminishes exponentially. Figure 4.7(a) shows the fraction of particles dropping out from a volume at each time step. The track length is represented as a function of the fit time (Lüthi *et al.*, 2005; Voth *et al.*, 2002) which is Δt , normalized by the Kolmogorov timescale τ_η . The particle drop out rate is constant across the time

step, but since this effect is cumulative the number of tracks with a certain track length decreases exponentially. Figure 4.7(b) shows the exponential decrease of the fraction of particle tracks for increasing track lengths. In a single set of total track length $60\tau_\eta$ successive short track sets with a track length of $3.5\tau_\eta$ were measured.

The decrease in the fraction of the tracked particle is shown in the two plots in figure 4.8, both obtained from the same set but with two different track lengths. The particle tracks are color coded with velocity magnitude normalized by the impeller velocity, which in this study is $u_{imp} = 166\text{mm/s}$. Figure 4.8(a) shows particle tracks with track length $1\tau_\eta$ and figure 4.8(b) shows particle tracks with track length $2\tau_\eta$. The track sets show a large scale mean shear structure whose order is of the measurement volume. The large scale structure of the flow from the tracks shows a predominant upward pumping mode accompanied by a cylindrical shearing mode, along the rotational direction of the impeller.

4.4 Velocity fields and statistics

To have a qualitative Eulerian picture of the large scale properties of the flow, a temporal average obtained by averaging samples separated by large time intervals of the velocity field is obtained. To represent the mean velocity field on regularly spaced grid points from the Lagrangian tracks an adaptive Gaussian windowing technique by Agui & Jimenez (1987) is used. To do this, tracks with track lengths $1\tau_\eta$ from track sets separated by $3.5\tau_\eta$ were selected and the velocities at their midpoints locations were used to interpolate onto regularly spaced grids with grid spacing equal to twice the mean interparticle distance, in this case, the mean distance between track midpoints was approximately 1η .

Figure 4.9 (a), (b) and (c) shows the mean-field of all three velocity components in an x-y plane at the central z-plane, i.e. the centre of the measurement volume and figure 4.9 (d) the magnitude of velocity normalized by the impeller velocity. A comparison of the mean velocity fields between the three components shows that the axial velocity component (u_y) is almost an order of magnitude higher than the other two components. The predominant upwelling of the flow is caused due to Ekman pumping between the bottom stationary and top rotating impeller.

The nature of the flow is also checked by quantifying the Lagrangian velocity distribution. The velocity components along the tracks are obtained using the fitting procedure, hence one would expect possible errors in the velocities estimated at the endpoints along the tracks which could lead to misinterpreting the statistics presented in this study. The effect of velocities calculated at the two edges of the tracks by comparing the pdfs obtained by chopping off the edges of the tracks obtained. Figure 4.10 shows the comparison of pdfs the Lagrangian velocity normalized by impeller velocity obtained for a track length of $tr_l = 2\eta$. In figure 4.10(a), the pdfs are obtained from all points along tracks with trimmed edges. The distribution obtained from the middle of the track clearly shows the

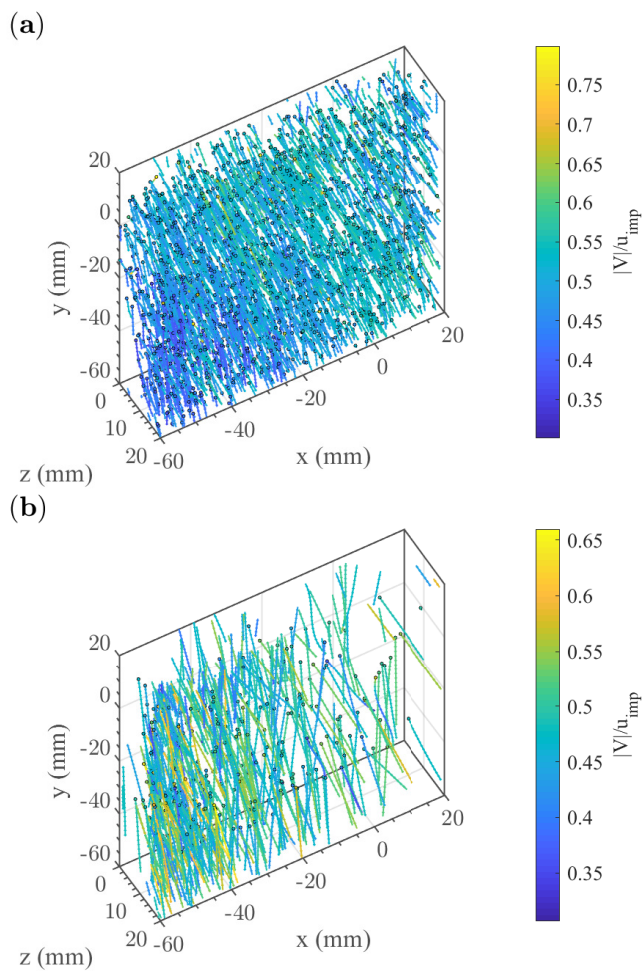


Figure 4.8: Example showing particle tracks from a single set with three different fixed track lengths of (a) $1\tau_\eta$ and (b) $2\tau_\eta$. The particle tracks are color coded with magnitude of velocity normalized by the impeller velocity, $u_{imp} = 166\text{mm/s}$.

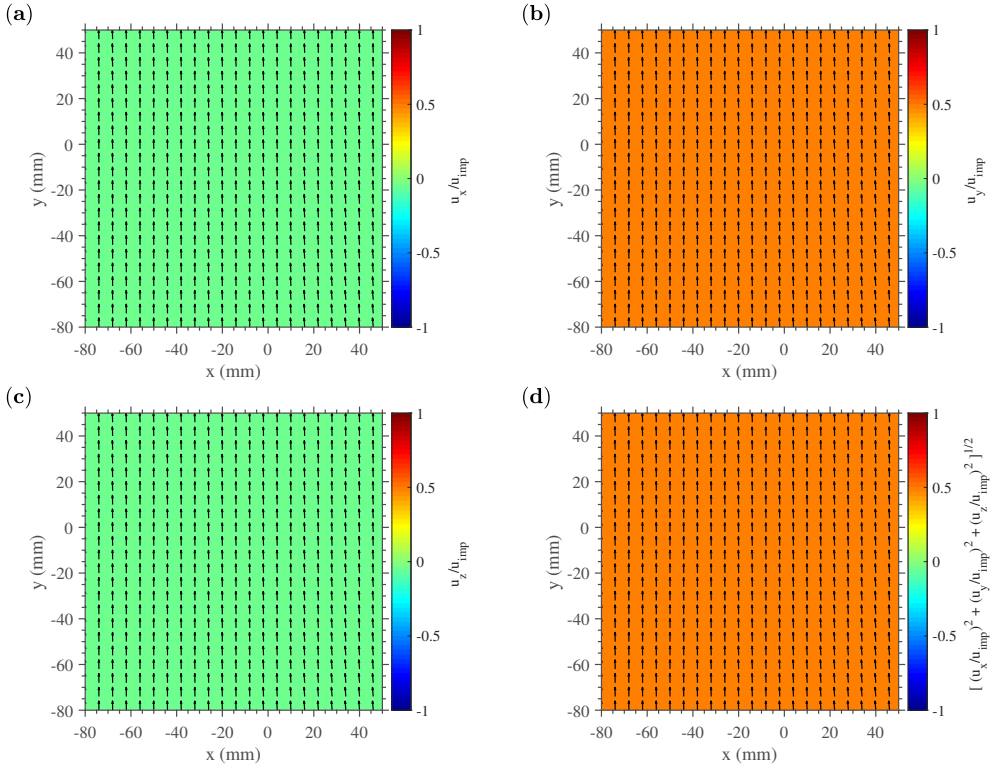


Figure 4.9: Spatial distribution of the time averaged mean velocity components (a) u_x (b) u_y (c) u_z and (d) the magnitude of velocity $\sqrt{u_x^2 + u_y^2 + u_z^2}$, normalized by the impeller velocity u_{imp} in a x-y plane at the center z-plane of the measurement volume.

Experimental Results

least irregularities in the distributions. The distributions are quite similar meaning the sample at one timestep is large enough since multiple time steps are needed for tracking, the statistics in this study were obtained from all points along tracks with the edges of the tracks trimmed.

In all cases, the transverse components distributions fall on top of each other showing symmetry. The distribution of the axial velocity component u_y shifted towards the positive value in figure 4.10(a), shows the dominance of the vertical velocity due to the upwelling.

Table 4.3: Velocity statistics calculated at the mid point from tracks with track length $2\tau_\eta$.

$\langle u_x \rangle / u_{imp}$	$\langle u_y \rangle / u_{imp}$	$\langle u_z \rangle / u_{imp}$
-0.03	0.5	-0.028
$\langle u_x'^2 \rangle$	$\langle u_y'^2 \rangle$	$\langle u_z'^2 \rangle$
10.2	7.2	10.6
$S_{u'_x}$	$S_{u'_y}$	$S_{u'_z}$
0	0	0
$F_{u'_x}$	$F_{u'_y}$	$F_{u'_z}$
3.4	4.2	3.4

The fluctuating velocity field was first computed by performing Reynolds decomposition using the mean velocity field obtained as discussed above and instantaneous velocity fields obtained using the interpolation scheme discussed (Agui & Jimenez, 1987). The RMS of the fluctuating velocity field was then obtained as $u_{i,rms} = \overline{(u_i - \bar{u}_i)^2}^{1/2}$. The spatial RMS field of the fluctuating velocities as shown in figure 4.11 gives an overview of the fluctuations in the flow. The fluctuations in the transverse directions are higher than those in the axial direction. A qualitative assessment of the spatial distribution of the RMS fluctuations shows that the fluctuations in the transverse directions are higher than that in the axial direction.

In the Lagrangian frame to calculate the fluctuating velocities, the mean $\langle u_i \rangle$ is subtracted from the Lagrangian velocities, $u'_i = u_i - \langle u_i \rangle$. The fluctuating velocities along the three velocity components were calculated in two ways:

1. Subtracting the mean obtained over the entire time steps or track length.
2. Subtracting the mean at each time step.

The pdfs of the fluctuating velocity components normalized by the impeller velocity u_{imp} for both the methods is shown in figures 4.12(a) and (b). The pdfs obtained from both methods hardly shows any differences. This also suggests that the number of samples every time step is a large enough sample physically for statistical convergence, meaning

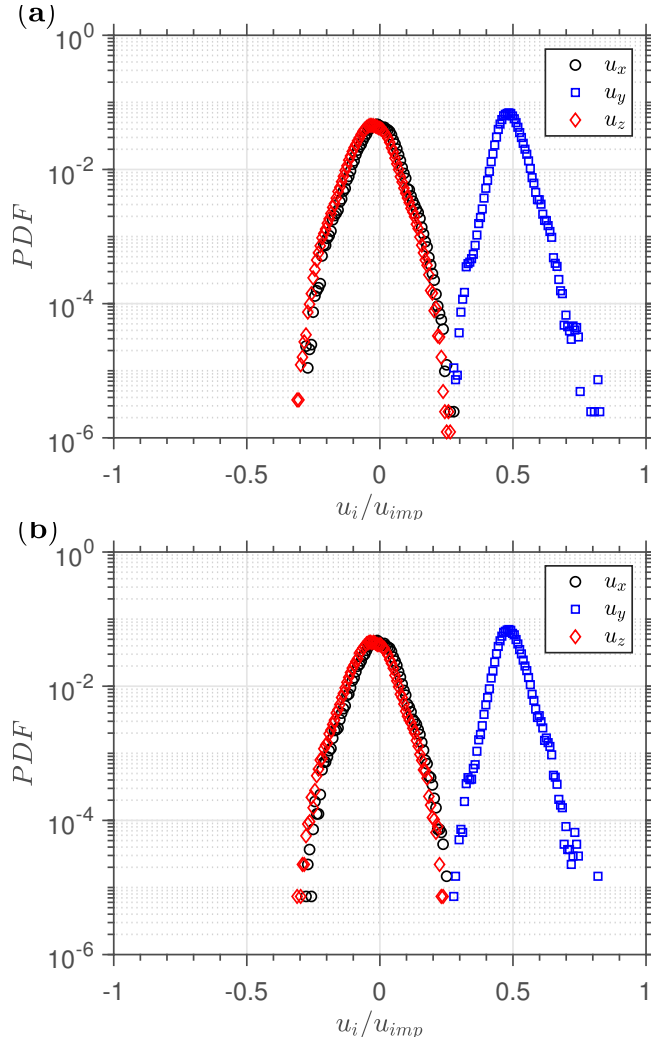


Figure 4.10: Comparison of pdfs of the Lagrangian velocity components normalized by impeller velocity u_{imp} for a track length of $2\tau_\eta$ using (a) all points along track and (b) middle point of the track.

Experimental Results

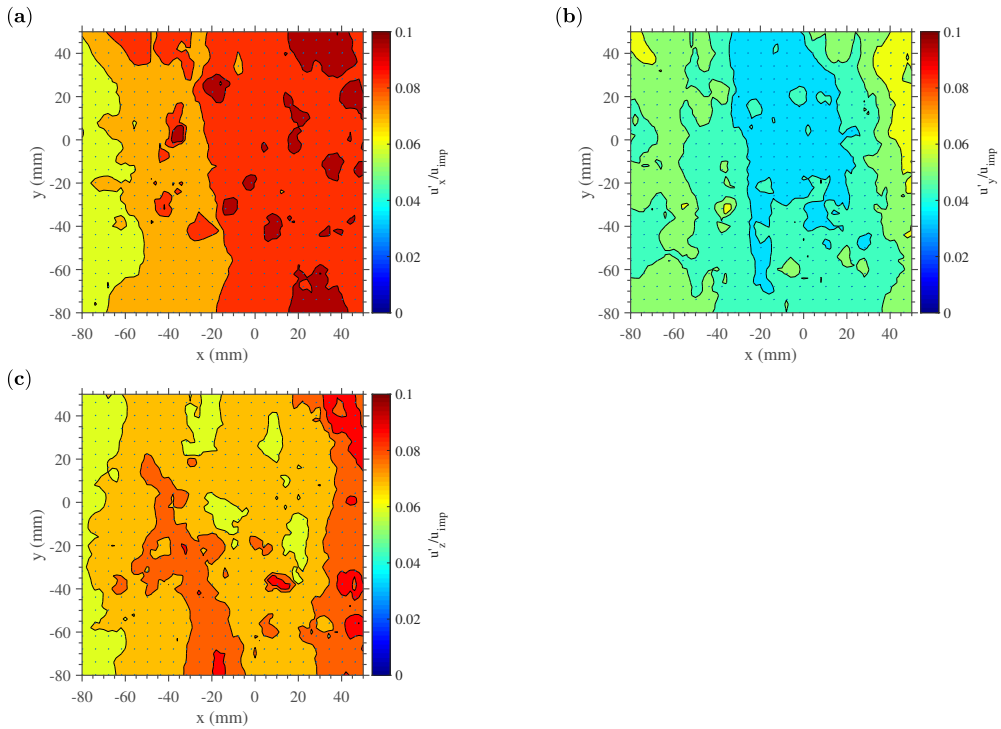


Figure 4.11: Spatial variation in rms of fluctuating velocity components normalised by the impeller velocity, in a x-y plane at the center z-plane of the measurement volume.

the mean at every time step is similar to the mean at all the time steps, whose values are given in table 4.3. This hence gives the confidence to remove endpoints, and even just use the middle track points as shown in figure 4.10(b). For the velocity statistics discussed in the remaining part of this section, fluctuating velocities obtained by subtracting the mean at each time step has been used.

The fluctuating velocity normalised by impeller rotation velocity is fitted to zero-mean Gaussian distributions using a least-squares approach. Symmetry similarities identified in figure 4.11 between the transverse components u_x and u_z is also seen the pdfs in figures 4.12(a) and (b). This cause of this effect was previously found discussed in Voth *et al.* (2002), the mean strain field generated by the Ekman pumping has the effect of amplifying the axial vorticity leading to an increase in transverse turbulent fluctuations. This effect can be seen by comparing the figure 4.11, with the normalized RMS fields in the transverse directions, $u_{x,rms} \approx 0.08$ and $u_{z,rms} \approx 0.075$, to that of the axial direction, $u_{y,rms} \approx 0.04$, producing a ratio of ≈ 0.5 . This result is in broad agreement with Voth *et al.* (2002) who also found a ratio of 0.5 between axial and transverse RMS fluctuations, because of this poloidal mode or the Ekman pumping mode.

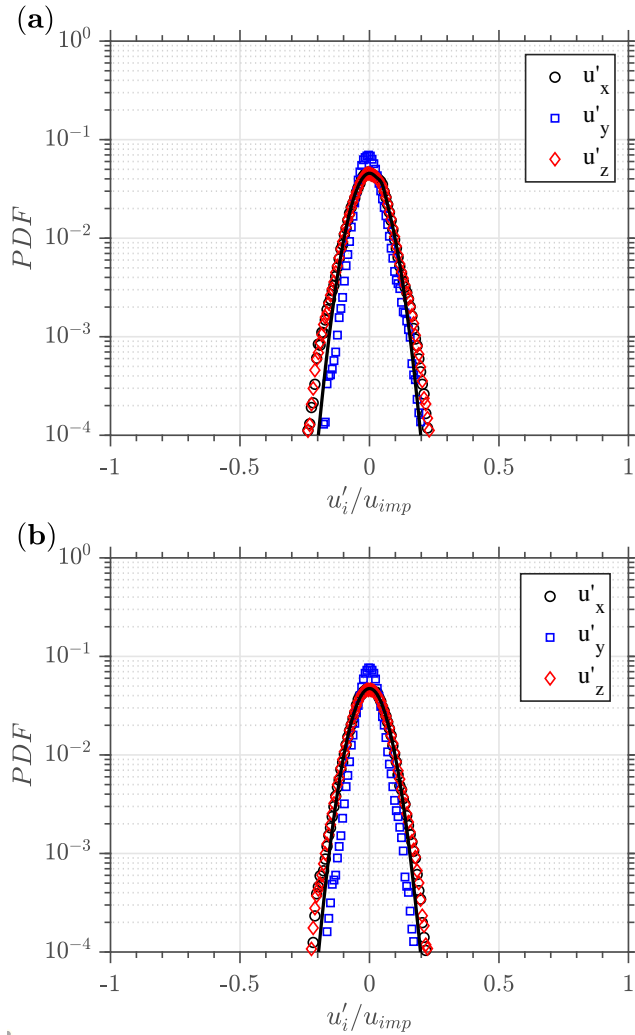


Figure 4.12: Comparison of pdfs of the fluctuating velocity components normalized by impeller velocity u_{imp} obtained (a) by subtracting the mean velocity obtained over the entire measurement time window or track length (b) by subtracting the mean at each time step.

To describe the level of variability about the mean, the variance or the second moment of the fluctuating quantity $u'_i = u_i - \langle u_i \rangle$ is calculated. Figure 4.13 shows the calculated variance of the velocity components for increasing track length. Since the flow is dominated in the axial direction and symmetry is expected in the transverse direction, as seen in the pdfs of the transverse components in figure 4.13, the value of the variance of the transverse fluctuating components should be close to each other. In figure 4.13, the ratio of the

Experimental Results

velocity variance in transverse and axial directions is about 1.34, when compared to the value of 1.5 reported in the literature (Lawson, 2015; Voth *et al.*, 2002; Worth, 2010).

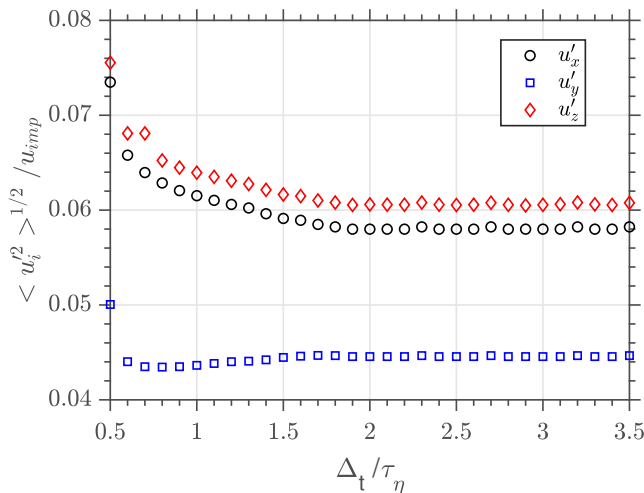


Figure 4.13: Measured velocity variance as a function of normalized track length Δ_t / τ_η .

Skewness is the third moment of u_i' normalized by the variance. Figure 4.14(a) shows the skewness of velocity components for an increasing track length for the available ranges. All three velocity components show a very small deviation from a zero skewness value for all the track lengths available. This shows that the velocity fluctuations along the track length are less intermittent.

The deviations in the pdfs of the velocity fluctuations from the Gaussian curve fitted in figure 4.12 can be quantified by measuring the flatness value of the distributions. Figure 4.14(b) shows the flatness value (F) of these velocity fluctuations for increasing track lengths. Flatness is the fourth moment of u_i' , normalized by the variance. Gaussian type flatness was reported by Voth *et al.* (2002), for particles in a von Karman flow, with measured flatness F around 2.8-3.2. The transverse components have a near to Gaussian flatness of 3, while the flatness value of the axial component has a slightly higher value of 4. The velocity flatness depends on the details of the large scales of the flow. In this flow, the flatness of the axial component with the smaller RMS is larger than Gaussian flatness and the flatness of the transverse components component with the larger RMS is closer to Gaussian flatness.

The statistics of velocity components were shown to be anisotropic and inhomogeneous at the measured region, which is the centre of the tank. The next section examines statistics of velocity gradients and in a later section that of acceleration, both being fundamentally small-scale quantities, and explores where, and to what extent, this behaviour holds in this flow.

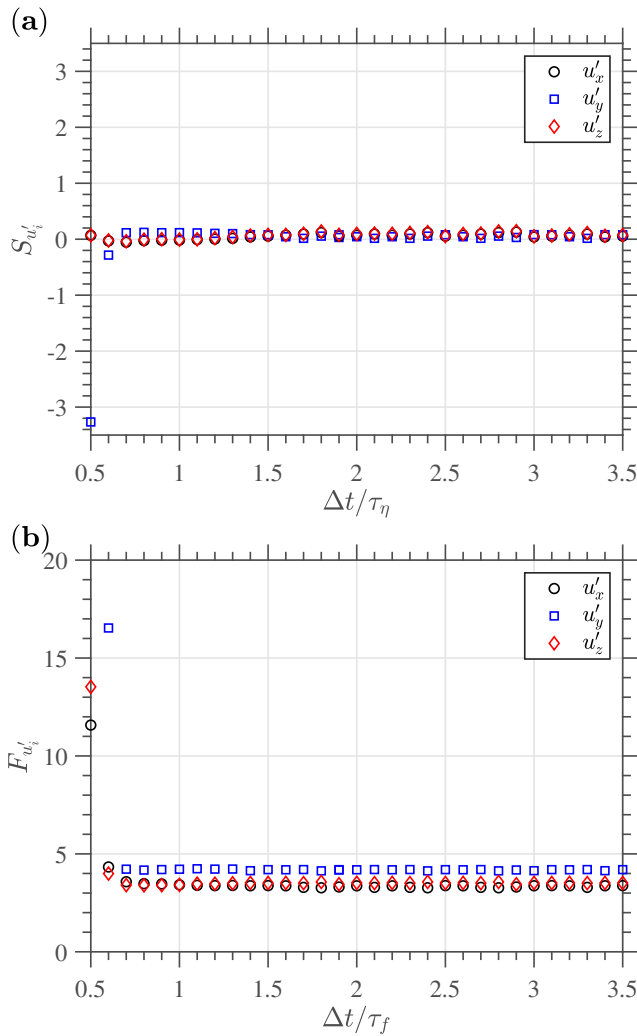


Figure 4.14: (a) Skewness of the velocity fluctuations and (b) flatness of the velocity fluctuations for increasing normalized track length $\Delta t/\tau_\eta$.

4.5 Velocity gradients

Elements of the velocity gradient tensor, $A_{ij} = \partial u_i / \partial x_j$, play an important role in the dynamics of turbulence, with the antisymmetric part of the velocity gradient tensor manifesting the rotational nature of turbulence, thereby vorticity and the symmetric part representing dissipative nature of turbulence, and thereby strain. Apart from vorticity and strain/dissipation, the characteristics of the field of velocity derivatives in turbulent flows reflect the physics of the turbulence as it is much more sensitive to the structure of the turbulence.

The spatial gradients at a point x_0 are estimated using the procedure explained in section 1.3.2, using weighted contributions from particles according to their distance $\|x_i - x_0\|$ from spatial location in question x_0 . Information from the closest 20 particles to the point in space where the spatial derivative is obtained is used along with information from times t and $t \pm 2 \Delta t$. The average inter-particle distance in the present fields from the tracked particles is approximately 3η .

4.5.1 Quality of velocity gradients

The quality of velocity gradients measurement is checked using the continuity equation. A divergence criterion where the trace of $\partial u_i / \partial x_j$, should be zero is a check of continuity and hence is used here.

Figure 4.15 shows the joint PDFs of $-\frac{\partial u_i}{\partial x_i}$ versus $\frac{\partial u_j}{\partial x_j} + \frac{\partial u_k}{\partial x_k}$. In all the cases, a higher amount of data points are close to the diagonal. Also, in all the cases, a correlation is examined between the terms on the left-hand side to those on the right-hand side. A correlation coefficient of $Q = 1$ denotes adherence to the incompressibility claim.

In all the cases, plotted in figure 4.15, the correlation coefficient Q is close to unity. The good correlation from the joint PDFs of the divergence terms demonstrates the accuracy of the filtering method involved in estimating these quantities. A close to unity correlation coefficients, hence proves that the steps involved in measuring these terms using the weighted polynomial (Lüthi *et al.*, 2005), clearly enhances the measurement quality and the accuracy of the terms obtained.

Since the velocity gradients, $\partial u_j / \partial x_j$ inherently describes differences in the velocity component values at closely spaced points, contributions from the large scales cancel almost entirely (Ishihara *et al.*, 2007; Mullin & Dahm, 2006). Hence the one-dimensional PDFs of the velocity gradients here are used to check the spatial resolution of the measured tracks. Figure 4.16(a) shows the one-dimensional PDFs of the diagonal components of the velocity gradient tensor. The tails of the PDFs are wide and extends up to $10/\tau_\eta$. This shows that the spatial resolution is not coarsened. Since any nonlinear function of a Gaussian is non-Gaussian, the non-Gaussian PDFs of the longitudinal velocity gradients with exponential tails also validates the accuracy of the measurement, as the PDFs of the velocities are Gaussian. Similar PDFs of the transverse velocity gradients are shown in figure 4.16(b).

4.5.2 Vorticity and strain

As shown above, the scanning particle tracking technique is successful in providing the full set of spatial velocity derivatives of the flow. To demonstrate the capability of the technique to recover most of the relevant results on the turbulent fine-scale structure,

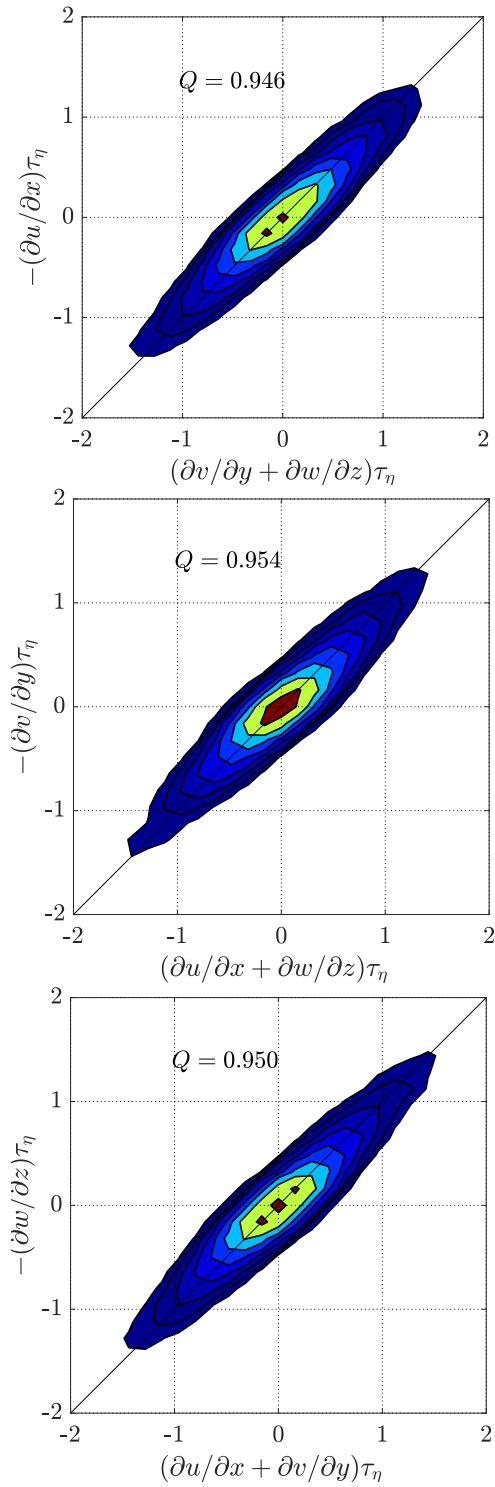


Figure 4.15: J-PDF of the continuity equation terms, $-\partial u_i/\partial x_i = \partial u_j/\partial x_j + \partial u_k/\partial x_k$.

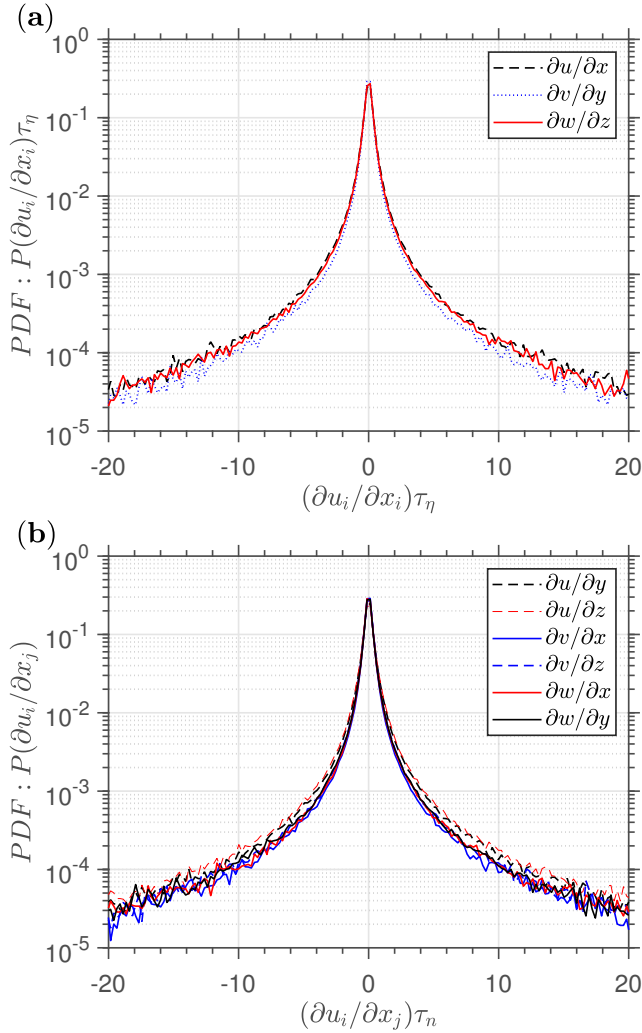


Figure 4.16: (a) PDFs of the longitudinal velocity gradients $\partial u_i / \partial x_i$. (b) PDFs of the transverse velocity gradients $\partial u_i / \partial x_j$, $i \neq j$

statistics of vorticity and strain that are specific to fluid turbulence as demonstrated by Lüthi *et al.* (2005) are now considered for the present data.

One distinctive feature of a 3D turbulent flow is the positive net enstrophy and strain production terms (Tsinober, 2009). The non-linear term responsible for enstrophy production is $\omega_i \omega_j s_{ij}$, which is the interaction between vorticity ω and the strain rate tensor s_{ij} . The strain production term $-s_{ij} s_{jk} s_{ki}$ plays an equal role along with enstrophy production term in processes like energy dissipation and vortex stretching. Hence a check on the positive rates of these two terms can be regarded as the most basic distinction of turbulence to a random Gaussian velocity field, which can be conducted to verify the

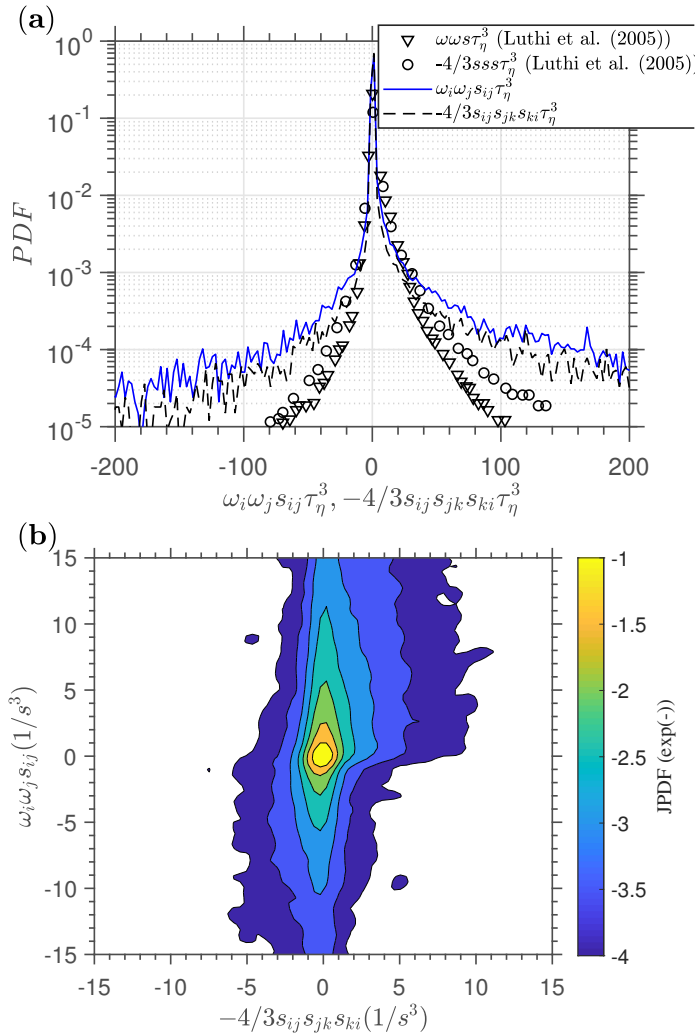


Figure 4.17: **(a)** PDFs of enstrophy production $\omega_i \omega_j s_{ij}$ and strain production $-4/3 s_{ij} s_{jk} s_{ki}$ terms. The symbols represent similar result from Lüthi *et al.* (2005) for a von Karman flow. **(b)** Logarithmic joint PDF of $\omega_i \omega_j s_{ij}$ and $-4/3 s_{ij} s_{jk} s_{ki}$.

measured tracks. Shtilman *et al.* (1993) using DNS of homogeneous turbulence showed that features of turbulence concerning vorticity and strain most of which are not observed in a Gaussian flow field, are specific to genuine fluid turbulence. Such a result was reproduced by Lüthi *et al.* (2005) to show the accuracy of their particle tracking technique. A similar result is reproduced here to demonstrate the capability of the particle technique in recovering most of the relevant results on the turbulent fine-scale structure, statistics of vorticity and strain that are specific to fluid turbulence. Figure 4.17 the PDFs of $\omega_i \omega_j s_{ij}$ and $-4/3 s_{ij} s_{jk} s_{ki}$ shows positive skewness for both enstrophy and strain production terms.

The results are compared to that obtained by Lüthi *et al.* (2005) for a von Karman flow. In figure 4.17(b) the logarithmic joint PDF of $\omega_i\omega_j s_{ij}$ and $-4/3s_{ij}s_{jk}s_{ki}$ also shows the positive skewness of these terms. In addition to this, it also shows the weak correlation between these two terms by showing how strong production of enstrophy inhibits strong production of strain and vice versa.

4.6 Acceleration measurements

The particle accelerations are measured using the steps detailed in section 2.3.5. This section begins by validating the accuracy of the measured acceleration from the tracks using single point kinematic relations, which is followed by several statistical results of the measured acceleration and comparing them to known or expected acceleration statistics.

4.6.1 Quality of the temporal derivatives

A stronger check on the accuracy of the measurement involving all the terms that could be measured, namely, Lagrangian accelerations, $a_i = Du_i/Dt$, local accelerations, $a_{l,i} = \partial u_i/\partial t$ and convective accelerations, $a_{c,i} = u_j \partial u_j/\partial x_j$, is performed as explained in section 2.3.5. This test is more difficult to pass compared to that shown for the continuity equation in figure 4.15 as all the terms in this test are derived in a different manner.

Figure 4.18, shows the joint pdf of Lagrangian acceleration and the sum of local and convective acceleration. The correlation coefficient Q , close to unity shows the high accuracy in the temporal gradients measured by the tracking method.

4.6.2 Acceleration alignment

The alignment between the Lagrangian accelerations, $a_i = \frac{Du_i}{Dt}$, and the summation of local accelerations $a_{l,i} = \frac{\partial u_i}{\partial t}$ and convective accelerations $a_{c,i} = u_j \frac{\partial u_j}{\partial x_j}$, is shown in figure 4.19 in terms of the PDF of the cosine of the angle between the two vectors. The PDF is strongly positively skewed, indicating that the two terms are statistically aligned.

In the same figure, the PDF of the cosine of the angle between the local acceleration and the advective term is also shown. The PDF is negatively skewed, indicating that the two terms are anti-aligned: the two terms partly compensate each other while contributing to the Lagrangian acceleration of the fluid particle. This observation hence also validates the accuracy of the measurement (Tsinober, 2009).

4.6.3 Acceleration variance

Estimation of acceleration can be subjected to errors due to erroneous tracks. Hence a primary concern in measuring accelerations is to determine whether the track lengths used

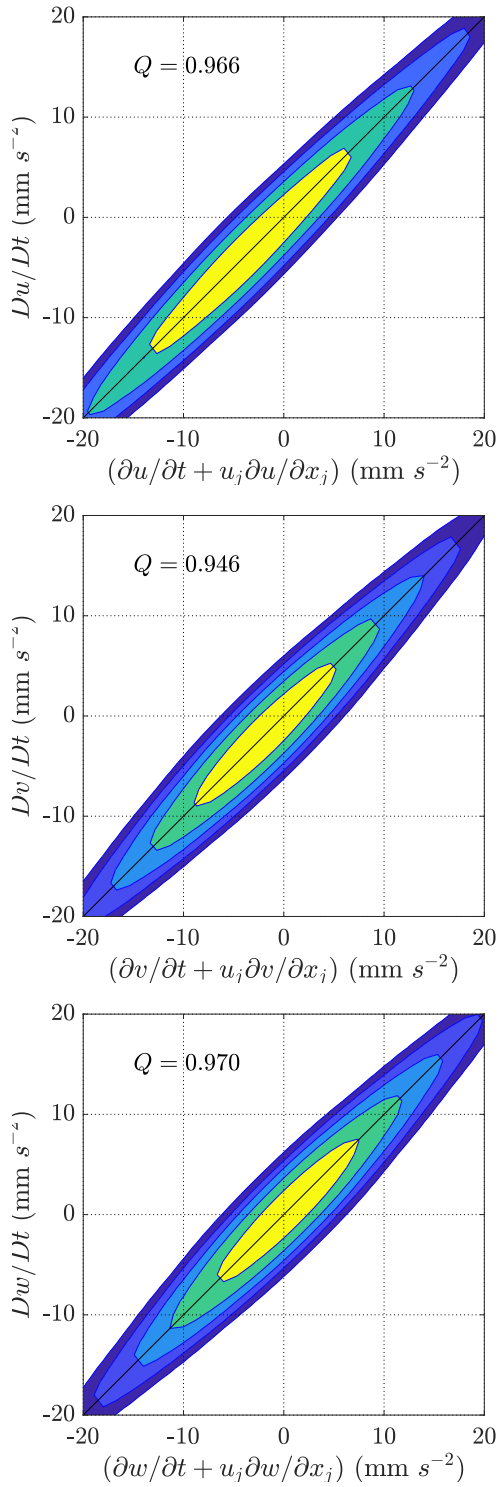


Figure 4.18: J-PDF of the acceleration terms from all three velocity components, $Du_i/Dt = \partial u_i/\partial t + u_j \partial u_i/\partial x_j$.

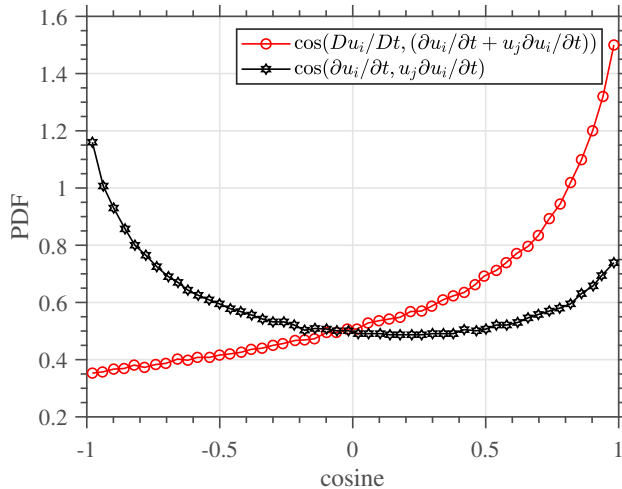


Figure 4.19: PDF of the cosine of the angle between the Lagrangian acceleration vector along trajectories, and the summation of the local acceleration and the advective acceleration (circles). PDF of the cosine of the angle between the local acceleration and advective acceleration (stars).

to estimate the acceleration are long enough to eliminate contributions from measurement error and still short enough not to average over the structure of the true trajectory. To examine this, the RMS acceleration is calculated as a function of normalized track length ($\Delta t/\tau_\eta$). Figure 4.20 shows the measured acceleration variance $\langle a_i^2 \rangle^{1/2}$, for the three different components as a function of the normalized track length $\Delta t/\tau_\eta$. There is a sharp turn up for times shorter than $1\tau_\eta$. The high variance at shorter track lengths could be either due to erroneous tracks or extreme accelerations captured for shorter tracks. The slow fall off at longer times is at least partly a result of the tracks averaging over the true trajectories. Around $1.5\tau_\eta$, the RMS values of the transverse components are approximately the same for all track lengths. The RMS of the axial component is slightly higher than the transverse components, with the ratio between the transverse to axial component RMS being 0.7. To evaluate the statistics, the acceleration measurements obtained from trajectories with track length above $1.5\tau_\eta$ have been used.

4.6.4 Acceleration probability density functions

The PDFs of the transverse (a_x), (a_z) and axial (a_y) Lagrangian acceleration (a_i) are shown on a log-linear plot in figure 4.21. The acceleration is normalized by the measured RMS acceleration, and track lengths greater than $1.5\tau_\eta$ are used. The first thing that stands out is the long stretched exponential tails, which demonstrates a strong deviation

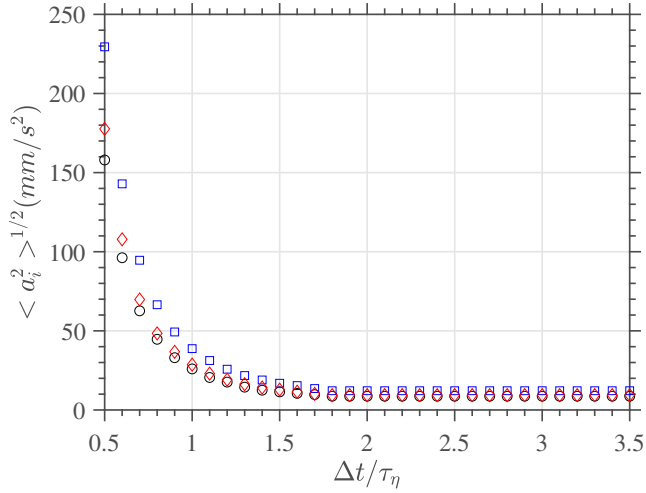


Figure 4.20: Measured acceleration variance as a function of normalized track length $\Delta t / \tau_\eta$.

from Gaussian behaviour as shown previously by Voth *et al.* (2002). As in the numerical simulation case in section 3.4.1, the reference curve fit of Voth *et al.* (2002) is given as

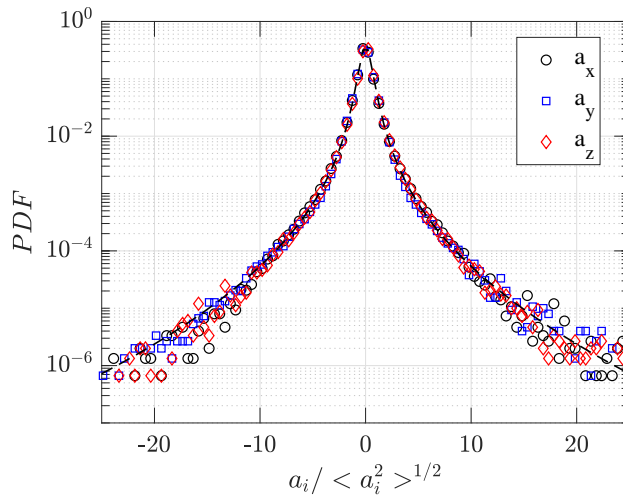


Figure 4.21: PDFs of the three components of acceleration components normalized by rms. The solid line represents a stretched exponential form given by Voth *et al.* (2002).

$$P(a) = C \exp(-a^2 / ((1 + |a\beta/\sigma|^\gamma)\sigma^2)), \quad (4.7)$$

where $\beta = 0.539$, $\gamma = 1.588$, and $\sigma = 0.508$ (Voth *et al.* (2002)). When compared to the transverse components, the PDF of the axial component deviates from the PDF function given by Voth *et al.* (2002) for a counter rotating impeller flow. Even though the PDFs of all the three components collapse until a width of $10a_{rms}$, the acceleration components are also not isotropic as the ratio of rms of axial component a_y to transverse components a_x is approximately 1.3. The intermittency in the acceleration components is studied in the next section.

4.6.5 Acceleration intermittency

Studying the flatness of the probability distributions of acceleration shown in figure 4.21 would be an effective way to measure of the extreme events relative to the events close to the mean. The flatness value given by $F_i = \frac{\langle a_i^4 \rangle}{\langle a_i^2 \rangle^2}$ is reported to be in the range of 23 to 30 by Mercado *et al.* (2012) showing increasing trend with increasing Re_λ as reported by Voth *et al.* (2002). The flatness value obtained by Mordant *et al.* (2004) was 55 ± 8 at $Re_\lambda = 690$.

The flatness value F_i obtained in the current study is shown in the table 4.4. The flatness values obtained from fourth-order moments of the transverse acceleration components show good agreement with those reported by Voth *et al.* (2002), Mordant *et al.* (2004) and Mercado *et al.* (2012), but the extreme intermittency in the acceleration along the axial direction is clearly seen in the high flatness value. The skewness of all three acceleration components was close to zero, showing their symmetry.

Table 4.4: Flatness value from the experiment.

F_x	F_y	F_z
67	60	71

Since the transverse component acceleration PDFs match with the expected PDF in a von Karman flow, the relative contribution to the second ($a_i^2 P(a_i) / \langle a_i^2 \rangle$) and fourth moments ($a_i^4 P(a_i) / \langle a_i^4 \rangle$) of these acceleration components is shown in figure 4.22. The area under these curves gives the fourth moment, and the scatter is often used to determine the level of convergence of the moment. The fourth moment shows a better convergence when compared to the results from Beck (2001) and Voth *et al.* (2002), with tracer particles in a von Karman flow.

To show the convergence of second and fourth moments, the positive part of the PDFs of the second and fourth moments of acceleration shown in figure 4.22 for all three components is shown in figure 4.23. One can derive an equation for the acceleration moments from the fit 4.7. This is plotted against the present data on figure 4.23 and

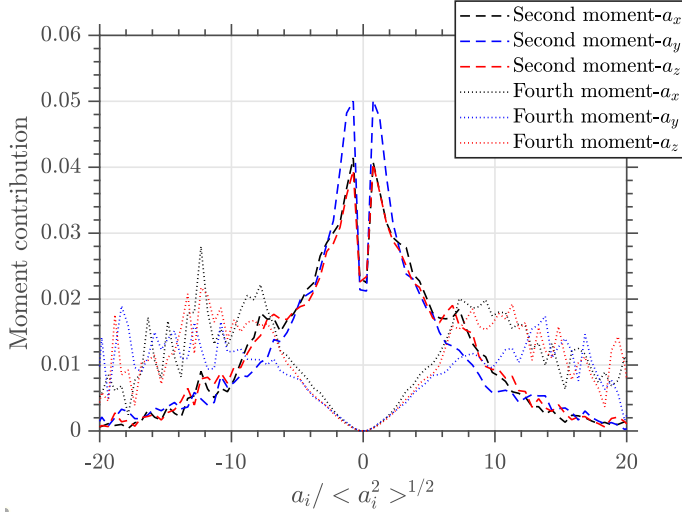


Figure 4.22: The relative contribution to the second ($a_x^2 P(a_x) / \langle a_x^2 \rangle$) and fourth moments ($a_x^4 P(a_x) / \langle a_x^4 \rangle$) of the acceleration components.

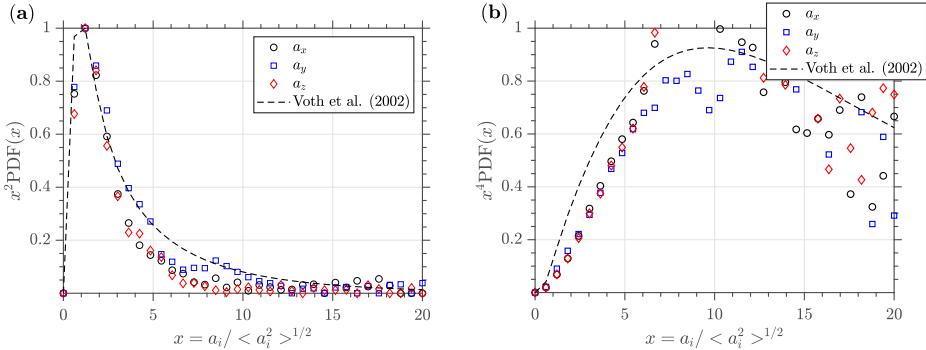


Figure 4.23: Contributions to the (a) second ($a_x^2 P(a_x) / \langle a_x^2 \rangle$) and (b) fourth moments ($a_x^4 P(a_x) / \langle a_x^4 \rangle$) of the acceleration components.

reasonable agreement is found. The fourth moment shows a very good convergence up to $10a_{rms}$ beyond which it starts to diverge somewhat, nevertheless following the stretched exponential trend.

4.7 Particle size

The accuracy of the obtained particle tracks and the extra information of scattered intensity corresponding to the center of the Gaussian sheet of individual particles can be now used to measure the size of the individual particles as previously shown in Chapter 3. Two different mean sizes of polystyrene particles are used in the experiment; TS-80 Microbeads

AS and TS-40 Microbeads AS, with batch numbers, 3I-080-1771 and 2B-040-1518, with mean diameters of $80\mu\text{m}$ and $40\mu\text{m}$ respectively. The density of the particles is 1.05kg/L .

For the sizing routine, the MATLAB program as discussed in section 2.3.7, was used to generate tables of scattering intensities over relevant ranges of angles and size parameters in increments of 0.001 degrees and 0.12 respectively. In the fitting procedure, a higher prediction interval of 97% was chosen such that the least-squares of difference between the data and the fit (χ^2) was below a certain value. In this study particle sizes obtained by setting three values of least squares of difference of 0.09, 0.05 and 0.01 corresponding to a difference between the fit and the data of 0.3, 0.2 and 0.1 was compared. Figure 4.24 shows an example of a typical fitting routine applied on particle scattering intensity data for a single particle from the three cameras. The measured intensities along the tracks for all the three cameras are obtained following the methodology discussed in section 2.3.3. Both the measured scattering intensity and the scattering intensity in the Mie fit are normalized by the respective highest scattering intensity along the track for the three cameras.

On average, a track length $tr_l = 1\tau_\eta$ provides a scattering angle range ($\Delta\theta_m$) of 2° . For a $80\mu\text{m}$ polystyrene particle the average half distance between two fringes in terms of scattering angle is 2.5° . Hence selecting all tracks with $tr_l > 1\tau_\eta$ will satisfy our condition that scattered intensity over at least half the fringe distance ($\Delta\theta/2$) is measured over the length of the track. For the $40\mu\text{m}$ particle case, the average fringe distance is slightly greater than 5° , hence $tr_l > 2\tau_\eta$ had to be selected, which also reduces the number of samples.

4.7.1 Results from two camera combinations

The experiment was performed using three cameras. The fitting procedure for particle sizing can be done with intensities only from one camera. But since at least two cameras are required for tracking we will now look systematically at how results look with the minimum of two cameras and evaluate the improvement/advantage of using three cameras. For the two-camera setup, stricter conditions of

1. Sizes obtained using individual cameras should match.
2. The least-squares difference between the data and the fit should be below 0.05.
3. The size obtained by fitting a curve over the combination of data from both the cameras should match the one obtained using individual cameras.

Cameras 1 and 2 are separated by an angle of 2° , which means the combination of the measured scattering angles from both the cameras is approximately continuous. Figure 4.25(a) and (b) shows an example of the data fit from the two-particle sizes considered

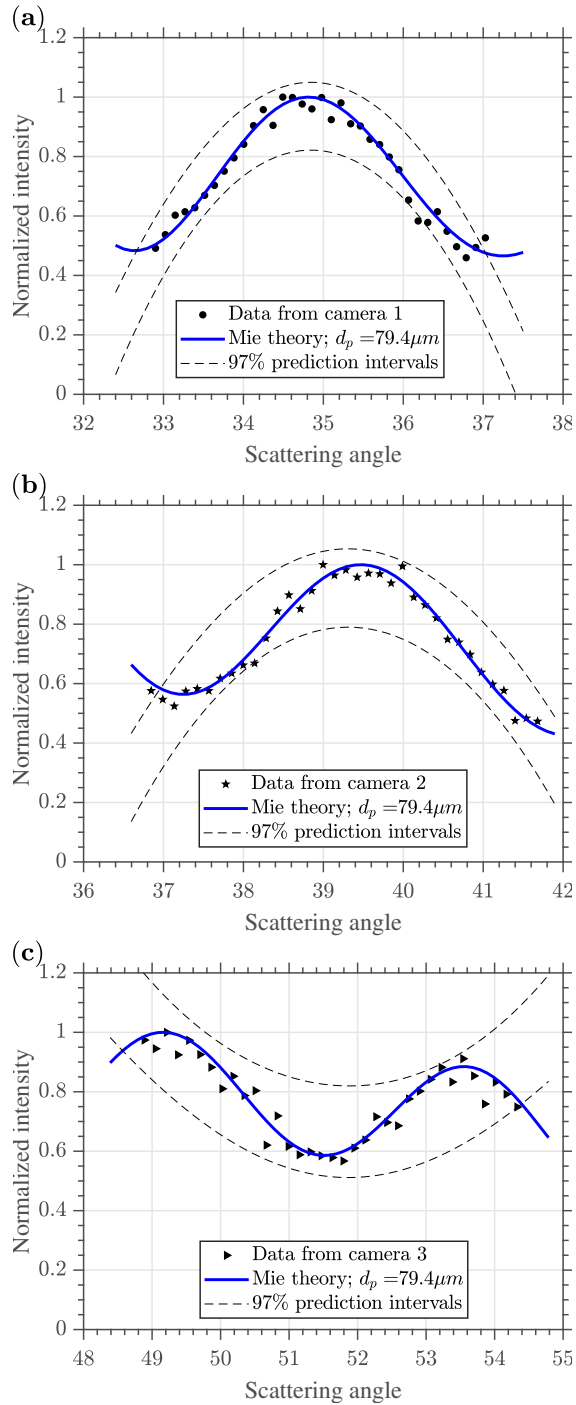


Figure 4.24: Example of best Mie fit for a particle intensity variation over the scattered angle obtained from the three cameras views.

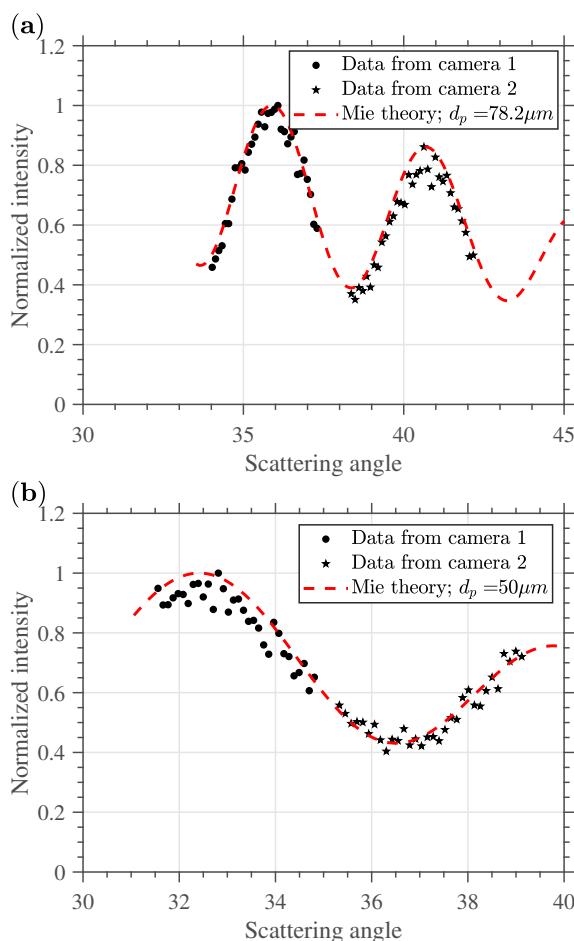


Figure 4.25: Sample scattering intensity data and best Mie fits over the scattering intensity from camera 1 and camera 2 for a particle from (a) particles with nominal mean diameter of $80\mu\text{m}$ and (b) particles with nominal mean diameter of $40\mu\text{m}$.

in this study. Cameras 2 and 3 are separated by an angle of 14° . Figure 4.26(a) and (b) shows an example of the fit of the same particles considered in figure 4.25. Cameras 1 and 3 are separated by an angle of 16° . Figure 4.27(a) and (b) shows the example fit from this case.

Figures 4.28(a)-(b) shows the pdfs of size distributions obtained from the three combinations (1&2, 2&3 and 1&3 respectively) for the first batch of particles with a nominal mean diameter of $80\mu\text{m}$ compared to the expected size distribution from the manufacturer, Microbeads AS. Similarly figure 4.29(a)-(b) shows the pdfs of size distributions obtained from the three combinations for the second batch of particles with a nominal mean diameter of $40\mu\text{m}$. The total number of particles sized for the particles with the nominal size $80\mu\text{m}$ are approximately 350000 and 120000 for the particles with a nominal size of $40\mu\text{m}$. The

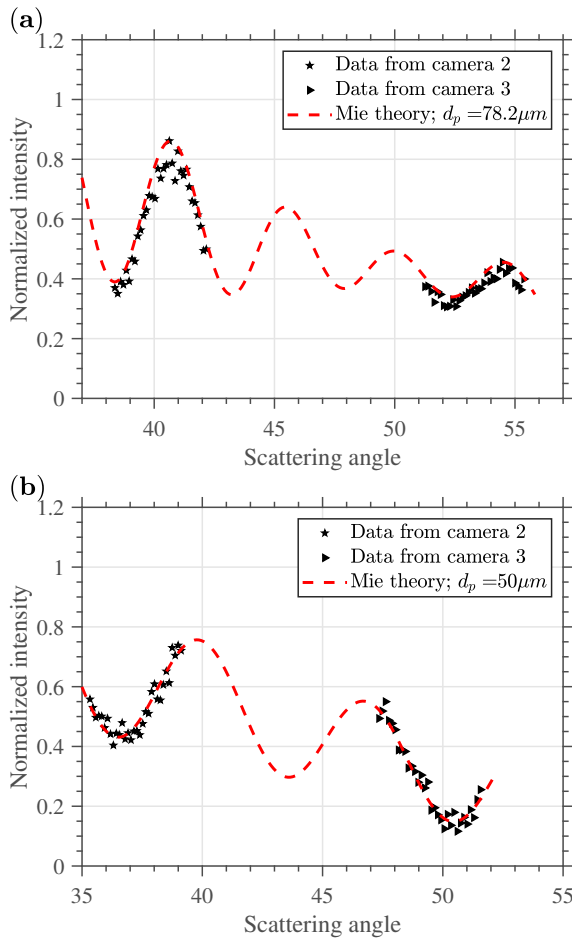


Figure 4.26: Example representing the of scattering intensity data and best Mie fits over the scattering intensity from camera 2 and camera 3 for a particle from (a) particles with nominal mean diameter of $80\mu\text{m}$ and (b) particles with nominal mean diameter of $40\mu\text{m}$.

camera combination 1&2 gave the highest percentage of acceptable fits according to the chosen conditions.

The measured SMD on the other hand is the same for all three combinations, but the percentage of particles successfully sized as shown in table 4.7 is lower when using a two-camera combination involving camera 3. Camera 3 is placed at an angle of approximately 45 degrees from the plane of the laser sheet. The intensities from camera 3 are hence weaker compared to that from camera 1 and 2. As a result of this, the chances of particles not detected from the third view is high compared to the first and the second view. Hence in many cases intensity variations (data points) along a track from camera 3 are lower compared to those on camera 1 and 2. To remind, the particles which are not triangulated using three cameras were triangulated using two camera triangulation technique.

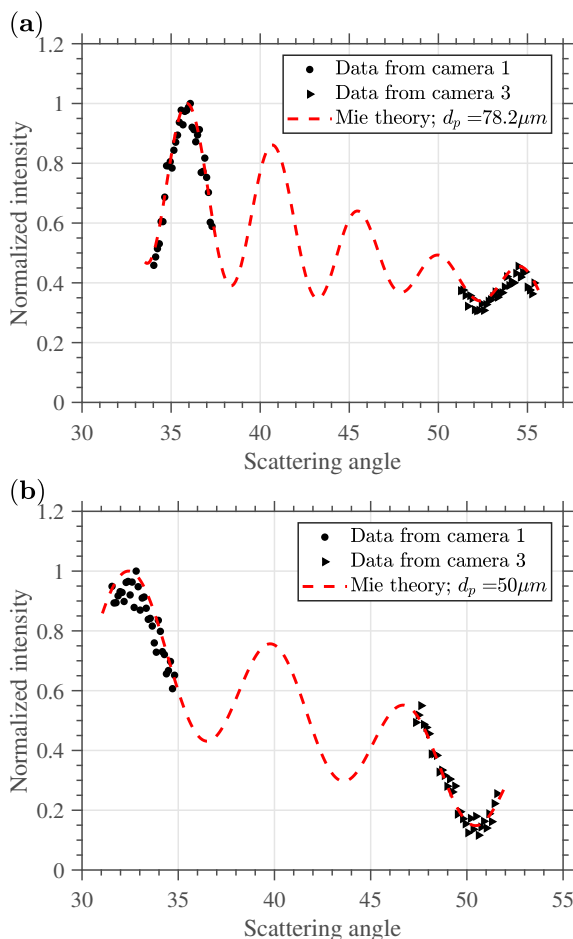


Figure 4.27: Example representing the of scattering intensity data and best Mie fits over the scattering intensity from camera 1 and camera 3 for a particle from **(a)** particles with nominal mean diameter of $80\mu\text{m}$ and **(b)** particles with nominal mean diameter of $40\mu\text{m}$.

In the figures 4.30, the respective particle is tracked or linked in time 35 times successfully. But since the particle intensity was not detected in the third camera view at the 20th time step, only the first 19 of the 35 intensity data from camera 3 could be used to fit the data. This becomes a major hindrance in measuring the particle size successfully when using only two camera combination especially when the track length is shorter and the data point in one of the view is drastically low compared to that from the other view. As the data points decrease the chances of mismatch in the fit is high. To show this, in figure 4.30(a) to (b) Mie fits from two-particle sizes close to the expected particle size is also plotted. In the case of two camera combination, the data from camera 3 individually fits well with Mie fit from the particle with size $81.4\mu\text{m}$, whereas the data from camera 1 and camera 2 when plotted individually matches with the fit from the particle with size

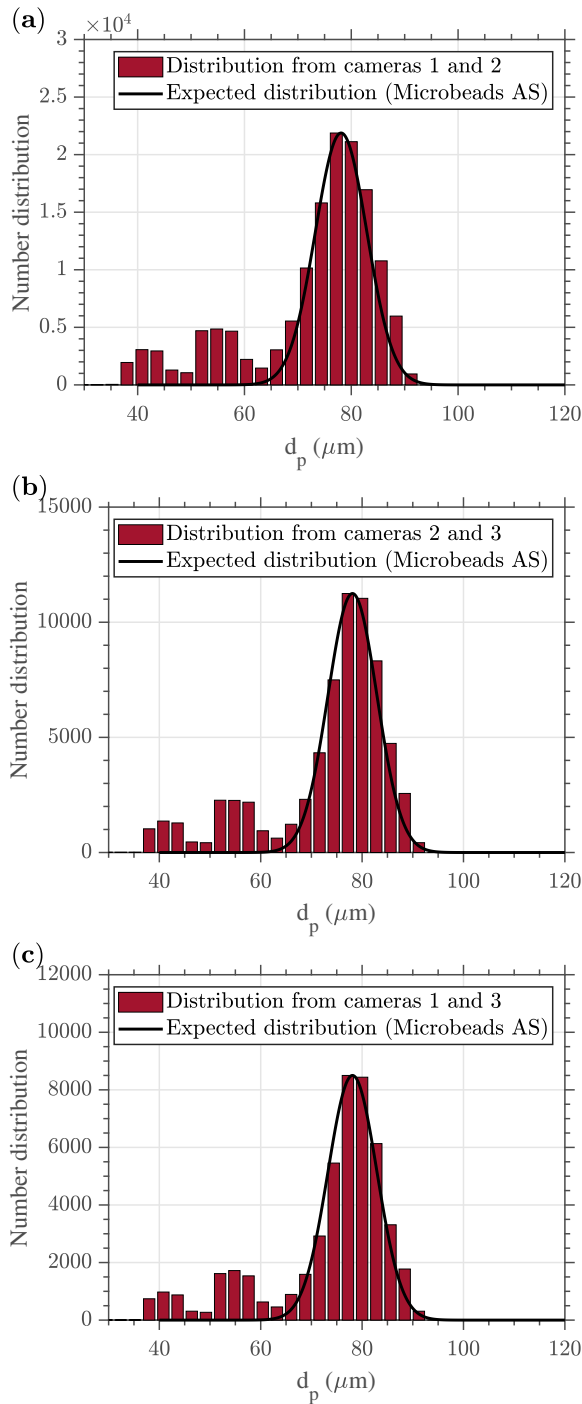


Figure 4.28: Number distribution and the corresponding SMD determined using the scanning technique, compared to the distribution obtained by the manufacturer (Microbeads AS), using the Coulter principle, for the first batch of particles with nominal mean diameter of $80 \mu\text{m}$ with a least squares difference of 0.09 for the three two-camera combinations (a) 1&2 (b) 2&3 and (c) 1&3.

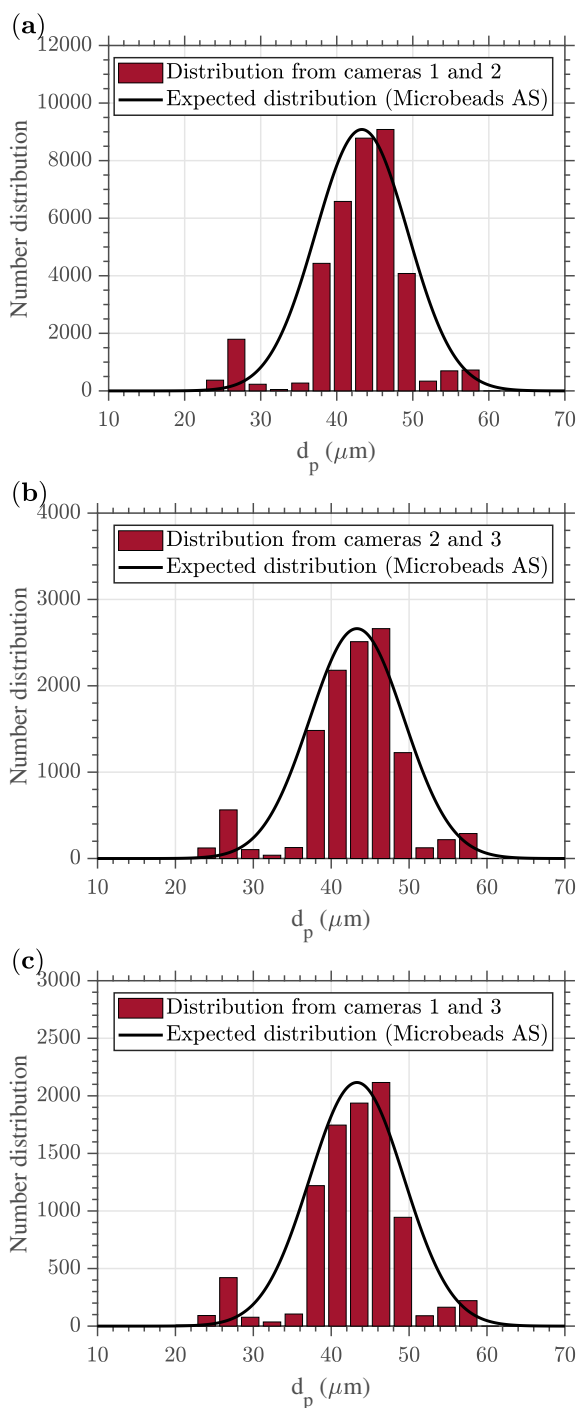


Figure 4.29: Number distribution and the corresponding SMD determined using the scanning technique, compared to the distribution obtained by the manufacturer (Microbeads AS), using the Coulter principle, for the first batch of particles with nominal mean diameter of $40\mu\text{m}$ with a least squares difference of 0.09 for the three two-camera combinations (a) 1&2 (b) 2&3 and (c) 1&3.

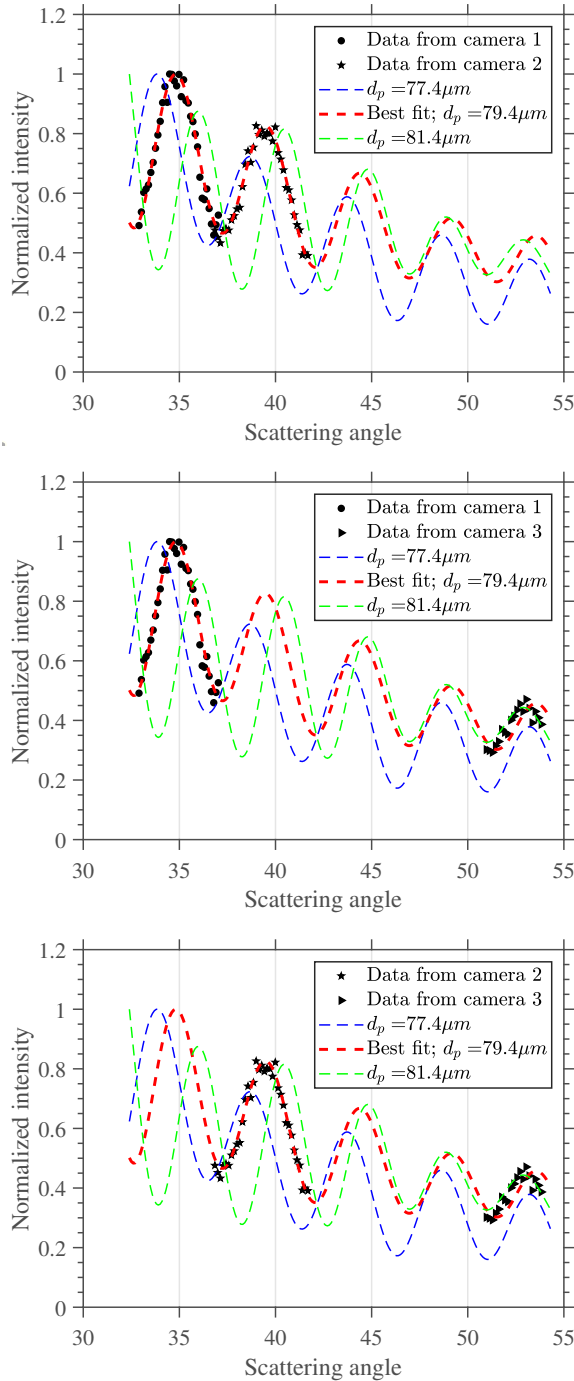


Figure 4.30: Comparison fit from three particle sizes over the intensity data distribution from three two camera combinations; **(a)** Camera 1 and 2 **(b)** Camera 2 and 3 **(c)** Camera 2 and 3. In all the plots, the fit from particle shown in red is the real fit.

Experimental Results

Table 4.5: Comparison of particle size measurement for the three combinations using two different least squares difference tolerance (χ^2).

Camera combination	80 μm		40 μm	
	% accepted	SMD	% accepted	SMD
1&2	46.76	78	24.5	45.8
2&3	22.17	78.1	7.6	45.8
1&3	16.17	78.2	6.1	45.8

79.4 μm . But when the data from camera 3 is combined with the data from camera 1 or camera 2, the best fit with the least-squares is obtained for the size 79.4, hence the size is accepted.

4.7.2 Results from all three camera combination

Figure 4.31 shows some typical examples of particle tracks for the first batch of particles with a nominal size of 80 μm , with different track lengths and the corresponding scattered intensity from the three different views plotted on a single axis, with the obtained best Mie fit plotted over the range of scattering angles obtained from the three views. Here the intensities are normalized by the highest intensity across the three views. Three different track lengths 1.5 τ_η , 2.5 τ_η and 3.5 τ_η have been chosen to represent the fitting on this batch of particles.

For this batch from the ensemble over the 8-time series measurements, a total of approximately 350000 particles are available. Figure 4.34(a)-(c) shows a comparison of the particle size distribution obtained by setting the three least-squares difference tolerance of 0.09, 0.05 and 0.01 respectively. The fraction of particle sizes accepted along with the measured mean particle sizes in terms of arithmetic means (D_{10}), SMD and volumetric mean (D_{30}) is given in table 4.6. Figures 4.34(a)-(c) and table 4.6 clearly shows both the shape of the distribution and the measured mean diameter are largely insensitive to the tolerance used except the fact that a considerably high percentage of samples are lost by tightening the χ^2 tolerance. The small peak towards the left tail of the distribution is seen in all three distributions in figures 4.34, which could be due to the presence of real particles of those sizes in the measurement tank or could be due to the effect of shorter tracks as discussed in the section 4.7.1. to check this the effect of different track lengths on this small peak is studied.

4.7.3 Effect of track length on sizing

to check if the second peak seen in the size distribution of the particles with nominal diameter 80, the effect of different track lengths on the measured size distribution is studied.

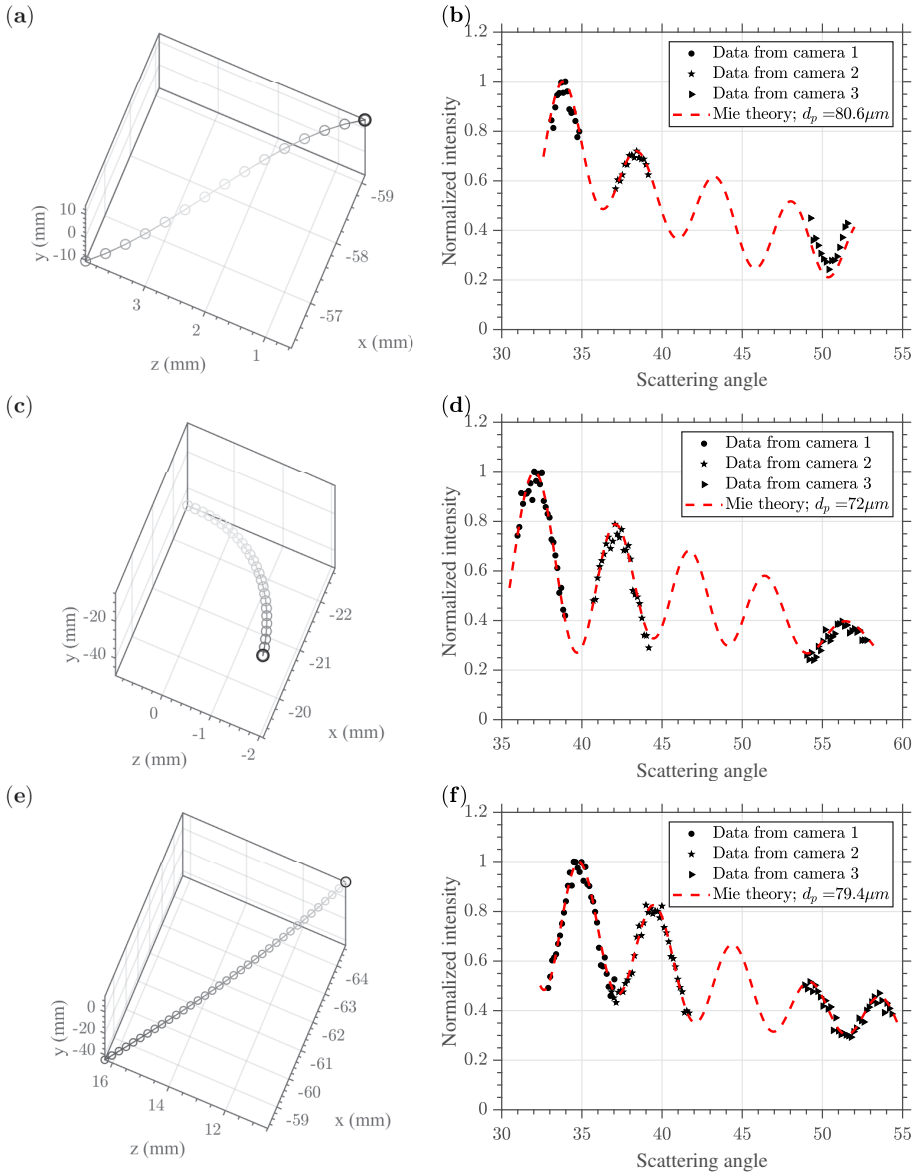


Figure 4.31: Examples of particle tracks and corresponding best Mie fits over the scattering intensity to estimate the particle size for the batch number 3I-080-1771 particles, from three track lengths of (a)-(b) $1.5\tau_\eta$; (c)-(d) $2.5\tau_\eta$ and (e)-(f) $3.5\tau_\eta$.

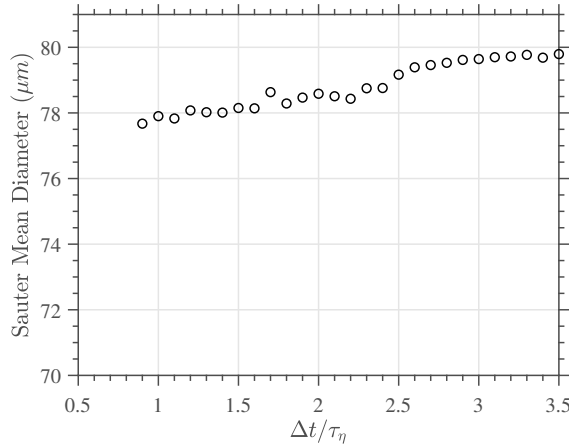


Figure 4.32: Sauter mean diameter obtained using particle size measurements from increasing track lengths.

Figure 4.33 shows the Sauter mean diameters obtained from the measured particle sizes for different track lengths ranging from $1\tau_\eta$ to $3.5\tau_\eta$. The measured SMD varies only gradually though the value is more close to the expected value of $80\mu m$ as the track length increases.

Since the accuracy of measured SMD improves with long tracks, it would be ideal to remove the measurements from shorter tracks, but in the current experiment, the sample size decreases drastically for longer tracks. To show this, the size distributions obtained from three-track length band ranges are shown in figure 4.33. The fraction of the peak count for the second peak to the left seems to be smallest for the middle and the last band, but still present. This shows that the presence of secondary peaks even for longer tracks, which again could be due to unequal data from the third camera, as discussed in the previous section, leading to mismatch or are real particles which got left in the measurement tank from previous experiments.

Table 4.6: Comparison of particle size measurement for the particles with nominal size of $80\mu m$ using different least squares difference tolerance (χ^2).

χ^2	% accepted	D_{10} (μm)	SMD (μm)	D_{30} (μm)
0.09	73.4	74.2	78	76.1
0.05	33.4	75	78.3	76.7
0.01	4	75.5	78.3	77.4

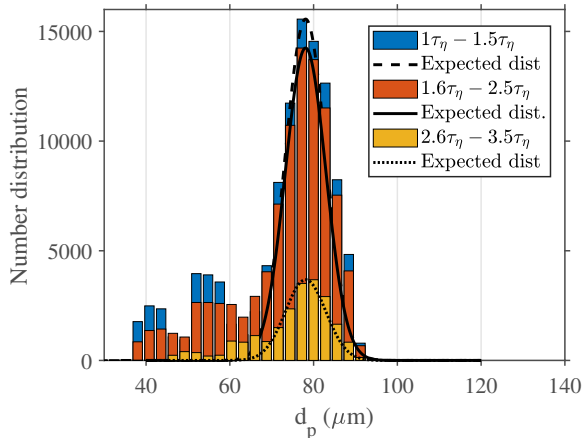


Figure 4.33: Comparison of size distributions from three track length bands.

The results from the scanning measurement technique were directly compared to the measurement results from the manufacturer, Microbeads AS. The size distribution supplied by the manufacturer was measured using Multisizer 3 from Beckman Coulter using the Coulter principle. The measured arithmetic mean (D_{10}) and the standard deviation was $78\mu\text{m}$ and $13.25\mu\text{m}$, respectively. The measurement report provided by the manufacturers consisted of calculation results between $5.6\mu\text{m}$ and $168.0\mu\text{m}$. We obtained the result, using calculations between the size ranges of $20\mu\text{m}$ and $120\mu\text{m}$.

Table 4.7: Comparison of particle size measurement for particles with nominal size of $40\mu\text{m}$ using two different least squares difference tolerance (χ^2).

χ^2	% accepted	D_{10} (μm)	SMD (μm)	D_{30} (μm)
0.09	70.34	44.8	46.1	45.5
0.05	33.75	44.5	45.9	45.2

Figure 4.35 shows examples for two track lengths, for the batch of particles with nominal size $40\mu\text{m}$. From the ensemble over the 8-time series measurements, a total of approximately 120000 particles are sized with a mean percentage deviation of the measured scattered intensity of 11%. Table 4.7 shows a comparison of the size distributions obtained using two χ^2 tolerances of 0.09 and 0.05. The resulting size distribution comparison is presented as a histogram in figure 4.36. The arithmetic mean (D_{10}) and the standard deviation, supplied by the manufacturers' measurement technique was $43.3\mu\text{m}$ and $6.06\mu\text{m}$ respectively. The result was obtained, using calculations between the size ranges of $20\mu\text{m}$ and $60\mu\text{m}$.

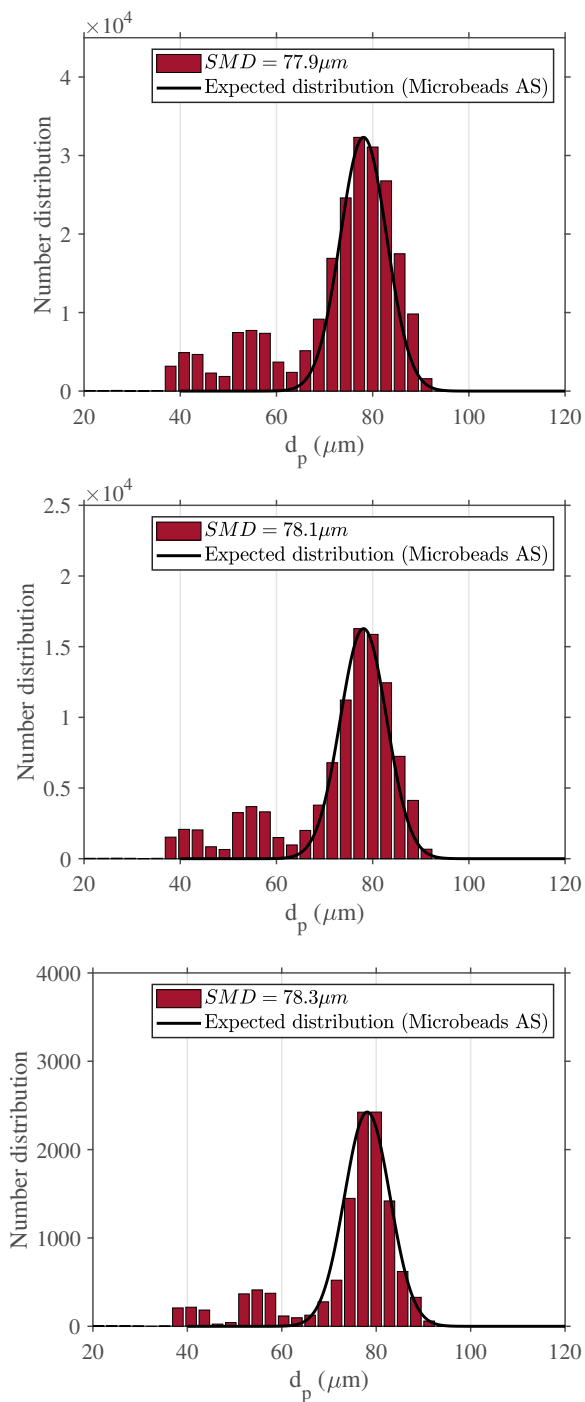


Figure 4.34: Number distribution and the corresponding SMD determined using the scanning technique, compared to the distribution obtained by the manufacturer (Microbeads AS), using the Coulter principle, for the first batch of particles with nominal size of $80\mu\text{m}$ with a least squares difference of **(a)** 0.09 **(b)** 0.05 and **(c)** 0.01.

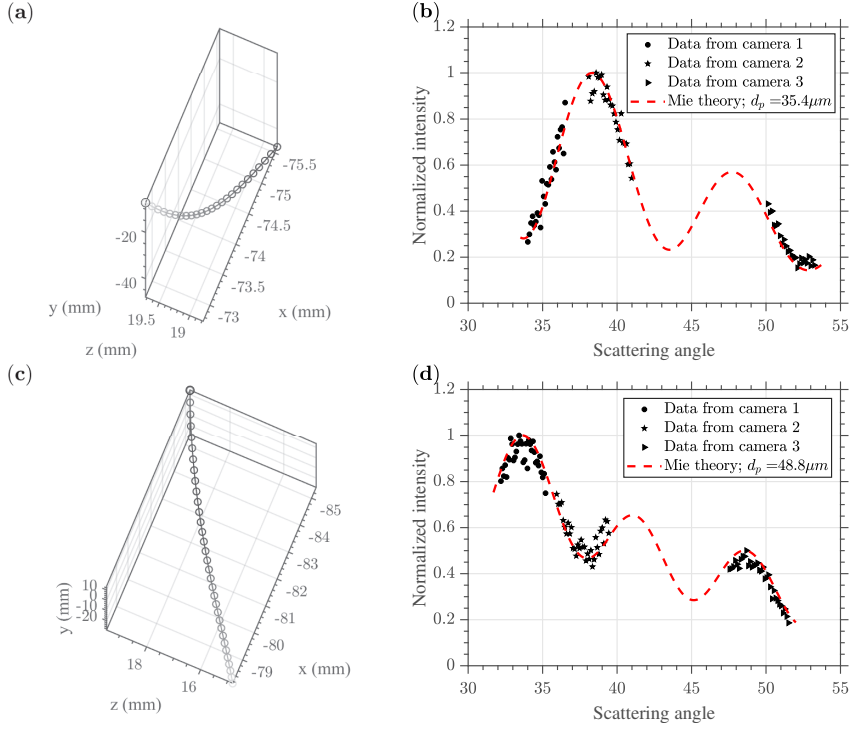


Figure 4.35: Examples of particle tracks and corresponding best Mie fits over the scattering intensity to estimate the particle size for the particles with nominal size of $40\mu\text{m}$, from two track lengths of (a)-(b) $2.5\tau_\eta$ and (c)-(d) $3.5\tau_\eta$.

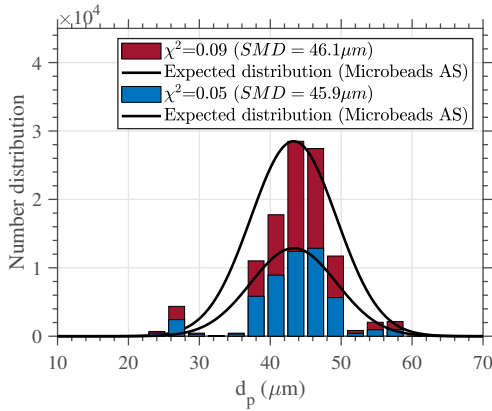


Figure 4.36: The number distribution the corresponding SMD determined using the scanning technique, compared to the distribution obtained by the manufacturer (Microbeads AS), using the Coulter principle, for the second batch of particles with nominal size of $40\mu\text{m}$, obtained using two least squares difference tolerance of 0.09 and 0.05.

To a first approximation, these values obtained from both the batches of particle from the experiment are in agreement with product manufacturers (Microbeads AS), specification. From the results obtained using three-camera combinations, it can be inferred that difference between the expected and measured particle sizes can be reduced considerably by increasing the measured scattering intensity variation data, which requires more camera views. Another way to increase the scattering intensity variation data is to have longer track lengths.

4.7.4 Sizing different sized particles simultaneously

Finally, the third set of experiment was performed where the flow was seeded with both particles with mean diameters $40\mu\text{m}$ and $80\mu\text{m}$. The seeding density in this experiment was slightly lowered compared to the seeding densities used in the previous two experiments. This was done to reduce the overlapping of larger $80\mu\text{m}$ particles on the smaller $40\mu\text{m}$ particles. The mean interparticle distance was approximately 6η . From the ensemble over the 8-time series measurements, a total of approximately 140000 sized particles were accepted with the least-squares tolerance of 0.09. The resulting size distribution comparison is presented as a histogram in figure 4.37. The SMD of the distribution corresponding to the peak in the left side in figure 4.37 was $43.4\mu\text{m}$ and that for the distribution with a peak on the right side was $78.4\mu\text{m}$. The bin size chosen to represent the measured distribution was $2\mu\text{m}$, which is also the measurement accuracy of the accepted sample.

4.8 Summary

A novel tracking and sizing technique based on a scanning laser methodology were demonstrated by taking measurements of a turbulent flow using a three-camera setup. The obtained Lagrangian tracks showed very good accuracy, proved using the joint PDFs of the continuity terms and the acceleration terms. Tracks with track-length greater than $tr_l = 1\tau_\eta$ were used to obtain the Lagrangian statistics, again, but statistic could also be calculated with a subset of tracks that are all the same length. Lagrangian measurements allow the direct measurement of velocity and acceleration in all three dimensions and characterize the flow from the Lagrangian perspective. The skewness and flatness of the velocity fluctuations showed a near to Gaussian value, showing that the measured velocity represents an actual turbulent flow. Joint pdfs of continuity and acceleration terms demonstrated high accuracy in the measurements. Small-scale anisotropy, characterized by the skewness and flatness of acceleration. The acceleration is found to be more intermittent along the tracks when compared to the velocity fluctuations. Profiles of the first through fourth moments of acceleration show significant anisotropy at the centre of the tank.

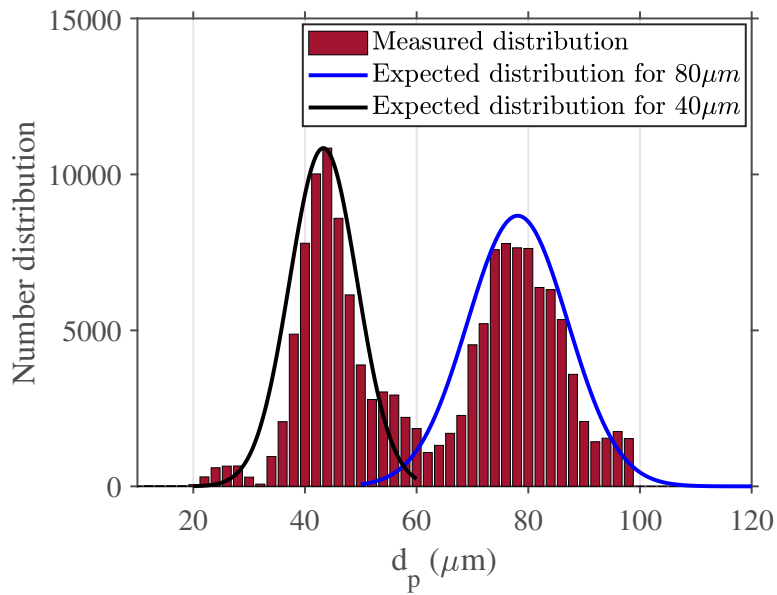


Figure 4.37: Number distribution from sizing two different sizes simultaneously, determined using the scanning technique, compared to the distribution obtained by the manufacturer (Microbeads AS), using the Coulter principle, for particles with nominal size of 40 μm and 80 μm .

Experimental Results

The novel method to measure the sizes of particles in the Mie regime, in a volume has been used to estimate the particle sizes from the deduced particle tracks. Two different nominal sizes of particles were used to test the method. Comparison of size distribution obtained from the measurements to that provided by the manufacturers (Microbeads AS) had a good agreement and showed that the size distribution obtained from the scanning sizing technique can be a useful tool for measurements of particle sizes inflows.

Chapter 5

Summary and conclusions

In this chapter, the main results and conclusions of this thesis are summarized and put into perspective regarding the development of scanning particle tracking and sizing.

5.1 Scanning particle tracking

A new variant for Lagrangian particle tracking technique based on a scanning laser technique has been introduced, tested and applied to a laboratory experiment. The technique is aimed at performing Lagrangian particle tracking at higher seeding densities. The main contribution of the present work is to improve the particle triangulation efficacy at higher seeding densities. The use of a fitted sheet space number, which serves to further restrict the particle search depth in the scanning direction. The new method accurately triangulates a large fraction of true particle locations for very high particle densities, up to an equivalent particle image density, where typical volumetric triangulation typically suffers from large fractions of falsely detected particles when the seeding density increases.

A parametric study identified optimal parameters for the scanning tracking measurements. The important control parameters are divided into controllable parameters like seeding density, the number of cameras, laser sheet thickness, sheet spacing and scan speed; uncontrollable parameters included noise level and deviation from the Gaussian profile of the laser. The technique can be measured with two cameras but the use of more than two cameras seems to improve the fraction of successfully triangulated particles even at the highest seeding density, thereby increasing aiding better particle tracking. The optimal sheet thickness is about one-twelfth the total scan depth and five times the sheet spacing. The fraction of successfully triangulated particles remains high in the presence of mild to moderate noise, and particle movement during the scan for finite scanning laser sheet speeds can be corrected if the sheet speed is at least two orders of magnitude larger than the characteristic velocity scale of the flow.

The technique was tested via synthetic experiments using a DNS database, mimicking the conditions of a previous scanning setup, for which the Lagrangian velocities and accelerations are calculated. Spatial resolution was demonstrated by a very good correlation of the Lagrangian acceleration with the local and convective accelerations. An inherent upper limit on the magnitude of accelerations measurable was found for very dense fields using the current tracking algorithm due to a reduced mean inter-particle distance. To avoid ambiguity when forming particle tracks, the more dense a particle field is, the smaller the permissible search radius about a particle's predicted location at a subsequent time step. A more advanced particle tracking algorithm could possibly permit larger accelerations to be detected at higher densities.

There are many questions regarding how Lagrangian statistics results apply to inhomogeneous turbulence. This thesis has presented Lagrangian statistics in an Ekman pumping flow obtained from moderately high seeding density experimental measurements. These measurements have allowed the investigation of single-particle, three-component Lagrangian statistics in position, velocity, and acceleration. The measurements from this central domain which is highly sheared, anisotropic and inhomogeneous, has allowed us to quantify how the Lagrangian statistics in the flow deviates from their expected values in homogeneous isotropic turbulence.

5.2 Scanning particle sizing

A novel method to measure the sizes of particles in the Mie regime, in a volume has been introduced. By using a scanning technique, existing problems in laser sheet based particle sizing, termed as "trajectory effect", was completely removed. Other concerns, such as limitations in particle concentration, blurring effect and overlapping particles were also tackled to an extent. In combination with the scanning particle tracking technique Kozul *et al.* (2019), the technique provides the position, velocity, acceleration and size/mass of the particles with high accuracy.

The measurement technique and experimental design consideration such as the measurement area, camera angle, measurable size ranges, camera aperture and the number of cameras have been discussed. The scanning sizing technique was applied to synthetic data, with known sizes, to demonstrate the ability of the technique to retrieve the particle sizes accurately. The addition of noise did not reduce the accuracy of the sizing technique drastically. 2% background Gaussian noise or Poisson noise produced results in an acceptable RMS error range. Of this, the error increases with decreasing particle size, due to the dominating influence of the noise on their scattered intensity. Whereas, misalignment in the cameras showed an opposite trend, where the error increases for larger particles, due to the mismatch arising due to the increasing scattering patterns. The numerical

assessment shows that serious errors can occur when the signal to noise ratio decreases or when there is a serious calibration error.

Scanning measurements from a three-camera setup from an upwelling flow were used to demonstrate the application of the sizing technique to experimental data. The obtained Lagrangian tracks showed very good accuracy, proved using the joint PDFs of the continuity terms and the acceleration terms. The tracks, with track-length greater than 10, were used to obtain the individual particle sizes.

The scanning sizing technique estimates the particle sizes from the estimated tracks. Comparison with manufacturers (Microbeads AS) measurement results showed that the scanning sizing technique can be a useful tool for measurements of particles/droplet sizes in flows.

5.3 Future Work

The tracking technique used in this work follows the nearest neighbour scheme (Malik *et al.*, 1993). This requires a predictor velocity, which in this work, the cross-correlated velocity field obtained from Scanning PIV (Lawson & Dawson, 2014) was used. The nearest neighbour tracking technique also has an inherent upper limit on the magnitude of the measurable accelerations due to a reduced mean inter-particle distance, at higher seeding densities. The criteria 2 and 3 in the current particle tracking heuristics could bias the result by avoiding large/intermittent accelerations. Increasing the search radius was an option to include intermittent acceleration events, but with increasing search radius the possibility of mismatch and hence erroneous tracks increases proportionally. An alternative would be, improving the particle tracking algorithm, which could also be a future scope of this current study. One such alternative to the 2 current tracking heuristic (a small modification to criteria 2) has been added to appendix C. The modification is: instead of choosing the candidate particle with minimum acceleration in step 2, all possible candidates within the search radius in step 2 are now projected forward in time. In the next step, among all candidates, the candidate nearest to the respective predicted location is chosen as the correct link. This procedure now avoids the condition of minimum acceleration. Modifying the current tracking algorithm with a more advanced particle tracking algorithm such as 'Shake the Box' (Schanz *et al.*, 2016) could also possibly permit larger accelerations to be detected at higher densities.

The particle sizing algorithm currently works only for particles that are assumed to be spherical in shape. In future works, efforts can be put into developing the current technique to measure non-spherical particles using the Mie theory (Bohren & Huffman, 1983) for non-spherical particles.

5.4 Prospectives

The development of an efficient algorithm to simultaneously measure the velocity and size of individual particles in a flow based on the scanning technique by Lawson (2015) can play an important role in understanding and predicting the response of particles in a turbulent flow. The study of Lagrangian turbulence and of turbulent transport of material particles has received growing interest in recent years (Toschi Bodenschatz 2009). However, in many situations, the size of the particles is not small with respect to turbulence scales, in particular the dissipative scale. One example is the plankton which, while neutrally buoyant, cannot be considered as a tracer because of its size in the order of few dissipative scales (Calzavarini *et al.*, 2009). When finite-sized or heavy particles interact with turbulent flows both large scale and small turbulent eddies can contribute to particle dispersion, depending on the local Stokes number (Bachalo (1994)). These interactions can cause particle clustering and segregation, which can alter the turbulent characteristics of the continuous medium in which they are immersed. This variation in the flow characteristics is higher for poly-disperse particle size distribution as compared to mono-disperse case (Sommerfeld (1990)).

The overall development of the current technique to measure the size and velocity of particles will benefit the future research of particle interactions in turbulent flows. In this context, the experimental technique proposed in this thesis assumes particular relevance.

References

- ADRIAN, R. J. 1991. Particle-imaging techniques for experimental fluid mechanics. *Annual Review of Fluid Mechanics*, **23**, 261–304.
- AGUI, J. C. AND JIMENEZ, J. 1987. On the performance of particle tracking. *Journal of Fluid Mechanics*, **185**, 447–468.
- BACHALO, W. D. 1994. Experimental methods in multiphase flows. *International Journal of Multiphase Flow*, **20**, 261 – 295.
- BACHALO, W. D. AND HOUSER, M. J. 1984. Phase/doppler spray analyzer for simultaneous measurements of drop size and velocity distributions. *Optical Engineering*, **23**, 583 – 590 – 8.
- BARTH, H. G. AND FLIPPEN, R. B. 1995. Particle size analysis. *Analytical Chemistry*, **67**, 257–272.
- BECK, C. 2001. On the small-scale statistics of lagrangian turbulence. *Physics Letters A*, **287**, 240 – 244.
- BLACK, D. L., MCQUAY, M. Q. AND BONIN, M. P. 1996. Laser-based techniques for particle-size measurement: A review of sizing methods and their industrial applications. *Progress in Energy and Combustion Science*, **22**, 267 – 306.
- BOHREN, C. R. AND HUFFMAN, D. R. *Absorption and Scattering of Light by Small Particles*. John Wiley and Sons, Ltd, 1983.
- BRÜCKER, C, HESS, D AND KITZHOFFER, J. 2012. Single-view volumetric PIV via high-resolution scanning, isotropic voxel restructuring and 3d least-squares matching (3d-LSM). *Measurement Science and Technology*, **24**, 024001.
- BRÜCKER, CH. 1995. Digital-particle-image-velocimetry (DPIV) in a scanning light-sheet: 3D starting flow around a short cylinder. *Experiments in Fluids*, **19**, 255–263.
- CALZAVARINI, E., VOLK, R., BOURGOIN, M., LÉVÊQUE, E., PINTON, J. F. AND TOSCHI, F. 2009. Acceleration statistics of finite-sized particles in turbulent flow: the role of faxén forces. *Journal of Fluid Mechanics*, **630**, 179–189.
- CIERPKA, C., LÜTKE, B. AND KÄHLER, C. J. 2013. Higher order multi-frame particle tracking velocimetry. *Experiments in Fluids*, **54**, 1533.
- DAMASCHKE, N., NOBACH, H. AND TROPEA, C. 2002. Optical limits of particle concentration for multi-dimensional particle sizing techniques in fluid mechanics. *Experiments in Fluids*, **32**, 143–152.

References

- DAMASCHKE, NILS, NOBACH, HOLGER, NONN, THOMAS I., SEMIDETNOV, NIKOLAY AND TROPEA, CAMERON. 2005. Multi-dimensional particle sizing techniques. *Experiments in Fluids*, **39**, 336–350.
- DOMANN, R. AND HARDALUPAS, Y. 2001. A study of parameters that influence the accuracy of the planar droplet sizing (pds) technique. *Particle & Particle Systems Characterization*, **18**, 3–11.
- DOMANN, ROLAND AND HARDALUPAS, YANNIS. 2003. Quantitative measurement of planar droplet sauter mean diameter in sprays using planar droplet sizing. *Particle & Particle Systems Characterization*, **20**, 209–218.
- DUMOUCHEL, C., YONGYINGSAKTHAVORN, P. AND COUSIN, J. 2009. Light multiple scattering correction of laser-diffraction spray drop-size distribution measurements. *International Journal of Multiphase Flow*, **35**, 277 – 287.
- ELSSINGA, G. E., SCARANO, F., WIENEKE, B. AND VAN OUDHEUSDEN, B. W. 2006. Tomographic particle image velocimetry. *Experiments in Fluids*, **41**, 933–947.
- FOURNEL, T., LAVEST, J.-M., COUDERT, S. AND COLLANGE, F. Self-calibration of piv video-cameras in scheinpflug condition. In *Particle Image Velocimetry: Recent Improvements*, pages 391–405, 2004.
- GESEMANN, S., HUHNS, F., SCHANZ, D. AND SCHRÖDER, A. From noisy particle tracks to velocity, acceleration and pressure fields using B-splines and penalties. In *18th Int. Symp. on the Application of Laser and Imaging Techniques to Fluid Mechanics, Lisbon, Portugal*, 2016.
- GOUESBET, G. AND BERLEMONT, A. 1999. Eulerian and lagrangian approaches for predicting the behaviour of discrete particles in turbulent flows. *Progress in Energy and Combustion Science*, **25**, 133 – 159. ISSN 0360-1285.
- GRAHAM, J., KANOV, K., YANG, X. I. A., LEE, M., MALAYA, N., LALESCU, C. C., BURNS, R., EYINK, G., SZALAY, A., MOSER, R. D. AND MENEVEAU, C. 2016. A web services accessible database of turbulent channel flow and its use for testing a new integral wall model for les. *Journal of Turbulence*, **17**, 181–215. (doi:10.1080/14685248.2015.1088656)
- GRASSMANN, A. AND PETERS, F. 2004. Size measurement of very small spherical particles by mie scattering imaging (msi). *Particle & Particle Systems Characterization*, **21**, 379–389.
- HARTLEY, R. AND ZISSERMAN, A. *Multiple view geometry in computer vision*. Cambridge University Press, 2003.
- HIRLEMAN, E. DAN AND BOHREN, CRAIG F. 1991. Optical particle sizing: an introduction by the feature editors. *Appl. Opt.*, **30**, 4685–4687.
- HOYER, K., HOLZNER, M., LÜTHI, B., GUALA, M., LIBERZON, A. AND KINZELBACH, W. 2005. 3D scanning particle tracking velocimetry. *Experiments in Fluids*, **39**, 923.
- ISHIHARA, TAKASHI, KANEDA, YUKIO, YOKOKAWA, MITSUO, ITAKURA, KEN'ICHI AND UNO, ATSUYA. 2007. Small-scale statistics in high-resolution direct numerical simulation of turbulence: Reynolds number dependence of one-point velocity gradient statistics. *Journal of Fluid Mechanics*, **592**, 335–366.
- KERKER, M. *The Scattering of Light and Other Electromagnetic Radiation*. Academic Press, Inc., 1969.

- KÖNIG, G., ANDERS, K. AND FROHN, A. 1986. A new light-scattering technique to measure the diameter of periodically generated moving droplets. *Journal of Aerosol Science*, **17**, 157 – 167.
- KNUTSEN, A. N., LAWSON, J. M., DAWSON, J. R. AND WORTH, N. A. 2017. A laser sheet self-calibration method for scanning PIV. *Experiments in Fluids*, **58**, 145.
- KOZUL, M., KOOTHUR, V., WORTH, N. A. AND DAWSON, J. R. 2019. A scanning particle tracking velocimetry technique for high-reynolds number turbulent flows. *Experiments in Fluids*, **60**, 137.
- KUZZAY, D., FARANDA, D. AND DUBRULLE, B. 2015. Global vs local energy dissipation: The energy cycle of the turbulent von kármán flow. *Physics of Fluids*, **27**, 075105.
- LAWSON, J. *A scanning PIV study of homogeneous turbulence at the dissipation scale*. PhD thesis, University of Cambridge, 2015.
- LAWSON, J. M., BODENSCHATZ, E., KNUTSEN, A. N., DAWSON, J. R. AND WORTH, N. A. 2019. Direct assessment of Kolmogorov’s first refined similarity hypothesis. *Physical Review of Fluids*, **4**, 022601.
- LAWSON, J. M. AND DAWSON, J. R. 2014. A scanning PIV method for fine-scale turbulence measurements. *Experiments in Fluids*, **55**, 1857.
- LAWSON, J. M. AND DAWSON, J. R. 2015. On velocity gradient dynamics and turbulent structure. *Journal of Fluid Mechanics*, **780**, 60–98.
- LECORDIER, B. AND WESTERWEEL, J. The EUROPIV synthetic image generator (SIG). In *Particle image velocimetry: recent improvements*, pages 145–161. Springer, 2004.
- LEPERA, S. D. *Development of a Novel Planar Mie Scattering Method for Measurement of Spray Characteristics*. PhD thesis, Virginia Polytechnic Institute and State University, 2012.
- LI, Y., PERLMAN, E., WAN, M., YANG, Y., MENEVEAU, C., BURNS, R., CHEN, S., SZALAY, A. AND EYINK, G. 2008a. A public turbulence database cluster and applications to study Lagrangian evolution of velocity increments in turbulence. *Journal of Turbulence*, **9**, 1–29.
- LI, YI, PERLMAN, ERIC, WAN, MINPING, YANG, YUNKE, MENEVEAU, CHARLES, BURNS, RANDAL, CHEN, SHIYI, SZALAY, ALEXANDER AND EYINK, GREGORY. 2008b. A public turbulence database cluster and applications to study lagrangian evolution of velocity increments in turbulence. *Journal of Turbulence*, **9**, N31. (doi:10.1080/14685240802376389)
- LOUHICHI, H., FOURNEL, T., LAVEST, J. M. AND BEN AISSIA, H. 2007. Self-calibration of scheinpflug cameras: an easy protocol. *Measurement Science and Technology*, **18**, 2616–2622.
- LÜTHI, B., TSINOBER, A. AND KINZELBACH, W. 2005. Lagrangian measurement of vorticity dynamics in turbulent flow. *Journal of Fluid Mechanics*, **528**, 87–118.
- LYNCH, K. P. AND SCARANO, F. 2015. An efficient and accurate approach to MTE-MART for time-resolved tomographic PIV. *Experiments in Fluids*, **56**, 66.
- MAAS, H. G., GRUEN, A. AND PAPANTONIOU, D. 1993. Particle tracking velocimetry in three-dimensional flows. *Experiments in Fluids*, **15**, 133–146.
- MALIK, N. A., DRACOS, T. AND PAPANTONIOU, D. A. 1993. Particle tracking velocimetry in three-dimensional flows. *Experiments in Fluids*, **15**, 279–294.

References

- MAXEY, M. R. AND RILEY, J. J. 1983. Equation of motion for a small rigid sphere in a nonuniform flow. *The Physics of Fluids*, **26**, 883–889.
- MERCADO, J. M., PRAKASH, V. N., TAGAWA, Y., SUN, C., LOHSE, D. AND FOR TURBULENCE RESEARCH), (INTERNATIONAL COLLABORATION. 2012. Lagrangian statistics of light particles in turbulence. *Physics of fluids*, **24**, 055106.
- MORDANT, N., CRAWFORD, A. M. AND BODENSCHATZ, E. 2004. Three-dimensional structure of the lagrangian acceleration in turbulent flows. *Physical review letters*, **93**, 214501.
- MOUNAÏM-ROUSSELLE, C. AND PAJOT, O. 1999. Droplet sizing by mie scattering interferometry in a spark ignition engine. *Particle & Particle Systems Characterization*, **16**, 160–168.
- MULLIN, JOHN A AND DAHM, WERNER JA. 2006. Dual-plane stereo particle image velocimetry measurements of velocity gradient tensor fields in turbulent shear flow. i. accuracy assessments. *Physics of Fluids*, **18**, 035101.
- NICKOLAS, S., IGNACIO, P. J., LAURE, V., IVANA, V. AND NICOLAS, M. 2017. Lagrangian acceleration statistics in a turbulent channel flow. *Physical Review Fluids*, **2**. ISSN 2469-990X. (doi:10.1103/physrevfluids.2.054602)
- NISHINO, K., KASAGI, N. AND HIRATA, M. 1989. Three-dimensional particle tracking velocimetry based on automated digital image processing. *Trans ASME J Fluid Eng*, **111**, 384–391.
- NOVARA, M. AND SCARANO, F. 2013. A particle-tracking approach for accurate material derivative measurements with tomographic PIV. *Experiments in Fluids*, **54**, 1584.
- OUELLETTE, N. T., XU, H. AND BODENSCHATZ, E. 2006. A quantitative study of three-dimensional lagrangian particle tracking algorithms. *Experiments in Fluids*, **40**, 301–313.
- PEREIRA, F., STÜER, H., GRAFF, E. C. AND GHARIB, M. 2006. Two-frame 3d particle tracking. *Measurement Science and Technology*, **17**, 1680–1692.
- PONCET, S., SCHIESTEL, R. AND MONCHAUX, R. 2008. Turbulence modeling of the von kármán flow: viscous and inertial stirrings. *International Journal of Heat and Fluid Flow*, **29**, 62–74.
- PORTA, A. LA, VOTH, G. A., CRAWFORD, A. M., ALEXANDER, J. AND BODENSCHATZ, E. 2001. Fluid particle accelerations in fully developed turbulence. *Nature*, **409**.
- QURESHI, N. M., ARRIETA, U., BAUDET, C., CARTELLIER, A., GAGNE, Y. AND BOURGOIN, M. 2008. Acceleration statistics of inertial particles in turbulent flow. *The European Physical Journal B*, **66**, 531–536.
- RAFFEL, M., WILLERT, C. E., SCARANO, F., KÄHLER, C. J., WERELEY, S. T. AND KOMPENHANS, J. *Particle image velocimetry: a practical guide*. Springer, 2018.
- SANKAR, S. V., IBRAHIM, K. M. AND BACHALO, W. D. 1994. Coherent scattering by multiple particles in phase doppler interferometry. *Particle & Particle Systems Characterization*, **11**, 35–42.
- SATO, Y. AND YAMAMOTO, K. 1987. Lagrangian measurement of fluid-particle motion in an isotropic turbulent field. *Journal of Fluid Mechanics*, **175**, 183–199.

- SCHANZ, D., GESEMANN, S. AND SCHRÖDER, A. 2016. Shake-The-Box: Lagrangian particle tracking at high particle image densities. *Experiments in Fluids*, **57**, 70.
- SCHANZ, D., GESEMANN, S., SCHRÖDER, A., WIENEKE, B AND NOVARA, M. 2013. Non-uniform optical transfer functions in particle imaging: calibration and application to tomographic reconstruction. *Measurement Science and Technology*, **24**, 024009.
- SCHARNOWSKI, S. AND KÄHLER, C. J. 2016. Estimation and optimization of loss-of-pair uncertainties based on PIV correlation functions. *Experiments in Fluids*, **57**, 23.
- SCHNEIDERS, J. F. G. AND SCARANO, F. 2016. Dense velocity reconstruction from tomographic PTV with material derivatives. *Experiments in Fluids*, **57**, 139.
- SCHRÖDER, A., GEISLER, R., ELSINGA, G. E., SCARANO, F. AND DIERKSHEIDE, U. 2008. Investigation of a turbulent spot and a tripped turbulent boundary layer flow using time-resolved tomographic piv. *Experiments in Fluids*, **44**, 305–316.
- SHTILMAN, L., SPECTOR, M. AND TSINOBER, A. 1993. On some kinematic versus dynamic properties of homogeneous turbulence. *Journal of Fluid Mechanics*, **247**, 65–77.
- SOLOFF, S. M., ADRIAN, R. J. AND LIU, Z. C. 1997. Distortion compensation for generalized stereoscopic particle image velocimetry. *Measurement Science and Technology*, **8**, 1441–1454.
- SOMMERFELD, MARTIN. 1990. Particle dispersion in turbulent flow: The effect of particle size distribution. *Particle & Particle Systems Characterization*, **7**, 209–220.
- SOODT, T., SCHRÖDER, F., KLAAS, M., VAN OVERBRÜGGEN, T. AND SCHRÖDER, W. 2012. Experimental investigation of the transitional bronchial velocity distribution using stereo scanning piv. *Experiments in Fluids*, **52**, 709–718.
- TAYALI, N. E. AND BATES, C. J. 1990. Particle sizing techniques in multiphase flows: A review. *Flow Measurement and Instrumentation*, **1**, 77 – 105.
- TOSHIO, H. AND JUN, S. 2004. High-speed scanning stereoscopic PIV for 3d vorticity measurement in liquids. *Measurement Science and Technology*, **15**, 1067–1078.
- TRIGGS, B., MCLAUCHLAN, P., HARTLEY, R. AND FITZGIBBON, A. Bundle adjustment – a modern synthesis. In *Vision Algorithms: Theory and Practice*, LNCS, pages 298–375. Springer Verlag, 2000.
- TROPEA, C. 2011. Optical particle characterization in flows. *Annual Review of Fluid Mechanics*, **43**, 399–426.
- TROPEA, C., XU, T. H., ONOFRI, F., GÉHAN, G., HAUGEN, P. AND STIEGLMEIER, M. 1996. Dual-mode phase-doppler anemometer. *Particle & Particle Systems Characterization*, **13**, 165–170.
- TSAI, R. 1987. A versatile camera calibration technique for high-accuracy 3d machine vision metrology using off-the-shelf tv cameras and lenses. *IEEE Journal on Robotics and Automation*, **3**, 323–344.
- TSINOBER, A. *An informal conceptual introduction to turbulence*, volume 483. Springer, 2009.
- VAN DE HULST, H. C. *Light scattering by small particles*. Dover Publications, Inc., 1981.

References

- VIRANT, M. AND DRACOS, T. 1997. 3D PTV and its application on lagrangian motion. *Measurement Science and Technology*, **8**, 1539.
- VOTH, G. A., LA PORTA, A., CRAWFORD, A. M., ALEXANDER, J. AND BODENSCHATZ, E. 2002. Measurement of particle accelerations in fully developed turbulence. *Journal of Fluid Mechanics*, **469**, 121–160.
- VOTH, G. A., SATYANARAYAN, K. AND BODENSCHATZ, E. 1998. Lagrangian acceleration measurements at large reynolds numbers. *Physics of Fluids*, **10**, 2268–2280.
- WIENEKE, B. 2012. Iterative reconstruction of volumetric particle distribution. *Measurement Science and Technology*, **24**, 024008.
- WILLERT, C. E. 2006. Assessment of camera models for use in planar velocimetry calibration. *Experiments in Fluids*, **41**, 135–145.
- WILLERT, C. E. AND GHARIB, M. 1991. Digital particle image velocimetry. *Experiments in fluids*, **10**, 181–193.
- WOOD, A., HWANG, W. AND EATON, J. 2005. Preferential concentration of particles in homogeneous and isotropic turbulence. *International Journal of Multiphase Flow*, **31**, 1220–1230.
- WORTH, J. *Tomographic PIV measurement of coherent dissipation scale structures*. PhD thesis, University of Cambridge, 2010.
- WORTH, N. A. AND NICKELS, T. B. 2011. Some characteristics of thin shear layers in homogeneous turbulent flow. *Philosophical Transactions of the Royal Society A: Mathematical, Physical and Engineering Sciences*, **369(1937)**, 709–722.
- YU, H., KANOV, K., PERLMAN, E., GRAHAM, J., FREDERIX, E., BURNS, R., SZALAY, A., EYINK, G. AND MENEVEAU, C. 2012. Studying lagrangian dynamics of turbulence using on-demand fluid particle tracking in a public turbulence database. *Journal of Turbulence*, **13**, 1–29.

Appendix A

Generalized Mie theory for a spherical particle

The theory scattering was explained by Maxwell, Debye and Fourier in different ways, but the theory from Mie became generalized, hence given the name generalized Mie theory (GLMT) (Bohren & Huffman (1983), Kerker (1969), van de Hulst (1981)). Following Bohren and Huffman's notation and development Bohren & Huffman (1983), the geometry of this problem is given in Figure A.1. The reference plane is denoted in black, the scattering plane in gray. The scattering plane is defined as the plane containing the propagation axis and the observer vector \mathbf{r} . The location of the observer is defined in the spherical polar coordinate system (R, θ, ϕ) , where \mathbf{r} is the vector distance between the scattering droplet and the observer, θ is the angle (on the scattering plane) between the light-propagation-axis and the observation, and ϕ is the angle between the reference plane and the scattering plane. The angle between the scattering plane and the polarization direction is denoted as γ . Scattering near $\theta = 0^\circ$ is often called "forward" scattering while scattering near $\theta = 180^\circ$ may be called "backward" scattering.

Light scattered by a spherical particle is in-homogeneously distributed in space depending upon its size, characterized by its diameter d_p , refractive index n , incident light of intensity I_o and wavelength λ , at the angle θ_s . The particle size is usually denoted by size parameter $\alpha = \pi d_p / \lambda$, which takes into account, the size and the wavelength. The flux of scattered light intensity (in Wm^{-2}), in direction θ_s at a distance of R from the scattering sphere is given by

$$I_s\{n, \theta_s\} = \frac{I_o \lambda^2}{4\pi^2 R^2} (i_1\{\alpha, n, \theta_s\} + i_2\{\alpha, n, \theta_s\}), \quad (\text{A.1})$$

where i_1 and i_2 are the intensity functions, given by,

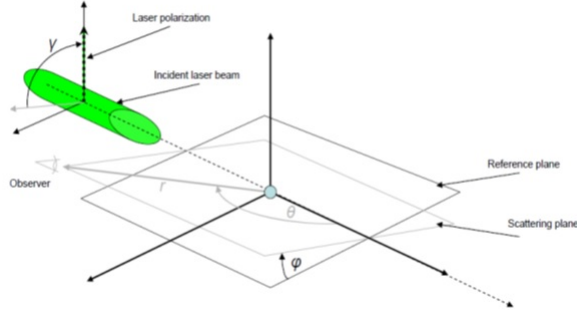


Figure A.1: Mie scattering geometry. Adpated LePera (2012)

$$i_1 = \left| \frac{2n+1}{n(n+1)} [a_n \pi_n + b_n \tau_n] \right|^2 \quad (\text{A.2})$$

$$i_2 = \left| \frac{2n+1}{n(n+1)} [a_n \tau_n + b_n \pi_n] \right|^2. \quad (\text{A.3})$$

Here the index 1 refers to as perpendicular or s polarization and the index 2 refers to parallel or p polarization. π_n and τ_n are the actual angular coefficients that contain the scattering angle, independent of n and α , and contributes to the angular behaviour of the scattered intensity. a_n and b_n , are the scattering coefficients, which contain information on the size and the optical properties of the particle. The equations for a_n and b_n are complicated functions of spherical Bessel functions and their derivatives. Fortunately, the Bessel functions satisfy simple recurrence relations with logarithmic derivatives, and thus can be simplified into the following:

$$a_n = \frac{\left[\frac{D_n(nx)}{n} + \frac{n}{x} \right] \psi_n(x) - \psi_{n-1}(x)}{\left[\frac{D_n(nx)}{n} + \frac{n}{x} \right] \xi_n(x) - \xi_{n-1}(x)} \quad (\text{A.4})$$

$$b_n = \frac{\left[n D_n(nx) + \frac{n}{x} \right] \psi_n(x) - \psi_{n-1}(x)}{\left[n D_n(nx) + \frac{n}{x} \right] \xi_n(x) - \xi_{n-1}(x)}, \quad (\text{A.5})$$

here ψ_n and ξ_n are the Ricatti-Bessel functions. A more complete discussion is covered in Bohren & Huffman (1983), whose notation has been adopted.

Appendix B

Laser sheet calibration

The self-calibration method described by Knutsen *et al.* (2017) works by combining information about the position of particles in object space (from triangulation) with its "sheet space number", which describes a particle's position relative to laser sheet. A laser sheet model is then fit to this data. The model, describes the orientation, width and position of the laser sheets throughout a scan, can be identified without requiring a complex traversing calibration target, which simplifies the procedure substantially.

The variation in illumination of the same particle in successive images throughout the scan, are exploited, as this provides information on the particle's position relative to the laser sheet. If the sheet's profile remains relatively constant and successive sheets are approximately uniformly spaced, then the intensity of light scattered from a single particle as the sheet is scanned across should correspond to the profile of the laser sheet. Figure B.1, illustrates a single particle captured with different illumination in four different images (sheets), with a Gaussian curve fitted to the points. Plotting this intensity variation of the various particles against the "sheet space number", n , and fitting a Gaussian distribution provides a measure of the sheet's position and width (see Figure 3). The centre of the fitted

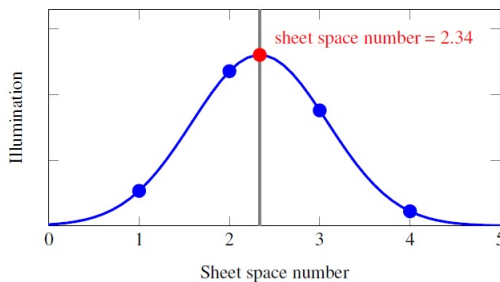


Figure B.1: Illustration of light scattered from a single particle throughout the course of a scan, and its calculated center position based on a Gaussian fit. (Knutsen *et al.* (2017)).

Gaussian distribution is the "sheet space" position of the particle, which represents the fractional sheet number where the scan would pass exactly through the particle location. A computationally inexpensive 3-point Gaussian fit (Willert & Gharib, 1991) is used to fit the sheet number and width of each particle efficiently.

Object matching is performed through a triangulation procedure. The sheet-space position of each particle together with its triangulated position are then used to find the sheet location and orientation through a piecewise-linear least squares fit to equation B.1. Here n_p is the sheet number of the particle in question, and n is the current sheet number of the sheet and image being investigated. The right hand side of equation B.1 is effectively the equation of plane for sheet n , with four fit coefficients A_n , B_n , C_n and D_n and object space coordinates x_p , y_p and z_p . To see this, note that when the particle is coplanar with the sheet, the left hand side vanishes.

$$n_p - n = A_n x_p + B_n y_p + C_n z_p + D_n \quad (\text{B.1})$$

The local spacing between planes Δz_n is

$$\Delta z_n = (A_n^2 + B_n^2 + C_n^2)^{-1/2} \quad (\text{B.2})$$

With $e_n = [A_n; B_n; C_n]_n^T$ as the unit normal of the plane and x_p as the particle object space position, equation B.1 can be written as

$$n_p - n = \frac{e_n x_p + d_{0,n}}{\Delta z_n} = \frac{d}{\Delta z_n} \quad (\text{B.3})$$

where $d_{0,n} = D_n \Delta z_n$ and d is the normal distance of the particle from the sheet center. As the sheet normal and spacing are not constant throughout the course of a scan, a piece-wise linear fit is performed whereby particles near sheet n and its neighbors are used to fit that sheet. This introduces a degree of smoothing and extrapolation of the coefficients of the first and last sheet, which can be controlled by adjusting the domain of the fit. This results in a gradually changing sheet normal and spacing, which is typical of many scanning mechanisms.

Since the width of the fitted Gaussian distribution from the scattered light from each particle is a measure of the laser sheet width, the e^{-2} beam width at each particle location can be estimated from its fit. The width of a sheet w_n is obtained by averaging the average e^{-2} width fitted for all particles near that sheet.

Appendix C

Modified particle tracking heuristics

The minimum acceleration criteria discussed in section 2.3.4, biases the result by avoiding possible high/intermittent acceleration events.

The algorithm was tested using numerical simulation of the direct numerical simulation (DNS) data of turbulent channel flow as discussed in section 3.7. All the experimental parameters except Δt was kept the same as in section 3.7. A smaller value of $\Delta t = 0.004$ was chosen to make the experiment time resolved, that would not miss out the possible high acceleration events of the flow. The particle tracking heuristics used in this study as discussed in section 2.3.4 was also performed to compare the differences both algorithm brings out in the estimated results.

A comparison of the estimated acceleration components using both the algorithm clearly shows that the new modifies algorithm can capture the high/intermittent acceleration events.

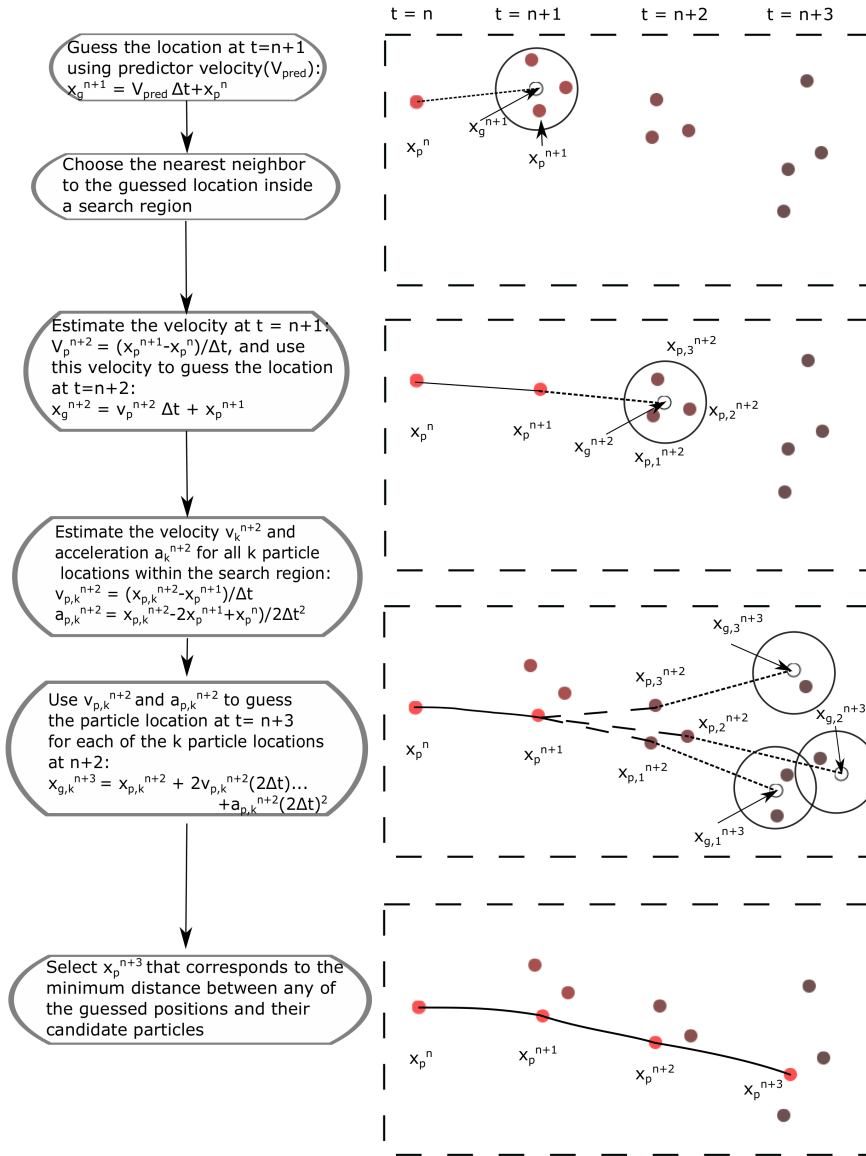


Figure C.1: Schematic representation of the particle tracking algorithm.

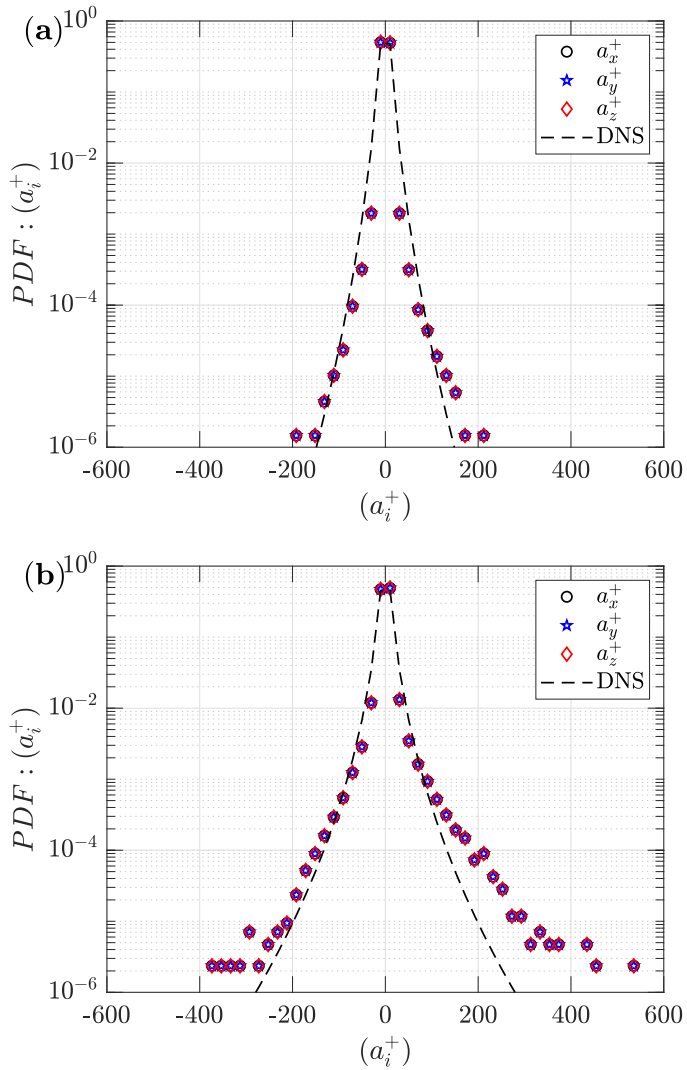


Figure C.2: Comparison of acceleration pdfs obtained using (a) the particle tracking technique used in this thesis to (b) the modified particle tracking technique.

